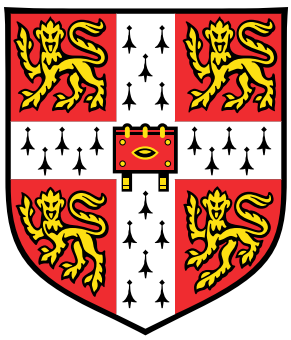

Generalised nonlinear stability of stratified shear flows: adjoint-based optimisation, Koopman modes, and reduced models

Thomas Scott Eaves

July 2016

This thesis is submitted for the degree
of Doctor of Philosophy

St John's College
and
Department of Applied Mathematics and Theoretical Physics
University of Cambridge

Generalised nonlinear stability of stratified shear flows: adjoint-based optimisation, Koopman modes, and reduced models

Thomas Scott Eaves

Abstract

In this thesis I investigate a number of problems in the nonlinear stability of density stratified plane Couette flow. I begin by describing the history of transient growth phenomena, and in particular the recent application of adjoint based optimisation to find nonlinear optimal perturbations and associated minimal seeds for turbulence, the smallest amplitude perturbations that are able to trigger transition to turbulence. I extend the work of Rabin *et al.* (2012) in unstratified plane Couette flow to find minimal seeds in both vertically and horizontally sheared stratified plane Couette flow. I find that the coherent states visited by such minimal seed trajectories are significantly altered by the stratification, and so proceed to investigate these states both with generalised Koopman mode analysis and by stratifying the self-sustaining process described by Waleffe (1997). I conclude with an introductory problem I considered that investigates the linear Taylor instability of layered stratified plane Couette flow, and show that the nonlinear evolution of the primary Taylor instability is not coupled to the form of the linearly unstable mode, in contrast to the Kelvin–Helmholtz instability, for example. I also include an appendix in which I describe joint work conducted with Professor Neil Balmforth of UBC during the 2015 WHOI Geophysical Fluid Dynamics summer programme, investigating stochastic homoclinic bifurcations.

This dissertation is the result of my own work and includes nothing which is the outcome of work done in collaboration except where specifically indicated in the text. Chapter 3 is a modification of Eaves & Caulfield (2015), and a version of Chapter 7 is submitted to the Journal of Fluid Mechanics by the same authors. The contents of Chapter 4 will be included in a manuscript co-authored with C. Caulfield and I. Mezić. The appendix contains joint work with N. Balmforth and appears in Eaves & Balmforth (2016). No parts of this dissertation have been submitted for any other qualification.

Thomas Eaves
19th April 2016

Between the successful defence of this thesis on 10th June 2016 and the submission of the final hard-bound version in July 2016, the contents of Chapter 4 are included in a manuscript submitted to Nature co-authored with C. Caulfield and I. Mezić, and the contents of Chapter 5 are included in a manuscript submitted to the Journal of Fluid Mechanics co-authored with C. Caulfield.

Thomas Eaves
1st July 2016

Acknowledgements

There are a number of people I would like to thank for their assistance during the course of my PhD study. Firstly I would like to thank my supervisor Professor Colm Caulfield for his help and support and for introducing me to this field. His initial proposal to look at minimal seeds in stratified plane Couette flow was the catalyst for the research presented herein, and his enthusiasm for this research has been infectious throughout. I would also like to thank Professor Igor Mezić and Dr Stuart Dalziel for their discussions that inspired the description of the dynamic mode decomposition algorithm and of Koopman modes in Chapter 4. In addition I would like to thank Professor Rich Kerswell for his constructive comments on the material contained in Chapter 5. The research presented in the appendix was the result of a very enjoyable summer spent in Woods Hole, made more so by the other student fellows and the staff at the GFD programme, and particularly due to my collaborator Professor Neil Balmforth and to Giovanni Fantuzzi.

My colleagues in DAMTP have also been an important source of help and friendship throughout my PhD study. In particular I would like to thank Dr John Taylor for help with the Diablo code, Dr Dan Lucas for help with the GMRES code, and Alexis Kaminski for numerous discussions about adjoint-based optimisation. The numerous experimentalists in DAMTP have helped bring fresh perspectives to my research and I am grateful to have been part of such a diverse group of researchers.

I am grateful to the University of Cambridge SIMS Scholarship Fund for funding my PhD research, and to DAMTP and St John's College for their support in attending conferences.

Finally I would like to thank my family for their endless encouragement, and my fiancée Clare for her love and support throughout.

Contents

CHAPTER 1

INTRODUCTION

Stability theory has been of central importance to fluid dynamics since the pioneering work of Reynolds (1883) demonstrated that the transition from laminar to turbulent flow in a cylindrical pipe is governed by a single dimensionless measure of the flow rate, now known as the Reynolds number. Since that time, there has been a vast amount of research identifying simple solutions to the Navier–Stokes equations in simple geometries, and investigating their stability properties. The study of stability has arisen in two parts, both historically and conceptually. The first is the question of whether or not a given solution is asymptotically stable, that is whether all sufficiently small amplitude perturbations eventually decay. This question can be effectively answered by linear stability theory. The second question is what is the domain of attraction of a known asymptotically stable solution, which is necessarily nonlinear.

For solutions that are not asymptotically stable, linear asymptotic stability analysis often provides a good indication of the subsequent evolution of the flow perturbed about such a solution at early times. Information such as the wavelength, phase speed, linear growth rate and structure of growing perturbations are readily obtained from the Orr–Sommerfeld equation, and the viscous Taylor–Goldstein equation (Taylor, 1931; Goldstein, 1931) in the stratified case,

at least numerically, and good agreement is often found with experiments in these regimes. A particularly early example of this is the linear Tollmien–Schlichting wave in a boundary layer, whose analytic form was determined by Tollmien (1929) and Schlichting (1933), and subsequently verified experimentally by Schubauer & Skramstad (1947).

In parallel shear flows, such an approach has identified the well-known Kelvin–Helmholtz instability, found in an unstratified or weakly stratified flow at a sharp vorticity interface. In the stratified case, Holmboe instabilities (1962) (Holmboe, 1962) have been found when a sharp density interface resides in a background shear flow, Taylor instabilities (1931) (Taylor, 1931) when two density interfaces in a background shear flow interact through a coupling of interfacial gravity waves, as well as a number of other instabilities associated with the presence of flow boundaries (Caulfield, 1994). Squire (1933) and Yih (1955) found conditions for such instabilities to be two-dimensional, and in many circumstances such instabilities meet these conditions. More recently, the concept of secondary instabilities has been investigated, in which a nonlinear evolution of a primary instability causes the primary instability to saturate and gives a new flow field which has its own linear instabilities. Mashayek & Peltier categorised the secondary instabilities of the stratified Kelvin–Helmholtz instability (Mashayek & Peltier, 2012a,b) and found a number of two- and three-dimensional secondary instabilities.

Despite these successes of linear theory, the investigation of the second, inherently nonlinear question is vital in order to understand why, for example, the laminar solution of plane Couette flow (PCF), the flow between two horizontal plates moving with nonzero relative velocity, is linearly stable at every Reynolds number (Romanov, 1973) and yet sustained turbulent dynamics has been observed experimentally for Reynolds numbers as low as 325 (Bottin & Chate, 1998). PCF is a two-state system in which both the laminar state and a chaotic turbulent state are asymptotically attracting, and their respective basins of attraction divide the entire state space into two distinct regions. These two regions are then separated by an edge manifold, or 'edge'. There is substantial evidence to demonstrate that for Reynolds numbers far above the critical Reynolds number for transition, many shear flows that have an asymptotically attracting laminar state are a two state system (see Duguet *et al.*, 2008). Near the critical Reynolds number for transition

below which turbulent dynamics cannot be maintained, there is growing evidence (see Chantry & Schneider, 2014) that the edge manifold becomes 'wrapped up' into the turbulent state, where the precise role of the edge manifold is less clear.

Under the assumption that the system of interest has a well-defined edge manifold that separates trajectories leading to either the laminar or turbulent attractor, we can also identify what happens to trajectories that begin on the edge manifold. Since we do not expect trajectories to become unbounded, initial conditions on the edge manifold are attracted to one of a collection of fixed points, periodic orbits, relative periodic orbits or chaotic attracting sets residing entirely within the edge manifold. An 'edge state' is a state in the edge manifold which is an attractor for trajectories on the edge. The simplest edge state structure is a single saddle in solution space of codimension one whose stable manifold, the collection of points in state space that are attracted to the edge state in the limit of infinite time, is precisely the edge manifold, and whose unstable manifold is directed into the basins of attraction of the laminar and turbulent attractors. In more complex scenarios, the edge manifold itself could contain multiple attractors, and the edge manifold is then the intersection in state space of the stable manifolds of the respective attractors. Many edge states have been identified in various fluid dynamical systems (see Duguet *et al.*, 2008), but their main role in the stability problem is providing a stable manifold that we can identify as an edge manifold and so distinguish regions of state space.

The importance of the domain of attraction of asymptotically stable solutions and of nonlinearity in stability theory was highlighted by Morkovin (1969), who identified the possibility of transition from a laminar to a turbulent state not involving linear growth mechanisms as 'bypass' transitions. In the language of dynamical systems, these 'bypass' transitions are simply the above observation that the state space contains not only an asymptotically stable laminar state, but also another asymptotically attracting state. Even for flows in which there is not a chaotic turbulent attractor, there can exist simple exact solutions that are asymptotically stable, for example the upper branch so-called Nagata solution in plane Couette flow (Nagata, 1990). Since these two (or more) attractors have different domains of attraction, it is possible that initial conditions nearby to the laminar state in state space do in fact transition to turbulence without displaying

any linear growth mechanism (see Rempfer, 2003).

The possibility of initial conditions close to the laminar state becoming turbulent, or following a long, energetic path in phase space before returning to the laminar solution requires linear or nonlinear mechanisms for substantial transient energy growth. Two well-known transient growth mechanisms are the Orr mechanism (Orr, 1907*a*,*b*) and the lift-up mechanism (see Landahl, 1980). These can be derived analytically from the Rayleigh equation (see Schmid & Henningson, 2000) and depend on the non-normality of the associated linear differential operator.

A common approach to investigating transient growth is optimal perturbation analysis, the search for the initial perturbation that leads to the most growth over some time interval. These ideas were applied originally to linear problems (Farrell, 1988*a*,*b*; Moore & Farrell, 1992; Farrell & Ioannou, 1993, 1996*a*,*b*), and have recently gained renewed interest (see Constantinou & Ioannou, 2011; Arratia *et al.*, 2013; Kaminski *et al.*, 2014) since the review of the linear 'direct-adjoint looping' (DAL) method by Schmid (2007).

However, any approach attempting to deduce information about the nonlinear flow evolution based upon a linearised set of equations contains an essential contradiction; linearising the equations of motion hard-wires into any results the idea that the variables being calculated are infinitesimally small and remain so for all times, unable to affect the flow in any way. The purpose of linear stability analysis in the dynamical systems view of the stability problem is simply to determine the asymptotic stability or instability of a given solution. When this solution is asymptotically stable, then energy stability (the monotonic decay of any finite amplitude perturbation) is sufficient for global asymptotic stability. When the solution is asymptotically stable but not globally asymptotically stable, for example when there is a co-existence of attracting laminar and turbulent states, the linear problem may provide insight into the types of physical mechanisms which might occur as a typical flow trajectory evolves. However, Pringle & Kerswell (2010) demonstrated that solutions to the linear transient growth problem are essentially *irrelevant* to the critical amplitude and flow structures required for the transition process; critical amplitudes for transition to turbulence based on a three-dimensional, fully localised nonlinear optimal initial condition are at least an order of magnitude smaller than the amplitude required for initial conditions

based on a finite amplitude version of the two-dimensional linear optimal perturbation. Even for cases in which the solution is asymptotically unstable, though the initial growth rate, wavelength and phase speed are often observed in the initial nonlinear departure from the unstable solution, the subsequent evolution of the flow is not necessarily tied to the linear stability properties of the original solution; exponential growth of an infinitesimal quantity remains infinitesimal.

This issue has been mostly glossed over due to the grand successes of linear stability theory in the prediction of various properties of the nonlinear saturation and longevity of solutions associated with linear instability in the Kelvin–Helmoltz problem, Rayleigh–Bernard convection and Taylor–Couette flow, amongst others (see Drazin & Reid, 1981). We demonstrate a primary linear instability that does not saturate at finite amplitude in Chapter 7 for an inherently stratified linear instability identified by Taylor (1931).

To understand critical conditions for transition to turbulence, it is necessary to identify the smallest amplitude perturbation to the laminar state that will eventually transition to turbulence, which we call the 'minimal seed', following Pringle & Kerswell (2010). The identification of minimal seeds is made possible by the generalisation of the DAL method to nonlinear problems of Pringle & Kerswell (2010), although a number of the key ideas have been used in control theory and data assimilation for some time (for a discussion, see the review by Luchini & Bottaro, 2014). Since the work of Pringle & Kerswell (2010) the nonlinear DAL method has been applied to the identification of minimal seeds (see Cherubini *et al.*, 2010; Monokrousos *et al.*, 2011; Pringle *et al.*, 2012; Rabin *et al.*, 2012), to bursting phenomena (Cherubini & De Palma, 2013) and to other nonlinear fluid dynamical optimisation problems for which the choice of norm that defines perturbation 'growth' is less rigidly constrained (Foures *et al.*, 2012, 2013, 2014). The application of the nonlinear DAL method to finding minimal seeds was recently summarised in the review by Kerswell *et al.* (2014).

Put in the language of edge manifolds, a minimal seed is the identification of the 'closest' approach of the edge manifold to the laminar state. Once such a minimal seed is identified, since it lies infinitesimally above the edge manifold and the edge manifold is the stable manifold of the edge state, its trajectory to the turbulent attractor will consist of following the edge manifold towards a

state in the edge manifold before eventually leaving the vicinity of the state along an unstable manifold, towards the turbulent attractor. Therefore, the edge state determines the minimal seed for turbulence in so far as it sets the shape of its own stable manifold. However, it is important to remember that this shape is not an intrinsic feature of the edge state, but rather of the equations of motion. The edge state and other states in the edge manifold determine a key component of the transition mechanism, since the closer an initial condition is to the edge manifold, the longer it will spend in the vicinity of such a state before being directed towards the turbulent attractor. The identification of a minimal seed, or lack thereof, is in some sense *the* stability problem in nonlinear fluid dynamics.

The minimal seed in unstratified PCF found by Rabin *et al.* (2012) exhibits just such a long residency time near a coherent state consisting of nearly streamwise independent rolls and streaks, before eventually transitioning to turbulence. This coherent state can be interpreted as a manifestation of the 'self-sustaining process' (SSP) physically described by Waleffe (1997), or equivalently as a finite Reynolds number realisation of the asymptotic vortex-wave interaction (VWI) of Hall & Smith (1991) as demonstrated numerically by Hall & Sherwin (2010). These solutions to the Navier–Stokes equations consist of small amplitude streamwise independent roll structures creating much larger amplitude velocity streaks in the flow, which in turn suffer instabilities to produce waves, which then reinforce the rolls, hence leading to a self-sustaining process. This process is in a delicate balance since the small amplitude roll structures are readily susceptible to viscous decay, and so the role of the waves is to inject energy into the rolls at a rate that exactly offsets this viscous decay.

In terms of the coherent state identified by Rabin *et al.* (2012) (a simple lower branch SSP/VWI state) to which their minimal seed is attracted for a substantial period of its evolution, trajectories in state space that eventually decay or grow correspond to the waves being either too energetic, and so reinforcing the rolls too much, thus transitioning to turbulence, or being not energetic enough, in which case the perturbation slowly decays back to the laminar solution. The SSP/VWI states are dynamically most sensitive to the feedback from the waves into the rolls since this is an inherently nonlinear process, whereas the rest of the cycle depends on linear transient growth and linear instability.

The importance of exact solutions, and particularly periodic orbits, of the Navier–Stokes equations is becoming increasingly recognised (see Kawahara *et al.*, 2012, for a review). Low-dimensional chaotic systems are often expressible in terms of suitable averages over unstable periodic orbits that are embedded in the chaotic attractor (Cvitanović, 1987; Cvitanović & Eckhardt, 1989). There is increasing evidence for a multitude of unstable steady states and unstable periodic orbits embedded in turbulent fluid flows (Eckhardt *et al.*, 2008; Kreilos & Eckhardt, 2012; Chandler & Kerswell, 2013), particularly after reduction of continuous symmetries (Willis *et al.*, 2013). Exact solutions of SSP/VWI type are claimed to be the 'skeleton' about which all turbulent motions in canonical shear flows are organised (Hall & Sherwin, 2010), and we will consider the effect of stratification on such solutions in this thesis via the identification of minimal seeds and their subsequent trajectories in stratified plane Couette flow.

Complementary to the search for unstable periodic orbits embedded in chaotic attractors is a phenomenological approach which attempts to reduce observed dynamics to the evolution of a small set of modes. Individually, such modes do not necessarily hold any meaning in terms of state space structures, but the sum of these modes and their evolution in time is meant to accurately represent a given state space trajectory or collection of trajectories. We may divide attempts at modal reduction into two broad categories, predictive and deductive. Predictive modal reductions typically project the equations of motion onto a set of modes that are intuited from observations of typical flow trajectories. For example, the SSP formulation of Waleffe (1997) essentially projects the equations of motion onto roll, streak and wave structures before further reduction onto an eight-dimensional system of ODEs. Most recently, Chantry *et al.* (2016) reproduce the phenomena of turbulent bands and spots in bounded shear flows by projection of the dynamics of the shear-normal direction onto only six modes.

Deductive modal reductions, on the other hand, are typically ignorant of the equations of motion, and are based instead on the decomposition of data gained from individual state space trajectories. The predictive ability of such reductions is often poor unless the trajectories studied visit a large enough region of state space. The value of such reductions instead lies in revealing fundamental physical processes that occur in a given flow which are otherwise obscured by complex

spatio-temporal behaviour. A popular data-driven deductive modal reduction is 'proper orthogonal decomposition' (POD) (Holmes *et al.*, 1998). However, POD often fails in the attempt to describe key physical processes because it decomposes the data into *energetic* structures rather than *dynamic*, evolving structures.

The search for important dynamic structures is made possible by analysing the spectral properties of the Koopman operator (Mezić, 2005), which evolves observables defined on a state space forward in time along a given trajectory. The Koopman operator provides Koopman modes which are dynamically evolving structures with associated (instantaneous) growth rates. The search for Koopman modes has gained considerable interest due to its recently reported numerical approximation for finding Koopman modes called 'dynamic mode decomposition' (DMD) (see Schmid & Sesterhenn, 2008; Rowley *et al.*, 2009; Schmid, 2010; Mezić, 2012, for a review). The DMD algorithm decomposes any data set, numerical or experimental, into a set of modes that approximate a subset of Koopman modes, and its popularity has arisen primarily due to the extremely computationally efficient algorithm provided by Schmid (2010), as well as numerous extensions and improvements (see Chen *et al.*, 2012, for example).

The primary focus of this thesis is to investigate the effect of the addition of a stable density stratification to the dynamical systems view of shear flows, particularly in vertically and horizontally sheared stratified PCF. The addition of a stable density stratification to PCF through either fixing the density of the fluid at each of the horizontal plates at different (statically stable) values in the vertically sheared case, or by applying a constant background density gradient in the spanwise direction in the horizontally sheared case, tends to inhibit vertical motions due to them being less energetically favourable. The density field is an active scalar, and its feedback onto the velocity field appears through the bulk Richardson number, which is a global measure of the ratio of potential energy to kinetic energy of the laminar state.

In addition to the inhibition of vertical motions, stratified shear flows may also exhibit oscillatory dynamics due to the presence of internal gravity waves, and also spontaneous layering in the horizontally sheared case due to a nonmonotonic dependence of density flux on the local Richardson number (Phillips, 1972; Oglethorpe *et al.*, 2013). All of these phenomena are likely to have a significant

impact on the transition process. We expect the inhibition of vertical motions to in some sense stabilise the flow, and so we expect minimal seeds in these flows to become of larger energy as the stratification strength is increased, so that the distance of the closest approach of the edge manifold to the laminar state increases.

The inhibition of vertical motions is likely also to disrupt significantly the SSP/VWI type coherent states visited by minimal seed trajectories since they rely on extremely small amplitude rolls that have components of motion in the direction of gravity. Given that the SSP/VWI ansatz is likely to be disrupted or even completely destroyed as the stratification strength increases, we need to identify new dynamical ingredients that could lead to self-sustaining motion, and the possibility of coupling with oscillating internal gravity waves is a prime candidate. Finally, since it is possible to have spontaneous layering in the horizontally sheared case, the very characteristics of the final chaotic turbulent state for the transition process can change significantly, and we expect this to have an impact on the transition process itself.

In particular, there are a number of important problems that we would like to address in this thesis in light of the above discussion. We would like to know how stratification affects minimal seeds in both vertically and horizontally sheared stratified PCF both in terms of the form and energy of the initial condition and in terms of its subsequent trajectory towards the turbulent attractor. Given the importance of the SSP/VWI type edge state visited by the unstratified minimal seed in PCF, we would like to investigate precisely how stratification perturbs the SSP/VWI ansatz. More generally, we would like to produce a reduced model not only for the edge state in such systems, but also for transient dynamics past the edge state, and to investigate the effect of stratification on such a model. We would also like to explore the nonlinear dynamics that produce and sustain layered stratifications in horizontally sheared flow, and to investigate therein the role of linear instability mechanisms, minimal seeds and edge states, and reduced models.

The plan of this thesis is as follows. In Chapter 2 we discuss the mathematical development of hydrodynamic stability theory through linear transient growth to nonlinear transient growth, the minimal seed in unstratified PCF found by Rabin *et al.* (2012), and its subsequent trajectory through state space during the transition to turbulence. We describe the numerical implementation used in this

thesis of the nonlinear DAL method for identifying minimal seeds and discuss the validation of the numerical method by comparing both to the results of Rabin *et al.* (2012) in the unstratified case and to newly computed linear transient growth results for the stratified case.

In Chapter 3 we investigate vertically sheared stratified PCF and how the minimal seed and its subsequent trajectory in state space, and the identifiable coherent structures on this trajectory, are affected by stratification and its inhibition of vertical motions. In particular, we focus on how the energy of the minimal seeds vary with increasing stratification, and how the coherent states, which in the unstratified case are SSP/VWI states, vary with increasing stratification and are disrupted due to the inhibition of vertical motions by static stability. As the bulk Richardson number is increased, the coherent states move away from the nearly streamwise aligned SSP/VWI solutions and take on an oblique three-dimensionality. We conclude by identifying a scaling law between the Reynolds number and bulk Richardson number at which we first expect the SSP/VWI ansatz to be disrupted by the presence of a stable stratification. The contents of this chapter are published in Eaves & Caulfield (2015).

In Chapter 4 we compute the Koopman modes present during the transition to turbulence of the minimal seeds found in Chapter 3 in order to find a reduced modal description of the transition process. We start by summarising the DMD algorithm used to compute the Koopman modes before describing the Koopman operator and its spectral properties and how it relates to DMD. Upon applying the DMD algorithm to the minimal seed trajectories, we see that for a number of parameter values we can reduce the dynamics on the transition to turbulence to only two or three modes, and that these modes provide an excellent approximation of the edge state and of the dynamics on its stable and unstable manifolds, not only in the vicinity of the edge state but over a substantial period of the evolution of the minimal seed. We conclude by speculating about a relationship between nearby exact coherent states and the existence of neutral Koopman modes on a given state space trajectory.

In Chapter 5 we return to the disruption of the SSP/VWI ansatz found in Chapter 3. We revisit the sequence of calculations presented by Waleffe (1997) that describe on physical grounds SSP/VWI type solutions and introduce the

effect of the density field at each stage in this process. We find that the first effect of the addition of a stable stratification as the bulk Richardson number is increased is to produce a bifurcation to oscillatory dynamics in the roll solution associated with internal gravity waves, and that the occurrence of this bifurcation is consistent with the scaling law presented in Chapter 3. We then continue by investigating the effect of stratification on the rest of the SSP process and find that the streaks, waves, and feedback of the waves onto the roll solution are essentially unaffected by the stratification for parameter values below the bifurcation point in the roll solutions.

In Chapter 6 we present preliminary findings in the search for minimal seeds in horizontally sheared stratified PCF, for which the SSP/VWI ansatz is disrupted once more, although for the horizontally sheared case the coherent states remain nearly streamwise independent, and temporal oscillations appear to dominate. The boundary conditions and direction of the shear in the horizontally sheared case allow the existence of a turbulent state, and hence a minimal seed, for much larger bulk Richardson numbers than for the vertically sheared case. For sufficiently large bulk Richardson numbers we find that the turbulent states consist of spontaneously formed layers in the density field. Unfortunately, the transition process to these layered states takes place over time scales that are too large for the current nonlinear DAL method to find minimal seeds over feasible computing time, but our preliminary findings indicate a reduction to quasi-one-dimensional dynamics through much of the transition process. We show preliminary results of a reduced model based on this observation, and believe that the full dynamics may be amenable to a completion of such a reduced model.

In Chapter 7 we change focus somewhat and consider the linear stability analysis and subsequent nonlinear evolution of the primary linear instabilities in three layer vertically sheared stratified PCF due to the ubiquitousness of layered states in stratified shear flows. The base flow under consideration is susceptible to primary linear instabilities of both Holmboe and Taylor type (Holmboe, 1962; Taylor, 1931), but not of Kelvin–Helmholtz type. The Taylor instability is the instability with largest growth rate for the parameter values we consider. We consider cases for which the base flow is susceptible to both Taylor and Holmboe instabilities, and also to only the Taylor instability. Unlike the Kelvin–Helmholtz instability,

which is well-known to saturate at finite amplitude and dominate the subsequent dynamics, we show that the nonlinear evolution of the primary Taylor instability is inevitably subsumed by the appearance of nonlinear Holmboe waves, whether or not the base flow has a primary Holmboe instability, and so the Taylor instability cannot be thought of as 'saturating' at finite amplitude.

In Chapter 8 we draw our conclusions and point to possible future research. We discuss the research contained in this thesis in the wider context of the dynamical systems view of turbulence and emphasise a number of possible new directions for the field that this work has pointed towards. The appendix contains results of a short research project conducted with Prof. Neil Balmforth investigating the effect of stochasticity on the dynamics nearby to homoclinic bifurcations in two- and three-dimensional model systems. The model systems chosen display dynamics from simple periodic orbits to Lorenz and Shilnikov type chaos. We generalise the deterministic analysis of Balmforth *et al.* (1994) to the stochastic case and derive asymptotically one-dimensional stochastic Poincaré maps for such systems. The contents of this appendix are published in Eaves & Balmforth (2016).

CHAPTER 2

NONLINEAR STABILITY

The laminar solution of plane Couette flow (PCF), in which the velocity field is a simple shear, is stable to linear normal mode perturbations at every Reynolds number (Romanov, 1973). The same is true for stratified PCF in which a statically stable density difference is maintained across the two horizontal plates and the density field has a constant gradient. Nevertheless, turbulent dynamics has been observed experimentally in unstratified PCF for Reynolds numbers greater than about 325 (Bottin & Chate, 1998). This phenomenon is not only restricted to PCF. Indeed, this is also true of other canonical shear flows such as pipe flow, which is stable to linear normal mode perturbations at every Reynolds number and yet displays turbulent dynamics, and plane Poiseuille flow, which is known to display turbulent dynamics for $Re \geq 1200$ (Tuckerman *et al.*, 2014), whereas the critical Reynolds number beyond which it is unstable to linear normal mode perturbations is $Re = 5772$ (see Orszag, 1971).

There have been numerous attempts to address the issue of observed turbulent dynamics at linearly asymptotically stable parameter values. These have progressed in mathematical complexity and in successful explanations as computational technology has advanced the types of problem we are able to tackle. This chapter proceeds historically by first summarising the topic of linear transient

growth for autonomous operators in Section 2.1, then describing the variational technique that can solve the linear transient growth problem for nonautonomous operators in Section 2.2. We then discuss how the variational technique can be generalised to solve nonlinear transient growth problems in Section 2.3. The nonlinear transient growth variational technique, or nonlinear 'direct-adjoint looping' (DAL), is the primary technique used here to investigate the nonlinear stability of stratified PCF, and so in Section 2.4 we describe how this technique is implemented numerically. In Section 2.5 we demonstrate that the numerical implementation of the nonlinear DAL reproduces known results, both in its high energy nonlinear regime where we compare to the unstratified work of Rabin *et al.* (2012) and in its low energy linear limit for stratified PCF. This gives us confidence to proceed into the nonlinear investigation of the stability of stratified PCF presented in Chapters 3 and 6.

2.1 Linear transient growth

If we linearise the equations of motion for a Newtonian fluid about a one dimensional base flow $\mathbf{U} = U(y)\hat{\mathbf{x}}$, we obtain the well-known Orr–Sommerfeld and Squire equations

$$\left[\left(\frac{\partial}{\partial t} + U\frac{\partial}{\partial x}\right)\nabla^2 - U''\frac{\partial}{\partial x} - \frac{1}{Re}\nabla^4\right]v = 0, \tag{2.1}$$

$$\left[\frac{\partial}{\partial t} + U\frac{\partial}{\partial x} - \frac{1}{Re}\nabla^2\right]\eta = -U'\frac{\partial v}{\partial z}, \tag{2.2}$$

where $\eta = \partial_z u - \partial_x w$ is the y-vorticity and primes denote differentiation with respect to y, and Re is the Reynolds number. This is to be solved along with the boundary conditions $v = v' = \eta = 0$ on solid walls or at ∞ and initial conditions $v = v_0$ and $\eta = \eta_0$ at $t = 0$. This can be written in the compact form

$$\frac{\partial}{\partial t}\begin{bmatrix} v \\ \eta \end{bmatrix} = \begin{bmatrix} \mathcal{L}_{OS} & 0 \\ \mathcal{L}_C & \mathcal{L}_{SQ} \end{bmatrix}\begin{bmatrix} v \\ \eta \end{bmatrix}, \tag{2.3}$$

where $\mathcal{L}_{OS}$, $\mathcal{L}_{SQ}$ and $\mathcal{L}_C$ are the Orr–Sommerfeld, Squire and coupling operators respectively. We can then ask which, if any, linear disturbances (v_0, η_0) grow as $t \to \infty$, answering the asymptotic linear stability problem, or transiently over

some finite time horizon $t \in [0, T]$. For such an autonomous system, we may answer both questions on a discretised spatial domain with methods taken from linear algebra, which we now outline.

Formally, consider the linear in time, autonomous differential equation for the state vector $\mathbf{q}(\mathbf{x}, t) \in \mathbb{R}^n \times \mathbb{R}$,

$$\frac{\partial \mathbf{q}}{\partial t} = \mathcal{A}\mathbf{q}, \tag{2.4}$$

where $\mathcal{A}$ is a differential operator in space only and is independent of time, so that it is autonomous, and independent of $\mathbf{q}$ so that the problem is linear. We denote the initial condition for this equation $\mathbf{q}_0 = \mathbf{q}(\mathbf{x}, 0)$. Then, since the equation is autonomous, its formal solution is given by

$$\mathbf{q}(\mathbf{x}, t) = \exp\left[\mathcal{A}t\right] \mathbf{q}_0. \tag{2.5}$$

More generally, we could write the solution to any autonomous or nonautonomous equation as $\mathbf{q} = \mathbf{\Phi}(t)\mathbf{q}_0$, where $\mathbf{\Phi}(t)$ is the propagator that maps an initial condition onto its value at time t. However, this operator is in general not expressible in closed form unless the operator $\mathcal{A}$ is autonomous.

The key question in stability theory is whether or not a given perturbation, or initial condition $\mathbf{q}_0$, will grow or decay in time. This requires a concept of size, and so we assign a norm to solutions $\mathbf{q}(\mathbf{x}, t)$, which we denote $\|\mathbf{q}\|$. It is convenient for the analysis that follows if the norm arises from an inner product, and so we write $\|\mathbf{q}\|^2 = \langle \mathbf{q}, \mathbf{q} \rangle$. This allows us to introduce the adjoint of the operator $\mathcal{A}$ as the operator $\mathcal{A}^\dagger$ that satisfies $\langle \mathbf{q}_1, \mathcal{A}\mathbf{q}_2 \rangle = \langle \mathcal{A}^\dagger \mathbf{q}_1, \mathbf{q}_2 \rangle$ for all $\mathbf{q}_1(\mathbf{x}, t)$ and $\mathbf{q}_2(\mathbf{x}, t)$. A physically relevant norm for a fluid system would be the total energy in the flow, but the following analysis does not require the form of the norm to be specified.

The stability problem can then be formulated by requiring the evaluation of the maximum achievable gain at each time t, which may be expressed as

$$G(t) = \max_{\mathbf{q}_0 \neq 0} \frac{\|\mathbf{q}(\mathbf{x}, t)\|^2}{\|\mathbf{q}_0\|^2}. \tag{2.6}$$

We may also define the absolute maximal gain as $G_{\max} := \max_{t \geq 0} G(t)$, which is allowed to be infinite in the case of linear asymptotic instability. Then, perturbations are able to grow either indefinitely or transiently if $G_{\max} > 1$.

Traditional linear stability analysis deals with the concept of asymptotic linear stability, that is the determination of $\lim_{t \to \infty} G(t)$. For example, if the operator

$\mathcal{A}$ has eigenvalues $\{\lambda_1, \ldots, \lambda_n\}$, labelled so that $\Re(\lambda_1) \geq \cdots \geq \Re(\lambda_n)$ and with corresponding eigenvectors $\{\mathbf{v}_1, \ldots, \mathbf{v}_n\}$, then for a general initial condition

$$\mathbf{q}_0 = \sum_{k=1}^{n} \alpha_k \mathbf{v}_k, \tag{2.7}$$

we have

$$\mathbf{q}(\mathbf{x}, t) \sim \alpha_1 \exp(\lambda_1 t)\mathbf{v}_1 \quad \text{as } t \to \infty. \tag{2.8}$$

Then the system is linearly asymptotically stable if and only if $\Re(\lambda_1) < 0$, in which case $\|\mathbf{q}(\mathbf{x}, t)\| \to 0$ and $G(t) \to 0$ as $t \to \infty$.

The use of asymptotic linear theory has successfully predicted the onset of transition to turbulence from a laminar state as a control parameter is moved through its critical value in in Rayleigh–Bernard convection, for which the Rayleigh number beyond which the steady conductive solution is linearly asymptotically unstable corresponds precisely with the Rayleigh number beyond which non-conductive dynamics are observed, and Taylor–Couette flow, for which the Reynolds number beyond which the laminar flow is linearly asymptotically unstable corresponds precisely with the Reynolds number beyond which non-laminar dynamics are observed (see Drazin & Reid, 1981). However, these flow configurations demonstrate only two of a few successful applications of asymptotic linear stability analysis to the prediction of transition to turbulence from a well-defined laminar state; supercritical transition to turbulence is a rare phenomenon in high Reynolds number fluid dynamics.

At first sight, an appealing way around this difficulty is to investigate instead $G(t)$ at intermediate, finite times and solve for $G_{\max}$ in the hope that instead of requiring linearised solutions to blow up exponentially to trigger turbulence, there might be initial conditions that grow sufficiently large in amplitude that they trigger transition before they are able to decay. To this end, we note that, formally,

$$G(t) = \max_{\mathbf{q}_0 \neq 0} \frac{\|\mathbf{q}(\mathbf{x}, t)\|^2}{\|\mathbf{q}_0\|^2} = \max_{\mathbf{q}_0 \neq 0} \frac{\|\exp[\mathcal{A}t]\,\mathbf{q}_0\|^2}{\|\mathbf{q}_0\|^2} = \|\exp[\mathcal{A}t]\|^2, \tag{2.9}$$

where the operator norm is defined as $\|\mathbf{B}\| := \max_{\mathbf{v}\neq 0} \|\mathbf{B}\mathbf{v}\|/\|\mathbf{v}\|$ for any operator $\mathbf{B}$ that acts on vectors $\mathbf{v}$. We may construct upper and lower bounds for $G(t)$ by noting that $\exp[\mathcal{A}t]\,\mathbf{v}_1 = \exp[\lambda_1 t]\,\mathbf{v}_1$, and so

$$G(t) \geq \exp[2\Re(\lambda_1)t]\,. \tag{2.10}$$

Also, by writing $\mathcal{A} = \mathbf{V}\mathbf{\Lambda}\mathbf{V}^{-1}$, we have

$$G(t) = \|\mathbf{V}\exp\left[\mathbf{\Lambda}t\right]\mathbf{V}^{-1}\|^2 \leq \|\mathbf{V}\|^2\|\exp\left[\mathbf{\Lambda}t\right]\|^2\|\mathbf{V}^{-1}\|^2 = \kappa(\mathbf{V})^2\exp\left[2\Re(\lambda_1)t\right], \tag{2.11}$$

where $\kappa(\mathbf{V}) := \|\mathbf{V}\|\|\mathbf{V}^{-1}\|$ is the condition number of the matrix operator $\mathbf{V}$ and is a measure of the relative size of the maximum and minimum eigenvalues of $\mathbf{V}$.

We have arrived at the bounds

$$\exp\left[2\Re(\lambda_1)t\right] \leq G(t) \leq \kappa(\mathbf{V})^2\exp\left[2\Re(\lambda_1)t\right], \tag{2.12}$$

from which we see the importance of the condition number $\kappa(\mathbf{V})$. In particular, if $\mathcal{A}$ were normal, i.e. that $\mathcal{A}\mathcal{A}^\dagger = \mathcal{A}^\dagger\mathcal{A}$, where $\mathcal{A}^\dagger$ is the adjoint of $\mathcal{A}$, then $\{\mathbf{v}_1, \ldots, \mathbf{v}_n\}$ is an orthonormal basis, and $\|\mathbf{V}\| = \|\mathbf{V}^{-1}\| = 1$. Hence, normal operators do not admit transient growth; it is impossible to have $G_{\max} > 1$ when $\Re(\lambda_1) < 0$. Linear transient growth is therefore synonymous with non-normality.

For autonomous operators we may calculate $G(t)$ explicitly via singular value decomposition. Let $t = t_0$ and consider $\mathbf{B} = \exp\left[\mathcal{A}t_0\right]$, the propagator up to time t_0. Then the singular value decomposition of $\mathbf{B}$ is the triplet of operators $(\mathbf{U}, \mathbf{V}, \mathbf{\Sigma})$ such that $\mathbf{B}\mathbf{V} = \mathbf{U}\mathbf{\Sigma}$, where $\mathbf{U}$ and $\mathbf{V}$ are unitary and $\mathbf{\Sigma} = \mathrm{diag}(\sigma_1, \ldots, \sigma_n)$ is a diagonal operator of singular values $\sigma_i \in \mathbb{R}$ with $\sigma_1 \geq \cdots \geq \sigma_n$. If we label the first columns of $\mathbf{U}$ and $\mathbf{V}$ as $\mathbf{u}_1$ and $\mathbf{v}_1$ then we observe that $\mathbf{B}\mathbf{v}_1 = \sigma_1\mathbf{u}_1$, and so $\|\mathbf{B}\mathbf{v}_1\| = \sigma_1\|\mathbf{u}_1\| = \sigma_1$ since $\mathbf{U}$ is unitary. The evaluation of $G(t_0)$ is then given by

$$\begin{aligned} G(t_0) = \|\mathbf{B}\|^2 &= \max_{\mathbf{x}\neq 0}\frac{\langle\mathbf{B}\mathbf{x}, \mathbf{B}\mathbf{x}\rangle}{\langle\mathbf{x}, \mathbf{x}\rangle} = \max_{\mathbf{x}\neq 0}\frac{\langle\mathbf{U}\mathbf{\Sigma}\mathbf{V}^\dagger\mathbf{x}, \mathbf{U}\mathbf{\Sigma}\mathbf{V}^\dagger\mathbf{x}\rangle}{\langle\mathbf{x}, \mathbf{x}\rangle} \\ &= \max_{\mathbf{x}\neq 0}\frac{\langle\mathbf{\Sigma}\mathbf{V}^\dagger\mathbf{x}, \mathbf{\Sigma}\mathbf{V}^\dagger\mathbf{x}\rangle}{\langle\mathbf{x}, \mathbf{x}\rangle} = \max_{\mathbf{y}\neq 0}\frac{\langle\mathbf{\Sigma}\mathbf{y}, \mathbf{\Sigma}\mathbf{y}\rangle}{\langle\mathbf{y}, \mathbf{y}\rangle} = \sigma_1^2(t_0), \end{aligned} \tag{2.13}$$

where the equality between the two lines follows since $\mathbf{U}$ is unitary. We therefore have an explicit equation for $G(t_0)$, and we can identify the initial condition that leads to this gain as $\mathbf{q}_0 = \mathbf{v}_1(t_0)$. We have made explicit the time dependence of the singular value $\sigma_1(t_0)$ and its singular vector $\mathbf{v}_1(t_0)$ to emphasise the fact that if we are interested in the gain at some other time t_1 then the operator $\mathbf{B}$ will be different, and the largest singular value and its associated singular vector which gives the initial condition $\mathbf{q}_0$ also will be different.

The above statement is simply that different initial conditions are most dangerous in terms of energy growth over different time horizons. For example, the

Orr mechanism (Orr, 1907*a*) in parallel shear flows is in some sense fast acting whilst the lift-up mechanism (see Landahl, 1980) is a cumulative effect, and so if the above decomposition were performed on such a flow, then an initial condition that utilises the Orr mechanism would be expected to be the solution for largest gain over a short time horizon, whereas an initial condition that utilises the lift-up mechanism would be expected to be the solution for largest gain over a sufficiently long time horizon.

We now have a technique to find numerically the initial conditions that lead to the largest gain of a given norm of the solution to our autonomous linear differential equation. However, an inherent simplification we have made is that of an autonomous operator. In many fluid dynamical problems, we are not interested in the stability of a static base state but instead wish to investigate the stability of some time-dependent solution. It is clear that similar ideas of non-normality giving transient growth should continue to hold when the operator $\mathcal{A}$ is nonautonomous. If our operator is time periodic, we may be able to employ ideas from Floquet analysis to generalise the calculation presented above. However, in the general case, we cannot follow the above calculation because it relies on an explicit knowledge of the form of the propagator $\mathbf{\Phi}(t)$. To overcome this problem, we may instead reformulate the identification of initial conditions that lead to the largest gain $G(t)$ as a variational problem instead of a linear algebra problem. For autonomous operators, the variational problem is less efficient at solving for $G(t)$ than the linear algebra approach. However, the variational problem is readily generalised to the fully nonlinear stability problem whereas the linear algebra approach is inherently tied to the linearity of the equations of interest. We therefore discuss the variational problem in the next section.

2.2 Variational method

Consider again the linear differential equation

$$\frac{\partial \mathbf{q}}{\partial t} = \mathcal{A}\mathbf{q}, \tag{2.14}$$

for $\mathbf{q} \in \mathbb{R}^n \times \mathbb{R}$ equipped with an inner product $\langle \cdot, \cdot \rangle$. Then to maximise the gain $G(t) = \max_{\mathbf{q}_0} \|\mathbf{q}(\mathbf{x}, t)\|^2 / \|\mathbf{q}_0\|^2$ we may extremise at each 'target time' $t = T$ over

all initial conditions $\mathbf{q}_0$ the extended, constrained Lagrangian

$$\mathcal{L}(\mathbf{q}, \mathbf{q}_0, \mathbf{q}^\dagger, \mathbf{q}_0^\dagger, T) = G(T) - \int_0^T \langle \mathbf{q}^\dagger, (\partial_t - \mathcal{A})\mathbf{q} \rangle \, \mathrm{d}t - \langle \mathbf{q}_0^\dagger, \mathbf{q}(\mathbf{x}, 0) - \mathbf{q}_0 \rangle, \quad (2.15)$$

where $\mathbf{q}^\dagger(\mathbf{x}, t)$ and $\mathbf{q}_0^\dagger(\mathbf{x})$ are vector Lagrange multipliers that enforce the linear differential equation at all points in space and time and its initial condition at all points in space respectively.

Taking variations of $\mathcal{L}$ with respect to $\mathbf{q}(\mathbf{x}, t)$ gives, after integrating by parts in time,

$$\frac{\delta \mathcal{L}}{\delta \mathbf{q}} = \left(\frac{\partial}{\partial t} + \mathcal{A}^\dagger \right) \mathbf{q}^\dagger + \left[\frac{2}{\|\mathbf{q}_0\|^2} \mathbf{q} - \mathbf{q}^\dagger \right]_{t=T} + (\mathbf{q}^\dagger - \mathbf{q}_0^\dagger)\Big|_{t=0}, \quad (2.16)$$

and so we see that we must set $\mathbf{q}^\dagger(\mathbf{x}, 0) = \mathbf{q}_0^\dagger(\mathbf{x})$ and $\mathbf{q}^\dagger(\mathbf{x}, T) = 2\mathbf{q}(\mathbf{x}, T)/\|\mathbf{q}_0\|^2$ as initial and end conditions on $\mathbf{q}^\dagger(\mathbf{x}, t)$, which in turn satisfies the linear differential equation

$$-\frac{\partial \mathbf{q}^\dagger}{\partial t} = \mathcal{A}^\dagger \mathbf{q}^\dagger. \quad (2.17)$$

Taking variations with respect to $\mathbf{q}_0$ gives

$$\frac{\delta \mathcal{L}}{\delta \mathbf{q}_0} = \mathbf{q}_0^\dagger - 2\frac{\|\mathbf{q}(\mathbf{x}, T)\|^2}{\|\mathbf{q}_0\|^4} \mathbf{q}_0, \quad (2.18)$$

which tells us how the gain changes with changes in the initial condition. This indicates that we may employ an iterative gradient-based optimisation procedure to find the maximal attainable gain as follows.

- Start with a guess for the optimal initial condition, $\mathbf{q}_0(\mathbf{x})$.
- Integrate forwards in time to $t = T$ using $\partial_t \mathbf{q} = \mathcal{A}\mathbf{q}$ to find $\mathbf{q}(\mathbf{x}, T)$.
- Assign $\mathbf{q}^\dagger(\mathbf{x}, T) = 2\mathbf{q}(\mathbf{x}, T)/\|\mathbf{q}_0\|^2$ as an end time condition.
- Integrate *backwards in time* to $t = 0$ using $-\partial_t \mathbf{q}^\dagger = \mathcal{A}^\dagger \mathbf{q}^\dagger$ to find $\mathbf{q}^\dagger(\mathbf{x}, 0)$.
- Assign $\mathbf{q}_0^\dagger(\mathbf{x}) = \mathbf{q}^\dagger(\mathbf{x}, 0)$ and evaluate $\delta\mathcal{L}/\delta\mathbf{q}_0$ using (2.18).
- If $\delta\mathcal{L}/\delta\mathbf{q}_0 = 0$ (or is zero within some prescribed tolerance), then $\mathbf{q}_0(\mathbf{x})$ solves the Euler–Lagrange equations and is the optimal initial condition. In addition, we know $G(T)$.

If $\delta\mathcal{L}/\delta\mathbf{q}_0 \neq 0$ then update the guess for $\mathbf{q}_0(\mathbf{x})$ using any gradient-based optimisation procedure. For example, steepest descent is $\mathbf{q}_0(\mathbf{x})^{(\text{new})} = \mathbf{q}_0(\mathbf{x})^{(\text{old})} + \epsilon\delta\mathcal{L}/\delta\mathbf{q}_0$ for some suitably small step-size ϵ.

- Repeat until convergence.

We call this algorithm linear direct-adjoint looping (DAL).

Returning to the transient Orr–Sommerfeld Squire problem, we let the state variable $\mathbf{q}(\mathbf{x},t) = \mathbf{u}(\mathbf{x},t)$, where $\mathbf{u}(\mathbf{x},t)$ is the infinitesimal fluid velocity perturbation about the base flow $\mathbf{U} = U(y,t)\hat{\mathbf{x}}$. We consider the maximisation of the kinetic energy density gain of the perturbation, so that our inner product becomes

$$\langle \mathbf{a}, \mathbf{b} \rangle = \frac{1}{V}\int_\Omega \mathbf{a}\cdot\mathbf{b}\ \mathrm{d}V, \tag{2.19}$$

where Ω is the fluid domain and V is its volume. Then $\|\mathbf{u}\|^2$ is directly proportional to the kinetic energy density of the perturbation velocity field. The Lagrangian that we use to maximise the energy gain and apply all the fluid dynamical constraints is

$$\begin{aligned}\mathcal{L}(\mathbf{u},\mathbf{u}_0,p,\mathbf{v},\mathbf{v}_0,q,T) = \frac{\|\mathbf{u}(\mathbf{x},T)\|^2}{\|\mathbf{u}_0(\mathbf{x})\|^2} - \left[\mathbf{v}, \frac{\partial\mathbf{u}}{\partial t} + \mathcal{A}\mathbf{u} + \nabla p - \frac{1}{Re}\nabla^2\mathbf{u}\right] \\ - [q, \nabla\cdot\mathbf{u}] - \langle \mathbf{v}_0, \mathbf{u}(\mathbf{x},0) - \mathbf{u}_0\rangle,\end{aligned} \tag{2.20}$$

where

$$\mathcal{A}u_i = U_j\frac{\partial}{\partial x_j}u_i + u_j\frac{\partial}{\partial x_j}U_i, \tag{2.21}$$

and $[\mathbf{a},\mathbf{b}] = \int_0^T \langle \mathbf{a},\mathbf{b}\rangle\ \mathrm{d}t$, and now $\mathbf{v}(\mathbf{x},t)$ is the Lagrange multiplier that enforces the linearised conservation of momentum equation and is called the 'adjoint velocity', $\mathbf{v}_0(\mathbf{x})$ enforces the initial condition, and $q(\mathbf{x},t)$ is the 'adjoint pressure' which enforces incompressibility. We have chosen to work directly with the linearised Navier–Stokes equations rather than the Orr–Sommerfeld, Squire and coupling operators because both the equation for $\mathbf{u}(\mathbf{x},t)$ and that for $\mathbf{v}(\mathbf{x},t)$ are readily integrated with only slight modifications to any standard time-stepping direct numerical simulation integration scheme.

Taking variations with respect to $\mathbf{u}(\mathbf{x},t)$ gives

$$\frac{\delta\mathcal{L}}{\delta\mathbf{u}} = \frac{\partial\mathbf{v}}{\partial t} + \mathcal{A}^\dagger\mathbf{v} + \frac{1}{Re}\nabla^2\mathbf{v} + \nabla q + \left(\frac{2}{\|\mathbf{u}_0\|^2}\mathbf{u} - \mathbf{v}\right)_{t=T} + (\mathbf{v}-\mathbf{v}_0)_{t=0}, \tag{2.22}$$

where

$$\mathcal{A}^\dagger v_i = \frac{\partial}{\partial x_j}\left(U_j v_i\right) - v_j \frac{\partial}{\partial x_i} U_j, \tag{2.23}$$

by integration by parts, provided that $\mathbf{v}(\mathbf{x}, t)$ satisfies the same boundary condition on $\partial\Omega$ as $\mathbf{u}(\mathbf{x}, t)$. This gives us the evolution equation for $\mathbf{v}(\mathbf{x}, t)$ along with its value at $t = T$ and at $t = 0$. We see clearly why we developed the original algorithm to integrate the adjoint equations backwards in time, because during the integration by parts in space and time required to obtain the equation for the adjoint velocity field, the sign of ∂_t changed once whilst the sign of ∇^2 changed twice, and so the equation for $\mathbf{v}(\mathbf{x}, t)$ is in part a backwards diffusion equation, and so is only well-posed mathematically if we integrate backwards in time.

Taking variations with respect to the direct pressure, $p(\mathbf{x}, t)$, we see that $\mathbf{v}(\mathbf{x}, t)$ is also incompressible,

$$\frac{\delta \mathcal{L}}{\delta p} = \nabla \cdot \mathbf{v}, \tag{2.24}$$

and taking variations with respect to the initial condition $\mathbf{u}_0(\mathbf{x})$ gives the compatibility condition with which we decide whether or not we started with the correct guess for $\mathbf{u}_0(\mathbf{x})$,

$$\frac{\delta \mathcal{L}}{\delta \mathbf{u}_0} = \mathbf{v}_0 - \frac{2\|\mathbf{u}(\mathbf{x}, t)\|^2}{\|\mathbf{u}_0\|^4}\mathbf{u}_0. \tag{2.25}$$

We therefore arrive at the following set of Euler–Lagrange equations that must be satisfied by an optimal initial condition $\mathbf{u}_0(\mathbf{x})$,

$$\frac{\partial \mathbf{u}}{\partial t} + \mathcal{A}\mathbf{u} + \nabla p - \frac{1}{Re}\nabla^2 \mathbf{u} = 0, \tag{2.26}$$

$$\nabla \cdot \mathbf{u} = 0, \tag{2.27}$$

$$\mathbf{v}(\mathbf{x}, T) = \frac{2}{\|\mathbf{u}_0\|^2}\mathbf{u}(\mathbf{x}, T), \tag{2.28}$$

$$\frac{\partial \mathbf{v}}{\partial t} + \mathcal{A}^\dagger \mathbf{v} + \nabla q + \frac{1}{Re}\nabla^2 \mathbf{v} = 0, \tag{2.29}$$

$$\nabla \cdot \mathbf{v} = 0, \tag{2.30}$$

$$\mathbf{v}(\mathbf{x}, 0) = \frac{2\|\mathbf{u}(\mathbf{x}, T)\|^2}{\|\mathbf{u}_0\|^4}\mathbf{u}_0(\mathbf{x}). \tag{2.31}$$

We call (2.26 – 2.27) the direct equations, (2.28) the end time condition, (2.29 - 2.30) the adjoint equations and (2.31) the compatibility condition. The structure

of the direct and adjoint equations are clearly similar, and so we note that if we have a time-stepping code that can integrate the direct equations, then modifying it to also integrate the adjoint equations is relatively straightforward.

This algorithm allows the computation of the most dangerous linear perturbations on any time varying base flow. However, at the core of this approach is an essential assumption, namely that the linear transient growth problem is relevant to the subsequent nonlinear dynamics. As we show in Chapter 7, even when a base flow has an asymptotic linear instability, the subsequent nonlinear evolution is not necessarily coupled to the form of the unstable linear mode. It is not at all clear how in general we should interpret an infinitesimal perturbation growing exponentially or transiently to 'finite amplitude' since the very equations that such a solution solves inherently maintain the perturbation at infinitesimal size. Without explicit finite amplitude and the associated nonlinear feedback into the base flow, there are numerous situations in which the approach outlined above is not only of limited application to the nonlinear problem, but is in fact irrelevant to it. For this reason, we do not dwell on the implementation and results of this linear DAL scheme and instead proceed directly to outline how the above approach can be modified to fully take into account the nonlinearity inherent in fluid dynamics and discuss some examples demonstrating how the conclusions that are reached about the nonlinear stability of such flows are entirely disconnected from the associated linear problem.

2.3 Nonlinear transient growth and minimal seeds

In principle the generalisation of linear DAL outlined above to the nonlinear case is straightforward since the derivation of the linear adjoint equations (2.29 - 2.30) relies only on integration by parts in space and time to move the operations onto the adjoint velocity field $\mathbf{v}(\mathbf{x}, t)$, and in the nonlinear problem it is still possible to calculate the required Fréchet derivatives. We will see however that the resulting algorithm contains computational difficulties that are not present in the linearised system, which indicate why the nonlinear variational problem has only recently been considered as computational resources have improved.

Consider the decomposition of the total velocity field into a base flow $\mathbf{U}$, which is assumed known, and departures from it, the perturbation field $\mathbf{u}$, so that

$$\mathbf{u}_{\text{tot}} = \mathbf{U}(\mathbf{x}, t) + \mathbf{u}(\mathbf{x}, t), \tag{2.32}$$

where there is no assumption about the size of $\mathbf{u}$. For PCF we have $\mathbf{U} = y\hat{\mathbf{x}}$.

To find nonlinear optimal perturbations that maximise some quantity of interest $\mathcal{J}[\mathbf{u}(\mathbf{x}, t)]$ over a given time interval T, we formulate a variational problem in much the same way as for the linear case, except that we must now prescribe an initial amplitude for the perturbation, which was arbitrary in the linear case. Perhaps the most natural way to do so in a fluid system is to prescribe the initial kinetic energy density of the perturbation, so that $\|\mathbf{u}_0\|^2 = 2E_0$, where $\|\cdot\|$ is the energy density based norm from the previous section. In fact, Foures *et al.* (2012) demonstrated that it is possible to use a suitable combination of seminorms, measures that satisfy all the properties of norms except for the condition that the zero vector is the unique vector that gives zero output, and still produce a well-defined optimisation scheme. For simplicity, we consider only the case of initial perturbation amplitude enforced with a single proper norm.

For now we leave the objective functional $\mathcal{J}[\mathbf{u}(\mathbf{x}, t)]$ unspecified so that we may consider a wide range of nonlinear optimisation problems. The direct generalisation of the linear scheme presented above would have $\mathcal{J}$ being the kinetic energy density of the flow at the target time T and will only depend on $\mathbf{u}(\mathbf{x}, T)$, but we will also consider $\mathcal{J}$ being the time averaged dissipation of energy in the flow, and so it will depend on $\mathbf{u}(\mathbf{x}, t)$ at all times leading up to the target time T.

The extended, constrained Lagrangian for the fully nonlinear optimisation is

$$\begin{aligned}\mathcal{L}(\mathbf{u}, \mathbf{u}_0, p, \mathbf{v}, \mathbf{v}_0, q, T, E_0, c) = \mathcal{J}[\mathbf{u}(\mathbf{x}, t)] - \left[\mathbf{v}, \frac{\partial \mathbf{u}}{\partial t} + \mathcal{N}\mathbf{u} + \nabla p - \frac{1}{Re}\nabla^2 \mathbf{u}\right] \\ - [q, \nabla \cdot \mathbf{u}] - \langle \mathbf{v}_0, \mathbf{u}(\mathbf{x}, 0) - \mathbf{u}_0 \rangle - (\|\mathbf{u}_0\|^2 - 2E_0)c,\end{aligned} \tag{2.33}$$

where

$$\mathcal{N}\mathbf{u} = (\mathbf{u} + \mathbf{U}) \cdot \nabla(\mathbf{u} + \mathbf{U}) \tag{2.34}$$

is the nonlinear advection operator which crucially contains the nonlinear advection term $\mathbf{u} \cdot \nabla \mathbf{u}$, and we have introduced the new Lagrange multiplier c which enforces the initial amplitude of the perturbation, $\|\mathbf{u}_0\|^2 = 2E_0$.

Taking variations with respect to all the direct and adjoint fields yields the following set of equations that must be satisfied by a nonlinear optimal perturbation initial condition $\mathbf{u}_0(\mathbf{x})$,

$$\frac{\partial \mathbf{u}}{\partial t} + \mathcal{N}\mathbf{u} + \nabla p - \frac{1}{Re}\nabla^2 \mathbf{u} = 0, \tag{2.35}$$

$$\nabla \cdot \mathbf{u} = 0, \tag{2.36}$$

$$\mathbf{v}(\mathbf{x}, T) = \frac{\delta \mathcal{J}}{\delta \mathbf{u}(\mathbf{x}, T)}, \tag{2.37}$$

$$\frac{\partial \mathbf{v}}{\partial t} + \mathcal{N}^\dagger \mathbf{v} + \nabla q + \frac{1}{Re}\nabla^2 \mathbf{v} = -\frac{\delta \mathcal{J}}{\delta \mathbf{u}(\mathbf{x}, t)}, \tag{2.38}$$

$$\nabla \cdot \mathbf{v} = 0, \tag{2.39}$$

$$\mathbf{v}(\mathbf{x}, 0) = 2c\mathbf{u}_0(\mathbf{x}), \tag{2.40}$$

where

$$\mathcal{N}^\dagger v_i = \frac{\partial}{\partial x_j}[(u_j + U_j)v_i] - v_j \frac{\partial}{\partial x_i}(u_j + U_j), \tag{2.41}$$

provided that $\mathbf{v}(\mathbf{x}, t)$ satisfies the same boundary conditions on $\partial\Omega$ as $\mathbf{u}(\mathbf{x}, t)$. We see immediately that the nonlinear adjoint equation (2.38) depends not only on the base flow $\mathbf{U}$ but also on the direct, nonlinear, perturbation velocity field $\mathbf{u}(\mathbf{x}, t)$ through the 'adjoint' advection operator $\mathcal{N}^\dagger$.

Although we will continue to use the term 'adjoint' for the operators and Lagrange multiplier fields in the nonlinear problem, we do so hesitatingly since in the language of the analysis of operators, the term 'adjoint' is reserved for linear operators only, and perhaps 'dual' would be a better terminology. Nevertheless we will continue to use 'adjoint' because there is a clear link between the nonlinear and linear adjoint advection operators, and the method of calculating them is essentially the same. In the abstracted formulation at the beginning of the Section 2.1, we observe that we can still make sense of the adjoint of a nonlinear operator $\mathcal{L}$ acting on $\mathbf{q}(\mathbf{x}, t)$ provided that we allow for the functional form $\mathcal{L}^\dagger = \mathcal{L}^\dagger[\mathbf{q}]$ so that $\mathcal{L}^\dagger$ depends on $\mathbf{q}(\mathbf{x}, t)$ itself, and only consider it in terms of its action on $\mathbf{q}^\dagger(\mathbf{x}, t)$, i.e. as the operation $\mathcal{L}^\dagger[\mathbf{q}]\mathbf{q}^\dagger$.

The dependence of the adjoint equations (2.38 – 2.39) on the direct field $\mathbf{u}(\mathbf{x}, t)$ presents the main difficulty in the implementation of nonlinear DAL over linear

DAL. From an entirely practical computational point of view, since the adjoint equations require knowledge of the direct field $\mathbf{u}(\mathbf{x}, t)$ at all times during its evolution, the direct field must be stored in the computer, requiring either a lot of memory or a lot of hard drive space, neither of which have been readily available until recently.

From a mathematical point of view, the adjoint equations in the nonlinear problem are no longer easy to deal with structurally. To explain, in principle the adjoint equations for the linear problem could be solved once and only once, in terms of the spectrum of the associated operator, since the background flow field $\mathbf{U}$ is supposed given, and the effect of updating the guess for the initial condition $\mathbf{u}_0(\mathbf{x})$ is only to change the end time condition for $\mathbf{v}(\mathbf{x}, T)$, and if we have a full knowledge of the behaviour of the adjoint equations, we can simply map this to the value at the initial time. However, in the nonlinear problem, every time we update the guess for the initial condition $\mathbf{u}_0(\mathbf{x})$, we effectively change not only the end time condition for $\mathbf{v}(\mathbf{x}, T)$ but also the equation satisfied by $\mathbf{v}(\mathbf{x}, t)$ at all intermediate times. Since the nonlinear evolution of velocity fields via the Navier–Stokes equations is inherently complicated and often chaotic, we stand little chance of gaining insight into the structure of the nonlinear problem's adjoint equations except on a case-by-case basis for each initial condition $\mathbf{u}_0(\mathbf{x})$.

We also obtain adjoint equations that depend on the direct field $\mathbf{u}(\mathbf{x}, t)$ in both the linear and nonlinear problems if the Fréchet derivative of $\mathcal{J}$ with respect to $\mathbf{u}(\mathbf{x}, t)$ is nonzero. For example, if we consider the kinetic energy gain at the target time T as our objective functional, then we have

$$\mathcal{J}[\mathbf{u}(\mathbf{x}, t)] = \|\mathbf{u}(\mathbf{x}, T)\|^2, \tag{2.42}$$

$$\frac{\delta \mathcal{J}}{\delta \mathbf{u}(\mathbf{x}, T)} = 2\mathbf{u}(\mathbf{x}, T), \tag{2.43}$$

$$\frac{\delta \mathcal{J}}{\delta \mathbf{u}(\mathbf{x}, t)} = 0, \tag{2.44}$$

whereas if we choose the time-averaged dissipation of energy over the time interval $t \in [0, T]$ as our objective functional, then we have

$$\mathcal{J}[\mathbf{u}(\mathbf{x}, t)] = \frac{1}{TRe} \int_0^T \|\nabla \mathbf{u}(\mathbf{x}, t)\|^2 \, \mathrm{d}t, \tag{2.45}$$

$$\frac{\delta \mathcal{J}}{\delta \mathbf{u}(\mathbf{x}, T)} = 0, \tag{2.46}$$

$$\frac{\delta \mathcal{J}}{\delta \mathbf{u}(\mathbf{x}, t)} = \frac{1}{TRe} \nabla^2 \mathbf{u}, \tag{2.47}$$

and so we start the backwards in time integration from the null condition $\mathbf{v}(\mathbf{x}, T) = 0$, but the adjoint equations for $\mathbf{v}(\mathbf{x}, t)$ gain a forcing term that is an anti-diffusion of the direct field $\mathbf{u}(\mathbf{x}, t)$.

In pipe flow, Pringle & Kerswell (2010) investigated nonlinear optimal perturbations that maximise the kinetic energy of the perturbation, and found that whilst the linear optimal perturbation consists of a pair of transiently growing two-dimensional streamwise vortices, the nonlinear optimal perturbation has an inherently three-dimensional initial condition which is localised in any given pipe cross-section. When evolved forwards in time, the initial condition 'unwraps' from its localised state onto a complex pattern of streamwise vortices and streaks that are of much higher amplitude than the streaks in the linear optimal perturbation. This makes sense intuitively; given a fixed amount of energy density E_0 with which to perturb a flow, the largest impact should come from localising the energy and hitting the flow hard in a single location, rather than spreading the energy out over the whole domain. This reasoning requires nonlinearity in order for localisation to occur, and so nonlinear DAL should be expected to produce larger energy gains than linear DAL, provided that E_0 is large enough.

Pringle & Kerswell (2010) also investigated the transition to turbulence induced by both linear optimal and nonlinear optimal perturbations. For subcritical transition in which a turbulent attractor and an asymptotically stable laminar state coexist, there is a smallest possible critical initial energy density $E_0 = E_c > 0$ such that at all initial energy densities $E_0 > E_c$ there is an initial condition that transitions to turbulence. However, Pringle & Kerswell (2010) were unable to converge nonlinear DAL above an energy density value $E_{\text{conv}} < E_c$ and so their nonlinear optimal perturbations eventually returned to the laminar state. Instead, Pringle & Kerswell (2010) uniformly rescaled the energies of both the nonlinear optimal perturbation found at E_{conv} and the linear optimal perturbation to investigate the critical amplitude of each initial condition that was able to trigger turbulence. As expected, the nonlinear optimal perturbation initial condition was able to trigger transition at initial energy densities two orders of magnitude smaller

than the initial energy density required for the linear optimal perturbation initial condition to trigger turbulence. The critical energy density required to trigger turbulence with the nonlinear optimal perturbation initial condition provided an upper bound for the true E_c, but E_c itself was not able to be determined. This problem was later addressed by Pringle *et al.* (2012).

Returning to PCF, both Monokrousos *et al.* (2011) and Rabin *et al.* (2012) took the nonlinear variational technique and found E_c. Monokrousos *et al.* (2011) used the time averaged dissipation of perturbation energy in the flow as the objective functional $\mathcal{J}$ and used a relatively large periodic domain and Reynolds number, whilst Rabin *et al.* (2012) used the gain of perturbation kinetic energy density as the objective functional $\mathcal{J}$ and focussed primarily on a smaller periodic domain and Reynolds number than Monokrousos *et al.* (2011), although they did show qualitative agreement with Monokrousos *et al.* (2011) when investigating the larger domain.

Not only were the objective functionals used by Monokrousos *et al.* (2011) and Rabin *et al.* (2012) different, but also the approach used to identify E_c. Monokrousos *et al.* (2011) used a 'laddering down' approach without imposing strong convergence criteria, whereby an initial condition that leads to turbulence is identified with initial energy density $E_0 = E_\alpha \gg E_c$, before being uniformly rescaled in energy to have initial energy density $E_0 = E_\beta < E_\alpha$. This rescaled initial condition is then used as an initial guess in nonlinear DAL to find a more efficient route to turbulence at $E_0 = E_\beta$. This new initial condition is then uniformly rescaled to have initial energy density $E_0 = E_\gamma < E_\beta$ and the process is repeated until any further reduction in E_0 renders nonlinear DAL no longer able to find an initial condition that transitions to turbulence, and this represents the best estimate of E_c using this scheme.

In contrast, whilst Rabin *et al.* (2012) used a similar laddering down approach to find E_c from above, they also demonstrated that E_c can be found from below. This is done by finding a nonlinear optimal perturbation with initial energy $E_0 < E_c$ and using this initial condition in nonlinear DAL with uniformly increased initial energy density to show that the 'minimal seed' for turbulence, the initial condition with energy density $E_0 = E_c$ connects continuously to a nonlinear optimal perturbation with $E_0 < E_c$. Viewed from a dynamical systems point of

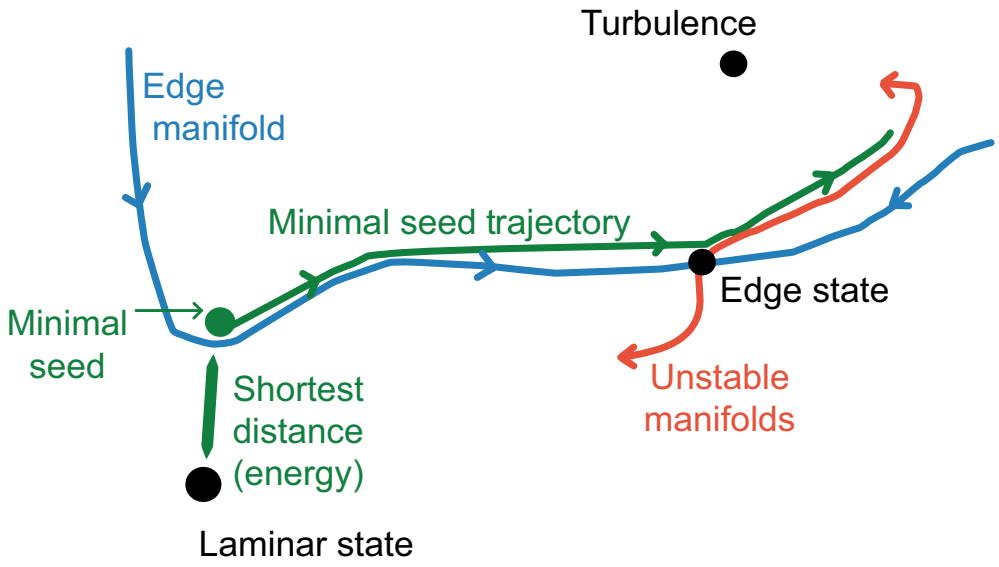

Figure 2.1: Cartoon of state space showing the laminar and turbulent states, the edge manifold, edge state and its unstable manifolds, the minimal seed initial condition, and the trajectory of the minimal seed through state space.

view, this result is not particularly surprising, given that the minimal seed and its initial energy density E_c represent the closest approach of the edge manifold to the laminar state, where the edge manifold is the manifold in state space that separates the basins of attraction of the laminar state and the turbulent attractor as shown in the sketch in Figure 2.1. The edge manifold is also the stable manifold of an 'edge state', and so initial conditions that lie just below the edge manifold experience substantial energy growth before decaying, as they evolve shadowing the edge manifold towards the edge state before returning to the laminar state. Such initial conditions are clear candidates for nonlinear optimal perturbations. These trajectories will be very similar to that of the minimal seed, since it lies on, or numerically just above the edge manifold, and itself evolves forward in time shadowing the edge manifold towards the edge state. The only difference is that as the minimal seed trajectory leaves the edge manifold, it does so towards the turbulent attractor rather than towards the laminar state, but until this point both trajectories are inherently extremely similar. However, in order for Rabin *et al.* (2012) to demonstrate this explicitly, they were required to increase substantially

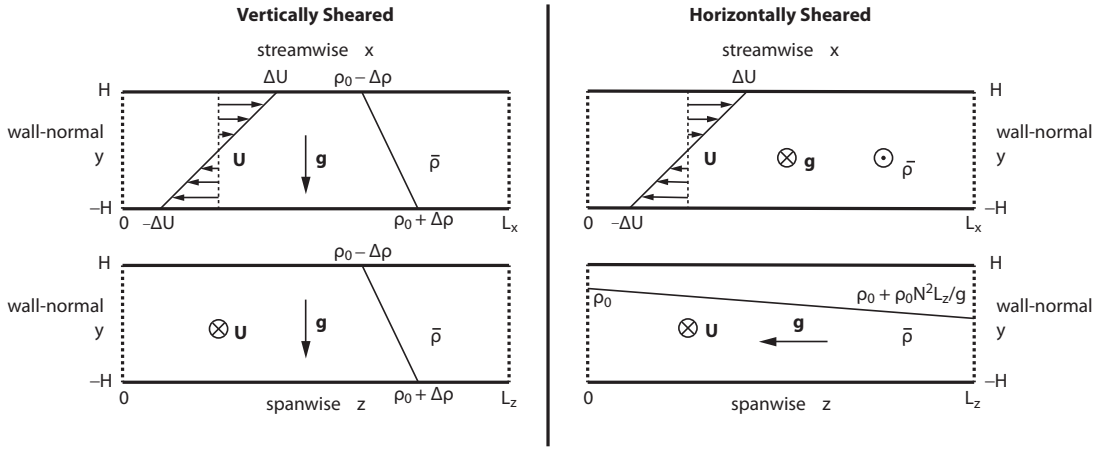

Figure 2.2: Diagram showing the co-ordinate system and the background laminar profiles for vertically sheared stratified PCF (left) and horizontally sheared stratified PCF (right). Solid walls are no-slip boundaries, dashed walls are periodic boundaries.

both the spatial and temporal resolutions in their numerical code to achieve convergence of nonlinear optimal perturbations in their nonlinear DAL scheme up to E_c.

The increase in resolution required to converge to E_c explicitly from below essentially renders this approach impractical for the identification of a large number of minimal seeds given currently available technology, and so for all the minimal seed approximations presented here, we use the laddering down approach and do not impose strong convergence criteria on nonlinear DAL.

The minimal seeds identified in Chapters 3 and 6 are for density stratified PCF, where we consider the gravitational direction parallel to the wall-normal direction in Chapter 3 (vertically sheared), and parallel to the spanwise direction in Chapter 6 (horizontally sheared). In each case we consider a linear, statically stable background density field and consider nonlinear perturbations to it. We write the total density field as $\rho_{\text{tot}} = \bar{\rho} + \rho$ where the background density field $\bar{\rho} = -y$ for the vertically sheared case and $\bar{\rho} = -z$ for the horizontally sheared case after appropriate nondimensionalisation. The geometries of both the vertically and horizontally sheared cases are illustrated in Figure 2.2.

Under the Boussinesq approximation for the density field, which is the assumption that density variations in the flow are small in comparison to a reference

background density value, the equations of motion for these systems are

$$\frac{\partial \mathbf{u}}{\partial t} + (\mathbf{u}+\mathbf{U})\cdot\nabla(\mathbf{u}+\mathbf{U}) = -\nabla p - \mathbb{V}Ri_B\rho\hat{\mathbf{y}} - \mathbb{H}Ri_B\rho\hat{\mathbf{z}} + \frac{1}{Re}\nabla^2\mathbf{u}, \tag{2.48}$$

$$\frac{\partial \rho}{\partial t} + (\mathbf{u}+\mathbf{U})\cdot\nabla(\bar{\rho}+\rho) = \frac{1}{RePr}\nabla^2\rho, \tag{2.49}$$

$$\nabla\cdot\mathbf{u} = 0, \tag{2.50}$$

where

$$Re = \frac{\Delta U H}{\nu}, \quad Pr = \frac{\nu}{\kappa}, \quad Ri_B = \frac{g\Delta\rho H}{\rho_0 \Delta U^2} \text{ or } \frac{N^2}{S^2}, \tag{2.51}$$

are the Reynolds number, Prandtl number and bulk Richardson numbers for the vertically and horizontally sheared cases respectively. ΔU is half the applied velocity difference across the two plates, H is half the distance that separates them, ν is the kinematic viscosity of the fluid, κ is the molecular diffusivity of density, g is the magnitude of the gravitational force, $\Delta\rho$ is half the applied density difference across the two plates in the vertically sheared case, ρ_0 is the mean density in the vertically sheared case, N is the applied background buoyancy frequency in the horizontally sheared case and $S = \Delta U/H$ is the applied background shear frequency in the horizontally sheared case. The parameters $\mathbb{V}$ and $\mathbb{H}$ are used for notational compactness and indicate whether we are considering the vertically sheared or horizontally sheared case, so that $\mathbb{V} = 1$ or 0 and $\mathbb{H} = 0$ or 1 in each of the two cases respectively.

The extended, constrained Lagrangian under consideration is then

$$\begin{aligned}
\mathcal{L}(\mathbf{u},\mathbf{u}_0,\rho,p,\mathbf{v},&\mathbf{v}_0,\eta,q,T,E_0,c) = \mathcal{J}[\mathbf{u}(\mathbf{x},t),\rho(\mathbf{x},t)] \\
&-\left[\eta,\ \frac{\partial\rho}{\partial t} + (\mathbf{u}+\mathbf{U})\cdot\nabla(\bar{\rho}+\rho) - \frac{1}{RePr}\nabla^2\rho\right] \\
-\left[\mathbf{v},\ \frac{\partial\mathbf{u}}{\partial t} + \mathcal{N}\mathbf{u} + \nabla p + \mathbb{V}Ri_B\rho\hat{\mathbf{y}} + \mathbb{H}Ri_B\rho\hat{\mathbf{z}} - \frac{1}{Re}\nabla^2\mathbf{u}\right] \\
-[q,\nabla\cdot\mathbf{u}] - \langle\mathbf{v}_0,\mathbf{u}(\mathbf{x},0)-\mathbf{u}_0\rangle - \langle\eta_0,\rho(\mathbf{x},0)-\rho_0\rangle \\
-(\|\mathbf{u}_0\|^2 + Ri_B\|\rho_0\|^2 - 2E_0)c,
\end{aligned} \tag{2.52}$$

where the 'adjoint density' $\eta(\mathbf{x},t)$ is the Lagrange multiplier enforcing the density evolution equation and η_0 is the Lagrange multiplier enforcing the initial condition

on the density field. The total energy density (kinetic plus potential) is given by

$$\mathbb{E} = \mathbb{K} + \mathbb{P} = \frac{\|\mathbf{u}\|^2}{2} + \frac{Ri_B\|\rho\|^2}{2}. \tag{2.53}$$

Taking variations with respect to all the parameters gives the following set of equations that must be satisfied by a nonlinear optimal perturbation $(\mathbf{u}_0(\mathbf{x}), \rho_0(\mathbf{x}))$,

$$\frac{\partial \mathbf{u}}{\partial t} + \mathcal{N}\mathbf{u} + \nabla p + \mathbb{V}Ri_B\rho\hat{\mathbf{y}} + \mathbb{H}Ri_B\rho\hat{\mathbf{z}} - \frac{1}{Re}\nabla^2\mathbf{u} = 0, \tag{2.54}$$

$$\frac{\partial \rho}{\partial t} + (\mathbf{u} + \mathbf{U}) \cdot \nabla(\bar{\rho} + \rho) - \frac{1}{RePr}\nabla^2\rho = 0, \tag{2.55}$$

$$\nabla \cdot \mathbf{u} = 0, \tag{2.56}$$

$$\mathbf{v}(\mathbf{x}, T) = \frac{\delta \mathcal{J}}{\delta \mathbf{u}(\mathbf{x}, T)}, \tag{2.57}$$

$$\eta(\mathbf{x}, T) = \frac{\delta \mathcal{J}}{\delta \rho(\mathbf{x}, T)}, \tag{2.58}$$

$$\frac{\partial \mathbf{v}}{\partial t} + \mathcal{N}^\dagger\mathbf{v} + \nabla q - \eta\nabla(\bar{\rho} + \rho) + \frac{1}{Re}\nabla^2\mathbf{v} = -\frac{\delta \mathcal{J}}{\delta \mathbf{u}(\mathbf{x}, t)}, \tag{2.59}$$

$$\frac{\partial \eta}{\partial t} + \mathbf{u} \cdot \nabla\eta - \mathbb{V}Ri_B\hat{\mathbf{y}} \cdot \mathbf{v} - \mathbb{H}Ri_B\hat{\mathbf{z}} \cdot \mathbf{v} + \frac{1}{RePr}\nabla^2\eta = -\frac{\delta \mathcal{J}}{\delta \rho(\mathbf{x}, t)}, \tag{2.60}$$

$$\nabla \cdot \mathbf{v} = 0, \tag{2.61}$$

$$\mathbf{v}(\mathbf{x}, 0) = 2c\mathbf{u}_0(\mathbf{x}), \tag{2.62}$$

$$\eta(\mathbf{x}, 0) = 2cRi_B\rho_0(\mathbf{x}). \tag{2.63}$$

It is again clear that if we have a time-stepping code that can integrate forwards in time the Boussinesq Navier–Stokes equations for both the velocity and density fields, then it is relatively straightforward to adjust this code to also integrate the adjoint equations (2.59 – 2.61). We will solve these equations on a computational domain given by $(x, y, z) \in [0, L_x] \times [-1, 1] \times [0, L_z]$, and the boundary conditions we need to apply for a Newtonian fluid and for the adjoint equations to be valid

are

$$[\mathbf{u}, \rho, \mathbf{v}, \eta](x = L_x) = [\mathbf{u}, \rho, \mathbf{v}, \eta](x = 0) \quad \text{(periodic in } x\text{)}, \tag{2.64}$$

$$[\mathbf{u}, \rho, \mathbf{v}, \eta](z = L_z) = [\mathbf{u}, \rho, \mathbf{v}, \eta](z = 0) \quad \text{(periodic in } z\text{)}, \tag{2.65}$$

$$[\mathbf{u}, \rho, \mathbf{v}, \eta](y = -1) = [\mathbf{u}, \rho, \mathbf{v}, \eta](y = 1) = 0 \quad \text{(no slip, fixed density)}. \tag{2.66}$$

For the objective functional $\mathcal{J}$ we will be considering both the total perturbation energy at the target time T,

$$\mathcal{J}[\mathbf{u}(\mathbf{x}, t), \rho(\mathbf{x}, t)] = \|\mathbf{u}(\mathbf{x}, T)\|^2 + Ri_B\|\rho(\mathbf{x}, T)\|^2, \tag{2.67}$$

$$\frac{\delta\mathcal{J}}{\delta\mathbf{u}(\mathbf{x}, T)} = 2\mathbf{u}(\mathbf{x}, T), \quad \frac{\delta\mathcal{J}}{\delta\rho(\mathbf{x}, T)} = 2Ri_B\rho(\mathbf{x}, T), \tag{2.68}$$

$$\frac{\delta\mathcal{J}}{\delta\mathbf{u}(\mathbf{x}, t)} = 0, \quad \frac{\delta\mathcal{J}}{\delta\rho(\mathbf{x}, t)} = 0, \tag{2.69}$$

and the time-averaged total dissipation of perturbation energy over the time interval $[0, T]$,

$$\mathcal{J}[\mathbf{u}(\mathbf{x}, t), \rho(\mathbf{x}, t)] = \frac{1}{TRe}\int_0^T \left(\|\nabla\mathbf{u}(\mathbf{x}, t)\|^2 + \frac{Ri_B}{Pr}\|\nabla\rho(\mathbf{x}, t)\|^2\right) \mathrm{d}t, \tag{2.70}$$

$$\frac{\delta\mathcal{J}}{\delta\mathbf{u}(\mathbf{x}, T)} = 0, \quad \frac{\delta\mathcal{J}}{\delta\rho(\mathbf{x}, T)} = 0, \tag{2.71}$$

$$\frac{\delta\mathcal{J}}{\delta\mathbf{u}(\mathbf{x}, t)} = \frac{2}{TRe}\nabla^2\mathbf{u}, \quad \frac{\delta\mathcal{J}}{\delta\rho(\mathbf{x}, t)} = \frac{2Ri_B}{TRePr}\nabla^2\rho. \tag{2.72}$$

We will consider two geometries, a narrow geometry 'N' with $L_x = 13.66$ and $L_z = 3.31$ used first by Butler & Farrell (1992) when investigating the linear optimal perturbations in unstratified PCF, and also considered by Rabin *et al.* (2012) where the unstratified minimal seed has been identified, and a wide geometry 'W' that is twice as wide in the spanwise direction, with $L_x = 13.66$ and $L_z = 6.62$. Rabin *et al.* (2012) found that geometry N gave minimal seed initial conditions that are localised in the streamwise direction, and we demonstrate below that geometry W gives minimal seed initial conditions that are also localised in the spanwise direction.

The focus of the minimal seed calculations in Chapters 3 and 6 is to extend the results of Rabin *et al.* (2012) from unstratified PCF into stratified PCF. To do

this, we fix $Re = 1000$ as in Rabin *et al.* (2012), choose $Pr = 1$ for convenience, and investigate the effect of changing Ri_B. The bulk Richardson number Ri_B is a bulk measure of the ratio of potential to kinetic energy in the flow, and we therefore expect that as Ri_B increases it has a stabilising effect on the flow. We therefore expect E_c to be an increasing function of Ri_B. We are interested in how the structure of the minimal seed initial condition and its subsequent trajectory in state space are affected by increasing the strength of the stratification.

2.4 Implementation

2.4.1 Diablo

In order to find nonlinear optimal perturbations of stratified PCF using nonlinear DAL, we use a modified version of the computational fluid dynamics solver 'Diablo' developed by Taylor & Bewley (see Taylor, 2008). We use a version of Diablo which integrates the Boussinesq Navier–Stokes equations for the velocity and density fields in a periodic PCF channel.

The spatial discretisation in this version of Diablo consists of a de-aliased Fourier decomposition in the two periodic directions, streamwise x and spanwise z, and a second-order finite difference scheme in the wall-normal direction y. Time-stepping is implemented by a combined implicit-explicit third order Runge–Kutta–Wray Crank–Nicholson scheme. This scheme treats all nonlinear terms explicitly and the diffusive terms implicitly using the well-known Crank–Nicholson method, and solves for the flow at time $t + \Delta t$ from time t in three stages, at $t + 8\Delta t/15$, at $t + 2\Delta t/3$ and finally at $t + \Delta t$. The flow is made incompressible by a pressure advection scheme in which an initial guess for $\mathbf{u}(\mathbf{x}, t + \Delta t)$ is produced using the pressure implicitly, before the guess is made incompressible by finding the additional pressure gradient required to project the initial guess onto an incompressible field.

Diablo also uses a fractional grid so that (u, w, p, ρ) are solved on a computational grid located exactly half way between the computational grid for v in the wall-normal direction. This well-used technique helps avoid spurious oscillations in the pressure field. Diablo also has parallel capability which is particularly

straightforward due to the finite difference scheme in the wall-normal direction. The wall-normal direction is split up into connected subdomains, or 'slices', and the numerical scheme solved in each slice. Information required by the finite difference scheme is passed from the top and bottom of each slice to neighbouring slices using an MPI library. This passing of information is relatively minimal because in the finite difference scheme each slice only communicates with its nearest neighbour and only passes on each computational field on a single x–z plane.

The most time-consuming part of the Diablo implementation is the computation of the nonlinear terms. Although the computational scheme uses Fourier modes in the two period directions, in order to calculate the nonlinear terms it does not compute the associated convolution but instead fast-Fourier transforms the complex fields into physical space, multiplies the relevant terms in physical space, and fast-Fourier transforms the answer back to the complex Fourier space. Since there are a large number of nonlinear terms, most of the computational time of the code is spent performing these fast-Fourier transforms, even though the number of fast-Fourier transforms used has been optimised.

The modification of Diablo to integrate the adjoint equations (2.59 – 2.61) is straightforward because the equations for $\mathbf{v}$ and η have very similar structure to those for $\mathbf{u}$ and ρ. The nonlinear advection terms in the direct equations have counterparts in the adjoint equations in which components of $\mathbf{u}$ multiply components of $\mathbf{v}$. The numerical scheme for the direct equations (2.54 – 2.55) gives a template for numerically implementing every type of term in the adjoint equations. The only difficulty we come across is the observation that for the adjoint equations, computing the nonlinear terms involving the wall-normal adjoint velocity $\hat{\mathbf{y}} \cdot \mathbf{v}$ explicitly leads to a numerically unstable numerical scheme, and so we must implement these terms implicitly. Other versions of Diablo already do this for the direct equations and so there is still a template for this implicit implementation. This solves the problem of numerical instability.

2.4.2 Resolution

For the narrow geometry N we use the resolution $128 \times 241 \times 32$ (in the streamwise, wall-normal and spanwise directions, respectively, as will be the convention throughout) and for the wide geometry W we use $128 \times 241 \times 64$. The 241 fi-

nite difference points in the wall-normal direction is split between 16 processors, each of which computes with 16 points of the wall-normal grid. The reason that this does not give a total of 256 points in the wall-normal direction is that each processor has one or two (depending on whether that processor contains the solid boundary in its domain) neighbouring processors that share a single wall-normal grid point with it. Rabin *et al.* (2012), who also based their code on Diablo, found this resolution to be sufficient to identify E_c using the laddering down approach, but needed to use a grid $128 \times 1536 \times 32$ to explicitly converge to E_c from below.

We typically use a fixed non-dimensional time-step $\Delta t \in [0.01, 0.05]$, defaulting to $\Delta t = 0.05$ unless the flow parameters require a smaller time-step to prevent numerical blow-up. For much of the time-evolution of initial condition guesses in nonlinear DAL, the flow field is not turbulent and the time-step could be taken to be much larger. However, since we wish to identify initial conditions that eventually transition to turbulence, we need to ensure that we can numerically evaluate the turbulent flow at least for a short period. We are prevented from easily avoiding this problem by using a variable time-step because of the need for checkpointing, which we now discuss.

2.4.3 Checkpointing

The integration of the adjoint equations (2.59 – 2.61) requires full knowledge of the direct fields $(\mathbf{u}(\mathbf{x}, t), \rho(\mathbf{x}, t))$. Given that the numerical approximations to the minimal seeds that we identify are only just able to transition to turbulence, we must choose a very large target time T in order to find them. We typically use $T = 300$ or 400. Combined with the typical time-step $\Delta t = 0.05$, this gives 6000 to 8000 computational time-steps (each of which is in fact subdivided into three). It is therefore not at all feasible to store $(\mathbf{u}(\mathbf{x}, t), \rho(\mathbf{x}, t))$ at every one of these times in computer memory or on hard-drive.

The solution that Rabin (2013) uses for this problem is to checkpoint. While integrating the direct equations (2.54 – 2.56) we save all the fields $(\mathbf{u}, \rho, p)$ on hard-drive every N time-steps, called a 'checkpoint'. Typically we choose $N = 50$. When we are N times steps from the end of the forward integration, we then proceed to save $(\mathbf{u}, \rho)$ at every time-step until the end of the integration. We then integrate backwards in time the adjoint equations (2.59 – 2.61) for N time-steps using the

stored velocity and density fields, deleting them when we no longer need them. We then read the fields $(\mathbf{u}, \rho, p)$ from the previous checkpoint, that is $2N$ time-steps from the end of the forward integration, and *re-do* the direct integration from $2N$ time-steps from the end to N time-steps from the end, storing $(\mathbf{u}, \rho)$ at every time-step. We now have knowledge of $(\mathbf{u}, \rho)$ that allows us to continue integrating backwards in time the adjoint equations for another N time-steps. We continue this re-loading and re-calculation of the direct field every N time-steps to evolve the adjoint fields back to time $t = 0$.

This process is time-consuming, but feasible given current computing resources. It is in fact not as time-consuming as it might at first appear, because the evolution of the direct equations is computationally cheaper than the evolution of the adjoint equations since the adjoint equations contain more coupling terms than the direct equations contain nonlinear terms, by approximately a factor of two. We find that it takes approximately three times as long to integrate the adjoint equations from $t = T$ to $t = 0$ along with loading and re-calculating the direct fields, than to integrate the direct equations from $t = 0$ to $t = T$.

The other issue with requiring the direct fields $(\mathbf{u}, \rho)$ at every time-step of the integration of the adjoint fields arises through the use of the three-step Runga–Kutta–Wray time integration scheme. Using checkpointing we can in principle obtain approximate direct fields at times t, $t + 8\Delta t/15$, $t + 2\Delta t/3$ and $t + \Delta t$, but since we are integrating the adjoint fields backwards in time using the same scheme, we in fact need to know the direct fields at times $t + \Delta t$, $t + 7\Delta t/15$, $t + \Delta t/3$ and t. In order to do this, when re-calculating the direct fields from each checkpoint we only store $(\mathbf{u}, \rho)$ at each integer time-step, and then use a cubic spline interpolation to obtain the direct fields at each fractional time-step. This not only saves further on the memory needed to store the direct fields, but also provides a better approximation to the direct fields at the times for which they are needed. It is for the huge algorithmic simplification given by choosing a fixed time-step Δt when implementing the above checkpointing that we do not allow the time-step to vary.

2.4.4 Update method

For simplicity, we use a simple-minded steepest descent process to update the

initial conditions in nonlinear DAL, whereby we adaptively choose ϵ and set

$$\mathbf{u}_0^{(\text{new})} = \mathbf{u}_0^{(\text{old})} + \epsilon \frac{\delta \mathcal{L}}{\delta \mathbf{u}_0} = \mathbf{u}_0^{(\text{old})} + \epsilon \left(\mathbf{v}_0^{(\text{old})} - 2c\mathbf{u}_0^{(\text{old})} \right), \tag{2.73}$$

$$\rho_0^{(\text{new})} = \rho_0^{(\text{old})} + \frac{\epsilon}{Ri_B} \frac{\delta \mathcal{L}}{\delta \rho_0} = \rho_0^{(\text{old})} + \frac{\epsilon}{Ri_B} \left(\eta_0^{(\text{old})} - 2cRi_B \rho_0^{(\text{old})} \right). \tag{2.74}$$

We use a scaled version of ϵ to update the density field, namely ϵ/Ri_B, in an attempt to ensure that the velocity and density fields converge at the same rate. It is not entirely clear how this should be achieved, but for small Ri_B the above method appears to work well. At an intuitive level, the update for $\mathbf{u}_0$ is of size $\epsilon c \mathbf{u}_0$ and this particular scaling of ϵ ensures that the update for ρ_0 is of size $\epsilon c \rho_0$, similarly. A more general method could have two different step sizes, $\epsilon_{\mathbf{u}}$ and ϵ_ρ which are each adaptively chosen, but for the results presented here, this simpler method was found sufficient.

Rabin (2013) investigated two other update methods, conjugate gradients and also a method that explicitly restricts to the hypersphere $\|\mathbf{u}_0\|^2 = 2E_0$ (in the unstratified case), but found little improvement in convergence with either method, and so we will use the simplest possible here. Monokrousos *et al.* (2011) used a relaxation-type update, but it is again unclear if this gives better convergence.

The only problems with prescribing the update method as above are that we still have an unknown Lagrange multiplier c, and we must also devise a scheme by which ϵ is adaptively updated. Rather than solving for the Lagrange multiplier c via the Euler–Lagrange equations, we can instead find it by explicitly imposing the energy constraint on the new initial condition. We require that

$$\begin{aligned} 2E_0 &= \left\| \mathbf{u}_0^{(\text{new})} \right\|^2 + Ri_B \left\| \rho_0^{(\text{new})} \right\|^2 \\ &= \left\| \mathbf{u}_0^{(\text{old})} + \epsilon \left(\mathbf{v}_0^{(\text{old})} - 2c\mathbf{u}_0^{(\text{old})} \right) \right\|^2 + Ri_B \left\| \rho_0^{(\text{old})} + \frac{\epsilon}{Ri_B} \left(\eta_0^{(\text{old})} - 2cRi_B \rho_0^{(\text{old})} \right) \right\|^2, \end{aligned} \tag{2.75}$$

which we can rearrange using $2E_0 = \|\mathbf{u}_0^{(\text{old})}\|^2 + Ri_B \|\rho_0^{(\text{old})}\|^2$ into the following quadratic equation for c,

$$\begin{aligned} 0 &= 8\epsilon E_0 c^2 - 4c \left[2E_0 + \epsilon \left(\langle \mathbf{v}_0^{(\text{old})}, \mathbf{u}_0^{(\text{old})} \rangle + \langle \eta_0^{(\text{old})}, \rho_0^{(\text{old})} \rangle \right) \right] \\ &\quad + 2 \left(\langle \mathbf{v}_0^{(\text{old})}, \mathbf{u}_0^{(\text{old})} \rangle + \langle \eta_0^{(\text{old})}, \rho_0^{(\text{old})} \rangle \right) + \epsilon \left(\left\| \mathbf{v}_0^{(\text{old})} \right\|^2 + \frac{1}{Ri_B} \left\| \eta_0^{(\text{old})} \right\|^2 \right). \end{aligned} \tag{2.76}$$

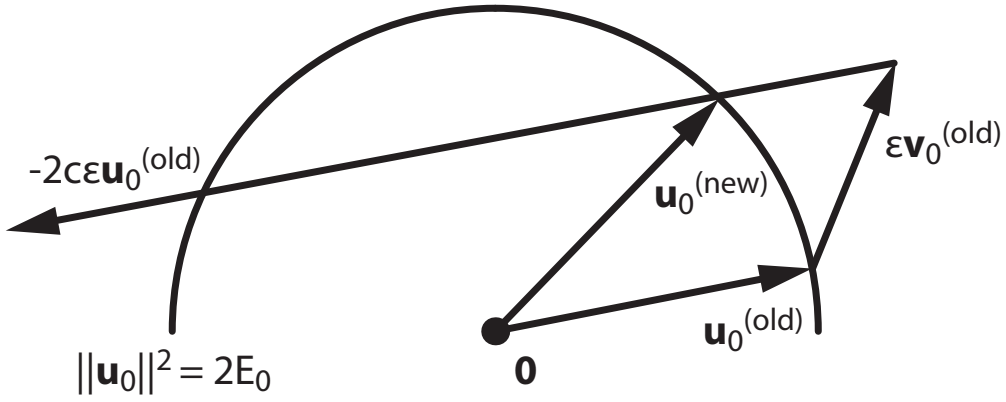

Figure 2.3: Diagram showing the geometrical interpretation of the choice of the multiplier c in (2.76) to enforce the energy constraint. $Ri_B = 0$ for simplicity.

We have arrived at two solutions for c. In order to decide which root to pick, we need to think geometrically about what the update method is doing. If we did not have the energy constraint in the Lagrangian $\mathcal{L}$ then we would instead find

$$\frac{\delta \mathcal{L}}{\delta \mathbf{u}_0} = \mathbf{v}_0, \quad \frac{\delta \mathcal{L}}{\delta \rho_0} = \eta_0, \tag{2.77}$$

and we expect that for most initial conditions, a higher value of the objective functional $\mathcal{J}$ is found by changing the energy of the initial condition. Therefore simply adding $\epsilon \mathbf{v}_0$ to our initial condition is likely to move us away from the hypersphere $\|\mathbf{u}_0\|^2 + Ri_B\|\rho_0\|^2 = 2E_0$, and the role of $2c\epsilon\mathbf{u}_0$ is to pull us back to this hypersphere. If (2.76) has no real roots for c, then ϵ is too large and we must reduce it, since no value of c is able to intersect the hypersphere. When there are two real roots, we should pick the smaller magnitude of the two since this finds the closest intersection of $\mathbf{u}_0 + \epsilon\mathbf{v}_0 - 2c\epsilon\mathbf{u}_0$ with the hypersphere to $\mathbf{u}_0$, and for the iteration to converge we need to provide updated initial conditions that are in the vicinity of the original initial condition. This geometrical interpretation is illustrated in Figure 2.3.

The requirement for two real solutions for c provides us with one method of adaptively changing the step-size ϵ. We also use three additional criteria. The first is the criterion that the new guess should give an improved result for the objective functional $\mathcal{J}$, that is

$$\mathcal{J}[\mathbf{u}(\mathbf{x},t)^{(\text{new})}, \rho(\mathbf{x},t)^{(\text{new})}] > \mathcal{J}[\mathbf{u}(\mathbf{x},t)^{(\text{old})}, \rho(\mathbf{x},t)^{(\text{old})}]. \tag{2.78}$$

If this is not the case, then our new guess has overshot, and we re-guess $\mathbf{u}_0^{(\text{new})}$ and $\rho_0^{(\text{new})}$ with a smaller value of ϵ, replacing it with $\epsilon/5$.

The second method we use to change ϵ adaptively is to keep track of consecutive gradients of the Lagrangian. Following Pringle *et al.* (2012) we compute

$$d = \frac{\left\langle \frac{\delta\mathcal{L}}{\delta\mathbf{u}_0^{(\text{new})}}, \frac{\delta\mathcal{L}}{\delta\mathbf{u}_0^{(\text{old})}} \right\rangle + \left\langle \frac{\delta\mathcal{L}}{\delta\rho_0^{(\text{new})}}, \frac{\delta\mathcal{L}}{\delta\rho_0^{(\text{old})}} \right\rangle / Ri_B}{\sqrt{\left(\left\| \frac{\delta\mathcal{L}}{\delta\mathbf{u}_0^{(\text{new})}} \right\|^2 + \left\| \frac{\delta\mathcal{L}}{\delta\rho_0^{(\text{new})}} \right\|^2 / Ri_B \right) \left(\left\| \frac{\delta\mathcal{L}}{\delta\mathbf{u}_0^{(\text{old})}} \right\|^2 + \left\| \frac{\delta\mathcal{L}}{\delta\rho_0^{(\text{old})}} \right\|^2 / Ri_B \right)}}, \tag{2.79}$$

which in essence measures the angle in state space between the two consecutive gradient vectors and is restricted to $|d| \leq 1$. Then, if the two consecutive gradient vectors are closely aligned, and $d > 0.95$ we replace ϵ with 2ϵ in the next initial condition guess, whereas if the two consecutive gradient vectors are poorly aligned, and $d < -0.5$ we replace ϵ with $\epsilon/5$ in the next initial condition guess. This means that we take larger step sizes when the risk of overshooting is reduced, and smaller step sizes when the risk of overshooting is increased.

Following Pringle *et al.* (2012) We also reduce the step-size if we find that

$$\left\| \frac{\delta\mathcal{L}}{\delta\mathbf{u}_0^{(\text{new})}} \right\|^2 + \left\| \frac{\delta\mathcal{L}}{\delta\rho_0^{(\text{new})}} \right\|^2 / Ri_B > 4 \left(\left\| \frac{\delta\mathcal{L}}{\delta\mathbf{u}_0^{(\text{old})}} \right\|^2 + \left\| \frac{\delta\mathcal{L}}{\delta\rho_0^{(\text{old})}} \right\|^2 / Ri_B \right), \tag{2.80}$$

in which case the new gradient is very large, and so we might inadvertently overshoot, even if the new and old gradients are closely aligned.

2.4.5 Convergence

Since we are considering a non-convex, nonlinear optimisation problem, then even if we converge there is no guarantee that we have found a global optimiser rather than a local optimiser. However, we can have some confidence that our optimal solutions are optimal in at least a large region of state space by considering a wide range of initial guesses for the initial conditions in nonlinear DAL. Pringle *et al.* (2012) and Rabin (2013) did precisely this and found the same optimal solutions for a wide range of initial guesses. Additionally, we show in the next section considering code verification that using a completely different code to Rabin *et al.* (2012) and a different objective functional $\mathcal{J}$, the minimal seed for turbulence that we identify is the same as the one found by Rabin *et al.* (2012).

In order to consider the convergence of nonlinear DAL, we monitor the normalised residual

$$R = \frac{\left\| \frac{\delta \mathcal{L}}{\delta \mathbf{u}_0} \right\|^2 + \left\| \frac{\delta \mathcal{L}}{\delta \rho_0} \right\|^2 / Ri_B}{\|\mathbf{v}_0\|^2 + \|\eta_0\|^2 / Ri_B}, \tag{2.81}$$

and also the individual residuals

$$R_{\mathbf{u}} = \frac{\left\| \frac{\delta \mathcal{L}}{\delta \mathbf{u}_0} \right\|^2}{\|\mathbf{v}_0\|^2}, \quad R_\rho = \frac{\left\| \frac{\delta \mathcal{L}}{\delta \rho_0} \right\|^2}{\|\eta_0\|^2}. \tag{2.82}$$

The reason for normalising the gradients by $\|\mathbf{v}_0\|^2$ and $\|\eta_0\|^2$ is that, at least in the case that the objective functional $\mathcal{J}$ depends only on the final time T, the equations satisfied by the adjoint fields $(\mathbf{v}(\mathbf{x}, t), \rho(\mathbf{x}, t))$ are linear and homogeneous in the adjoint fields and so their amplitude is arbitrary. The gradients themselves therefore also contain this arbitrary scaling and so we factor this amplitude out.

When laddering down to find E_c, if we are at an initial energy $E_0 \gg E_c$ then for large target times an extremely large number of initial conditions reach the turbulent attractor and have the same high value of $\mathcal{J}$. Therefore for $E_0 \gg E_c$ we cannot expect, and indeed never see, small values for any of these residuals. When finding a more efficient route to turbulence we must simply wait until the values of $\mathcal{J}$ do not improve any further with more iterations. Throughout this process, we normally have $0 \ll R \lesssim 1$. This appears to be the best nonlinear DAL can do until we are very close to E_c.

When we are 'close' to E_c, there are no longer a large number of initial conditions that transition to turbulence and have large values for $\mathcal{J}$. In fact, when we are at E_c there is by definition generically a unique solution unless the edge manifold is flat near E_c or there are two or more widely separated minimal seeds. We might therefore expect the value of R to start converging to smaller values. What we see in all the minimal seeds presented here is that R does not decrease at all until we are within a few significant figures of E_c, after which R drops to about 10^{-4} and apparently will go no further. If we then look at E_0 just below E_c we typically find $R \approx 10^{-5}$. The only way that we can determine if we are at the minimal seed or not is to run a case with E_0 at what would otherwise be the next value in the laddering down procedure, below the determined value for E_c, for a very large number of iterations and verify that R and $\mathcal{J}$ saturate without significantly increasing, and that $\mathcal{J}$ attains values consistent only with a return to the

laminar state. This is unsatisfying, but Rabin *et al.* (2012) suggest that if we were to increase substantially our spatial resolution then we might be able to reduce R further, if only by a small amount, and that our method for finding estimates for E_c is at least consistent. This is the current state of nonlinear DAL's technology and without significant improvements in the understanding for precisely why convergence proves difficult we cannot foresee an improved algorithm.

If we run nonlinear DAL at very low initial energy densities E_0 then we in fact converge to the linear optimal perturbations for any given flow with R dropping below 10^{-16} within 20 to 30 iterations. Again, we do not understand why the linear problem converges very easily whilst the nonlinear minimal seed problem does not, but this is a widely reported issue in the literature (see Pringle & Kerswell, 2010; Rabin *et al.*, 2012; Pringle *et al.*, 2012).

As we discuss below, we do have the knowledge that the newly written code exactly reproduces the unstratified minimal seed of Rabin *et al.* (2012). In addition, all the minimal seeds presented here are continuously connected to the unstratified case via the bulk Richardson number Ri_B as a control parameter. We find that all the minimal seeds share similar initial condition structures and initial time evolutions, which gives us confidence that even if we have not converged to the exact value of E_c, we at least have a self-consistent set of state space trajectories that are critical in some sense. This gives us confidence that their further investigation is warranted.

2.5 Verification

We performed two separate tests to verify that the newly written numerical code accurately implements nonlinear DAL. The first was to demonstrate that we converge to the same minimal seed as Rabin *et al.* (2012) in unstratified PCF in the narrow geometry N using the newly written code and a different objective functional $\mathcal{J}$. Both the code used here and that used by Rabin *et al.* (2012) are based on the Diablo framework, but the code used here is a completely rewritten DAL solver and departs from the code written by Rabin *et al.* (2012) at the basic Diablo level. The second test was to verify that the numerical code operated at small initial energy densities E_0 reproduces results for linear optimal perturbations in

stratified PCF that were computed in Matlab using singular value decomposition. We now discuss the results of each test in turn.

2.5.1 Unstratified minimal seed

Rabin *et al.* (2012) considered unstratified PCF in the narrow geometry N and found the nonlinear optimal perturbations that maximised the total kinetic energy at the target time T, with objective functional

$$\mathcal{J}[\mathbf{u}(\mathbf{x},t)] = \|\mathbf{u}(\mathbf{x},T)\|^2, \tag{2.83}$$

over a range of initial energy densities E_0. Their main results are shown in Figure 2.4, which plots the maximum possible gain in kinetic energy density over its initial value, optimised further over all target times T to find $G_{\max}$ as a function of initial energy density E_0. We see that for small initial energy densities, nonlinear DAL converged to 'quasi-linear' optimal perturbations. These solutions are slightly nonlinearly modified versions of the linear optimal perturbation of Butler & Farrell (1992). If E_0 is small enough, the kinetic energy density gain is precisely that of the linear optimal perturbation of Butler & Farrell (1992) and its structure is indistinguishable from the linear optimal result.

For large initial energy densities E_0, nonlinear DAL identifies initial conditions that eventually trigger turbulence. The inverse proportionality of kinetic energy density gain with respect to initial kinetic energy density E_0 for large E_0 is consistent with the same turbulent attractor being reached by all the initial conditions, so that the objective functional $\mathcal{J}$ takes the same value as E_0 is varied in this range.

There is a clear discontinuity in the achievable kinetic energy density gain, jumping from around 1120 to around 60 000 at $E_0 \approx 2.25\times10^{-6}$. This is clearly the initial kinetic energy density beyond which it is possible to transition to turbulence and so we identify E_c. Rabin *et al.* (2012) provide the bounds $2.225 \times 10^{-6} < E_c < 2.250 \times 10^{-6}$ since nonlinear DAL was unable to find initial conditions that transition to turbulence at the lower bound but did find an initial condition that transitions to turbulence at the upper bound. This initial condition is labelled the 'minimal seed' for turbulence and is shown in Figure 2.5 along with snapshots of its subsequent evolution.

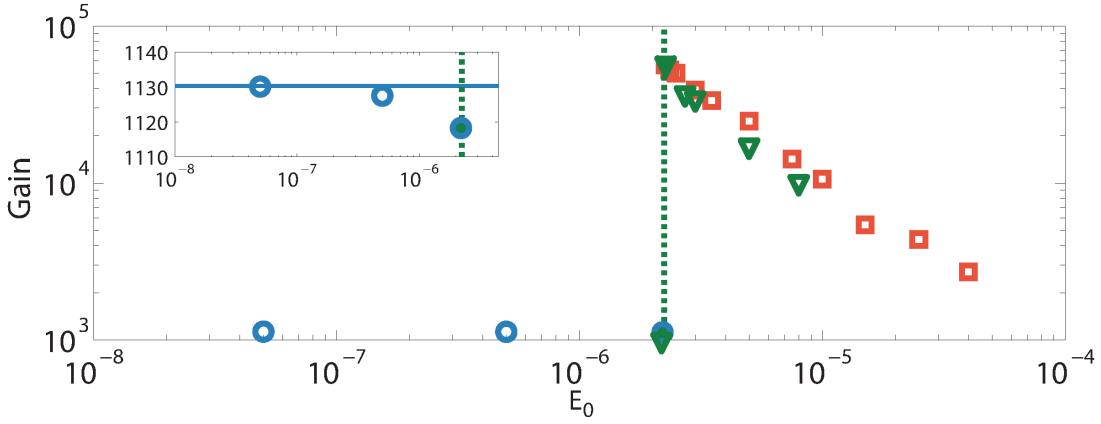

Figure 2.4: Nonlinear optimal perturbations in unstratified PCF in geometry N at Reynolds number $Re = 1000$. Kinetic energy density gain as a function of initial kinetic energy density E_0. Blue circles and red squares: Maximum achievable kinetic energy gain from Rabin *et al.* (2012) using total kinetic energy at the target time T as the objective functional, optimised further over all target times T. Green triangles: Kinetic energy gain of nonlinear optimal perturbations that maximise the time averaged dissipation of kinetic energy objective functional over the fixed target time $T = 300$. Green dashed line is $E_0 = E_c$. Inset shows quasi-linear regime and the linear optimal perturbation result (blue line). Figure adapted from Rabin *et al.* (2012).

The minimal seed initial condition consists of a streamwise localised disturbance with structures tilted against the mean shear. The initial phase of its evolution consists of these structures being tilted over by the mean shear, resulting in an energy increase via the Orr mechanism (see Orr, 1907*a*). The structures are further sheared out until they occupy the full domain. The oblique wave mechanism then transfers energy into streamwise aligned, nearly streamwise independent streaks of streamwise velocity. This structure persists for a substantial time period, utilising the lift-up mechanism (see Landahl, 1980) to self-sustain as in the self-sustaining process of Waleffe (1997). This structure is very weakly unstable, and eventually the instability sets in and transition to turbulence occurs. This sequence of events is a common feature of minimal seed trajectories in unstratified PCF, as outlined

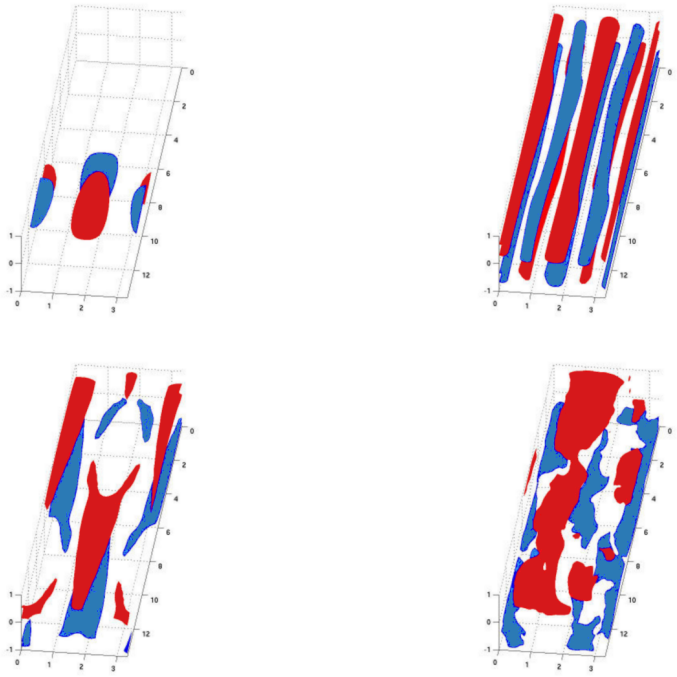

Figure 2.5: Isosurfaces of perturbation streamwise velocity $u = \pm 0.6 \max(u)$ for the evolution in time of the unstratified minimal seed in geometry N with initial kinetic energy density $E_0 = 2.25 \times 10^{-6}$. Top left: $t = 0$, top right: $t = 150$, bottom left $t = 250$, bottom right $t = 350$. Figure adapted from Rabin (2013).

by Duguet *et al.* (2013).

To verify that the newly written code is working, we perform the laddering down procedure for the same flow geometry and parameters used by Rabin *et al.* (2012) to find the minimal seed. In doing so we also verify the hypothesis by Rabin *et al.* (2012) that the use of kinetic energy density at the target time T as the objective functional $\mathcal{J}$ and the use of the time averaged dissipation of kinetic energy over the time interval $[0, T]$ as considered by Monokrousos *et al.* (2011) should produce the same minimal seed for a fixed geometry and parameter set. From a dynamical systems point of view this hypothesis is fairly clear, since both measures take on heightened values in the turbulent attractor compared to the laminar state, and so provided that the target time T is large enough, all initial conditions are inevitably attracted to one or the other of these states. Hence there is no *a priori* reason why the two different objective functionals should

find different minimal seeds in the limit of $T \to \infty$. It is of course possible that different minimal seeds could be identified if either one of the objective functionals repeatedly finds a local optimiser, and the alternative method is able to find a better optimal initial condition.

Figure 2.4 also shows the kinetic energy density gains of initial conditions found as a result of the nonlinear optimisation scheme run with the new code and with the time averaged dissipation of kinetic energy objective functional

$$\mathcal{J}[\mathbf{u}(\mathbf{x},t)] = \frac{1}{TRe}\int_0^T \|\nabla \mathbf{u}(\mathbf{x},t)\|^2 \, \mathrm{d}t, \tag{2.84}$$

for a *fixed* target time $T = 300$. We see that for $E_0 > E_c$ the gain achieved by these new initial conditions lies slightly below those found by Rabin *et al.* (2012). This is because in the transition to turbulence, all these initial conditions overshoot in energy before relaxing onto the turbulent attractor. The initial conditions of Rabin *et al.* (2012) had an additional optimisation over target time T to find the absolute highest achievable gain, and this occurs during the overshoot period at times $t < 300$, before relaxing onto the turbulent attractor. In contrast for the fixed target time calculations with $T = 300$ all these initial conditions reach the turbulent attractor and so their final energies are lower than those of Rabin *et al.* (2012).

The choice of the fixed target time $T = 300$ was due to the minimal seed of Rabin *et al.* (2012) requiring an optimised target time $T \approx 300$ for the optimal energy gain to be reached and so the minimal seed initial condition we find here with the new code and different objective functional has almost exactly the same kinetic energy gain in Figure 2.4 as that of Rabin *et al.* (2012). We also find that if we reduce E_0 below the E_c found by Rabin *et al.* (2012) we are no longer able to find initial conditions that transition to turbulence, confirming the hypothesis about the equivalence of the two objective functions for finding minimal seed initial conditions and verifying the unstratified part of the new code. The initial condition and subsequent trajectory that we find has the same structure as that shown in Figure 2.5 up to a shift in the periodic directions and we find the same bounds on the critical initial energy density, $2.225 \times 10^{-6} < E_c < 2.250 \times 10^{-6}$.

2.5.2 Stratified linear optimal perturbations

We also need to verify that the stratified part of the new code has been implemented accurately. There have been no reported calculations of stratified nonlinear optimal perturbations and so the best test we have is to compare nonlinear DAL run at very low initial energies, so that we are in the linear regime, to linear optimal perturbations calculated using the singular value decomposition method.

Since the singular value decomposition method relies on the finding the gain of a single norm, we are forced to use the total energy density objective functional $\mathcal{J}$ since the initial constraint is also on the total energy density. We therefore optimise for the total perturbation energy at the target time T and set

$$\mathcal{J}[\mathbf{u}(\mathbf{x},t),\rho(\mathbf{x},t)] = \|\mathbf{u}(\mathbf{x},T)\|^2 + Ri_B\|\rho(\mathbf{x},T)\|^2. \tag{2.85}$$

The equation for inviscid linear perturbations about a one-dimensional base flow and background stratification $(\mathbf{U}(y),\bar{\rho}(y))$ is called the Taylor–Goldstein equation (Taylor, 1931; Goldstein, 1931). To find linear optimal perturbations in vertically sheared stratified PCF, we used a version of the Matlab-based viscous Taylor–Goldstein equation solver of Smyth *et al.* (2011), modified to find optimal perturbations instead of normal mode solutions. We additionally optimise over the target time T so that the highest achievable energy density gain $G_{\max} \equiv G(T_{\text{opt}})$ is found.

Figure 2.6 shows the gain $G(T_{\text{opt}})$ and the optimal time T_{opt} for the four horizontal wavenumber vectors (n_x, n_z) with highest energy density gain, quantised with respect to the narrow geometry N, at Reynolds number $Re = 1000$ and Prandtl number $Pr = 1$ for bulk Richardson numbers in the range $0 \leq Ri_B \leq 0.3$. We reproduce the unstratified result of Butler & Farrell (1992) which has $G(T_{\text{opt}}) = 1130$ and $T_{\text{opt}} = 125.25$.

The most striking feature of Figure 2.6 is the extremely rapid reduction in both $G(T_{\text{opt}})$ and T_{opt} as the bulk Richardson number Ri_B is increased. It is expected that the maximum achievable energy density gain should decrease as the bulk Richardson number, or stratification strength, increases since a strong stable stratification tends to inhibit vertical motions and stabilise flows. However, the extent of the rapid suppression of possible gains is surprising.

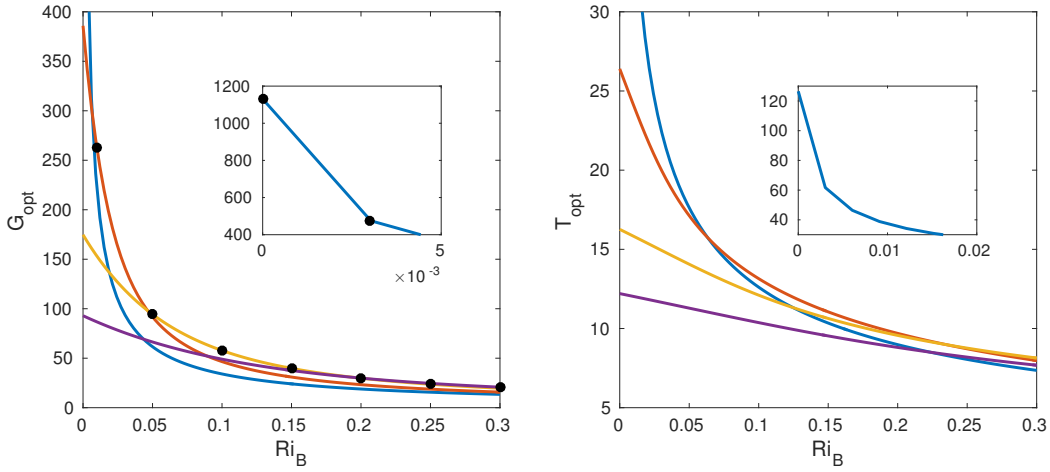

Figure 2.6: Linear optimal perturbations of stratified PCF in geometry N at Reynolds number $Re = 1000$, Prandtl number $Pr = 1$ and bulk Richardson numbers $0 \leq Ri_B \leq 0.3$. for wavenumbers $(n_x, n_z) = (0, 1)$ (blue), $(1, 1)$ (red), $(2, 1)$ (yellow) and $(3, 1)$ (purple), quantised by the geometry N. Left: Lines: Energy density gain at the optimal target time, $G(T_{\text{opt}})$ from singular value decomposition method. Dots: Energy density gain using nonlinear DAL with target time $T = T_{\text{opt}}$. Right: Optimal target time, T_{opt}, from singular value decomposition method.

We see that when $Ri_B \approx 0.007$ we have a transition in the form of the linear optimal perturbation from a streamwise independent solution with wavenumber $(0, 1)$ to an oblique mode with wavenumber $(1, 1)$. The linear optimal perturbations with wavenumber $(0, 1)$ are streamwise aligned vortices that primarily use the lift-up mechanism to extract energy from the base flow over a very long time period. In contrast, the linear optimal perturbations with wavenumber $(1, 1)$ consist of oblique structures that are aligned against the mean shear and extract energy from the base flow through the fast acting Orr mechanism in which the background shear tilts the structures over to become aligned with it, resulting in transient energy growth. This transition from the long lasting lift-up to the fast acting Orr mechanism makes sense in the context of stratified flows because the lift-up mechanism relies explicitly on vertical motions for perturbation growth whilst the Orr mechanism does not necessarily incorporate such vertical motions.

Also plotted in Figure 2.6 are the total energy density gains at a number of bulk Richardson numbers Ri_B found by nonlinear DAL run at very low initial

energy densities E_0 in the linear regime where the target time T is chosen to be the optimal target time T_{opt} found by the singular value decomposition method. We see that the agreement is excellent, and so we have confidence that the newly written code represents the stratified terms accurately, at least in the linear regime.

The observation that the maximum achievable gain and optimal target time decrease rapidly with Ri_B and that the optimal solutions change from streamwise independent structures that use the lift-up mechanism to oblique structures that use the Orr mechanism is not restricted only to this specific set of parameters. We also performed the same calculation in the much larger geometry $4\pi \times 2 \times 2\pi$ and higher Reynolds number $Re = 1500$, considered by Monokrousos *et al.* (2011) in the unstratified case, and found the same generic behaviour.

The final feature of note is that the 'magic' value for the bulk Richardson number, 0.25, does not appear to carry any significance in the linear optimal perturbation results, as demonstrated by the linear optimal perturbations of an infinite stratified shear found by Farrell & Ioannou (1993) and of a stratified shear layer found by Kaminski *et al.* (2014). The reason that this value is important is due to the Miles–Howard theorem (see Miles, 1961; Howard, 1961) which states that if the *gradient* Richardson number, a locally measured equivalent of the bulk Richardson number, is greater that 0.25 everywhere in a base flow then the flow is linearly asymptotically stable to normal mode inviscid perturbations. Although this result has nothing to do with transient linear optimal perturbations, or indeed the transition to turbulence, it is often misused in this way to parametrise ocean mixing events. We have demonstrated here that even within the linear regime, the requirements of the theorem are very strict and that no inference about the value 0.25 can be made outside of the admissibility of inviscid, linear, normal mode instabilities.

CHAPTER 3

VERTICALLY SHEARED MINIMAL SEEDS

In this chapter we identify minimal seeds for turbulence in vertically sheared stratified PCF. To find minimal seeds, we use the direct-adjoint looping (DAL) method described in Chapter 2 for finding nonlinear optimal perturbations that optimise the time averaged total dissipation of energy in the flow. These minimal seeds are located adjacent to the edge manifold, the manifold in state space that separates trajectories which transition to turbulence from those which eventually decay to the laminar state. The edge manifold is also the stable manifold of the system's edge state. Therefore, the trajectories from the minimal seed initial conditions spend a large amount of time in the vicinity of some states: the edge state; another state contained within the edge manifold; or even in dynamically slowly varying regions of the edge manifold, allowing us to investigate the effects of a stable stratification on any coherent structures associated with such states.

The stratified coherent states we identify at moderate Reynolds number display an altered form from their unstratified counterparts for bulk Richardson numbers $Ri_B = g\Delta\rho H/(\rho_r \Delta U^2) \approx O(Re^{-1})$, and exhibit chaotic motion for larger Ri_B. We demonstrate that at high Reynolds number the suppression of vertical motions by stratification strongly disrupts input from the waves to the roll velocity structures in the SSP/VWI ansatz, thus preventing the waves from reinforcing the viscously

decaying roll structures adequately, when $Ri_B \sim O(Re^{-2})$.

In Section 3.1 we once more outline the algorithm used to find minimal seeds discussed in Chapter 2, which is the same nonlinear direct-adjoint looping (DAL) method used by Rabin *et al.* (2012) and is the nonlinear culmination of optimal perturbation analysis developed first for steady linear problems, later for time varying linear problems (see Schmid, 2007), and most recently for fully nonlinear dynamics (see e.g. Pringle & Kerswell (2010); Cherubini *et al.* (2010), and for reviews Luchini & Bottaro (2014); Kerswell *et al.* (2014)). In Section 3.2 we show the results of the DAL method applied to vertically sheared stratified PCF. In Section 3.3 we interpret the identified trajectories of minimal seeds for turbulence in vertically sheared stratified PCF in the language of SSP/VWI states, and demonstrate that the presence of a surprisingly weak stable stratification can still significantly modify the whole interaction by disrupting the nonlinear feedback from the waves into the roll structures, principally through an inhibition of vertical motions. We draw our conclusions in Section 3.4.

3.1 Direct-Adjoint Looping (DAL) method

As outlined in Chapter 2, we consider vertically sheared stably stratified Boussinesq PCF with a linear equation of state in which fluid flows between two parallel horizontal plates moving in opposite directions with relative speed $2\Delta U$, separated by a distance $2H$, across which a constant density difference $2\Delta\rho$ is maintained from a reference density $\rho_r \gg \Delta\rho$. Nondimensionalising with respect to ΔU, H and $\Delta\rho$, and decomposing the total velocity and density fields as $(\mathbf{u}_{\rm tot}, \rho_{\rm tot}) = (\mathbf{U}, \bar{\rho}) + (\mathbf{u}, \rho)$, where $(\mathbf{U}, \bar{\rho})$ is the laminar state, we obtain

$$\begin{aligned}
\frac{\partial \mathbf{u}}{\partial t} + (\mathbf{u}+\mathbf{U})\cdot\nabla(\mathbf{u}+\mathbf{U}) &= -\nabla p - Ri_B\rho\hat{\mathbf{y}} + \frac{1}{Re}\nabla^2\mathbf{u}, \\
\frac{\partial \rho}{\partial t} + (\mathbf{u}+\mathbf{U})\cdot\nabla(\rho+\bar{\rho}) &= \frac{1}{RePr}\nabla^2\rho, \\
\nabla\cdot\mathbf{u} &= 0, \\
(\mathbf{u},\rho)(y=\pm 1) &= (\mathbf{0},0), \\
\mathbf{U} = y\hat{\mathbf{x}}, \quad &\text{and} \quad \bar{\rho} = -y. \qquad (3.1)
\end{aligned}$$

with the three nondimensional parameters: Reynolds number Re; Prandtl number Pr; and bulk Richardson number Ri_B defined as

$$Re = \frac{\Delta U H}{\nu},\ Pr = \frac{\nu}{\kappa},\ Ri_B = \frac{g\Delta\rho H}{\rho_r \Delta U^2}, \tag{3.2}$$

where ν is the kinematic viscosity and κ is the diffusivity of density. For the calculations presented here, following Rabin *et al.* (2012), we choose $Re = 1000$, set $Pr = 1$, and vary Ri_B.

We define a *nonlinear optimal perturbation* as an initial condition $(\mathbf{u}, \rho)(t = 0) = (\mathbf{u}_0, \rho_0)$ of given initial total energy density (kinetic energy density plus potential energy density) E_0, defined as

$$E_0 = \left\langle \mathbf{u}_0 \cdot \mathbf{u}_0 + Ri_B \rho_0^2 \right\rangle /2, \text{ where } \langle \mathbf{a}, \mathbf{b} \rangle \equiv \frac{1}{V} \int_V \mathbf{a} \cdot \mathbf{b}\ \mathrm{d}V, \tag{3.3}$$

that maximises, over a given time horizon T, a given quantity of interest $\mathcal{J}(\mathbf{u}, \rho, T)$. Here, V is the volume of the computational domain. In order to find minimal seeds for turbulence, which are initial conditions whose trajectories eventually transition to turbulence, we typically choose an appropriately large value $T = 300$, and we consider a functional $\mathcal{J}$ that takes heightened values in the turbulent state. With the presence of a density field, it is possible to find large amplitude waves that have an instantaneously large total energy, but are not a turbulent state. Therefore, rather than choosing the total energy density at T as $\mathcal{J}$, as was done by Rabin *et al.* (2012) for unstratified minimal seeds, we choose the total time averaged dissipation of total energy density, the stratified generalisation of the objective functional chosen by Monokrousos *et al.* (2011), for an equivalent minimal seed calculation.

We thus write

$$\mathcal{J} = \frac{1}{TRe} \left[\nabla \mathbf{u} : \nabla \mathbf{u} + \frac{Ri_B}{Pr} \nabla\rho \cdot \nabla\rho \right], \tag{3.4}$$

where $[\mathbf{a}, \mathbf{b}] \equiv \int_0^T \langle \mathbf{a}, \mathbf{b} \rangle\ \mathrm{d}t$, and the maximisation of $\mathcal{J}$ can be conducted by taking variations of the augmented and constrained functional $\mathcal{L}$:

$$\begin{aligned} \mathcal{L} \ = \ & \mathcal{J}(\mathbf{u}, \rho, T) - \left[\frac{\partial \mathbf{u}}{\partial t} + N(\mathbf{u}) + \nabla p + Ri_B \rho \hat{\mathbf{y}} - \frac{1}{Re} \nabla^2 \mathbf{u}, \mathbf{v} \right] - [\nabla \cdot \mathbf{u}, q] \\ & - \left[\frac{\partial \rho}{\partial t} + (\mathbf{u} + \mathbf{U}) \cdot \nabla(\bar{\rho} + \rho) - \frac{1}{RePr} \nabla^2 \rho, \eta \right] + \langle \mathbf{u}_0 - \mathbf{u}(0), \mathbf{v}_0 \rangle \\ & + \langle \rho_0 - \rho(0), \eta_0 \rangle - \left(\|\mathbf{u}_0\|^2 + Ri_B \|\rho_0\|^2 - 2E_0 \right) c, \end{aligned} \tag{3.5}$$

where $N(\mathbf{u}) = (\mathbf{u}+\mathbf{U})\cdot\nabla(\mathbf{u}+\mathbf{U})$. The Lagrange multipliers $\mathbf{v}$, q and η are termed the adjoint velocity, pressure and density and together enforce the Boussinesq Navier–Stokes equations (3.1) on $\mathbf{u}$ and ρ. The initial conditions and initial energy are enforced by $\mathbf{v}_0$, η_0 and c. Taking variations with respect to $\mathbf{u}$, ρ, $\mathbf{u}_0$ and ρ_0 yields the following system of 'adjoint' or 'dual' equations that must also be satisfied at all times and points in space by a nonlinear optimal perturbation:

$$\frac{\partial \mathbf{v}}{\partial t} + N^\dagger(\mathbf{v},\mathbf{u}) + \frac{1}{Re}\nabla^2\mathbf{v} + \nabla q - \eta\nabla(\bar{\rho}+\rho) - \frac{1}{ReT}\nabla^2\mathbf{u} = 0, \tag{3.6}$$

$$\frac{\partial \eta}{\partial t} + (\mathbf{U}+\mathbf{u})\cdot\nabla\eta + \frac{1}{RePr}\nabla^2\eta - Ri_B\,\hat{\mathbf{y}}\cdot\mathbf{v} - \frac{Ri_B}{RePrT}\nabla^2\rho = 0, \tag{3.7}$$

$$\nabla\cdot\mathbf{v} = 0, \tag{3.8}$$

$$\mathbf{v}(T) = 0, \quad \eta(T) = 0, \tag{3.9}$$

$$\mathbf{v}(0) - c\mathbf{u}_0 = 0, \quad \eta(0) - c\rho_0 Ri_B = 0, \tag{3.10}$$

$$\langle \mathbf{u}_0, \mathbf{u}_0\rangle + \left\langle Ri_B\rho_0^2\right\rangle - 2E_0 = 0, \tag{3.11}$$

where $N^\dagger(v_i,\mathbf{u}) = \partial_j\left((U_j+u_j)v_i\right) - v_j\partial_i(U_j+u_j)$.

The first step of the DAL method to find a nonlinear optimal perturbation is to choose an initial condition guess $(\mathbf{u}_0,\rho_0)$ of energy density E_0. This initial condition is then integrated forwards in time to $t=T$ using the direct Boussinesq Navier–Stokes equations (3.1). These flow fields are stored, and used to integrate backwards in time the adjoint fields $\mathbf{v}$ and η from the null 'end' conditions (3.9) using the adjoint equations (3.8), which actually depend on the direct fields $(\mathbf{u},\rho)$. Once values for the adjoint variables are obtained at $t=0$, we have compatibility conditions (3.10) relating $\mathbf{v}(0)$ to $\mathbf{u}_0$ and $\eta(0)$ to ρ_0 that must be satisfied by a nonlinear optimal perturbation. If not satisfied, these compatibility conditions yield gradient information for the objective functional $\mathcal{J}$ with respect to changes in the initial condition $(\mathbf{u}_0,\rho_0)$, allowing a refined guess for the nonlinear optimal perturbation to be made. This sequence of steps is continued until convergence.

For large T, any initial condition that eventually becomes turbulent will be a turbulent seed using this method. The minimal seed, however, has the special property of having the lowest critical initial energy density $E_0 = E_c$ of all such seeds. We first identify a perturbation that causes turbulence, with initial energy density $E_0 = E_\alpha \gg E_c$. This initial condition is then used as an initial guess for

Ri_B	E_c (N)	E_c (W)
0	$2.225 \times 10^{-6} < E_c < 2.250 \times 10^{-6}$	$8.925 \times 10^{-7} < E_c < 8.950 \times 10^{-7}$
10^{-4}	$2.250 \times 10^{-6} < E_c < 2.275 \times 10^{-6}$	N/A
10^{-3}	$2.600 \times 10^{-6} < E_c < 2.625 \times 10^{-6}$	N/A
3×10^{-3}	$3.450 \times 10^{-6} < E_c < 3.475 \times 10^{-6}$	$1.450 \times 10^{-6} < E_c < 1.475 \times 10^{-6}$
10^{-2}	$6.300 \times 10^{-6} < E_c < 6.400 \times 10^{-6}$	$2.450 \times 10^{-6} < E_c < 2.575 \times 10^{-6}$

Table 3.1: Values of the critical energy density E_c, the energy of the minimal seed, for various bulk Richardson numbers Ri_B in the two geometries N and W. The upper bound corresponds to the flow evolutions shown in subsequent figures. The lower bound corresponds to an E_0 at which a turbulent state cannot be attained.

the DAL method at a smaller initial energy density $E_0 = E_\beta < E_\alpha$, with uniformly rescaled energy. The DAL method then finds a more efficient route to turbulence at $E_0 = E_\beta$. This more efficient initial condition is then uniformly rescaled to have energy density $E_0 = E_\gamma < E_\beta$, and the process is repeated. This 'laddering down' is continued until $E_0 = E_c$, at which point any further reduction in E_0 cannot find an initial condition leading to turbulence.

3.2 Stratified minimal seeds for turbulence

We investigate two geometries, namely the 'narrow' geometry 'N' investigated by Rabin *et al.* (2012) in the unstratified case, $4.35\pi \times 2 \times 1.05\pi$, one of the geometries considered by Butler & Farrell (1992) for linear, unstratified optimal perturbations in which the unstratified minimal seeds are localised in the streamwise direction but essentially fill the spanwise width, and $4.35\pi \times 2 \times 2.10\pi$ a 'wide' geometry 'W', which is twice as wide, and allows for localisation in the spanwise direction also. We used a modified version of the parallelised direct numerical time-stepper Diablo (Taylor, 2008) to solve the direct and adjoint equations, which uses Fourier modes in the streamwise x and spanwise z directions, and finite differences in the wall-normal y direction, and uses a combined implicit-explicit Runge-Kutta-Wray Crank-Nicholson time integration scheme. The resolution for geometry N was $128 \times 256 \times 32$ and for geometry W was $128 \times 256 \times 64$.

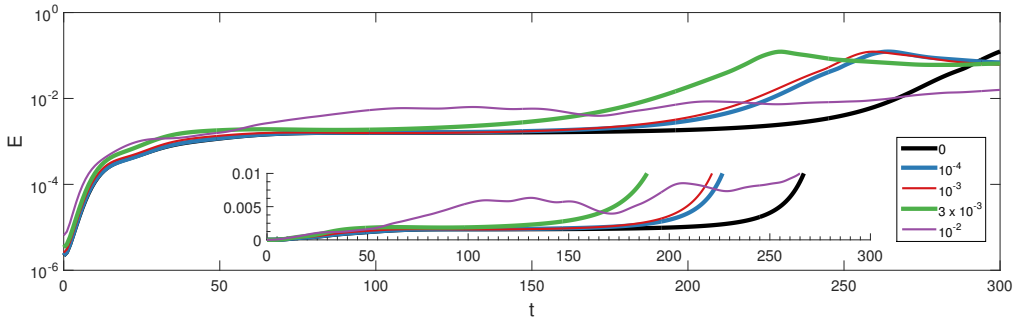

Figure 3.1: Time variation of energy density $E(t)$ as defined in (3.12) for the minimal seed trajectories in geometry N for $Ri_B = 0$, black, 10^{-4}, red, 10^{-3}, blue, 3×10^{-3}, green and 10^{-2}, purple.

Using the laddering down approach described above, we have converged to the minimal seed for $Ri_B = 0$ (confirming quantitatively the unstratified case of Rabin *et al.* (2012) using a different code, and objective functional $\mathcal{J}$), $Ri_B = 10^{-4}$, 10^{-3}, 3×10^{-3} and 10^{-2} in geometry N and $Ri_B = 0$, 3×10^{-3} and 10^{-2} in geometry W, using the fixed value $T = 300$ for all bulk Richardson numbers except for the largest, $Ri_B = 10^{-2}$, for which we use $T = 400$. The respective values of $E_c(Ri_B)$ are shown in Table 3.1. We immediately see that E_c is an increasing function of Ri_B, as expected, since a stable stratification inhibits vertical motions, and so a transition process involving vertical motions should be expected to require a larger energy input. Interestingly, E_c in geometry W is approximately 40% of E_c in geometry N for the same Ri_B. Since E_c, as defined in (3.3), is an energy density, and the volume of geometry W is twice that of geometry N, this suggests that the minimal seeds in geometry W are spanwise localised, and that the narrow geometry N actually requires higher maximum amplitudes of perturbation in the minimal seed due to the enforced spanwise periodicity.

3.2.1 'Narrow' geometry N

Figure 3.1 shows the time evolution from the minimal seed initial conditions for geometry N of the total energy density $E(t)$ defined as

$$E(t) = \frac{1}{2}\left\langle \mathbf{u}\cdot\mathbf{u} + Ri_B\rho^2 \right\rangle = K(t) + P(t), \tag{3.12}$$

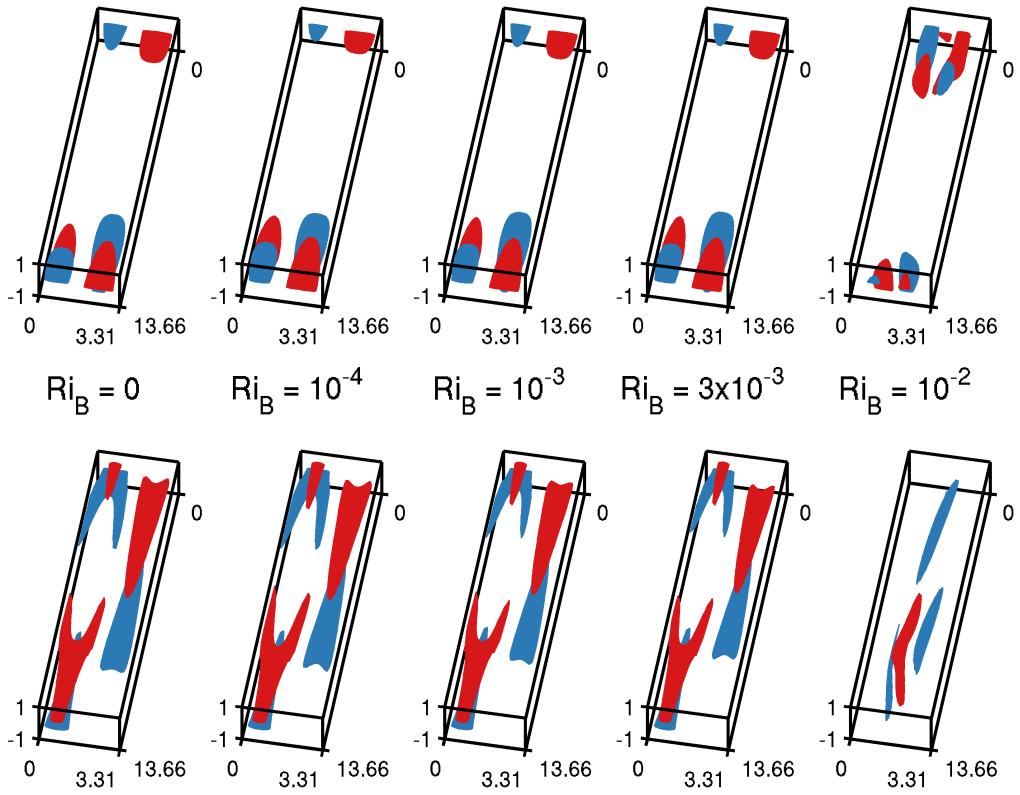

Figure 3.2: Isosurfaces of streamwise perturbation velocity $u = \pm 0.6\max(u)$ at $t = 0$ (top row) and $t = 25$ (bottom row) for the minimal seed trajectories in geometry N for $Ri_B = 0$, 10^{-4}, 10^{-3}, 3×10^{-3}, and 10^{-2}, from left to right.

where $K(t)$ is the kinetic energy density, $P(t)$ is the potential energy density, and angled brackets denote volume averaging as defined in (3.3). Streamwise velocity $u = \pm 0.6\max(u)$ isosurfaces are plotted in figures 3.2, 3.3 and 3.4 at times $t = 0$ and 25, $t = 70$ and 150, and $t = 210$ and 280 respectively.

The unstratified minimal seed, as shown in the leftmost column, consists of a localised patch of flow structures aligned against the mean shear, unwrapping via the Orr mechanism (see Orr, 1907*a*) into an array of streamwise aligned structures with a distinct oblique component, shown in the bottom left panel of Figure 3.2. These oblique structures then transfer energy into streamwise independent streaks through the oblique wave mechanism in which structures with wavenumbers $(k_x, k_z) = (0, \pm a)$ interact nonlinearly to move energy into the wavenumeber

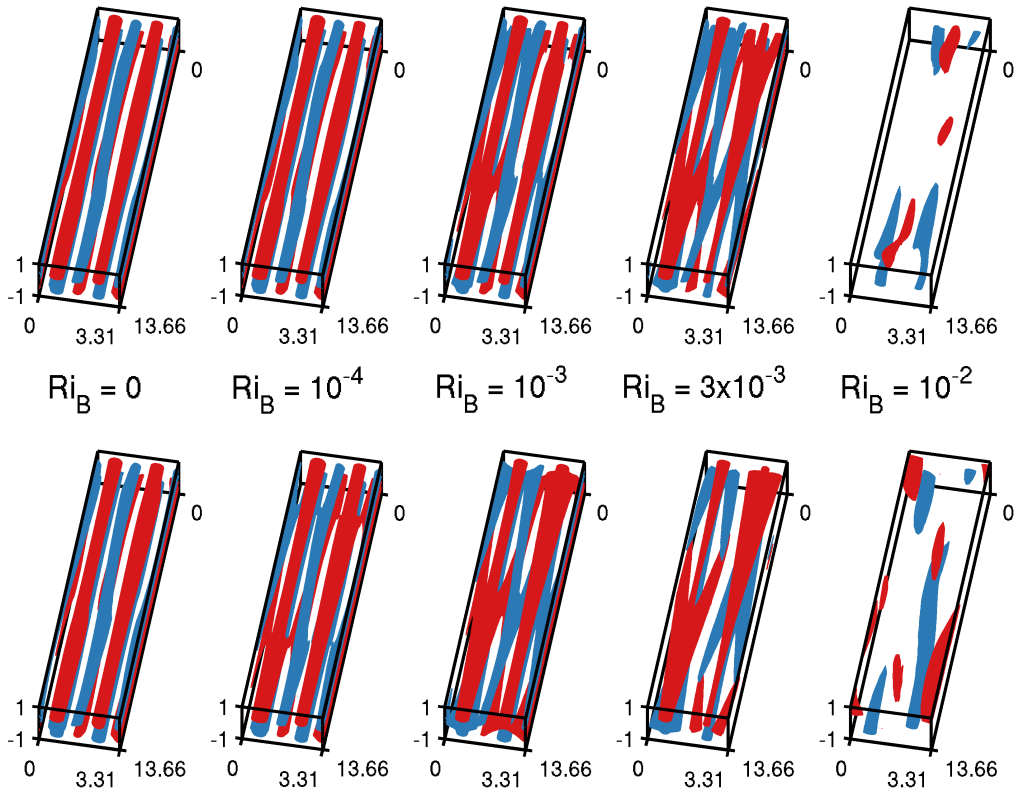

Figure 3.3: Isosurfaces of streamwise perturbation velocity $u = \pm 0.6 \max(u)$ at $t = 70$ (top row) and $t = 150$ (bottom row) for the minimal seed trajectories in geometry N for $Ri_B = 0$, 10^{-4}, 10^{-3}, 3×10^{-3}, and 10^{-2}, from left to right.

$(k_x, k_z) = (0, 0)$. These streaks are then able to 'self-sustain' for a long period of the flow's evolution, as shown in the leftmost column of Figure 3.3, by utilising the lift-up mechanism (described by Landahl, 1980) and their own instability to offset viscous decay, (see Waleffe, 1997), before eventually being of large enough amplitude to transition to a high energy oblique structure, as shown in the leftmost column of Figure 3.4, which is visited only transiently, leading to a break down to small scale turbulence due to an instability reminiscent of the Kelvin–Helmholtz instability. The energetics of these sequential growth mechanisms in unstratified minimal seed trajectories were discussed by Pringle *et al.* (2012) and Duguet *et al.* (2013).

This transition mechanism has been interpreted by Rabin *et al.* (2012) as an

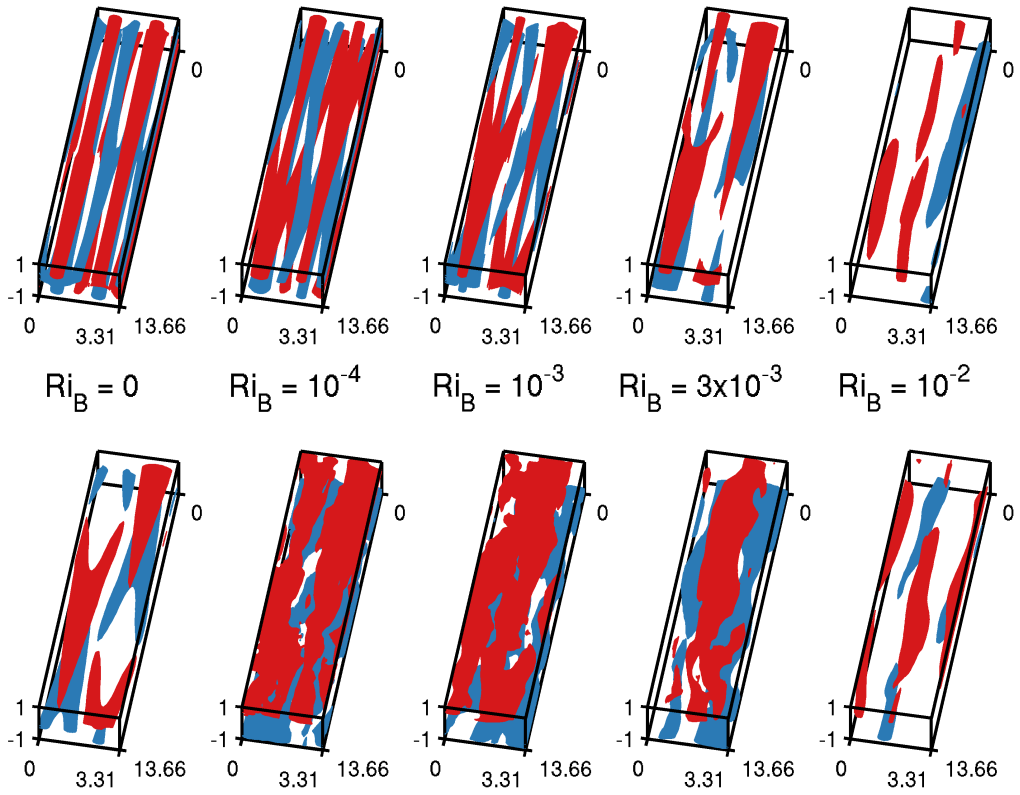

Figure 3.4: Isosurfaces of streamwise perturbation velocity $u = \pm 0.6 \max(u)$ at $t = 210$ (top row) and $t = 280$ (bottom row) for the minimal seed trajectories in geometry N for $Ri_B = 0$, 10^{-4}, 10^{-3}, 3×10^{-3}, and 10^{-2}, from left to right.

initial concentration of energy in a small region of the flow, allowing a minimisation of the total energy input whilst maximising the local energy input. From this point, the most efficient way to transition to turbulence is by exploiting the lift-up mechanism on a high energy flow structure and thus increasing the total energy of the flow to a point beyond which it is sufficiently unstable to become turbulent. As shown in Figure 3.1, there is a sustained period of near-constant energy density $E(t)$, and during this time the flow is only very slowly changing, indicating that the flow trajectory is near a coherent state. The isosurfaces plotted in the leftmost columns of Figure 3.3 show that this state is very reminiscent of an SSP/VWI state. As Ri_B is increased to $Ri_B = 10^{-4}$ and 10^{-3}, the minimal seed, its trajectory, and the coherent state to which it approaches, remain very

similar to the unstratified case, as can be seen from the flow isosurfaces shown in the second and third columns of Figures 3.2, 3.3 and 3.4, although there are the beginnings of an oblique structure appearing in the coherent states to which these flows evolve.

As Ri_B is increased further, the behaviour changes qualitatively. The minimal seed for $Ri_B = 3 \times 10^{-3}$, (as shown in the fourth column, top row of Figure 3.2) still consists of a localised patch of flow structures aligned against the mean shear, which unwrap via the Orr mechanism into the same array of streamwise aligned structures with a distinct oblique component, followed by the oblique wave mechanism. However, the newly created streamwise independent streaks are visited only transiently, no longer able to be sustained, and the flow evolves into a new, fully three dimensional coherent state which is shown in the fourth column of Figure 3.3. This new stratified coherent state is different from the unstratified SSP/VWI state visited by the unstratified minimal seed trajectory, with the stratified coherent state being clearly more three dimensional and very reminiscent of the stratified edge states recently reported by Olvera & Kerswell (2014).

Figure 3.1 shows that in the cases $Ri_B = 10^{-4}$, 10^{-3} and 3×10^{-3}, transition to turbulence is apparently faster than the unstratified case, with the same accuracy in the estimated value of E_c, and the same time target time $T = 300$. However, the time taken to transition to turbulence is a function of how close our numerical estimates for the minimal seed initial conditions are to the edge manifold. In the limit of successively better approximations to the 'ideal' minimal seed, which lies exactly on the edge manifold, $t_{transition} \to \infty$. Therefore, since the value of E_c is only bracketed to a certain accuracy, the time to transition for the minimal seeds presented here is most likely to be affected by the actual value of E_c relative to the energy bracket for E_c found here.

The minimal seed for $Ri_B = 10^{-2}$ is once again of a qualitatively different character. Although it still consists of a localised patch of flow structures that unwrap via the Orr mechanism, there appears to be no quasi-steady flow structure into which it evolves. The flow is now chaotic with a weak oscillation, with no single structure dominating the flow evolution. Indeed, due to the chaotic nature of the dynamics on the edge manifold that this trajectory follows, the DAL method struggled to identify turbulent solutions without extending the optimisation time

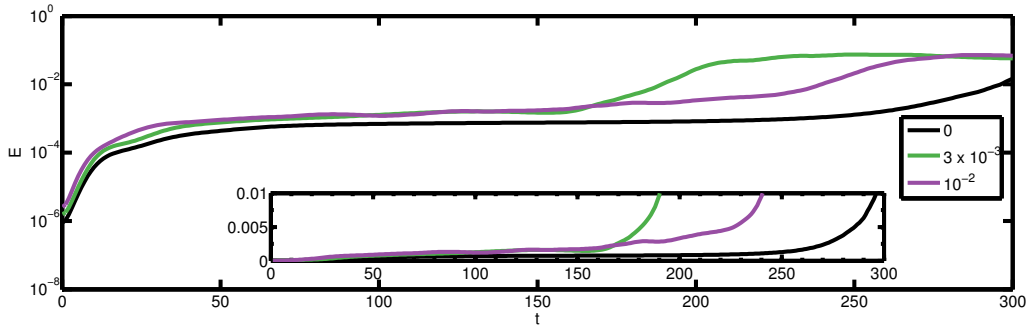

Figure 3.5: Time variation of energy density $E(t)$ as defined in (3.12) for the minimal seed trajectories in geometry W for $Ri_B = 0$, black, 3×10^{-3}, green, and 10^{-2}, purple.

interval to $T = 400$. Even after extending the optimisation time interval, the DAL method required up to ten times as many iterations to identify initial conditions that transition to turbulence for the flow with $Ri_B = 10^{-2}$ compared to the number of iterations required for flows with smaller bulk Richardson numbers, apparently because of the chaotic nature of the edge manifold.

3.2.2 'Wide' geometry W

As already noted, the minimal seeds in the narrow geometry N are streamwise localized, but fill much of the spanwise extent of the computational domain. To investigate to some extent the sensitivity of the identified minimal seeds to the flow geometry, we also calculate minimal seeds in geometry W, which is twice as wide in the spanwise direction. Figure 3.5 shows the time evolution from the minimal seed initial conditions of the total energy density $E(t)$ as defined in (3.12) for the wide geometry W. Streamwise velocity $u = \pm 0.6 \max(u)$ isosurfaces are plotted in Figures 3.6, 3.7 and 3.8 at times $t = 0$ and 25, $t = 70$ and 150, and $t = 210$ and 280 respectively.

The $Ri_B = 0$ unstratified minimal seed trajectory in this wider geometry shares the same characteristic evolution as the minimal seed trajectory in the narrower geometry, but with the addition of spanwise localisation, that is a streamwise and spanwise localised patch of flow structures aligned against the mean shear which unwrap via the Orr mechanism into a streamwise aligned structure with a distinct oblique component, as shown in the leftmost column of Figure 3.6,

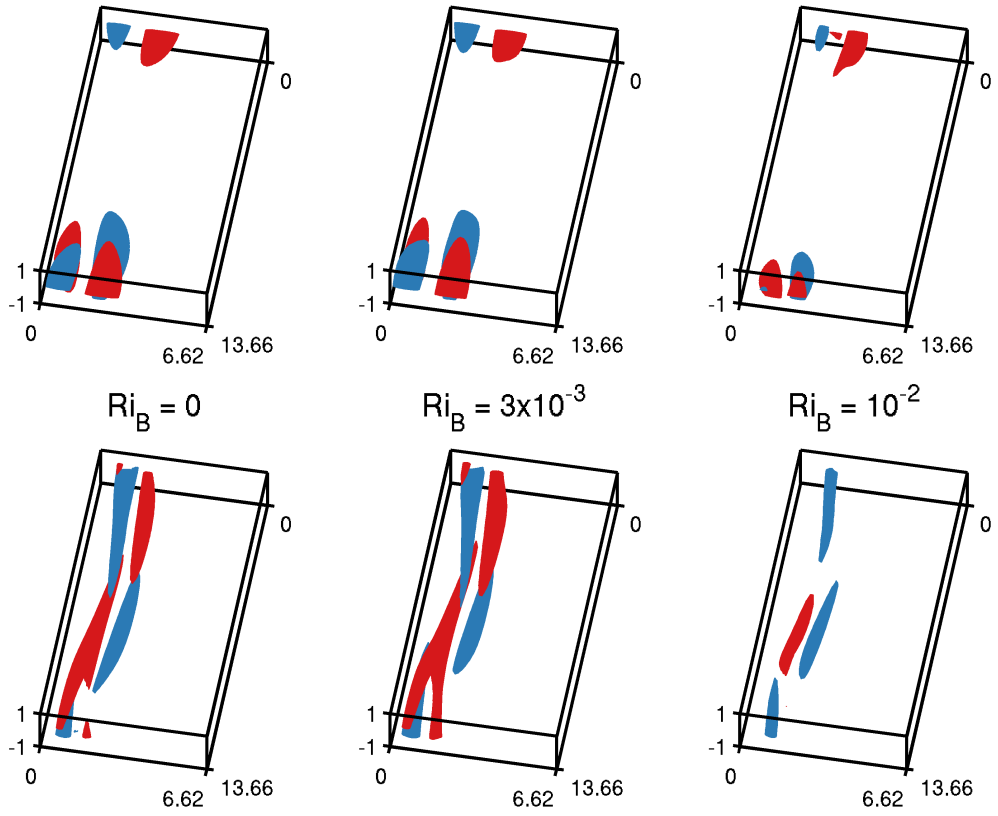

Figure 3.6: Isosurfaces of streamwise perturbation velocity $u = \pm 0.6 \max(u)$ at $t = 0$ (top row) and $t = 25$ (bottom row) for the minimal seed trajectories in geometry W for $Ri_B = 0$, 3×10^{-3}, and 10^{-2}, from left to right.

before utilising the oblique wave mechanism to produce a spanwise isolated pair of streaks, reminiscent of the non-localised structure seen in geometry N. As is apparent in the tabulated values of E_c listed in Table 3.1, these structures are slightly less energetic than the minimal seeds identified in the narrow geometry N, in that, as already noted, the critical values of the energy density E_c (i.e. the energy divided by the volume of the computational domain) in geometry W are approximately 40% of the equivalent values determined in geometry N.

These streaks survive in the flow for an extended period of time, as shown in the leftmost column of Figure 3.7, and are another realisation of an SSP/VWI coherent structure. These streaks eventually transition to a high energy spanwise isolated oblique structure, as shown in the leftmost column of Figure 3.8, which

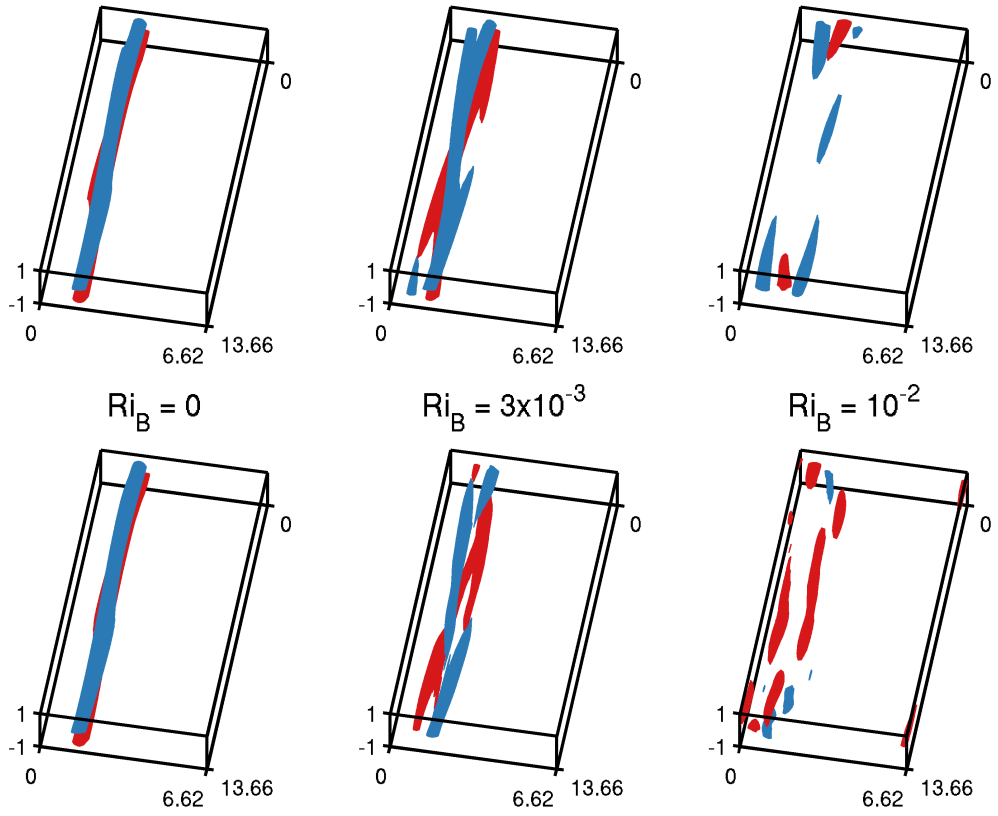

Figure 3.7: Isosurfaces of streamwise perturbation velocity $u = \pm 0.6 \max(u)$ at $t = 70$ (top row) and $t = 150$ (bottom row) for the minimal seed trajectories in geometry W for $Ri_B = 0$, 3×10^{-3}, and 10^{-2}, from left to right.

is visited only transiently, before breaking down to small scale turbulence. This sequence of events, as well as the spanwise localisation, are both consistent with those reported by Monokrousos *et al.* (2011) and verified using a different objective functional by Rabin *et al.* (2012) in the domain $4\pi \times 2 \times 2\pi$ at the larger Reynolds number $Re = 1500$.

The minimal seed trajectory for $Ri_B = 3 \times 10^{-3}$ (shown in the middle column of Figures 3.6, 3.7 and 3.8) again shares the same characteristic evolution as the equivalent minimal seed trajectory in the narrow flow geometry N. The initial condition consists of the same spanwise and streamwise localised patch of flow structures aligned against the mean shear as in the unstratified flow, which again unwrap via the Orr mechanism into a streamwise aligned structure with a distinct

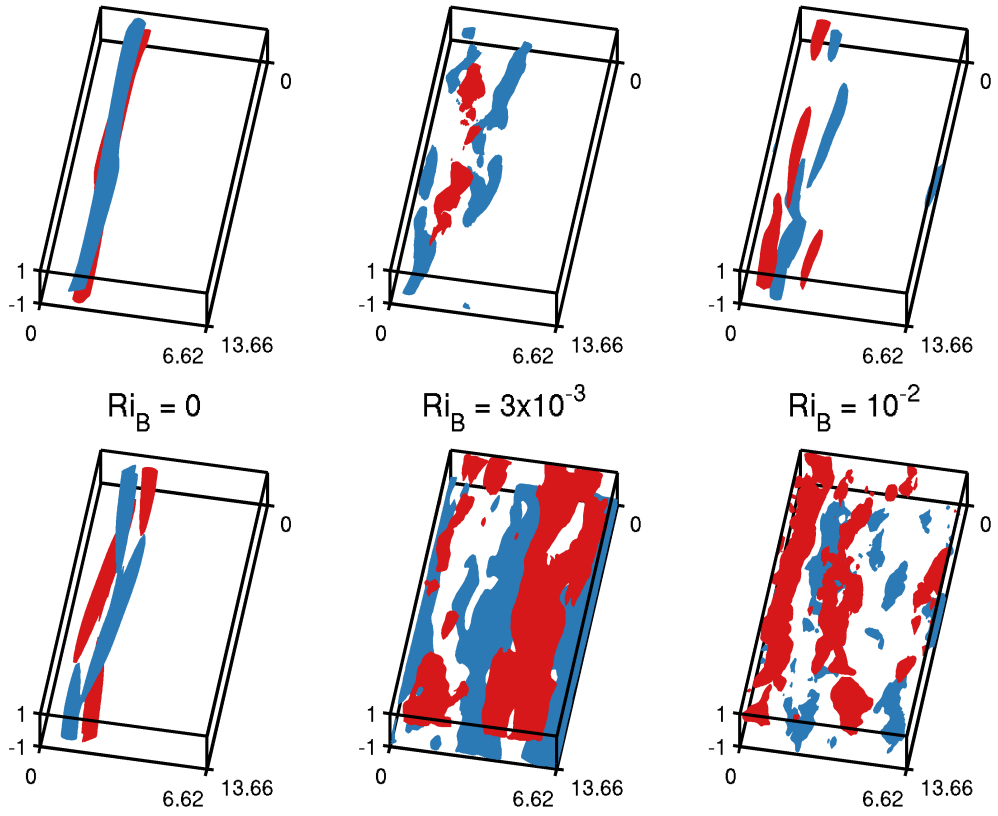

Figure 3.8: Isosurfaces of streamwise perturbation velocity $u = \pm 0.6 \max(u)$ at $t = 210$ (top row) and $t = 280$ (bottom row) for the minimal seed trajectories in geometry W for $Ri_B = 0$, 3×10^{-3}, and 10^{-2}, from left to right.

oblique component, as shown in the lower row, middle column of Figure 3.6. The oblique wave mechanism transfers energy into a pair of spanwise isolated streaks that are visited only transiently, and the flow evolves onto a long lived spanwise localised three dimensional coherent state which has the same oblique characteristics as the one found in the narrow geometry N. This structure is eventually no longer able to be maintained, and transition to turbulence occurs.

Furthermore, the minimal seed trajectory for $Ri_B = 10^{-2}$ in geometry W is also a spanwise localised version of the equivalent trajectory in the narrower geometry N, as can be seen by comparison of the rightmost columns of Figures 3.2, 3.3 and 3.4 and Figures 3.6, 3.7 and 3.8. The initial condition in geometry W consists of a streamwise and spanwise localised patch of flow structures that unwrap via the

Orr mechanism into a flow which quickly becomes chaotic. The flow continues in much the same way as its small domain version, until eventually transitioning to turbulence. Once again, it appeared computationally more difficult to identify the minimal seed for the flow with $Ri_B = 10^{-2}$ than for the flows with smaller bulk Richardson numbers, requiring two or three times as many iterations, although this convergence was still faster than for the equivalent flow with the same $Ri_B = 10^{-2}$ in the narrower geometry N.

3.3 Rolls, streaks and waves

To analyse the effect that stratification has on the SSP/VWI states, we decompose the full perturbation velocity and density fields into roll, streak and wave components. First, we define $\boldsymbol{\mathcal{U}} = \langle \mathbf{u} \rangle_x$ and $\Theta = \langle \rho \rangle_x$, where $\langle \mathbf{a} \rangle_x = \frac{1}{L_x} \int_0^{L_x} \mathbf{a} \, \mathrm{d}x$, and decompose $\mathbf{u} = \boldsymbol{\mathcal{U}} + \hat{\mathbf{u}} = \boldsymbol{\mathcal{U}}_r + \boldsymbol{\mathcal{U}}_s + \hat{\mathbf{u}}$ and $\rho = \Theta + \hat{\rho}$, so that

$$(\mathbf{u}, \rho) = (\boldsymbol{\mathcal{U}}_r + \boldsymbol{\mathcal{U}}_s + \hat{\mathbf{u}}, \rho) = (0, \mathcal{V}, \mathcal{W}, 0)_{roll} + (\mathcal{U}, 0, 0, \Theta)_{streak} + (\hat{u}, \hat{v}, \hat{w}, \hat{\rho})_{wave}, \tag{3.13}$$

where the r subscript denotes the streamwise independent wall-normal and spanwise roll velocity and the s subscript denotes the streamwise independent streamwise streak velocity. As originally argued independently by Hall & Smith (1991) and Waleffe (1997), at high Reynolds number, if there are rolls in the flow of typical amplitude $O(\epsilon)$ with $\epsilon \ll 1$, then their decay rate due to viscosity is $O(Re^{-1})$. During the $O(Re)$ time in which they survive in the flow, they can advect streamwise velocity through the $O(1)$ shear of PCF a distance $O(\epsilon Re)$ and so produce $O(\epsilon Re)$ streaks in the flow. If the amplitude of these streaks is sufficiently large, they can undergo an instability which creates a wave field. The nonlinear self interaction of this wave field then puts energy back into the rolls, and provided that this input of energy is sufficient to balance the viscous decay of the rolls, a 'self-sustaining process' associated with this 'vortex-wave interaction' is possible. Supposing that the streaks need to be $O(1)$ to become unstable requires $\epsilon = Re^{-1}$ and so a quadratic self-interaction of the wave field of $O(Re^{-1})$ is sufficient. Hall & Sherwin (2010) showed that there is a numerically exact solution in unstratified PCF for asymptotically large Re such that the rolls have $\mathcal{V}, \mathcal{W} = O(Re^{-1})$ and the streaks have $\mathcal{U} = O(1)$ throughout the domain. The waves inject en-

ergy into the rolls primarily in an $O(Re^{-1/3})$ critical layer where the background PCF plus the streak flow has the same velocity as the wave velocity, within which $(\hat{u}, \hat{v}, \hat{w}) = O(Re^{-5/6}, Re^{-7/6}, Re^{-5/6})$, giving an integrated Reynolds stress contribution over the critical layer of $O(Re^{-1})$. The waves essentially provide an $O(Re^{-1})$ jump across the critical layer in the component of the roll velocity normal to the critical layer through their Reynolds stresses. Such scalings have been used successfully to provide initial guesses for a search for numerically exact solutions of the Navier–Stokes equations (see Waleffe, 2001; Wedin & Kerswell, 2004).

To see how this scaling is affected by the addition of a stable stratification, we examine the energetics for the total energy density of the rolls and of the streaks. We obtain

$$\begin{aligned}\frac{\mathrm{d}}{\mathrm{d}t}K_r(t) = \frac{1}{2}\frac{\mathrm{d}}{\mathrm{d}t}\left\langle|\boldsymbol{\mathcal{U}}_r|^2\right\rangle_{y,z} &= \Big\langle -Ri_B\mathcal{V}\Theta - \boldsymbol{\mathcal{U}}_r\cdot\left\langle\hat{\mathbf{u}}\cdot\nabla\hat{\mathbf{u}}\right\rangle_x \\ &\qquad -\frac{1}{Re}\nabla\boldsymbol{\mathcal{U}}_r : \nabla\boldsymbol{\mathcal{U}}_r\Big\rangle_{y,z}, \qquad (3.14)\\ \frac{\mathrm{d}}{\mathrm{d}t}K_s(t) = \frac{1}{2}\frac{\mathrm{d}}{\mathrm{d}t}\left\langle|\boldsymbol{\mathcal{U}}_s|^2\right\rangle_{y,z} &= \Big\langle -\mathcal{V}\mathcal{U} - \boldsymbol{\mathcal{U}}_s\cdot\left\langle\hat{\mathbf{u}}\cdot\nabla\hat{\mathbf{u}}\right\rangle_x \\ &\qquad -\frac{1}{Re}\nabla\boldsymbol{\mathcal{U}}_s : \nabla\boldsymbol{\mathcal{U}}_s\Big\rangle_{y,z}, \qquad (3.15)\\ \frac{\mathrm{d}}{\mathrm{d}t}P_s(t) = \frac{1}{2}\frac{\mathrm{d}}{\mathrm{d}t}\left\langle Ri_B\Theta^2\right\rangle_{y,z} &= \Big\langle Ri_B\mathcal{V}\Theta - Ri_B\Theta\left\langle\hat{\mathbf{u}}\cdot\nabla\hat{\rho}\right\rangle_x \\ &\qquad -\frac{Ri_B}{RePr}\nabla\Theta\cdot\nabla\Theta\Big\rangle_{y,z}, \qquad (3.16)\end{aligned}$$

where $\langle\mathbf{a}\rangle_{y,z} = \frac{1}{2L_z}\int_{-1}^{1}\int_0^{L_z}\mathbf{a}\,\mathrm{d}z\mathrm{d}y$, $K_r(t)$ is the roll kinetic energy density, $K_s(t)$ is the streak kinetic energy density, and $P_s(t)$ is the streak potential energy density. Note that $K_r(t) + K_s(t) + K_w(t) = K(t)$, where $K_w(t)$ is the wave kinetic energy density

$$K_w(t) = \frac{1}{2}\langle|\hat{\mathbf{u}}|^2\rangle. \qquad (3.17)$$

Taking $\epsilon = Re^{-1}$, the correct scaling for the viscous decay time is obtained from (3.14). We also see from (3.15) that when $\mathcal{V} = O(Re^{-1})$ is sustained over a period of $O(Re)$, we obtain streaks $\mathcal{U} = O(1)$. We can also obtain the scaling of Hall & Sherwin (2010) for the wave velocities, and their Reynolds stress contribution,

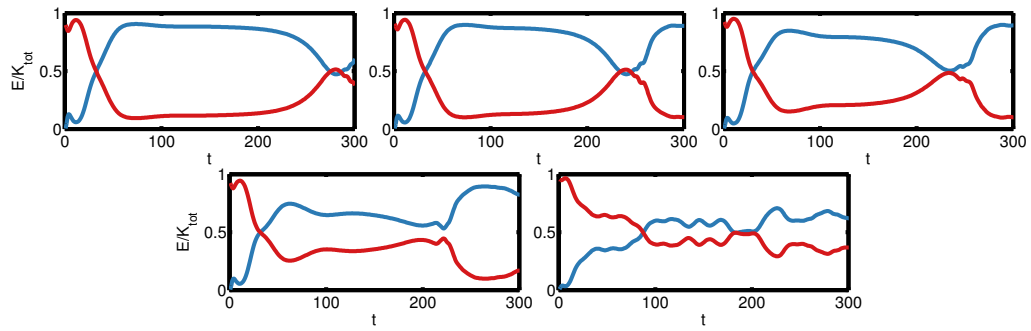

Figure 3.9: Time dependence of normalised streak kinetic energy density K_s/K as defined in (3.15) (plotted with a blue line) and normalised wave kinetic energy density K_w/K as defined in (3.17) (plotted with a red line) for the minimal seed trajectories in geometry N for $Ri_B = 0$ (upper left), 10^{-4} (upper middle), 10^{-3} (upper right), 3×10^{-3} (lower left), 10^{-2} (lower right).

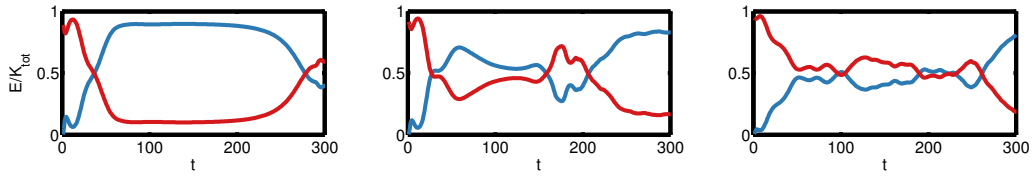

Figure 3.10: Time dependence of normalised streak kinetic energy density K_s/K as defined in (3.15) (plotted with a blue line) and normalised wave kinetic energy density K_w/K as defined in (3.17) (plotted with a red line) for the minimal seed trajectories in geometry W for $Ri_B = 0$ (left), 3×10^{-3} (middle) and 10^{-2} (right)

under the assumption that they act over an $O(Re^{-1/3})$ critical layer, and balance the viscous dissipation there.

For stratified PCF with $Ri_B \neq 0$ there is a new buoyancy flux term $-Ri_B \mathcal{V}\Theta$ entering the energetics of the rolls. Comparing the first term in the right-hand side of (3.15) to that of (3.16), which are production terms for the streak kinetic energy density and streak potential energy density respectively, we see that $\Theta = O(1)$ everywhere for a passive scalar field placed in a self-sustaining process. Thus, (3.14) shows that a buoyancy flux associated with the streak flow effective across the whole domain provides a contribution to the kinetic energy density K_r of the rolls of $O(Ri_B Re^{-1})$, and is able to disrupt fully the flux of wave Reynolds stress input of $O(Re^{-3})$ over the $O(Re^{-1/3})$ critical layer when $Ri_B = O(Re^{-2})$.

This simple-minded high Reynolds number scaling argument, which is domain size independent, is not inconsistent with the moderate Reynolds number minimal seed calculations presented above for which the unstratified coherent state visited by the unstratified minimal seed trajectory is no longer a viable solution for sufficiently large $Ri_B \approx 3 \times 10^{-3}$, and the new coherent states have a modified roll structure that is no longer streamwise independent.

Figures 3.9 and 3.10 show the time evolution of the streak kinetic energy density $K_s(t)$, as defined in (3.15) and plotted with a blue line, and the wave kinetic energy density $K_w(t)$, as defined in (3.17) and plotted with a red line, normalised by the total kinetic energy $K(t)$ for each of the minimal seed trajectories in geometries N and W respectively. It is clear that for $Ri_B = 0$, 10^{-4} and 10^{-3}, there is a balance (shown by the approximate plateaux in the streak and wave energy components) between these energies (and also the residual roll kinetic density density $K_r(t)$, which is not shown as it is, unsurprisingly, appreciably smaller in magnitude) for a large period of the flow evolution. For $Ri_B = 3 \times 10^{-3}$, this balance has been significantly disrupted, and is not maintained purely by the velocity fields. There also is a small amplitude oscillation, and for $Ri_B = 10^{-2}$ the above-mentioned weakly oscillatory nature of the flow is clear. The unstratified self-sustaining process is completely disrupted for $Ri_B \gtrsim 3 \times 10^{-3}$ as expected.

3.4 Discussion

Using the direct-adjoint looping (DAL) method, we have computed minimal seeds for turbulence (the initial conditions of smallest possible initial perturbation energy density $E_c(Ri_B)$ that transition to turbulence) in stratified PCF for a range of bulk Richardson numbers Ri_B in two geometries: a narrow geometry labelled N, which apparently allows only streamwise localisation of the minimal seed initial condition; and a twice as wide geometry W which also allows spanwise localisation. In the unstratified case we converge to the same minimal seed found by Rabin *et al.* (2012) in geometry N, although here we use the time averaged dissipation rate objective functional in the DAL method instead of the total energy density at the target time, and a minimal seed very similar to that of Monokrousos *et al.* (2011) in geometry W.

Since a stable stratification inhibits vertical motions, we see an increase of E_c with Ri_B, as expected. The minimal seeds follow trajectories in state space close to the edge manifold towards a state in the edge manifold. These trajectories are found to spend a large amount of time in the vicinity of such a state. For unstratified flows, these coherent states are a realisation of an SSP/VWI state, and for sufficiently small Ri_B the coherent states are largely unchanged. For $Ri_B \approx Re^{-1}$ there is a slow draining of energy into the density field, creating a highly modified, yet still stationary coherent state, while for larger Ri_B the coherent states feature inherently three-dimensional chaotic motion with weak oscillations.

Examining the flow in terms of roll, streak and wave components as defined in (3.13) demonstrates that the density field is expected, at asymptotically higher Reynolds number, to have a significant disrupting effect on the SSP/VWI process, and hence the coherent states, when $Ri_B = O(Re^{-2})$ through a removal of energy from vertical motion in the rolls, which is not entirely inconsistent with the minimal seed trajectories found at moderate Reynolds number. The effects of stratification on a wide class of exact coherent states in shear flows have yet to be studied in detail. We have demonstrated here that stratification disrupts the well-established high Reynolds number SSP/VWI states in PCF for the small value $Ri_B = O(Re^{-2})$ by affecting the energy input into the roll structures, the most delicate part of the interaction process, through an inhibition of vertical motions. For larger bulk Richardson numbers, we also observe chaotic solutions. We believe therefore that a careful re-examination of the SSP/VWI ansatz must be made for the case of stratified shear flows even with a very weak stratification when $Re \gg 1$, an important class of flows common in both environmental and industrial contexts.

CHAPTER 4

KOOPMAN MODES ON THE EDGE OF CHAOS

Much effort has been put into finding edge states and their associated dynamics that take trajectories through the 'edge of chaos' (phrase used by Vollmer *et al.*, 2009). Typically, edge states are found by elaborate bisection of the edge manifold (see Duguet *et al.*, 2008; Schneider *et al.*, 2010) and once identified, their unstable manifolds may be probed using a shooting bisection (see van Veen & Kawahara, 2011). The search for the unstable manifold is time-consuming, and the same method is not suitable for investigating the stable manifold since not only do the equations of motion need to be integrated backwards in time, which is ill-posed, but also the stable manifold is a multi-dimensional object and so there is *a priori* no single natural direction towards the edge state on the stable manifold to consider.

Rather than explicitly calculating edge states and their stable and unstable manifolds, we want to arrive at a reduced dynamical model for this transition scenario. We use the minimal seed trajectories as a 'most likely' or 'most efficient' route to turbulence that furnishes us with a natural choice of direction along the edge state's unstable manifold. The reduced model must decompose the dynamics into a number of modes that contain information about the growing and decaying structures along the trajectory.

A number of nonlinear decomposition methods of state space trajectories result in such a reduced model. We use here the language of Koopman mode analysis (Mezić, 2005) and its recently reported, computationally inexpensive approximation, dynamic mode decomposition (DMD) (Schmid, 2010). Koopman modes represent structures that are growing and decaying along a given state space trajectory and so it is likely that they represent well the stable and unstable manifolds of the edge state.

We use the idea of finding dynamically important modes given by Koopman mode analysis by applying DMD to the minimal seed trajectories to find growing and decaying dynamic modes on these trajectories that turn out to be excellent approximations to the dynamics on the stable and unstable manifolds in the vicinity of the edge state. These excellent approximations arise despite the fact that the explicit formulas for the Koopman modes given by Mezić (2005) and later summarised in Mezić (2012), and also the provable link between DMD modes and Koopman modes given by Rowley *et al.* (2009), are only valid for dynamics evolving on an attractor of a dynamical system. Bagheri (2013) examined Koopman modes of the cylinder wake at Reynolds numbers just beyond the Hopf bifurcation from the steady state, both on the limit cycle and during a transition from the unstable steady state towards the limit cycle. It was found that DMD did not provide a good approximation for this transition scenario except for very nearby to the unstable steady state, but the nature of the transition is very different to that discussed here. For our case, the minimal seed trajectories transition to turbulence via coherent states that provide a local structure to the state space, whereas the transition considered by Bagheri (2013) is simply one of a direct connection between an unstable and a stable state. We might expect DMD to work more successfully for our structured transition scenario.

Another popular method of modal decomposition is 'proper orthogonal decomposition' (POD) (see Holmes *et al.*, 1998), which decomposes a velocity field into a number of modes which are mutually orthogonal and represents the largest energy structures of a time-averaged flow field. Out of all orthogonal projections, POD is closest to the flow field after a given finite number of terms in a least-squares, energy norm sense. However, there are a number of problems with POD for our application to the transition scenario.

Firstly, POD is an expansion of time-averaged quantities, and so if the dynamics of interest are on a simple attractor then POD may give useful information. However, for transient scenarios like our dynamically evolving minimal seed trajectories, or on subregions of a chaotic attractor, this may not be suitable. Of particular concern is that POD only identifies the structures with the largest energy content, and so instabilities are often not captured by POD. Although these structures will *eventually* become important, over the time interval in which POD is calculated these growing structures may be of very small amplitude (see Amsallem & Farhat, 2012).

Another problem with POD is at the fundamental level of searching for mutually orthogonal structures. There is no reason why important dynamical structures, like the stable and unstable manifolds of an edge state, should be orthogonal. Koopman mode analysis and DMD do not assume orthogonality of the resulting modes, but we emphasise that the main benefit of using Koopman mode analysis and DMD is that we obtain *dynamical* rather than *energetic* modes.

In this chapter we perform the DMD algorithm over a number of short time intervals during the evolution of the minimal seeds along the edge manifold and towards the turbulent attractor. We no longer know whether the modes found by DMD are approximations to finite time Koopman modes, but for brevity we will continue to use the term Koopman mode, since the relation to true Koopman modes is made clear in Section 4.2, and the same DMD algorithm is being employed. We acknowledge that finding 'Koopman modes' away from an attractor via such a method is taking somewhat of a mathematical leap of faith, but as we show in Section 4.3 the results of doing so provide remarkable agreement with the actual flow evolution, thus suggesting a possible generalisation of the Koopman formalism.

Although DMD is an approximation to Koopman mode analysis, it is easier conceptually to first introduce DMD and then to introduce Koopman mode analysis, before comparing the two ideas showing both their similarities and differences. In Section 4.1 we describe DMD and the algorithm discussed by Schmid (2010), and in Section 4.2 we generalise to the Koopman operator and describe the similarities with and deficiencies of DMD. In Section 4.3 we show how DMD describes the trajectory nearby to the edge state for the unstratified minimal seed in the

narrow geometry N found by Rabin *et al.* (2012). Finally in Section 4.4 we investigate DMD when applied at different time intervals along the trajectories of a number of unstratified and stratified minimal seed trajectories to investigate the bifurcation in time structure of each set of modes and how this affects the reduced model.

4.1 Dynamic mode decomposition

Suppose that we have a spatially and temporally discretised state space trajectory for a state vector $\mathbf{q}(\mathbf{x}, t)$, which we may write as a 'snapshot' at each discrete time $t_n = n\delta t$ as a p-dimensional column vector $\mathbf{q}_n \in \mathbb{R}^p$. For example this might be a list of Fourier coefficients, or velocity values at each gridpoint. Then, given that the evolution of $\mathbf{q}(\mathbf{x}, t)$ is governed by the nonlinear equation of motion

$$\frac{\partial \mathbf{q}}{\partial t} = \mathcal{N}(\mathbf{q}, \mathbf{x}, t)\mathbf{q}, \tag{4.1}$$

we want to decompose $\mathbf{q}(\mathbf{x}, t)$ into a set of modes $\{\mathbf{m}_i(\mathbf{x}, t)\}$ with amplitudes $\{c_i(t)\}$ which are dynamically important in the sense that they respect the action of $\mathcal{N}$, so that

$$\mathbf{q}(\mathbf{x}, t) = \sum_i c_i(t)\mathbf{m}_i(\mathbf{x}, t). \tag{4.2}$$

We allow both the amplitudes and the modes to depend on time, to allow for both a given structure to remain static, but grow or decay in amplitude, so that c_i varies, and also for a variation in the structure itself as time advances.

We wish to extract $\{(\mathbf{m}_i, c_i)\}$ from the discretised data $\{\mathbf{q}_n\}$. To do this, we suppose that for each n there exists a matrix $N_n \in \mathbb{R}^{p\times p}$ such that

$$\mathbf{q}_{n+1} = N_n\mathbf{q}_n, \tag{4.3}$$

which maps the snapshot at time $n\delta t$ onto the snapshot at time $(n+1)\delta t$. The matrix N_n might not exist, but it suffices to consider the above equation in a least-squares sense (or indeed any other norm, but DMD as laid out by Schmid (2010) uses a least-squares approach).

The first simplification of DMD is the assumption that N_n changes only slowly with n, i.e. that in some suitable norm,

$$\left\| \frac{\partial N_n}{\partial n} \right\| \ll 1. \tag{4.4}$$

We might imagine that this approximation is good only for trajectories on or nearby to a sufficiently simple attractor, or over a sufficiently small time interval $[t_0, t_n]$.

We may write

$$N_n = N_0 + n\frac{\partial N_0}{\partial n} + O((n\delta t)^2), \tag{4.5}$$

and so we arrive at the approximation

$$N_0\mathbf{q}_n \approx N_n\mathbf{q}_n - n\frac{\partial N_0}{\partial n}\mathbf{q}_n \equiv \mathbf{q}_{n+1} + \mathbf{E}. \tag{4.6}$$

Then, DMD requires that the error is small, that is $\|\mathbf{E}\| \ll \|\mathbf{q}_{n+1}\|$, and so we find

$$\mathbf{q}_{n+1} \approx N_0\mathbf{q}_n \approx N_0^{n+1}\mathbf{q}_0. \tag{4.7}$$

Schmid (2010) arrives at this formula directly by requiring that the discretised version of the nonlinear operator $\mathcal{N}$ may be approximated by a constant matrix over the whole state space trajectory $\{\mathbf{q}_j\}$, which we see is entirely equivalent to the calculations above, except that here we provide a condition for this to hold.

Now consider a finite time horizon with discrete times given by $\{t_0, \ldots, t_n\}$ and consider the matrices $Q_0, Q_1 \in \mathbb{R}^{p\times n}$ constructed columnwise from the snapshots $\{\mathbf{q}_j\}$, given by

$$Q_0 = [\mathbf{q}_0\ \mathbf{q}_1\ \ldots\ \mathbf{q}_{n-1}], \quad Q_1 = [\mathbf{q}_1\ \mathbf{q}_2\ \ldots\ \mathbf{q}_n]. \tag{4.8}$$

Then the DMD assumption (4.7) gives

$$Q_1 = N_0Q_0. \tag{4.9}$$

We see that eigenvectors and eigenvalues of N_0 are likely to give dynamically important information that is carried through from t_0 to t_n by exponentially growing or decaying modes. However, although we know Q_0 and Q_1, we do not yet know N_0, and indeed N_0 may not actually exist.

We could solve for N_0 directly in the least-squares sense. Then the eigenvectors and eigenvalues of N_0 are precisely the dynamical modes of interest. However, the least-squares problem for N_0 is often not very well posed since typically we have $p \gg n$. Schmid (2010) avoids this problem by instead of solving for N_0 directly, we

suppose that $Q_1 = Q_0 A + R$ and perform the following least-squares minimisation problem, where R is the solution to

$$\min_R \|R\| = \min_A \|Q_1 - Q_0 A\|, \tag{4.10}$$

and we note that a sensible choice of A is given by restricting to the form

$$A = \begin{bmatrix} 0 & & & & a_0 \\ 1 & 0 & & & a_1 \\ & \ddots & \ddots & & \vdots \\ & & 1 & 0 & a_{n-2} \\ & & & 1 & a_{n-1} \end{bmatrix}, \tag{4.11}$$

with ones on the lower off-diagonal, unknowns $\{a_0, \ldots, a_{n-1}\}$ in the last column and zeroes elsewhere. We are then optimising only over a discrete set of size n. DMD chooses to minimise in the least-squares sense, and so we take the l_2 norm in (4.10), but of course we could choose other norms. For an oscillatory data set $\{\mathbf{q}_i\}$ the above form of A may not be the most appropriate, and we might consider instead only inserting ones on every n_{freq} rows where $t_{n_{\text{freq}}} - t_0$ is the period of oscillation.

It is possible to solve exactly for the vector $\mathbf{a} = (a_0, \ldots, a_{n-1})$ since if $Q_0 = QR$ is the economy-size QR-decomposition of Q_0, then the solution is

$$\mathbf{a} = R^{-1} Q^\dagger \mathbf{q}_n. \tag{4.12}$$

However, Schmid (2010) claims that this can give a numerically unstable algorithm, and so suggests the following computationally cheaper algorithm based on singular value decomposition.

Consider the singular value decomposition of Q_0, so that $Q_0 = U \Sigma V^\dagger$ with U and V unitary and Σ a diagonal matrix of real singular values. Then (4.9) can be rearranged to give an expression for a pre-conditioned version of N_0, namely

$$U^\dagger N_0 U = U^\dagger Q_1 V \Sigma^{-1} \equiv \tilde{A}. \tag{4.13}$$

The matrix U in fact contains the POD modes of Q_0 and so this is actually the projection of the constant evolution operator N_0 onto a POD basis. This formulation also gives the advantage of being able to search only for the most important modes,

by focusing only on the first few singular values. This is particularly valuable when the data sets of interest are quite large, because singular value decomposition used to search only for the largest singular values is computationally much cheaper than explicitly finding the vector $\mathbf{a}$ above.

We can now find the DMD modes. Let the spectrum of $\tilde{A}$ be the eigenvectors $\{\mathbf{y}_1, \ldots, \mathbf{y}_N\}$ with eigenvalues $\{\mu_1, \ldots, \mu_N\}$. Then the ith DMD mode is

$$\mathbf{m}_i = U\mathbf{y}_i \subset \mathbb{C}^p, \tag{4.14}$$

and its time evolution is given by the action of N_0,

$$N_0\mathbf{m}_i = N_0U\mathbf{y}_i = U\tilde{A}\mathbf{y}_i = \mu_iU\mathbf{y}_i = \mu_i\mathbf{m}_i, \tag{4.15}$$

and so iterations of the evolution operator N_0 result in multiplication by the eigenvalues $\{\mu_i\}$.

The DMD mode expansion written in the modal decomposition given in (4.2) therefore takes the particular form

$$\mathbf{q}(\mathbf{x}, t) = \Re\left[\sum_{i=1}^{N} c_i \exp(\lambda_i t)\mathbf{m}_i(\mathbf{x})\right], \tag{4.16}$$

where $\{c_1, \ldots, c_N\} \subset \mathbb{C}$ are *constants*, and the growth rates $\{\lambda_1, \ldots, \lambda_N\} \subset \mathbb{C}$ are given by $\lambda_i = \log(\mu_i)/\delta t$.

The only remaining task is to identify the amplitude constants $\{c_1, \ldots, c_N\}$. Schmid (2010) does not prescribe how to do this, but we find that a sensible method is to perform another least-squares calculation where we require $\{c_1, \ldots, c_N\}$ to be the least-squares solution to

$$\Re\left(\begin{bmatrix} \mathbf{m}_1 & \cdots & \mathbf{m}_N \\ \mu_1\mathbf{m}_1 & \cdots & \mu_N\mathbf{m}_N \\ \vdots & \ddots & \vdots \\ \mu_1^n\mathbf{m}_1 & \cdots & \mu_N^n\mathbf{m}_N \end{bmatrix}\begin{bmatrix} c_1 \\ c_2 \\ \vdots \\ c_N \end{bmatrix}\right) = \begin{bmatrix} \mathbf{q}_0 \\ \mathbf{q}_1 \\ \vdots \\ \mathbf{q}_n \end{bmatrix}, \tag{4.17}$$

and so we require that the amplitudes $\{c_1, \ldots, c_N\}$ represent the original snapshots accurately. If n is too large for this to be computationally efficient, we could instead restrict to solving the above only for the first $m < n$ snapshots. We solve for more than just one snapshot because if μ_i is complex, then we have an oscillating mode

$\mathbf{m}_i$, and more than one snapshot is required to find the correct complex amplitude that correctly takes into account the oscillation.

If the solution $\mathbf{q}(\mathbf{x}, t)$ resides on an attractor, then for sufficiently large n we expect the eigenvalues $\{\mu_1, \ldots, \mu_N\}$ to be of unit modulus and so the modal expansion consists only of the mean and of neutrally oscillating modes. This provides a good convergence check for such solutions.

In the more general case when the dynamics are evolving and not residing on an attractor, or indeed if the attractor is chaotic and we are interested only in a small region of it, we can perform DMD over a small number of snapshots n to find dynamically evolving, dynamically important modes. We say that a mode $\mathbf{m}_i$ is important in the expansion (4.16) if it is growing in time, so $\Re(\lambda_i) > 0$, or if $|c_i|$ is large in comparison to the other complex amplitudes.

4.2 The Koopman operator

To put the DMD algorithm on a more secure mathematical framework, we would like to address the three main restrictions that go into the algorithm. Two of these restrictions are the discretisation of both space and time. We would like a decomposition that makes sense in continuous time and continuous space, and to be confident that any discretised version accurately represents the continuous version in the appropriate limit. The third restriction, and possibly most important, is that of an assumption of a constant-in-time governing evolution operator N_0. We would like a framework in which this operator is in principle allowed to vary in time. As well as addressing all of these issues, we do not want to move away from the central concept of finding a modal decomposition that represents *dynamical* information that inherently encodes the governing nonlinear operator $\mathcal{N}$. Such a formalism is provided by the Koopman operator.

The Koopman operator was first considered by Koopman (1931) for non-dissipative Hamiltonian systems, and so significantly pre-dates DMD. Mezić (2005) describes how the Koopman operator may be generalised, and used successfully, in the description of dissipative fluid dynamical systems. The DMD algorithm was first presented in a talk by Schmid & Sesterhenn (2008) before the later publication by Schmid (2010). Meanwhile, Rowley *et al.* (2009) demonstrated that DMD

modes are finite-dimensional approximations to a subset of Koopman modes restricted to the Krylov subspace spanned by the flow snapshots. We now describe the Koopman operator, Koopman modes, and discuss where DMD might fail in its description of them.

Consider the general dynamical system

$$\dot{\mathbf{z}} = \mathbf{F}(\mathbf{z}), \tag{4.18}$$

defined on some state space $\mathbf{z} \in \mathcal{M}$, and let $\mathbf{\Phi}(t)$ be the propagator operator, so that $\mathbf{z}(t) = \mathbf{\Phi}(t)\mathbf{z}_0$ evolves an initial condition onto its position in state space after a time t. Then for any observable $\mathbf{q} : \mathcal{M} \to \mathbb{R}^n$, the value of $\mathbf{q}$ after time t, given that the dynamical system started at $\mathbf{z}_0 \in \mathcal{M}$, is

$$\mathbf{q}[t; \mathbf{z}_0] = \mathbf{q}(\mathbf{\Phi}(t)\mathbf{z}_0). \tag{4.19}$$

The Koopman operator, which is in fact a family of operators labelled by time t, is the infinite dimensional linear operator $\mathcal{K}_t$ defined by

$$\mathcal{K}_t\mathbf{q}(\mathbf{z}_0) = \mathbf{q}(\mathbf{\Phi}(t)\mathbf{z}_0), \tag{4.20}$$

that evolves any observable from its initial value onto its value at time t. The fact that $\mathcal{K}_t$ is linear in $\mathbf{q}$ follows immediately from its definition. The fact that it is infinite dimensional reveals that we have not simplified fluid dynamics into linear algebra; the Koopman operator is in general a very complicated object.

The benefit of having defined a linear operator is that we can now define Koopman eigenfunctions $\phi_{\lambda;t}$ to be the eigenfunctions, or special observables, of the Koopman operator $\mathcal{K}_t$ with corresponding eigenvalues λ, in the sense that

$$\mathcal{K}_t\phi_{\lambda;t}(\mathbf{z}_0) = \exp(\lambda t)\phi_{\lambda;t}(\mathbf{z}_0). \tag{4.21}$$

To demonstrate this concept, we consider the following simple example given by Mezić (2012). Let $\lambda > 0$ and consider the linear dynamical system

$$\dot{z} = -\lambda z, \tag{4.22}$$

which has solution

$$\Phi(t)z_0 = z_0 \exp(-\lambda t). \tag{4.23}$$

Consider the observable $q(z) = z$. Then,

$$\mathcal{K}_t q(z_0) = q(z_0 \exp(-\lambda t)) = z_0 \exp(-\lambda t) = \exp(-\lambda t) q(z_0), \tag{4.24}$$

and so $q(z) = z$ is an eigenfunction of the Koopman operator for this dynamical system, with eigenvalue $-\lambda$. It is perhaps not surprising that such a simple linear dynamical system has such a simple Koopman eigenfunction and associated eigenvalue. Rowley *et al.* (2009) show that for linear, stable dynamical systems, the spectrum of the Koopman operator contains the spectrum of the linear dynamical system. However, the spectrum of the Koopman operator is larger than this simple set of solutions, as can be demonstrated by considering the observable $q(z) = z^n$. We then have

$$\mathcal{K}_t q(z_0) = q(z_0 \exp(-\lambda t)) = z_0^n \exp(-n\lambda t) = \exp(-n\lambda t) q(z_0), \tag{4.25}$$

and so $q(z) = z^n$ is an eigenfunction of the Koopman operator for this dynamical system with eigenvalue $-n\lambda$. In fact, if ϕ_{λ_1} and ϕ_{λ_2} are both eigenfunctions of the Koopman operator, then so is their product, $\phi_{\lambda_1}\phi_{\lambda_2}$, which can be shown straightforwardly from the definitions. We should not interpret this as the Koopman operator creating nonlinearity out of linearity (which sounds undesirable at best), but instead that it is able to represent nonlinear observables evolving under linear dynamics.

So far we have only defined Koopman eigenfunctions, which are properties of $\mathcal{K}_t$ and therefore properties of the dynamical system $\mathbf{z} \in \mathcal{M}$. Koopman eigenfunctions are special observables on the state space $\mathcal{M}$. However, we are usually not able to choose our observable to be such a special observable, but are instead given an observable, like the velocity field in fluid dynamics. What we must do is expand our given observable into Koopman *modes*, which are related to how the Koopman eigenfunctions interact with our given observable. On an attractor, the Koopman mode is the projection of our observable onto the Koopman eigenfunction, which can be obtained by taking the inner product with respect to the invariant measure of the attractor of our observable with the associated eigenvector of the Perron–Frobenius operator, which is the adjoint of the Koopman operator under the same inner product. Mezić (2012) provides an explicit formula for the Koopman modes for dynamics on an attractor of a dynamical system, and there is no equivalent formula for transient dynamics.

To define Koopman modes on an attractor in the fluid dynamical framework requires an additional abstraction. Consider a vector-valued observable which is a vector field on a physical domain $\Omega \subset \mathbb{R}^n$. Then we write this observable as $\mathbf{q}(\mathbf{x}; \mathbf{z})$ for $\mathbf{x} \in \Omega$ and $\mathbf{z} \in \mathcal{M}$. The time evolution of $\mathbf{q}(\mathbf{x}; \mathbf{z})$ is wrapped up in $\mathbf{z}$, which follows a trajectory through $\mathcal{M}$ as time varies. At each time, i.e. at each $\mathbf{z}$, we have a single vector field defined at every physical point $\mathbf{x} \in \Omega$. The Koopman mode $\mathbf{m}_{\lambda;t}(\mathbf{x})$ for this observable, associated with the Koopman eigenfunction $\phi_{\lambda;t}(\mathbf{z})$ is the projection of $\mathbf{q}(\mathbf{x}; \mathbf{z})$ onto $\phi_{\lambda;t}(\mathbf{z})$.

Given Koopman eigenvalues $\{\lambda_1, \ldots, \lambda_N\}$ with $\Re(\lambda_1) > \cdots > \Re(\lambda_N)$ for the attractor of a dynamical system, we can find the Nth Koopman mode by evaluating

$$\begin{aligned}&\mathbf{m}_{\lambda_N}(\mathbf{x})\phi_{\lambda_N}(\mathbf{z}) \\ &= \lim_{T\to\infty} \frac{1}{T} \int_0^T \exp(-\lambda_N t) \left(\mathbf{q}(\mathbf{x}; \mathbf{\Phi}(t)\mathbf{z}) - \sum_{j=1}^{N-1} \exp(\lambda_j t) \mathbf{m}_{\lambda_j}(\mathbf{x}) \phi_{\lambda_j}(\mathbf{z}) \right) \, \mathrm{d}t.\end{aligned} \tag{4.26}$$

Since the dynamics are assumed to be on an attractor, the Koopman modes are independent of initial condition, and in addition the infinite time average is well-defined. Mezić (2012) calls this procedure 'generalised Laplace analysis', and we see that in effect, to find the next Koopman mode, we identify the next fastest growing structure after all faster growing structures have been subtracted out. If in addition, as is typically the case in fluid dynamics, the attractor is *bounded*, then we must in fact have $\Re(\lambda_i) \leq 0$ and for all neutrally oscillating modes with $\Re(\lambda_i) = 0$, the Koopman mode is given by the simpler Fourier average formula

$$\mathbf{m}_{\lambda_i}(\mathbf{x})\phi_{\lambda_i}(\mathbf{z}) = \lim_{T\to\infty} \frac{1}{T} \int_0^T \exp(-\lambda_i t) \mathbf{q}(\mathbf{x}; \mathbf{\Phi}(t)\mathbf{z}) \, \mathrm{d}t. \tag{4.27}$$

Armed with the set of Koopman modes, we would like to write down the expansion of the observable $\mathbf{q}$ in these modes. However, unlike for the DMD algorithm, the expansion provided by the Koopman operator contains an as yet unseen continuous spectrum. Mezić (2005) shows that the expansion can be written as

$$\mathbf{q}(\mathbf{x};\mathbf{z})$$

$$= \bar{\mathbf{q}}(\mathbf{x}) + \sum_j \exp(\lambda_j t)\mathbf{m}_{\lambda_i}(\mathbf{x})\phi_{\lambda_j}(\mathbf{z}) + \int_0^\infty \exp(2\pi i\alpha t)[\mathrm{d}E(\alpha)\mathbf{q}(\mathbf{x};\mathbf{z})] \tag{4.28}$$

$$\equiv \bar{\mathbf{q}}(\mathbf{x}) + \mathbf{q}_{ap}(\mathbf{x};\mathbf{z}) + \mathbf{q}_c(\mathbf{x};\mathbf{z}), \tag{4.29}$$

where $\bar{\mathbf{q}}(\mathbf{x})$ is the average of $\mathbf{q}(\mathbf{x};\mathbf{z})$ over the attractor, and E is a complex, continuous, operator-valued spectral measure. E is as yet a completely unknown object, and there have been no major investigations into it.

We recognise that the expansion contains three parts, the mean, the almost-periodic, and the continuous parts. The presence of or lack of each of these terms describes different types of attractors. Quasi-periodic attractors do not contain the continuous part, axiom A attractors (see Young, 2002) do not contain the almost-periodic part, and skew-periodic attractors (see Broer & Takens, 1993) contain all three parts.

The Koopman mode analysis of a jet in cross-flow by Rowley *et al.* (2009) finds the Koopman expansion under the assumption that the continuous spectrum can be neglected. They find only two significant modes of oscillation, a fast mode and a slow mode. The slow mode is very similar in structure to the principal POD mode, but the fast mode only appears in a POD expansion in the 6th term and is contaminated by other frequencies, whereas the Koopman modes are relatively clean. Koopman mode analysis demonstrates that the jet is essentially governed by only two fundamental physical processes. Rowley *et al.* (2009) in fact use their own version of DMD to estimate the Koopman modes, and as with every DMD study to date, a continuous spectrum is inherently missing from the resulting expansion.

The expansion (4.28) allows us to draw comparisons between Koopman mode analysis and the DMD algorithm. The most obvious deficiency of DMD is the lack of the continuous spectrum, and it is not at all clear how to incorporate this into an improved algorithm.

Mezić (2012) claims that the numerical evaluation of the expression for the Nth Koopman mode given by (4.26) can produce very accurate results even when the discretisation of $\mathbf{x} \in \Omega$ is relatively coarse, provided that the averaging time horizon is very large. In contrast, DMD is inherently associated with short-term

dynamics, and yet provided the discretisation of $\mathbf{x} \in \Omega$ is fine enough, it can also produce very accurate results with very few snapshots in time. It is not known when or why DMD provides a good approximation to Koopman mode analysis (Mezić, personal communication), but from a practical point of view, when choosing to either evaluate (4.26) directly or to perform the DMD algorithm, there appears to be a trade-off between temporal extent and spatial coarseness of the available data set. An additional consideration is that the Laplace-like integral given in (4.26) is numerically challenging to calculate due to the exponential divergence in the size of the various terms.

The above discussion has focussed only on the description of the dynamics on an attractor of a dynamical system. The Koopman modes are in fact only given by (4.26) if we are on an attractor, since the expression involves an infinite time average, and the resulting modes lose any information about initial conditions. Indeed, the expansion given by (4.28) is only valid on an attractor. The infinite time average is needed even for an unbounded attractor when there is an unstable Koopman mode, and $\Re(\lambda_1) > 0$.

At the beginning of this chapter we claimed that we were interested in investigating the minimal seed trajectories using Koopman and DMD ideas, and particularly to probe the dynamics nearby to the edge state. The edge state is a saddle-like object in state space that separates the basins of attraction of the two attractors and is not itself an attractor unless the dynamics are artificially restricted to the edge manifold.

In the full state space the edge state has expanding and contracting directions, and so we might imagine that if we were to compute integrals like the generalised Laplace integral in (4.26), but only over a *finite* time interval when the trajectory is in the vicinity of the edge state, the same notion of finding the next fastest growing mode by subtracting off the contributions from all faster growing modes might give a set of dynamical structures that describe the behaviour nearby to the saddle point. We do not know if such a calculation would find Koopman modes as defined formally, but we hope that we would at least find dynamically important transient structures which may be calculated straightforwardly. In addition, the very idea of restricting to a finite time interval makes the fundamental assumption of a constant time evolution operator N_0 in the DMD algorithm more likely to be

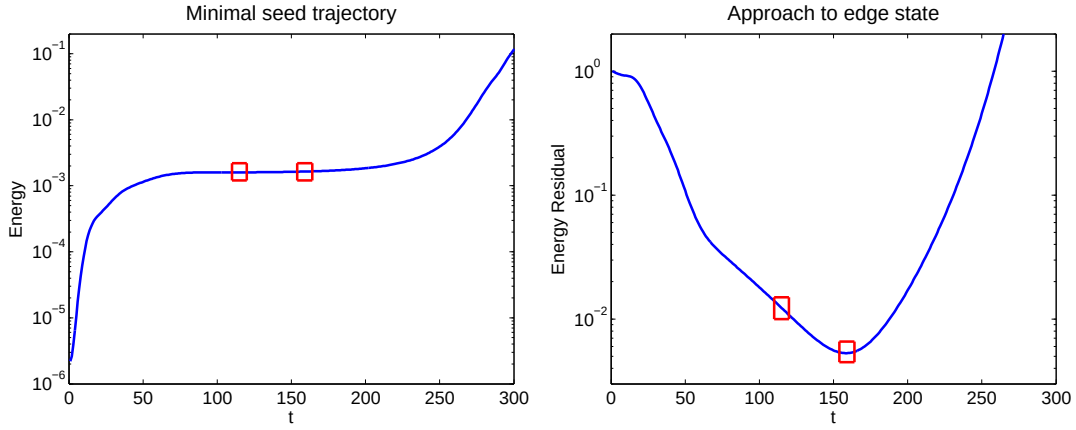

Figure 4.1: Left: Evolution of the energy density of the calculated minimal seed showing the two time intervals in which 11 snapshots of the flow field are used for DMD (red boxes). Right: Energy residual of the approach of the minimal seed trajectory to the converged numerically exact edge state solution shown in Figure 4.3l and the two time intervals in which 11 snapshots of the flow field are used for DMD (red boxes).

valid.

We now discuss the results of applying the DMD algorithm to the minimal seed trajectories found in Chapter 3.

4.3 Manifolds of the unstratified edge state

We take the unstratified PCF minimal seed trajectory in the narrow geometry N as shown in the first columns of Figures 3.2, 3.3 and 3.4 and investigate the stable and unstable manifolds near the edge state visited by the trajectory using DMD. The evolution in time of the energy density of this minimal seed is shown once more in Figure 4.1, where we also show the approach of the minimal seed to the edge state $\mathbf{u}_{\mathrm{GMRES}}$, which we have numerically converged using the GMRES algorithm (see Chandler & Kerswell, 2013), by plotting the energy residual

$$\frac{\|\mathbf{u}(t)-\mathbf{u}_{\mathrm{GMRES}}\|_2^2}{\|\mathbf{u}_{\mathrm{GMRES}}\|_2^2}. \tag{4.30}$$

We then apply DMD to this trajectory both during the approach to the edge state at $t = 110$ and around its closest approach to the edge state at $t = 159$.

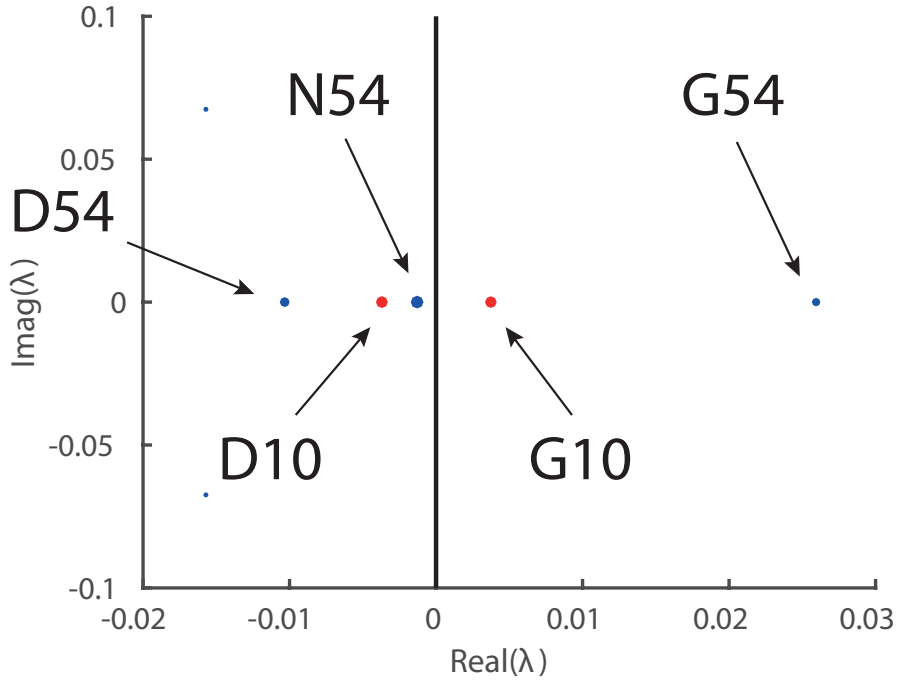

Figure 4.2: Complex eigenvalue plane. Eigenvalues of the DMD algorithm from 11 flow field snapshots from $t = 110$ to $t = 120$ (red) and from $t = 154$ to $t = 164$ (blue). Area of dots scales with $(a_n)^{1/4}$ (for emphasis, to make all modes visible to the eye) where a_n the magnitude of the nth mode. Solid line: Stability boundary $\Re(\lambda) = 0$.

For the minimal seed trajectory, we take the observable to be the flow field $\mathbf{u}(\mathbf{x}, t)$ and consider 11 snapshots of the flow field at unit time intervals between $t = 110$ and $t = 120$, where the flow evolution is approaching the edge state, and also between $t = 154$ and $t = 164$ when the flow is at its closest approach to the edge state. We use singular value decomposition to find only the first six DMD modes, and so in the notation of Section 4.1 we take the number of snapshots to be $n = 10$, each separated by a time interval $\delta t = 1$, the number of modes to be $N = 6$ and the length of each snapshot's state vector to be $p = 3 \times 128 \times 241 \times 32 = 2\,961\,408$, which is formed of each of the three velocity components on the original computational grid.

The eigenvalues computed using DMD are shown in Figure 4.2, where the area of the symbols indicates the magnitude of a given mode in a decomposition of the

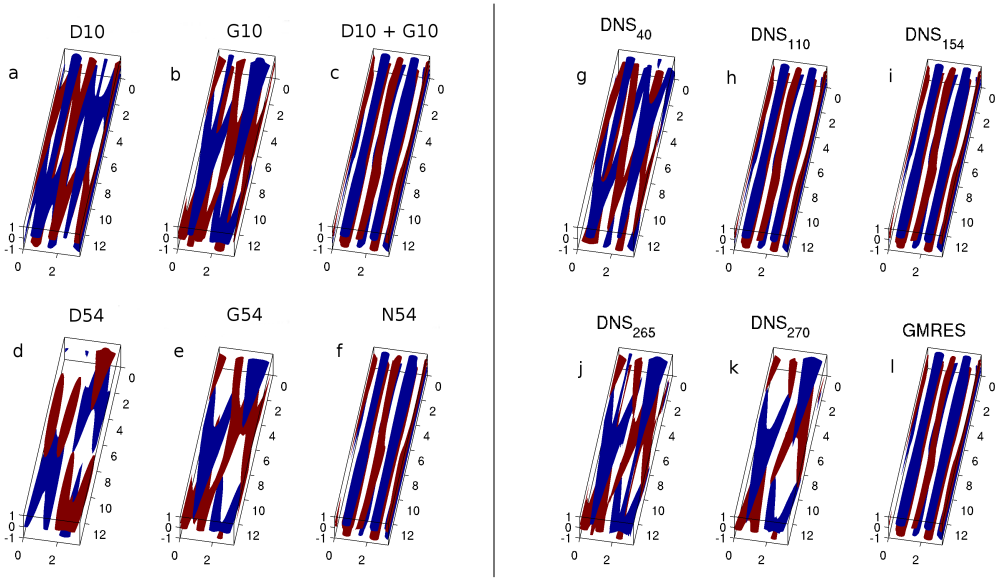

Figure 4.3: Isosurfaces for streamwise velocity $u = \pm 0.6 \max(u)$ at Left: $t = 110$ for a) D10, b) G10, c) D10 plus G10, and at $t = 154$ for d) D54, e) G54 and f) N54. Right: the minimal seed evolution in a fully nonlinear flow realisation at g) $t = 40$ approaching the edge state, h) $t = 110$ where DMD is performed, i) $t = 154$ where DMD is performed, j) $t = 265$ leaving the edge state, k) $t = 270$ leaving the edge state and l) the numerically exact steady state converged with GMRES.

flow field over the time interval of the DMD algorithm into the Koopman modes. We see that for $t = 110$ there are only two important eigenvalues, one slightly stable (D10) and one slightly unstable (G10), whilst for $t = 154$ there are three important eigenvalues, a growing (G54) and a decaying mode (D54) and a nearly neutral mode (N54). The corresponding modes are shown on the left of Figure 4.3 where we plot isosurfaces of streamwise velocity $u = \pm 0.6 \max(u)$ for D10 (Figure 4.3a), G10 (Figure 4.3b), and their sum (Figure 4.3c) and D54 (Figure 4.3d), G54 (Figure 4.3e) and N54 (Figure 4.3f). For comparison, on the right of Figure 4.3 we also show the actual flow realisation at $t = 40$ during the approach to the edge state (Figure 4.3g), the two times for the DMD algorithm, $t = 110$ (Figure 4.3h) and $t = 154$ (Figure 4.3i) and whilst leaving the edge state at $t = 265$ (Figure 4.3j) and $t = 270$ (Figure 4.3k) and the converged edge state using GMRES (Figure 4.3l). We see that for DMD applied at $t = 110$, the decaying mode D10 is visually similar to the fully nonlinear flow realisation at $t = 40$ and the growing mode G10

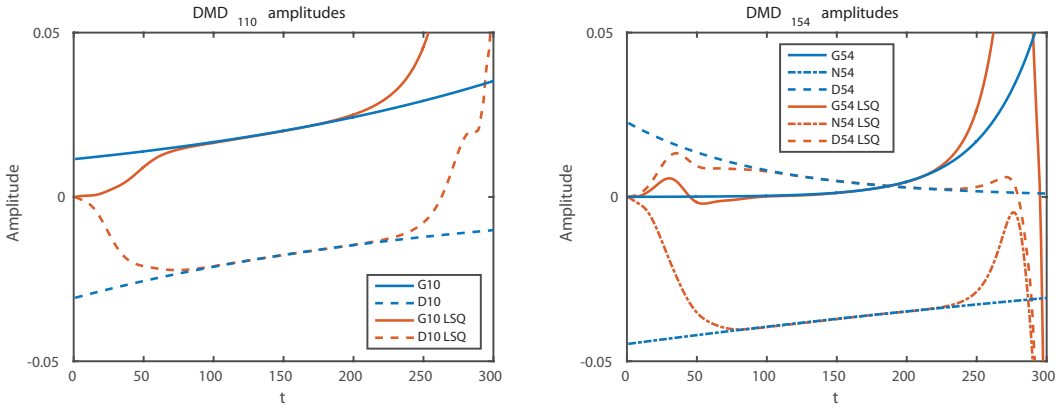

Figure 4.4: Left: Amplitudes of the growing G10 (solid) and decaying D10 (dashed) modes at $t = 110$ predicted by DMD (blue) and calculated from a least squares fit to the nonlinear flow evolution (red). Right: Amplitudes of the growing G54 (solid), decaying D54 (dashed) and neutral N54 (dot-dashed) modes at $t = 154$ predicted by DMD (blue) and calculated from a least squares fit to the nonlinear flow evolution (red).

is similar to the the flow at $t = 265$, whilst for the DMD applied at $t = 154$, the growing mode G54 is similar to the flow at $t = 270$. Given that DMD is a finite dimensional short-time approximation, that we have used such short time intervals for the application of DMD, along with temporal coarseness in the snapshots of the flow evolution, the comparison is remarkable.

For a quantitative comparison, we plot in Figure 4.4 the amplitudes in the linear combination of the growing, decaying and neutral modes (where applicable) $(\mathbf{u}_1, \mathbf{u}_2, \mathbf{u}_3)$ predicted by each DMD result and calculated from the nonlinear flow evolution,

$$\mathbf{u}_{DMD} = a_1 e^{\lambda_1 (t-t_0)} \mathbf{u}_1 + a_2 e^{\lambda_2 (t-t_0)} \mathbf{u}_2 + a_3 e^{\lambda_3 (t-t_0)} \mathbf{u}_3, \tag{4.31}$$

$$\mathbf{u}_{LSQ} = b_1(t)\mathbf{u}_1 + b_2(t)\mathbf{u}_2 + b_3(t)\mathbf{u}_3, \tag{4.32}$$

where $t_0 = 110$ or 154 and (a_1, a_2, a_3) are the constants from a least squares fit to $\mathbf{u}$ over the time interval of the DMD algorithm, and (b_1, b_2, b_3) are calculated at each individual time from a least squares fit to $\mathbf{u}(t)$. In Figure 4.5 we plot the energy residual of these expansions, defined at each time as

$$\frac{\|\mathbf{u}_{DMD} - \mathbf{u}\|_2^2}{\|\mathbf{u}\|_2^2}, \quad \frac{\|\mathbf{u}_{LSQ} - \mathbf{u}\|_2^2}{\|\mathbf{u}\|_2^2}. \tag{4.33}$$

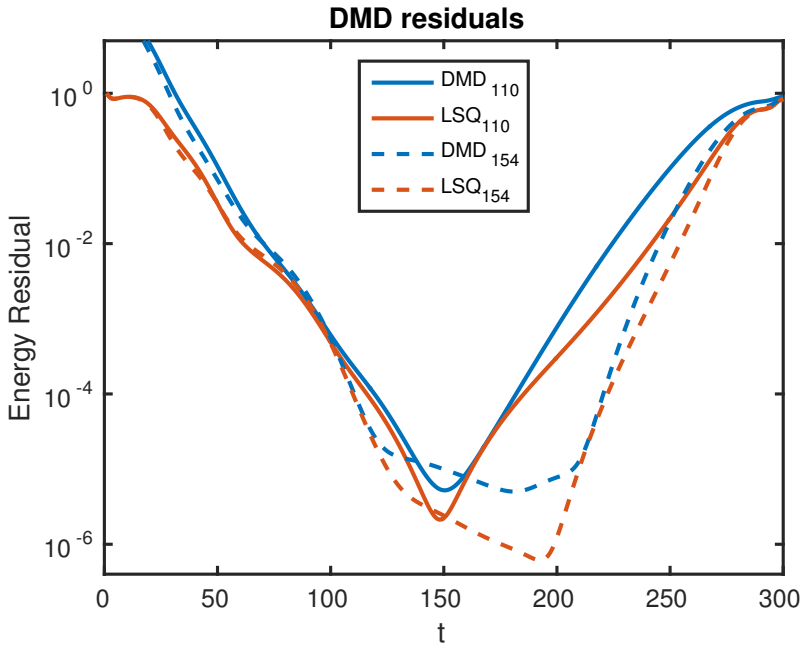

Figure 4.5: Energy residual of the linear combination predicted by DMD (blue) and calculated from a least squares fit to the nonlinear flow evolution (red) for $t = 110$ (solid) and $t = 154$ (dashed).

In both figures we see clearly that the extremely simplifying assumption in DMD that the flow is always governed by the same evolution matrix approximation to the Koopman operator provides very good agreement. In the actual flow evolution, we expect the operator to be a function of time, and so the Koopman modes and eigenvalues to be continuously varying functions of time. We have shown here that only allowing for one of these effects, namely that the eigenvalue may change with time but that the shape of the mode remains constant, we are able to maintain small energy residuals in our expansion. At the comparison time $t = 40$ the energy residuals are below 11.5% and at the comparison time $t = 270$ the energy residuals are below 16.5%. At each of these times one mode has completely dominated over the other, and the flow looks nothing like the structure it maintains nearby to the edge state.

4.4 Bifurcations in time

In the previous section we found that applying the DMD algorithm over different time intervals not only produced slightly different mode structures, but also gave a different number of modes which appeared to be 'important', in the sense that they were either growing modes, or their amplitude was large in comparison to the other modes. It is difficult to see where an extra mode comes from from when changing from $t_0 = 110$ to $t_0 = 154$ when we only have two sets of modes, widely separated in time.

In order to address the problem of the emergence of an extra mode, we now proceed to vary the start of the time interval, t_0, in integer increments from $t_0 = 0$ to $t_0 = 250$, keeping the number of snapshots $n = 10$ separated by a time interval $\delta t = 1$ fixed, and find the first six DMD modes, so that $N = 6$, for each of the minimal seed trajectories with $Ri_B = 0$, 3×10^{-3} and 10^{-2} in both the narrow geometry N and the wide geometry W as discussed in Chapter 3. For computational efficiency, we no longer use the full velocity field $\mathbf{u}$ as the observable, but restrict our calculation instead only to the streamwise velocity component u. This reduces p by a factor of three, and so we now have $p = 128 \times 241 \times 32 = 987\,136$ for geometry N and $p = 128 \times 241 \times 64 = 1\,974\,272$ for geometry W. The restriction to only the streamwise velocity component does not significantly affect the results if we re-run the cases in the previous section. The modes visually have very similar structures, and the eigenvalues and residuals are not significantly affected.

Figures 4.6 and 4.7 show the real part of each of the six DMD growth rates as a function of initial time t_0 for each of the minimal seeds in geometry N and W respectively, where the size of the symbols scales with the amplitude of each mode, for emphasis. All of the DMD modes have a complicated bifurcation structure, particularly at later times when the flow field is becoming turbulent. We see that for bulk Richardson numbers $Ri_B = 0$ and 3×10^{-3}, a two or three mode description of the dynamics on the edge manifold nearby to the edge state appears to be sufficient.

Of particular note is the emergence of the third mode in the previous section as t_0 was increased from 110 to 154. The panel at the top of Figure 4.6 shows that the decaying mode D10 at $t_0 = 110$ is continuously connected to the neutral

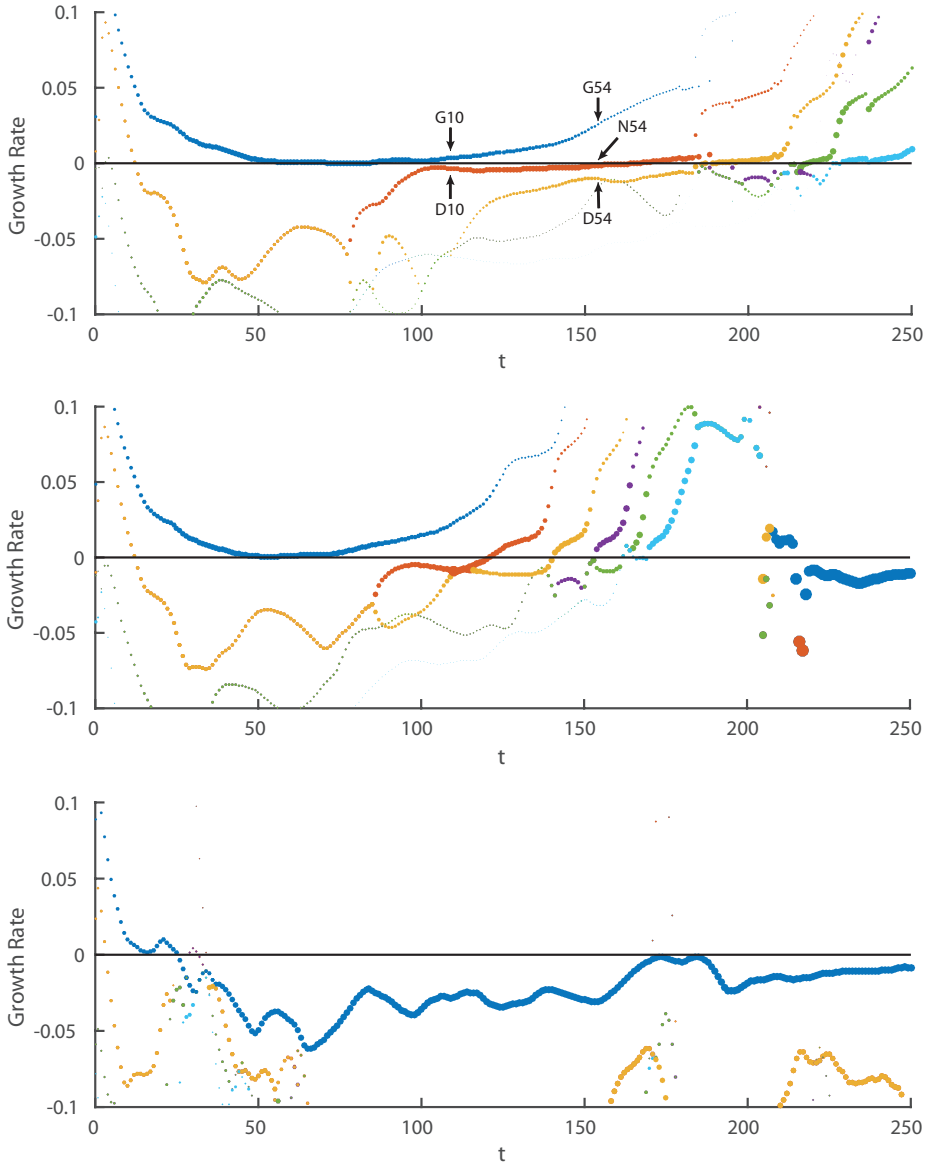

Figure 4.6: Six largest DMD growth rates as a function of initial time t_0 for the minimal seed trajectories in the narrow geometry N for bulk Richardson numbers $Ri_B = 0$ (top), 3×10^{-3} (middle) and 10^{-2} (bottom). Area of dots scales with $(a_n)^{1/2}$ (for emphasis, to make all modes visible to the eye) where a_n the magnitude of the nth mode. The modes in Figure 4.2 are labelled on the top plot.

mode N54 at $t_0 = 154$, and that the decaying mode D54 at $t_0 = 154$ arises from a DMD mode that was unimportant at smaller t_0. Additionally, the neutral mode at $t_0 = 154$ in fact crosses the axis to gain a positive growth rate very close by to

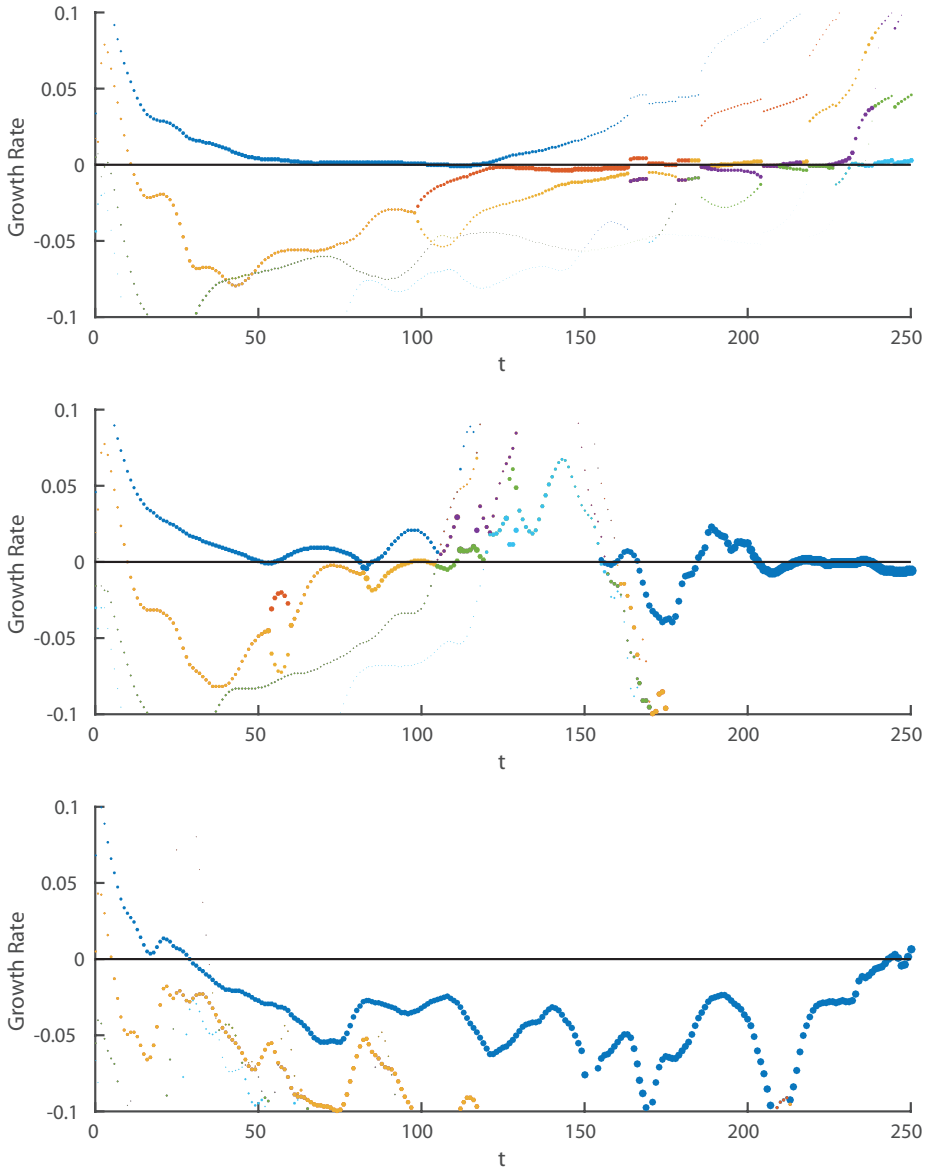

Figure 4.7: Six largest DMD growth rates as a function of initial time t_0 for the minimal seed trajectories in the wide geometry W for bulk Richardson numbers $Ri_B = 0$ (top), 3×10^{-3} (middle) and 10^{-2} (bottom). Area of dots scales with $(a_n)^{1/2}$ (for emphasis, to make all modes visible to the eye) where a_n the magnitude of the nth mode.

the time at which the minimal seed trajectory is closest to the edge state.

All the minimal seed trajectories for bulk Richardson numbers $Ri_B = 0$ and 3×10^{-3} show occurrences of DMD growth rates swapping signs towards the end of

the shadowing of the edge manifold, which is where we expect the closest approach to the edge state to occur. This might hint at an efficient method of searching for coherent structures in which neutral eigenvalues of the DMD algorithm run over short time intervals are identified, and a GMRES search for an exact solution is then performed at these locations using as initial guesses the DMD modes. This hypothesis certainly warrants further investigation.

The DMD algorithm appears to have failed completely in both geometries for the bulk Richardson number $Ri_B = 10^{-2}$. DMD identifies only one important mode for each of the edge manifold trajectories, but these modes have a negative growth rate throughout their evolution along the edge manifold. Whilst the energy density of the minimal seeds during this phase does not increase significantly, and in fact oscillates chaotically, there is certainly not a persistent energy loss as the DMD modes suggest. There are a number possible explanations for this. Firstly, since for this bulk Richardson number the trajectories along the edge manifold are chaotic, the Koopman formalism suggests that there should be a continuous spectrum in a modal expansion of the dynamics. As already noted, DMD does not admit such a continuous spectrum. However, DMD has worked well for a number of turbulent flows (see Schmid, 2010; Mezić, 2012), and so this explanation feels unsatisfactory. Another possibility is that since the trajectories are chaotic and persist for a long period of time, the assumption of a constant evolution operator N_0 may well be breaking down.

While the above reasons could be valid in explaining why DMD does not capture the true dynamics, neither of them explain explicitly the apparent persistent loss of energy from the system. What is most likely is that for these chaotic trajectories, unlike the quieter edge manifold trajectories of the other bulk Richardson numbers, the chaotic nature of the flow provides a number of fast time scales on which the dynamics evolve, and re-inject energy into the flow. The extreme temporal coarseness, with snapshot spacing $\delta t = 1$, is unlikely to capture any of these fast time scales, and it seems reasonable that were we to increase the temporal resolution, some fast time scale modes with positive growth rates would emerge, and help to offset the apparent energy loss that DMD predicts.

Another possible explanation for the apparent energy loss might be due to the chosen observable. As the bulk Richardson number increases, the stratification

becomes more and more important, and as wave motions appear in the dynamics, it is possible to store energy in the density field, resulting in a drain of energy from the velocity components. However, expanding the observable to include the density perturbation ρ as well as the streamwise velocity perturbation u in the DMD algorithm does not change the results for the $Ri_B = 10^{-2}$ minimal seed trajectory in the narrow geometry N shown in Figure 4.6.

4.5 Discussion

Despite the drawbacks of the simplifying assumptions used in the DMD algorithm, we have demonstrated here that DMD provides excellent descriptions of the dynamics along the edge manifold of our systems, provided that those dynamics are not chaotic. For non-chaotic edge manifold trajectories, we reduce the full nonlinear dynamics to the evolution of only two or three modes, and these modes are related to the dynamics approaching and leaving the edge state. The reduced models provided by DMD applied over two different fixed time intervals provide an accurate approximation to the fully nonlinear dynamics over a substantial period of the state space trajectory for the unstratified minimal seed of Rabin *et al.* (2012). This agreement is improved if we allow for the eigenvalues of the DMD modes to vary in time in an attempt to approximate more accurately the action of the Koopman operator, for which both the eigenvalues and the modes vary in time for transient trajectories.

When tracking the eigenvalues of the DMD algorithm applied over different time intervals, we see the appearance of neutral modes, and hypothesise a connection between these neutral modes and the presence of nearby coherent states. In addition, this bifurcation in time analysis showed that the largest bulk Richardson number $Ri_B = 10^{-2}$ reveals the drawbacks of DMD as applied to chaotic trajectories, which we would like to understand in much greater depth. We ruled out the possibility that the failure of DMD was due to missing the physics of the density perturbation ρ and conclude that the chaotic nature of the state space trajectory combined with the temporal coarseness of the snapshots is responsible for this error. Chen *et al.* (2012) introduced an 'optimised' DMD algorithm which is claimed to better represent noisy or chaotic trajectories and involves allowing

for a residual error in the reproduction of each snapshot rather than just the final snapshot.

The mathematical leap of faith at the beginning of this chapter appears to have been worthwhile, and has opened up a number of further research questions relating to DMD and Koopman modes. Despite the Koopman mode analysis outlined by Mezić (2012) being an infinite time theory for attractors, the central ideas appear to transfer onto finite time horizons. We would like to know if this is a consequence of the somewhat simple nature of saddle-like edge states, or if an extended theory of transient 'quasi-Koopman modes' exists.

CHAPTER 5

STRATIFYING THE SELF-SUSTAINING PROCESS

5.1 Finding the self-sustaining process

We described the basic arguments behind the self-sustaining process in Chapter 3. Here we discuss how in practice the self-sustaining process was identified by Waleffe (1997) in unstratified PCF and generalise his calculations to the stratified case in order to help identify precisely how SSP breaks down. In the description of SSP by Waleffe (1997), there are four stages to constructing SSP and closing the loop to form a self-sustaining mechanism.

Firstly, Waleffe (1997) identifies the streamwise averaged wall-normal and spanwise 'roll' velocities by solving a linearised set of equations for those components and searching for viscously decaying solutions in the absence of a wave field. Waleffe (1997) shows that there is a solution with the vertical roll velocity symmetric about the mid-plane of PCF for every spanwise wavenumber k, and that there is a unique spanwise wavenumber $k \approx 1.2$, independent of Reynolds number, that has the smallest viscous decay rate. This solution could then be taken as the candidate roll solution in the SSP since it survives longest if in isolation. However, Waleffe (1997) chooses instead the nearby value $k = 5/3$, motivated by the geometry of the minimal box study of Hamilton *et al.* (1995), as the candidate

roll solution and develops the rest of the process from that start point.

Secondly, once the candidate roll solution had been found, Waleffe (1997) proceeds to calculate the steady-state streak field associated with the lift-up mechanism's advection of the background PCF shear profile by numerically solving the streamwise averaged streamwise velocity equation in the absence of a wave field and viewing the rolls as a time-independent forcing. Although the roll solution would decay viscously at the known viscous decay rate if placed in isolation in an actual flow, in the spirit of a self-sustaining mechanism the rolls are held fixed at a given amplitude when finding the streaks. This is done in the hope that when the SSP loop is closed, the wave field is in fact sufficient to sustain the rolls at their given amplitude. This requires an amplitude of the rolls to be chosen, and two sensible candidates are that the rate of advection by the rolls matches either the streak diffusion rate or the roll's own viscous decay rate. This selects the weakest rolls that are able to survive in the flow long enough to create the largest amplitude streaks. For the parameters chosen by Waleffe (1997), namely spanwise wavenumber $k = 5/3$, and Reynolds number $Re = 400$, these two criterion give the maximum vertical roll velocity to be either 0.013 or 0.024. For simplicity, Waleffe (1997) chooses the maximum vertical roll velocity to be 0.02, and so we do so here.

Thirdly, once the streak field has been computed, the wave field is identified by investigating the linear instability of the streaks viewed together with the background PCF shear as a base flow about which all the equations of motion are linearised. This linear stability analysis contains a single free parameter, the streamwise wavenumber α. It is found that for this set of parameters there is a band of streamwise wavenumbers α for which there is instability, and a marginal streamwise wavenumber $\alpha_0 \approx 1.1$ at which the instability is just neutral, neither growing nor decaying, so that all disturbances with $\alpha > \alpha_0$ are linearly asymptotically stable. Waleffe (1997) uses this marginal solution as the candidate wave field, arguing that for a self-sustaining process, we are not interested in growing or decaying modes, but instead marginally stable modes that are able to just sustain the motion of the rolls in a steady state scenario. The marginal solution for the parameters used by Waleffe (1997) takes the form of a sinusoidal modulation to the streak field.

Finally, to close the loop of SSP, Waleffe (1997) investigates the feedback of

the candidate wave field onto the candidate roll solution. When computing the candidate roll solution, all the wave field terms in the equations of motion were neglected. Waleffe (1997) then re-introduces these terms and views them as a time-independent forcing in the roll equations and compares the rolls that are driven by this forcing to the original candidate solution. As alluded to in Chapter 3, this is the least rigorous part of the derivation of SSP, and the comparison made by Waleffe (1997) is qualitative and only indicative of agreement. However, it is difficult to see how to do any better without an optimisation over parameters and whilst keeping so many assumptions. Nevertheless, as pointed out in Chapter 3, such a methodology has been applied more carefully to produce numerically exact solutions in shear flows (see Wedin & Kerswell, 2004), without dropping nonlinear terms and without somewhat arbitrarily picking amplitudes and domain sizes. Such solutions were directly inspired by the work of Waleffe (1997).

In this chapter, we extend the work of Waleffe (1997) by completing step-by-step all the parts of Waleffe's argument, but now carrying through the density field and investigating how it affects each of the four steps of the process in order to gain a deeper understanding of the disruption of SSP in stratified shear flow laid out in Chapter 3.

5.2 Equations of motion for stratified SSP

The equations of motion for vertically sheared stratified PCF are

$$\frac{\partial \mathbf{u}}{\partial t} + (\mathbf{u}+\mathbf{U})\cdot\nabla(\mathbf{u}+\mathbf{U}) + \nabla p + Ri_B\rho\hat{\mathbf{y}} - \frac{1}{Re}\nabla^2\mathbf{u} = 0, \tag{5.1}$$

$$\frac{\partial \rho}{\partial t} + (\mathbf{u}+\mathbf{U})\cdot\nabla(\bar{\rho}+\rho) - \frac{1}{RePr}\nabla^2\rho = 0, \tag{5.2}$$

$$\nabla\cdot\mathbf{u} = 0, \tag{5.3}$$

where $Re = \Delta U H/\nu$, $Pr = \nu/\kappa$ and $Ri_B = g\Delta\rho H/\rho_0\Delta U^2$, and the background fields are $\mathbf{U} = y\hat{\mathbf{x}}$ and $\bar{\rho} = -y$.

We can then decompose the flow fields into rolls, streaks and waves, so that

$$(\mathbf{u},\rho) = (0,\mathcal{V},\mathcal{W},0)_{roll} + (\mathcal{U},0,0,\Theta)_{streak} + (\hat{u},\hat{v},\hat{w},\hat{\rho})_{wave}, \tag{5.4}$$

where $\boldsymbol{\mathcal{U}} = \langle \boldsymbol{u}\rangle_x$ and $\Theta = \langle\rho\rangle_x$, where $\langle\mathbf{a}\rangle_x = \int_0^{L_x}\mathbf{a}\,\mathrm{d}x/L_x$. In unstratified SSP, the two velocity components $\mathcal{V}$ and $\mathcal{W}$ are typically of small amplitude $O(1/Re)$ and

so they satisfy a linearised, closed set of incompressible equations whose solutions consist of large-scale circular motion in the spanwise wall-normal plane, and so we call them 'rolls'. The streamwise mean streamwise velocity $\mathcal{U}$ is called the 'streak' velocity because it represents streamwise independent deviations from the background shear profile, causing the total mean flow to contain faster and lower speed regions, and producing a 'streaky' appearance to the dynamics. We decide to label Θ as the 'streak' density field due to the similarity between the equations of motion for $\mathcal{U}$ and Θ. In the unstratified limit $Ri_B \to 0$ both $\mathcal{U}$ and Θ are advected passively by the roll velocities. Finally, we label the remaining velocity and density fields as 'waves' since they depend on all three spatial directions and typically have a complex spatial structure. They can be viewed as a wavy instability of the streaks.

This decomposition gives the following set of equations for the rolls and streaks:

$$\frac{\partial \mathcal{V}}{\partial t} + \frac{\partial P}{\partial y} - \frac{1}{Re}\nabla_2^2 \mathcal{V} + Ri_B \Theta = -\hat{\mathbf{y}} \cdot (\boldsymbol{\mathcal{U}} \cdot \nabla_2 \boldsymbol{\mathcal{U}} + \langle \hat{\mathbf{u}} \cdot \nabla \hat{\mathbf{u}} \rangle_x) \tag{5.5}$$

$$\frac{\partial \mathcal{W}}{\partial t} + \frac{\partial P}{\partial z} - \frac{1}{Re}\nabla_2^2 W = -\hat{\mathbf{z}} \cdot (\boldsymbol{\mathcal{U}} \cdot \nabla_2 \boldsymbol{\mathcal{U}} + \langle \hat{\mathbf{u}} \cdot \nabla \hat{\mathbf{u}} \rangle_x) \tag{5.6}$$

$$\frac{\partial \mathcal{V}}{\partial y} + \frac{\partial \mathcal{W}}{\partial z} = 0 \tag{5.7}$$

$$\frac{\partial \Theta}{\partial t} - \mathcal{V} - \frac{1}{RePr}\nabla_2^2 \Theta = -\boldsymbol{\mathcal{U}} \cdot \nabla_2 \Theta - \langle \hat{\mathbf{u}} \cdot \nabla \hat{\rho} \rangle_x \tag{5.8}$$

$$\frac{\partial \mathcal{U}}{\partial t} + \mathcal{V} - \frac{1}{Re}\nabla_2^2 \mathcal{U} = -\hat{\mathbf{x}} \cdot (\boldsymbol{\mathcal{U}} \cdot \nabla_2 \boldsymbol{\mathcal{U}} + \langle \hat{\mathbf{u}} \cdot \nabla \hat{\mathbf{u}} \rangle_x) \tag{5.9}$$

where the equations have been arranged so that the left-hand sides contain only linear terms, and the right-hand sides only nonlinear terms. Here ∇_2^2 is the 2-dimensional Laplacian. The first four equations (5.5 – 5.8) are the coupled equations for the rolls and streamwise mean density field and the final equation (5.9) is that for the velocity streaks.

To find the rolls, we shall drop the right-hand sides of (5.5 – 5.8) and solve analytically the resulting set of linear PDEs that couple $\mathcal{V}$ and $\mathcal{W}$ with Θ. To find the streaks we solve numerically the velocity streak equation (5.9) in steady state dropping only the wave-wave interaction term from the right-hand side in order to account fully for the roll-based advection.

5.3 Rolls and their interaction with the density field

The linearised coupled roll and streamwise mean density equations are

$$\frac{\partial \mathcal{V}}{\partial t} + \frac{\partial P}{\partial y} - \frac{1}{Re}\nabla_2^2 \mathcal{V} + Ri_B \Theta = 0, \tag{5.10}$$

$$\frac{\partial \mathcal{W}}{\partial t} + \frac{\partial P}{\partial z} - \frac{1}{Re}\nabla_2^2 W = 0, \tag{5.11}$$

$$\frac{\partial \mathcal{V}}{\partial y} + \frac{\partial \mathcal{W}}{\partial z} = 0, \tag{5.12}$$

$$\frac{\partial \Theta}{\partial t} - \mathcal{V} - \frac{1}{RePr}\nabla_2^2 \Theta = 0. \tag{5.13}$$

We can use incompressibility to combine (5.10) and (5.11) to give

$$\nabla_2^2 P = Ri_B \frac{\partial \Theta}{\partial y}, \tag{5.14}$$

which we may then use in ∇_2^2(5.10) to give

$$\left(\frac{\partial}{\partial t} - \frac{1}{Re}\nabla_2^2\right)\nabla_2^2 \mathcal{V} = -Ri_B \frac{\partial^2 \Theta}{\partial z^2}. \tag{5.15}$$

We may now take the operation $(\partial_t - \nabla_2^2/RePr)$ to eliminate Θ,

$$\left(\frac{\partial}{\partial t} - \frac{1}{RePr}\nabla_2^2\right)\left(\frac{\partial}{\partial t} - \frac{1}{Re}\nabla_2^2\right)\nabla_2^2 \mathcal{V} = -Ri_B \frac{\partial^2 \mathcal{V}}{\partial z^2}, \tag{5.16}$$

which upon multiplying through by $RePr$ gives

$$\left(Pr\frac{\partial}{\partial t} - \nabla_2^2\right)\left(\frac{\partial}{\partial t} - \nabla_2^2\right)\nabla_2^2 \mathcal{V} = -Re^2 Pr\, Ri_B \frac{\partial^2 \mathcal{V}}{\partial z^2} \tag{5.17}$$

$$= Ra\frac{\partial^2 \mathcal{V}}{\partial z^2}, \tag{5.18}$$

where $Ra = Re^2 Pr(-Ri_B)$ is the 'Rayleigh' number.

We have found a single equation satisfied by $\mathcal{V}$ which is to be solved given the boundary conditions $\mathcal{V}(\pm 1) = 0$ (no penetration), $\mathcal{W}(\pm 1) = 0$ (no slip) and $\Theta(\pm 1) = 0$ (fixed density). The appearance of the Rayleigh number in this equation makes it clear that we are solving a system closely related to convection. This is not particularly surprising since we are specifically looking for viscously, or thermally, dissipating roll-like solutions whose growing or steady versions are ubiquitous in convection, where the direction of gravity is reversed in relation to the density gradient.

5.3.1 Base case $Ri_B = 0$

Setting $Ri_B = 0$ and choosing a viscous decay rate λ^2 and spanwise wavenumber k so that we may write $[\mathcal{V}(y,z,t), \mathcal{W}(y,z,t)] = [\hat{V}(y)\cos kz, \hat{W}(y)\sin kz]e^{-\lambda^2 t/Re}$ gives

$$(D^2 - k^2)(D^2 - k^2 + \lambda^2)\hat{V} = 0, \tag{5.19}$$

where $D = \mathrm{d}/\mathrm{d}y$, which we must solve with the boundary conditions $\hat{V}(\pm 1) = D\hat{V}(\pm 1) = 0$ (no slip). Waleffe (1997) writes down the y-symmetric solution

$$\hat{V}(y) \propto \frac{\cos \mu y}{\cos \mu} - \frac{\cosh ky}{\cosh k}, \tag{5.20}$$

where $\mu^2 = \lambda^2 - k^2$ and $k \tanh k + \mu \tan \mu = 0$.

Waleffe (1997) then proposed that the rolls take the form with the smallest possible λ. Here, this gives $\lambda \approx 3.04$ and $k \approx 1.2$, but as already stated we use instead $k = 5/3$ and $\lambda \approx 3.09$ for consistency with Waleffe (1997).

The solution which is y-asymmetric is

$$\hat{V}(y) \propto \frac{\sin \mu y}{\sin \mu} - \frac{\sinh ky}{\sinh k}, \tag{5.21}$$

where $\mu^2 = \lambda^2 - k^2$ and $k \coth k - \mu \cot \mu = 0$, which for $k = 5/3$ gives $\lambda \approx 4.63$.

5.3.2 Effect of density on the rolls

We look for static diffusing solutions with $\partial\Theta/\partial t = -(\lambda^2/Re)\Theta$ to give the same time dependence as that for $\mathcal{V}$ and $\mathcal{W}$ as required by the linearity of the governing equations. Arguably, it might be more natural to search for the alternative time dependence $\partial/\partial t = -\lambda^2/RePr$ (thus changing the meaning of λ, but giving the same results). However, there are two main reasons not to do this. Firstly, in order to reduce substantially the parameter space it is required to investigate and to find results with the most relevance to the minimal seeds found above, we will specialise to the case $Pr = 1$, making the distinction moot. Secondly, we wish to make clear how these new results extend those of Waleffe (1997) and in particular how they connect to the existing results as $Ri_B \to 0$. In this limit, the roll dynamics are completely independent of Θ and so such an explicit dependence on Pr is unwanted.

Writing $[\mathcal{V}(y,z,t),\mathcal{W}(y,z,t)] = [\hat{V}(y)\cos kz, \hat{W}(y)\sin kz]e^{-\lambda^2 t/Re}$ in (5.15) gives

$$(D^2-k^2+\lambda^2)(D^2-k^2)\hat{V}\cos kz e^{-\lambda^2 t/Re} = ReRi_B\frac{\partial^2\Theta}{\partial z^2}, \tag{5.22}$$

and so we must set $\Theta(y,z,t) = \hat{\Theta}(y)\cos kz e^{-\lambda^2 t/Re}$, so that

$$(D^2-k^2)(D^2-k^2+\lambda^2)\hat{V} = -k^2 ReRi_B\hat{\Theta}, \tag{5.23}$$

$$(D^2-k^2+Pr\lambda^2)\hat{\Theta} = -RePr\hat{V}, \tag{5.24}$$

or

$$(D^2-k^2)(D^2-k^2+\lambda^2)(D^2-k^2+Pr\lambda^2)\hat{V} = -k^2 Ra\hat{V}, \tag{5.25}$$

which may be obtained directly from (5.18). However, it is easier to deal directly with the pair (5.23 – 5.24) in what follows.

y-symmetric solutions

To solve (5.23 – 5.24) we write the solution as a sum over trigonometric functions and find a dispersion relation for the decay rate λ^2. We note that we can solve (5.25) directly as a bi-cubic relation for its eigenvalues, but we find that the series solution method shown here provides greater insight into how the solutions vary in parameter space. Solutions with y-symmetry satisfying the boundary conditions $\hat{V}(\pm1) = \hat{\Theta}(\pm1) = 0$ take the form

$$\hat{V} = \sum_{n=1}^{\infty} v_n \cos\frac{(2n-1)\pi y}{2}, \tag{5.26}$$

$$\hat{\Theta} = \sum_{n=1}^{\infty} \theta_n \cos\frac{(2n-1)\pi y}{2}, \tag{5.27}$$

$$\theta_n = \frac{RePr}{\left(\frac{2n-1}{2}\right)^2\pi^2 + k^2 - Pr\lambda^2}v_n, \tag{5.28}$$

where the final equality relating the coefficients θ_n to v_n is obtained from (5.24).

To obtain v_n we integrate (5.23) to get

$$\int_{-1}^{1}(D^2-k^2)(D^2-k^2+\lambda^2)\hat{V}\cos\frac{(2m-1)\pi y}{2}\mathrm{d}y = -k^2 ReRi_B\theta_m \equiv \beta_m v_m, \tag{5.29}$$

where $\beta_n = k^2 Ra/((2n-1)^2\pi^2/4 + k^2 - Pr\lambda^2)$.

Then, integrating by parts four times, and using the symmetry $D^2\hat{V}|_1 = D^2\hat{V}|_{-1}$, we get

$$\beta_m v_m = \left(k^2 + \frac{(2m-1)^2\pi^2}{4}\right)\left(k^2 - \lambda^2 + \frac{(2m-1)^2\pi^2}{4}\right) v_m + D^2\hat{V}\Big|_1 (2m-1)\pi(-1)^{m+1}. \tag{5.30}$$

Since the governing equations are linear, we may choose $D^2\hat{V}|_1 = C$ for some constant C. Our solution is therefore

$$\hat{V}(y) = C\sum_{n=1}^{\infty} \frac{(2n-1)\pi(-1)^{n+1}\cos\left(\frac{(2n-1)\pi y}{2}\right)}{\frac{k^2 Ra}{(2n-1)^2\pi^2/4+k^2-Pr\lambda^2} - \left(k^2 + \frac{(2m-1)^2\pi^2}{4}\right)\left(k^2 - \lambda^2 + \frac{(2m-1)^2\pi^2}{4}\right)}. \tag{5.31}$$

Then, in the final boundary condition $D\hat{V}(\pm 1) = 0$, the multiplicative constant C can be cancelled, and we are left with the dispersion relation for $\lambda(k)$:

$$\sum_{n=1}^{\infty} \frac{\frac{(2n-1)^2\pi^2}{4}\left(\frac{(2n-1)^2\pi^2}{4} + k^2 - Pr\lambda^2\right)}{\left(k^2 + \frac{(2n-1)^2\pi^2}{4}\right)\left(k^2 - \lambda^2 + \frac{(2n-1)^2\pi^2}{4}\right)\left(k^2 - Pr\lambda^2 + \frac{(2n-1)^2\pi^2}{4}\right) - k^2 Ra} = 0. \tag{5.32}$$

Solving this equation numerically for the unstratified case $Ri_B = 0$, i.e. $Ra = 0$, gives the same curve $\lambda(k)$ and optimal choice of λ and k as in Section 5.3.1.

The sum has poles in its denominators, which for $Pr = 1$ are located at

$$\lambda_n^2 = \pm i\left[\frac{-k^2 Ra}{\frac{(2n-1)^2\pi^2}{4} + k^2}\right]^{1/2} + k^2 + \frac{(2n-1)^2\pi^2}{4} \tag{5.33}$$

which lie in the complex plane when $Ra \neq 0$, since $Ra < 0$.

In the unstratified case, $Ra = 0$, these poles lie on the real axis, and the sum is positive for λ just less than λ_n and negative for λ just greater than λ_n. The zeros of the sum occur exactly once for $\lambda_n < \lambda < \lambda_{n+1}$. As $-Ra$ is increased, the poles split in two and move away from the axis, and the change of sign along the real axis at first occurs twice for each pole, and then not at all as the influence of the poles moves further away from the real axis. This effect is shown in Figure 5.1, where the real part of the sum in (5.32) is evaluated for λ in the complex plane for $k = 1.2$ and $-Ra = 0$, 10 and 100. The green regions have a positive value of the sum, white regions a negative value of the sum, black lines are the

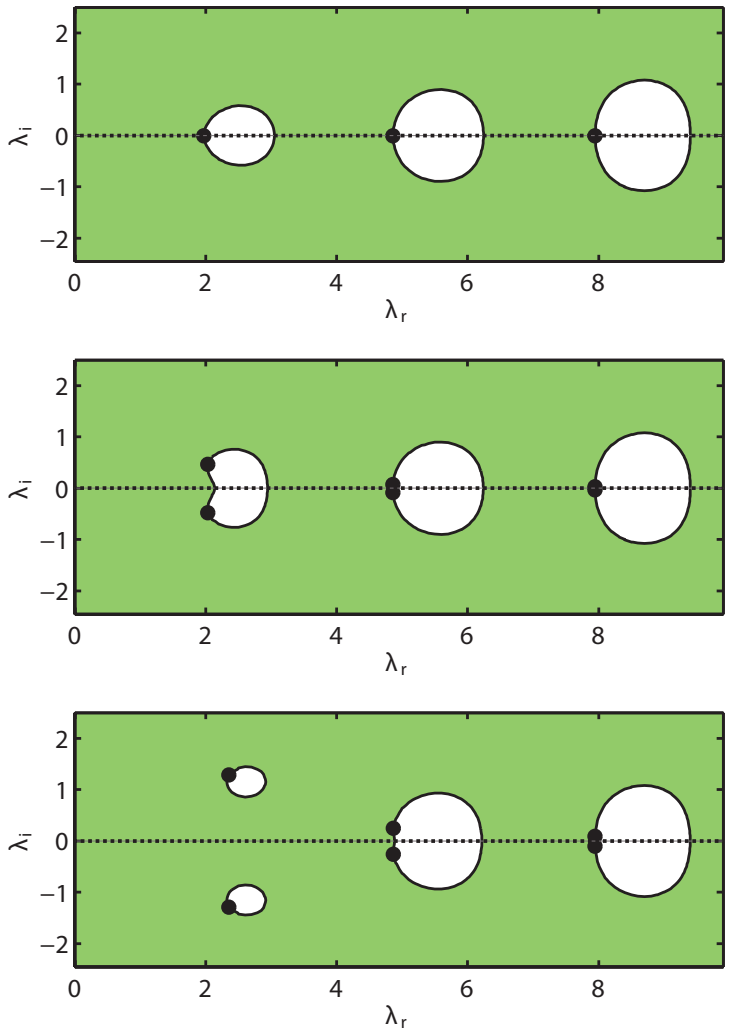

Figure 5.1: Evaluation of the real part of the sum in (5.32) for $k = 1.2$ and $-Ra = 0$ (top), 10 (middle) and 100 (bottom). Green regions show positive values of sum, white regions show negative values, black lines show contours of zero values of the sum, and black dots the position of the poles. Solutions to (5.32) correspond to crossing points of the black contours with the real axis, marked with the dashed line.

contours where the sum is zero, and black dots the position of the poles. Solutions to the dispersion relation correspond to the black contours intersecting with the real axis.

We can trace the solution for λ as a function of k using the arc-length con-

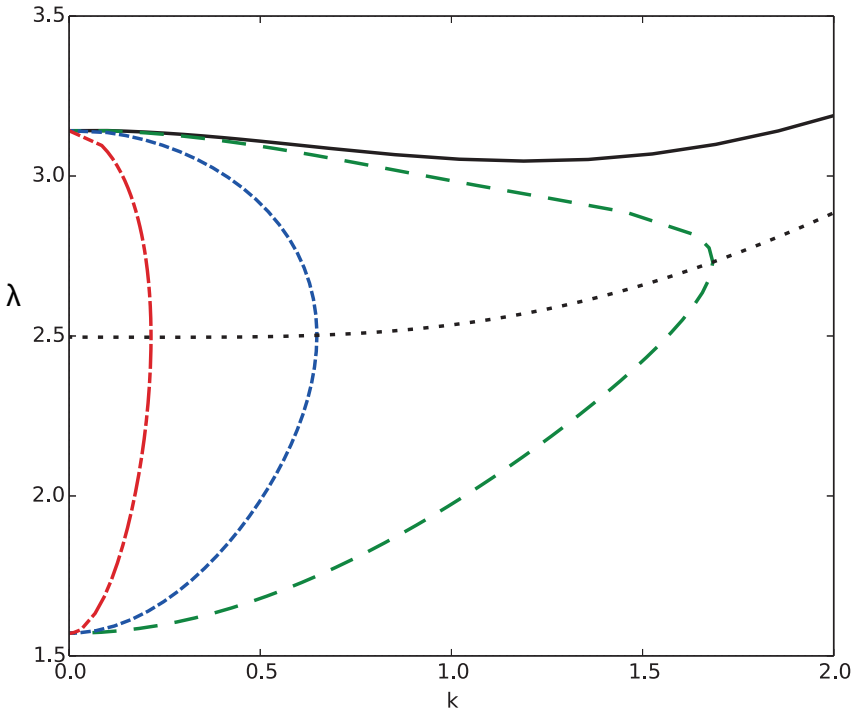

Figure 5.2: Lowest branch of solutions $\lambda(k=0)=\pi$ to the eigenvalue equation (5.32) when $Pr=1$ for $-Ra=0$ (upper black line), 10 (green), 100 (blue) and 1000 (red). Lower black line is locus of turning points k^{crit} as a function of $-Ra$. This is the k for which there is exactly one solution for each $-Ra$.

tinuation software AUTO07p. This is particularly straightforward because when $k=0$, the sum is independent of Ra, and so the results for λ should be the same as in the unstratified case when $k=0$, giving $\lambda\tan\lambda=0$. We therefore have infinitely many solutions $\lambda(k=0)=n\pi$ labelled by integers n, which provide analytic starting points for a continuation in k and Ra.

Figure 5.2 shows the solutions with $\lambda(k=0)=\pi$ in the $k-\lambda$ plane for $-Ra=0$, 10, 100 and 1000. For $Ra\neq 0$, there are two solutions for each $0<k<k^{crit}(Ra)$, which correspond to the two poles near $\lambda=\pi$ moving away from the real λ axis as $-Ra$ is increased, giving two crossing points for each n of the zero contour in Figure 5.1 with the real axis. $k=k^{crit}(Ra)$ is the value of k at which the two poles have moved sufficiently far away for the two solutions to coincide. For $k>k^{crit}$, the two poles are too far from the real axis to provide a solution associated with

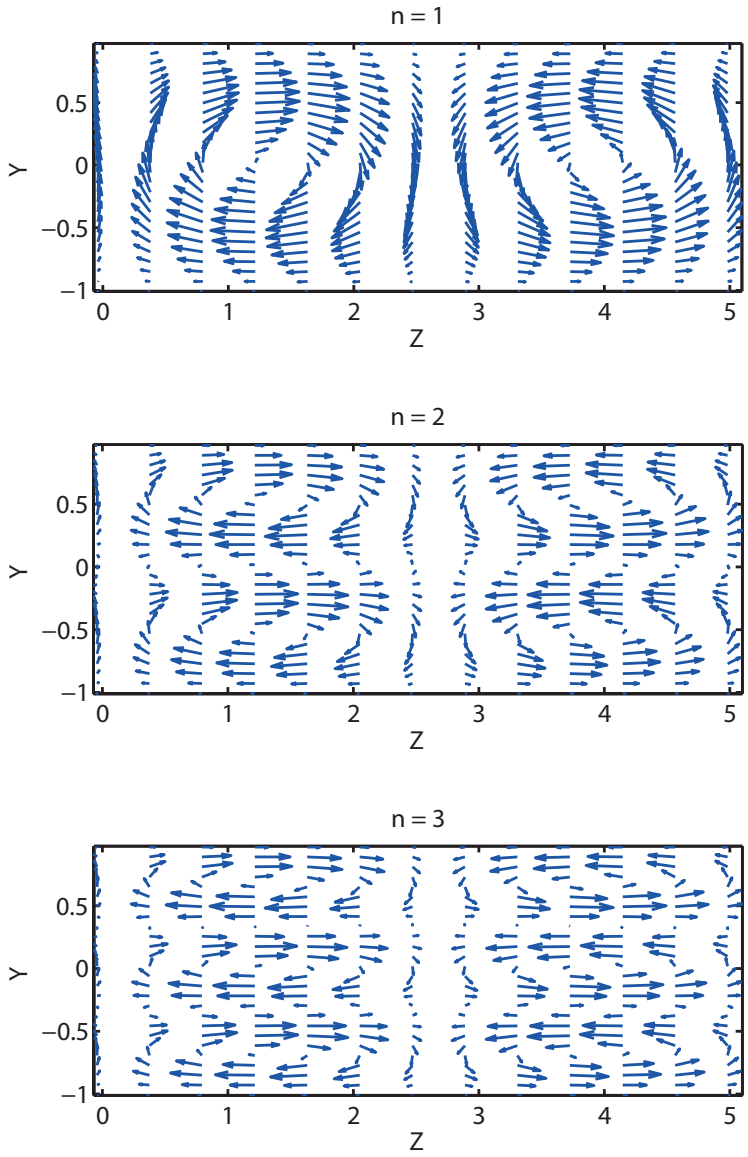

Figure 5.3: The vector field $[\mathcal{V}, \mathcal{W}]$ for solutions at $k = 1.2$ and $Pr = 1$ and $-Ra = 10$ corresponding to branches $n = 1$, 2 and 3. The corresponding values of λ are 2.95, 6.24 and 9.40 respectively.

the branch $\lambda(k = 0) = \pi$. Also plotted in Figure 5.2 is the locus of $k^{crit}(Ra)$ as $-Ra$ is varied.

The other branches $\lambda(k = 0) = n\pi$ produce very similar diagrams, but k^{crit} decreases much more slowly with increasing $-Ra$. The branch $n = 1$ corresponds

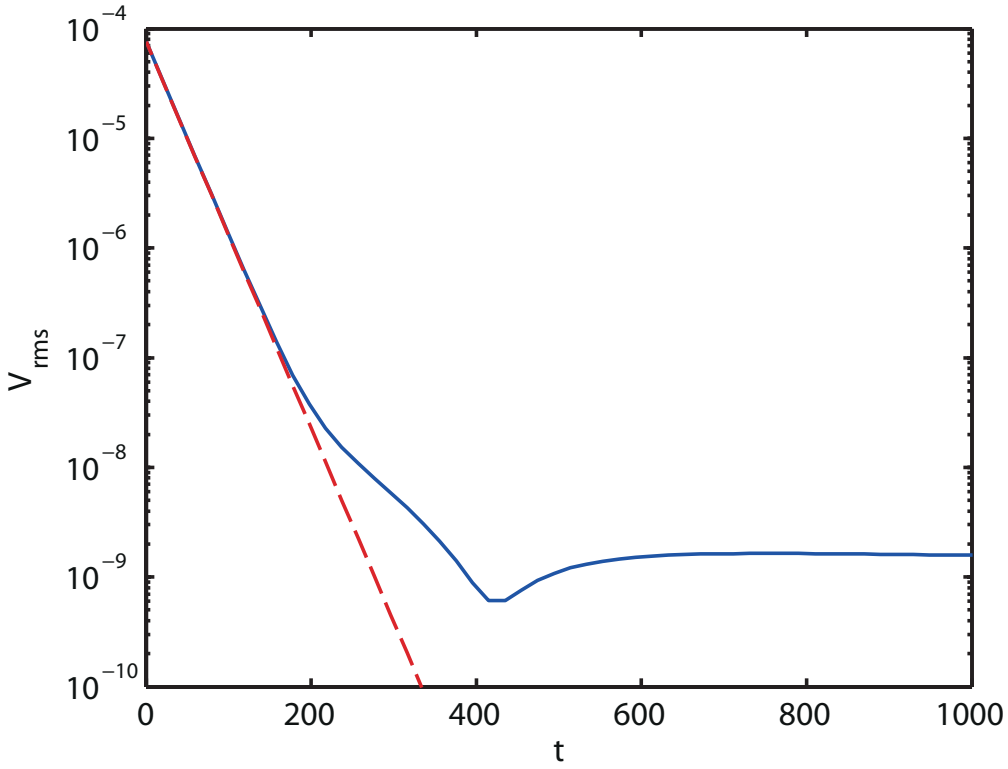

Figure 5.4: Blue: $\mathcal{V}_{rms}$ against time t for an $n = 2$ solution at $-Ra = 10$ with $k = 2.4$ and $Pr = 1$ and $\lambda = 6.37$. Red: Predicted viscous decay for this solution.

to two counter-rotating rolls that span the whole vertical extent of the domain. General n has two adjacent columns of n vertically arranged rolls. Figure 5.3 shows the vector field $[\mathcal{V}, \mathcal{W}]$ for solutions at $k = 1.2$ and $-Ra = 10$ corresponding to branches $n = 1$, 2 and 3.

When verifying numerically with a 2D version of Diablo that these solutions exist and have the correct decay rates, it appears that the solutions with $n > 1$ for a given k are very unstable, and are difficult to sustain in the flow for a long period of time. For example, a solution at $-Ra = 10$ with $n = 2$ and $k = 2.4$, after an initial period with the correct decay rate, suffers an instability in which the two adjacent columns of two vertically aligned rolls merge to form two adjacent single rolls. $\mathcal{V}_{rms}(t)$ is shown in Figure 5.4 along with the expected viscous decay for this solution. The departure from viscous decay occurs after a time approximately given by λ^2/Re.

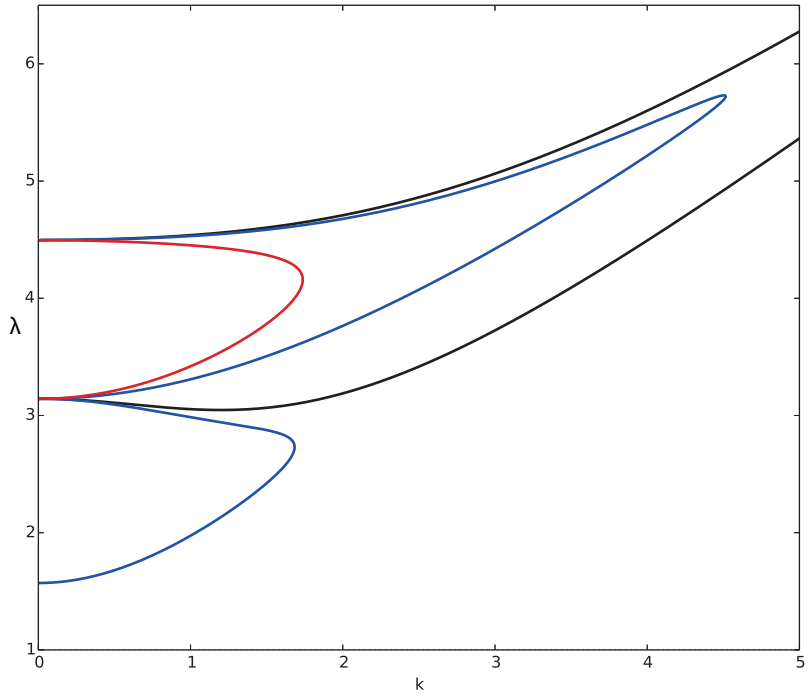

Figure 5.5: Symmetric (lower curves) and asymmetric (upper curves) roll solutions $\lambda(k)$ with $n = 1$ at $Pr = 1$ and $-Ra = 0$ (black), 10 (blue) and 100 (red). Solutions at $k = 5/3$ are used in streak and wave calculations.

y-asymmetric solutions

Solutions that are y-asymmetric that satisfy the boundary conditions $\hat{V}(\pm 1) = \hat{\Theta}(\pm 1) = 0$ take the form

$$\hat{V} = \sum_{n=1}^{\infty} v_n \sin n\pi y, \tag{5.34}$$

$$\hat{\Theta} = \sum_{n=1}^{\infty} \theta_n \sin n\pi y, \tag{5.35}$$

$$\theta_n = \frac{RePr}{n^2\pi^2 + k^2 - Pr\lambda^2} v_n, \tag{5.36}$$

and an analogous calculation to that above gives the dispersion relation

$$\sum_{n=1}^{\infty} \frac{n^2\pi^2\left(n^2\pi^2 + k^2 - Pr\lambda^2\right)}{\left(k^2 + n^2\pi^2\right)\left(k^2 - \lambda^2 + n^2\pi^2\right)\left(k^2 - Pr\lambda^2 + n^2\pi^2\right) - k^2 Ra} = 0. \tag{5.37}$$

When $Pr = 1$ this sum has poles in its denominators at

$$\lambda_n^2 = \pm i \left[\frac{-k^2 Ra}{n^2\pi^2 + k^2} \right]^{1/2} + k^2 + n^2\pi^2, \tag{5.38}$$

and so we see that the same arguments apply in terms of our search for one or two solutions with $\lambda_n < \lambda < \lambda_{n+1}$ for each n.

We may use the same continuation procedure from the known solution at $k = 0$ where the stratified and unstratified solutions match. The new asymmetric solution branches are given by $\tan\lambda = \lambda$, from which we can continue into $k > 0$. Figure 5.5 shows results of this continuation for the $n = 1$ branch for both symmetric and asymmetric solutions when $Pr = 1$.

Case for an oscillating, diffusing density field

Simply initialising a direct numerical simulation restricted to the two-dimensional spanwise and wall-normal flow with Waleffe's optimal rolls gives a density field and roll structure that oscillate in time. After isosurfaces of density are bent by the rolls sufficiently, the rolls then reverse direction, and the density isosurfaces begin to straighten, and then bend in the opposite direction.

This suggests that we should look for oscillatory solutions. Such oscillations must be restricted to frequencies less than $N = \sqrt{Ri_B}$. Setting

$$[\mathcal{V}(y,z,t), \mathcal{W}(y,z,t)] = [\hat{V}(y)\cos kz, \hat{W}(y)\sin kz] e^{-\lambda^2 t/Re + i\alpha\sqrt{Ri_B}t}, \tag{5.39}$$

and

$$\Theta(y,z,t) = \hat{\Theta}(y)\cos kz e^{-\lambda^2 t/Re + i\alpha\sqrt{Ri_B}t}, \tag{5.40}$$

where we expect $|\alpha| \leq 1$, gives

$$\begin{aligned} (D^2 - k^2)(D^2 - k^2 + \lambda^2 - i\alpha Re\sqrt{Ri_B})\hat{V} &= -k^2 Re Ri_B \hat{\Theta}, \\ (D^2 - k^2 + Pr\lambda^2 - i\alpha RePr\sqrt{Ri_B})\hat{\Theta} &= -RePr\hat{V}, \end{aligned} \tag{5.41}$$

and solutions with y-symmetry automatically satisfying the two boundary conditions $\hat{V}(\pm 1) = \hat{\Theta}(\pm 1) = 0$ take the form

$$\hat{V} = \sum_{n=1}^{\infty} v_n \cos\frac{(2n-1)\pi y}{2} \tag{5.42}$$

$$\hat{\Theta} = \sum_{n=1}^{\infty} \theta_n \cos \frac{(2n-1)\pi y}{2} \tag{5.43}$$

$$\theta_n = \frac{RePr}{\left(\frac{2n-1}{2}\right)^2 \pi^2 + k^2 - Pr\lambda^2 + i\alpha RePr\sqrt{Ri_B}} v_n \tag{5.44}$$

The same procedure as above gives the dispersion relation for α and λ as

$$\sum_{n=1}^{\infty} \frac{\frac{(2n-1)^2\pi^2}{4} b_n}{\left(k^2 + \frac{(2n-1)^2\pi^2}{4}\right) a_n b_n - k^2 Ra} = 0, \tag{5.45}$$

where

$$a_n = \left(k^2 - \lambda^2 + \frac{(2n-1)^2\pi^2}{4} + i\alpha Re\sqrt{Ri_B}\right), \tag{5.46}$$

$$b_n = \left(k^2 - Pr\lambda^2 + \frac{(2n-1)^2\pi^2}{4} + i\alpha RePr\sqrt{Ri_B}\right). \tag{5.47}$$

When $Pr = 1$, the poles are now at

$$\lambda_n^2 = i\left(\alpha Re\sqrt{Ri_B} \pm \left[\frac{-k^2 Ra}{\frac{(2n-1)^2\pi^2}{4} + k^2}\right]^{1/2}\right) + k^2 + \frac{(2n-1)^2\pi^2}{4}. \tag{5.48}$$

We see that α pulls the lower pole from the purely diffusive case up towards the real axis once more, and so the lower branch solutions are valid for a larger range of k.

In fact, we have that α places the nth lower pole on the real axis for

$$\alpha_n^2 = \frac{k^2}{\frac{(2n-1)^2\pi^2}{4} + k^2} < 1 \tag{5.49}$$

independent of Ra. Therefore, there is always a solution for any number of rolls in adjacent vertical columns at any wavenumber k that is either purely diffusive or oscillatory.

Figure 5.6 shows the $n = 1$ branch of solutions for $-Ra = 0$, 10, 100 and 1000 with $Pr = 1$, allowing for a nonzero α. Solutions with nonzero α are valid only for $k > k^{crit}$, and may be continued from the bifurcation at $k = k^{crit}$ where $\alpha = 0$ to larger k, with α gradually increasing towards 1. A typical variation of α with k is shown in Figure 5.7 for $-Ra = 100$.

In this set-up, the frequency of oscillations is $\omega = \alpha N$. Recall that the dispersion relation for internal gravity waves in an infinite ambient with constant

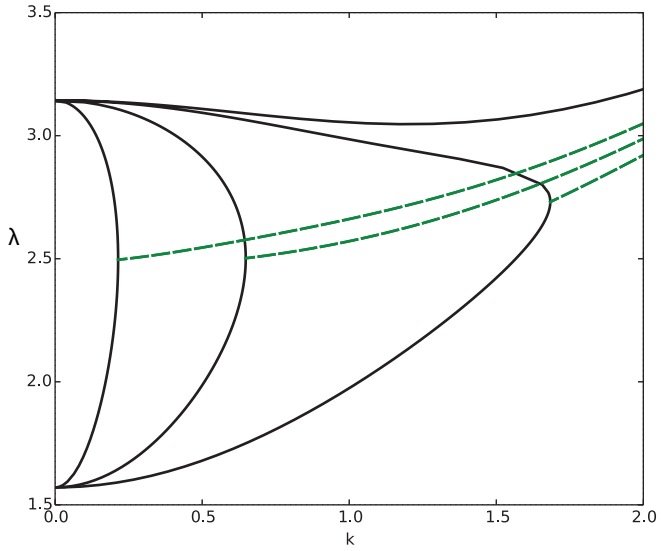

Figure 5.6: Lowest branch of solutions $\lambda(k = 0) = \pi$ to the eigenvalue equation (5.32) at $Pr = 1$ for $-Ra = 0$ (upper black line), 10, 100 and 1000 (all in black, same lines as Figure 5.2). Green lines show new branch of oscillatory solutions for each of the nonzero Ra with α increasing from 0 towards 1 as k increases.

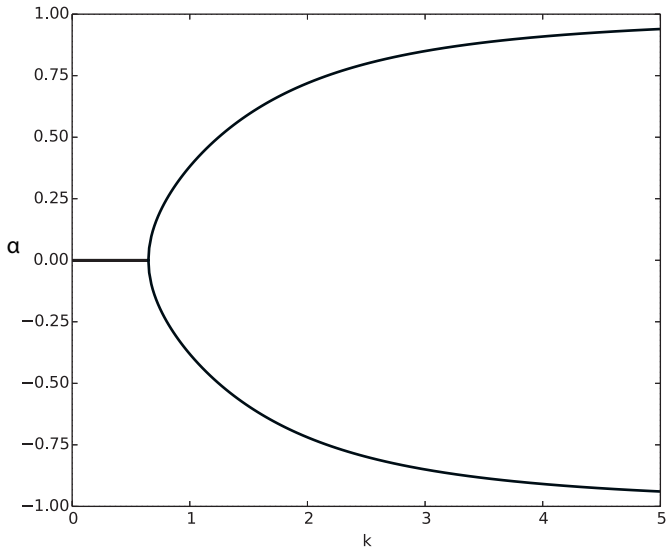

Figure 5.7: Variation of α with k for $n = 1$ solutions to the eigenvalue equation (5.32) at $Pr = 1$ and $-Ra = 100$.

buoyancy frequency N is $\omega = (\cos\theta)N$, where θ is the angle the wavevector makes with the vertical, i.e.

$$\cos^2\theta = \frac{k^2}{k^2 + l^2}, \tag{5.50}$$

where k is the horizontal wavenumber, and l is the vertical wavenumber.

The value of α required to pull solutions back to the real line therefore has the form of a quantised internal gravity wave with vertical wavenumber $l = (2n - 1)\pi/2$, corresponding to a vertical wavelength

$$L_y = \frac{2\pi}{l} = \frac{4}{2n-1}, \tag{5.51}$$

which for $n = 1$ is $L_y = 4$, twice the height of the domain. The lowest quantisation therefore allows for half a wavelength to fit in the domain.

y-asymmetric solutions

The equivalent oscillating asymmetric solutions are once again obtained by the mapping $(2n-1)^2\pi^2/4 \mapsto n^2\pi^2$ in the above calculations.

General solution of (5.23)

To confirm that the method of series solution followed by parameter continuation has in fact found all the possible solutions, we now solve (5.23) analytically. y-symmetric solutions to (5.23) when $Pr = 1$ of the form $\cosh\mu y$ satisfy

$$(\mu^2 - k^2)(\mu^2 - k^2 + \lambda^2)^2 = -k^2 Ra, \tag{5.52}$$

which is solved by the following three roots for μ^2,

$$\begin{aligned}\mu_0^2 = \frac{3k^2 - 2\lambda^2}{3} &+ \left(\frac{\lambda^6}{27} - \frac{k^2 Ra}{2} + \sqrt{-k^2 Ra\left(\frac{\lambda^6}{27} - \frac{k^2 Ra}{4}\right)}\right)^{1/3} \\ &+ \left(\frac{\lambda^6}{27} - \frac{k^2 Ra}{2} - \sqrt{-k^2 Ra\left(\frac{\lambda^6}{27} - \frac{k^2 Ra}{4}\right)}\right)^{1/3},\end{aligned} \tag{5.53}$$

$$\mu_\pm^2 = \frac{3k^2 - 2\lambda^2}{3} - \frac{1}{2}\left(\frac{\lambda^6}{27} - \frac{k^2 Ra}{2} + \sqrt{-k^2 Ra\left(\frac{\lambda^6}{27} - \frac{k^2 Ra}{4}\right)}\right)^{1/3} \tag{5.54}$$

$$
\begin{aligned}
&- \frac{1}{2}\left(\frac{\lambda^6}{27} - \frac{k^2 Ra}{2} - \sqrt{-k^2 Ra\left(\frac{\lambda^6}{27} - \frac{k^2 Ra}{4}\right)}\right)^{1/3} \\
&\pm \frac{\sqrt{3}i}{2}\Bigg[\left(\frac{\lambda^6}{27} - \frac{k^2 Ra}{2} + \sqrt{-k^2 Ra\left(\frac{\lambda^6}{27} - \frac{k^2 Ra}{4}\right)}\right)^{1/3} \\
&- \left(\frac{\lambda^6}{27} - \frac{k^2 Ra}{2} - \sqrt{-k^2 Ra\left(\frac{\lambda^6}{27} - \frac{k^2 Ra}{4}\right)}\right)^{1/3}\Bigg].
\end{aligned}
$$

We see that as $Ra \to 0$, we have $\mu_0^2 \to k^2$ and $\mu_\pm^2 \to k^2 - \lambda^2$, which are the two roots for the unstratified case. Also note that the discriminant of the cubic equation (5.52) is $D = k^2 Ra(4\lambda^6 - 27k^2 Ra) < 0$ for $Ra < 0$, and so $\mu_\pm$ are always complex.

Then, the boundary conditions $\hat{V}(\pm 1) = D\hat{V}(\pm 1) = \hat{\Theta}(\pm 1) = 0$ give

$$
\begin{aligned}
&\mu_0 \tanh \mu_0 \left[(\mu_+^2 - k^2)(\mu_+^2 - k^2 + \lambda^2) - (\mu_-^2 - k^2)(\mu_-^2 - k^2 + \lambda^2)\right] \\
&+\mu_+ \tanh \mu_+ \left[(\mu_-^2 - k^2)(\mu_-^2 - k^2 + \lambda^2) - (\mu_0^2 - k^2)(\mu_0^2 - k^2 + \lambda^2)\right] \\
&+\mu_- \tanh \mu_- \left[(\mu_0^2 - k^2)(\mu_0^2 - k^2 + \lambda^2) - (\mu_+^2 - k^2)(\mu_+^2 - k^2 + \lambda^2)\right] = 0. \quad (5.55)
\end{aligned}
$$

Writing $\mu_\pm = a \pm ib$, it is possible to demonstrate that the left-hand side of (5.55) is always imaginary, for real λ^2 and μ_0. Note that the product of the roots is $\mu_0^2|\mu_\pm^2|^2 = k^2[(k^2 - \lambda^2)^2 + (-Ra)] > 0$ and so $\mu_0^2 > 0$ always, i.e. μ_0 is always real when λ^2 is real.

Figure 5.8 shows the real valued solutions to the eigenvalue problem (5.55) for $k \in [0, 10]$ and $\lambda \in [0, 25]$ for $-Ra = 10$, 100 and 1000. It is clear that the solution is the same as that for the analysis of the Fourier series solution presented above. There are discrete branches of solutions each connected to $\lambda(k = 0) = n\pi$. We can see clearly that for larger n the value of k_c decreases less rapidly as $-Ra$ increases.

5.4 Streaks

To extend into the stratified flow the work of Waleffe (1997) we now restrict to the case considered by Waleffe (1997), setting $Re = 400$ and $k = 5/3$. We set $Pr = 1$ and investigate the effect of changing Ri_B on the $n = 1$ branches of solutions for

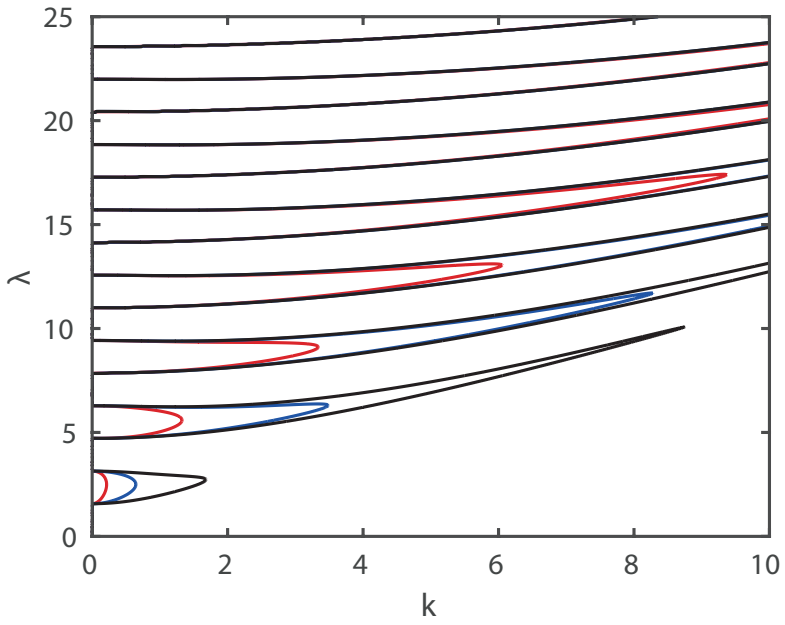

Figure 5.8: Real valued y-symmetric solutions to the eigenvalue problem (5.55) for $-Ra = 10$ (blue), 100 (red) and 1000 (black)

both symmetric and asymmetric rolls. In particular we study the rolls defined in Table 5.1 and indicated at $k = 5/3$ in Figure 5.5.

The streaks are found by setting the amplitude of the rolls to be constant and fixed in time in the spirit of a self-sustaining process, in the hope that in the actual flow there is some wave mechanism which ensures this non-decay. The streaks $\mathcal{U}$ are then the steady state solution to

$$\frac{\partial \mathcal{U}}{\partial t} + \mathcal{V} + \mathcal{V}\frac{\partial \mathcal{U}}{\partial y} + \mathcal{W}\frac{\partial \mathcal{U}}{\partial z} = \frac{1}{Re}\nabla_2^2 \mathcal{U}, \tag{5.56}$$

which is easily computed using a slightly modified version of the two-dimensional spanwise and wall-normal Diablo solver. Again following the convention of Waleffe (1997) we set $V = \max[\hat{V}(y)] = 0.02$ as the somewhat arbitrary roll amplitude.

At this point we note the apparent contradiction in retaining the nonlinear advection terms in (5.56) when we did not keep equivalent nonlinear advection terms when solving for Θ, even though the equations satisfied by each are essentially of the same structure. Since we expect $(\mathcal{V}, \mathcal{W}) = O(1/Re)$, dropping the nonlinear self-advection of the rolls is reasonable. However, we argued in Chapter 3 that

$-Ra$	λ_{sym}	λ_{asym}
0	3.09360	4.63266
10	2.78795	4.61106
	2.65782	3.58570
100	N/A	4.29137
	N/A	3.97383

Table 5.1: Decay rates for the $n = 1$ symmetric and asymmetric static, decaying roll solutions at $k = 5/3$ and $Pr = 1$ with varying Rayleigh number Ra. "N/A" indicates parameter values for which there is no static decaying solution with $n = 1$.

$(\mathcal{U}, \Theta) = O(1)$ for SSP, and so are unable to neglect the nonlinear advection terms in (5.56).

Nevertheless, there are a number of reasons for neglecting the nonlinear advection terms when solving for Θ. Firstly, and most simply, neglecting the nonlinear terms gave us an analytically tractable set of equations to solve and we gained a lot of insight from these solutions. When these solutions are substituted into a fully nonlinear numerical simulation, they still follow the correct decay rate for a substantial period of their evolution as seen in Figure 5.4, and their structure is only slightly altered from the linear modal form. Secondly, and more subtly, we are actually solving inherently different problems for Θ and for $\mathcal{U}$. When solving for Θ we are looking for decaying solutions with $\partial/\partial t = -\lambda^2/Re$ and the nonlinear terms appear to be less important for such a solution. In contrast, when solving for $\mathcal{U}$ in steady state, we are setting $\partial/\partial t = 0$ and so the structures of the two equations are very different. We find that $\mathcal{U}$ and Θ have different forms to each other, but this is likely due to solving equations with non-obvious different structures.

Figure 5.9 shows the spanwise mean streak velocity profile produced by each of the roll solutions in Table 5.1. We see from the inserts that there is a slight variation in the streak structure as $-Ra$ is increased, but it is clear that the change is minimal and the streaks are essentially unchanged by stratification. The variation of the spanwise mean total density profile is even less apparent between

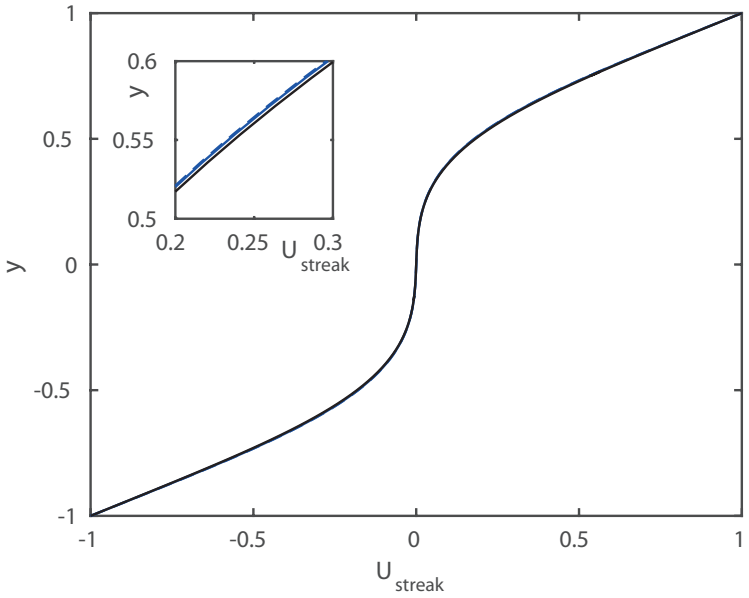

Figure 5.9: Spanwise mean of steady state streaks produced from roll solutions in Table 5.1. Symmetric rolls: single S-shape. Asymmetric rolls: double S-shape. Solutions for $-Ra = 0$ (black), 10 (blue) and 100 (red). Solid lines show upper branch solution, dashed lines show lower branch solution. Top left: zoomed plot for symmetric roll solutions. Bottom right: zoomed plot for asymmetric roll solutions.

the different parameter values, and so we do not show it here.

5.5 Waves

In order to find the wave fields, we view the streaks $\mathcal{U}(y, z)$, and streamwise mean density perturbation $\Theta(y, z)$, as a time independent base flow about which we linearise and conduct a linear stability calculation. Since the base flow depends on two coordinates, the linearised equations are not as simple as the stratified equivalent of the well-known Orr–Sommerfeld and Squire equations for linear disturbances about a one dimensional base flow. We may still perform the same manipulations as those involved in deriving the Orr–Sommerfeld and Squire equations to produce the following closed system that the wave solutions must satisfy:

$$\left(\frac{\partial}{\partial t}+(y+\mathcal{U})\frac{\partial}{\partial x}-\frac{1}{Re}\nabla^2\right)\nabla^2\hat{v}=\left(\frac{\partial^2\mathcal{U}}{\partial y^2}-\frac{\partial^2\mathcal{U}}{\partial z^2}\right)\frac{\partial\hat{v}}{\partial x} - 2\frac{\partial\mathcal{U}}{\partial z}\frac{\partial^2\hat{v}}{\partial x\partial z}+2\frac{\partial^2}{\partial x\partial y}\left(\hat{w}\frac{\partial\mathcal{U}}{\partial z}\right) - Ri_B\left(\frac{\partial^2}{\partial x^2}+\frac{\partial^2}{\partial z^2}\right)\hat{\rho}, \tag{5.57}$$

$$\left(\frac{\partial}{\partial t}+(y+\mathcal{U})\frac{\partial}{\partial x}-\frac{1}{Re}\nabla^2\right)\hat{\eta}=\left[\frac{\partial\mathcal{U}}{\partial z}\frac{\partial}{\partial y}-\left(1+\frac{\partial\mathcal{U}}{\partial y}\right)\frac{\partial}{\partial z}\right]\hat{v} - \left(\hat{v}\frac{\partial}{\partial y}+\hat{w}\frac{\partial}{\partial z}\right)\frac{\partial\mathcal{U}}{\partial z}, \tag{5.58}$$

$$\left(\frac{\partial^2}{\partial x^2}+\frac{\partial^2}{\partial z^2}\right)\hat{w}=-\frac{\partial\hat{\eta}}{\partial x}-\frac{\partial^2\hat{v}}{\partial y\partial z}, \tag{5.59}$$

$$\left(\frac{\partial}{\partial t}+(y+\mathcal{U})\frac{\partial}{\partial x}-\frac{1}{RePr}\nabla^2\right)\hat{\rho}=\hat{v}-\hat{v}\frac{\partial\Theta}{\partial y}-\hat{w}\frac{\partial\Theta}{\partial z}, \tag{5.60}$$

where $\hat{\eta}=\partial\hat{u}/\partial z-\partial\hat{w}/\partial x$ is the wall-normal wave vorticity.

As expected, if we restrict attention to one dimensional base flows, setting $\partial(\mathcal{U},\Theta)/\partial z=0$, we recover the Orr–Sommerfeld and Squire equations with the simple addition of a density field. The extra terms we now have are not readily interpreted in terms of obvious physical mechanisms like the Orr or lift-up mechanisms and have not really been investigated systematically in any great detail.

The main advantage for one dimensional base flows in the absence of a density field of writing the equations in Orr–Sommerfeld and Squire form is that the number of functions required to solve for is reduced to two. This is because $\hat{w}$ decouples from the equations for $\hat{v}$ and $\hat{\eta}$, and (5.59) may be used simply to extract $\hat{w}$ from the solution found for $\hat{v}$ and $\hat{\eta}$. However, in the two-dimensional base flow case no such decoupling occurs, and (5.59) must be solved alongside the other equations if left in their present form.

We wish to search for normal mode solutions where all the variables are proportional to $\exp(\sigma t+i\alpha x)$, where α is the streamwise wavenumber and σ is the growth rate. The candidate wave solution is then the wave field that is just marginal, neither growing nor decaying, so that $\sigma=0$. For the solution found by Waleffe (1997) this occurs for the marginal streamwise wavenumber $\alpha_0\approx 1.1$.

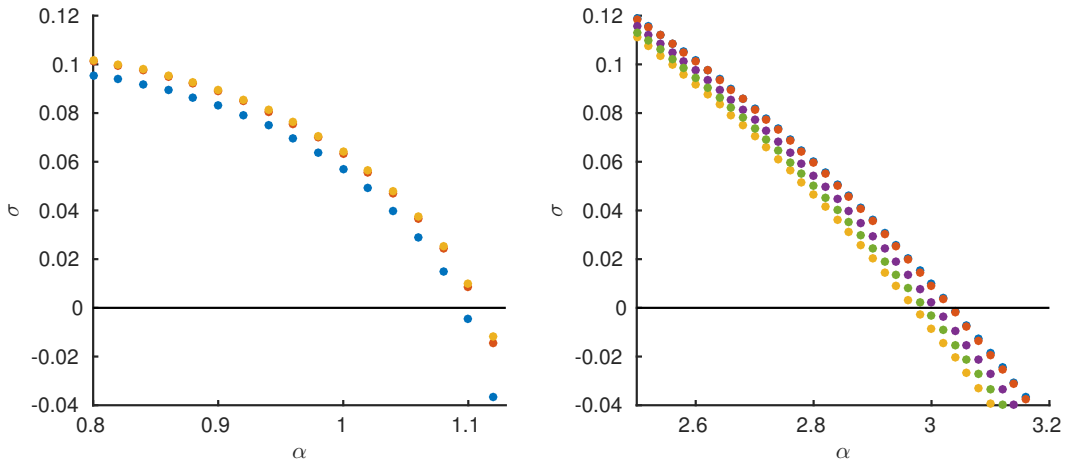

Figure 5.10: Growth rate σ against streamwise wavenumber α of fastest growing linear instability for the symmetric (left) and asymmetric (right) steady state streak solutions for $-Ra = 0$ (blue) 10 (upper branch, red, lower branch, yellow) and 100 (upper branch, purple, lower branch, green). Black line shows marginal stability level.

Although we can in principle solve (5.57 – 5.60) via discretisation followed by a matrix eigenvalue problem, there is substantial effort required to implement this numerically. We instead use a modified version of the two-dimensional spanwise and wall-normal, three component version of the direct numerical integrator Diablo that solves the Navier–Stokes equations linearised about any two-dimensional fields $(\mathcal{U}(y,z), \Theta(y,z))$ for any input streamwise wavenumber α. We then compute the fastest growing linear mode by brute force time-stepping from a number of randomised solenoidal initial conditions at each α and wait until the solution has converged to an exponentially growing or decaying state. We monitor the amplitude of the linear solution and require that a measure of the instantaneous growth rate converge in a moving time average sense. The main disadvantage of this method is that we will only find the fastest growing linear mode, and so if there are other growing modes with smaller growth rates, we will not be able to compute them.

Figure 5.10 shows the growth rates of the fastest growing linear modes for both the symmetric and asymmetric streak solutions over a range of α that contains the marginal mode with $\sigma = 0$. We see that the calculations agree with those of

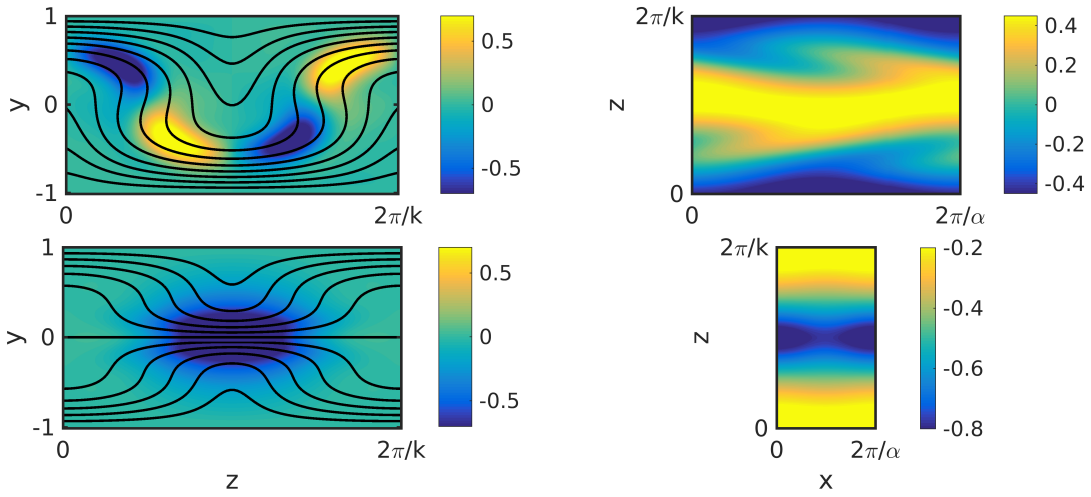

Figure 5.11: Marginal wave solutions for the $-Ra = 0$ symmetric (top) and asymmetric (bottom) solutions. Left: y-z slice. Colour, vertical velocity wave mode. Black, contours of streak plus background PCF shear. Right: z-x midplane $y = 0$ (top) and quarterplane $y = -0.5$ (bottom), streak plus 15% amplitude streamwise wave mode.

Waleffe (1997) for the unstratified symmetric case, for which the marginal solution has $\alpha_0 \approx 1.1$. For all values of $-Ra$ we see that the growth rate curves and the marginal wavenumbers are little affected by stratification. For the symmetric solutions, the stratification increases the marginal wavenumber whilst for the asymmetric solutions, the stratification decreases the marginal wavenumber from its unstratified value $\alpha_0 \approx 3.05$.

We see a striking difference between the symmetric and asymmetric solutions. For a given amplitude of rolls, $\max[\hat{V}(y)] = 0.02$, the wavenumber for marginal waves is much larger for the asymmetric solutions than for the symmetric solutions. Waleffe (1997) found that that as $\max[\hat{V}(y)]$ is increased, the steady state streak solutions $\mathcal{U}$ develop larger gradients and the resulting waves have larger maximum growth rates, and the marginal wavenumber increases significantly. This indicates that for a comparable streamwise wavelength of marginal solution, asymmetric roll solutions require much smaller amplitudes than the symmetric roll solutions.

Figure 5.11 shows the marginal wave field for both the symmetric and asymmetric unstratified $-Ra = 0$ solutions. We plot both the vertical wave velocity field above contours of the streak velocity plus background PCF shear on a vertical y-z slice, and also a representative candidate SSP solution for the streamwise velocity

on a horizontal x-z slice with the streak velocity plus 15% by amplitude streamwise wave velocity. We see from the vertical slices that both the wave solutions are concentrated about regions of high shear, as might be expected.

The midplane $y = 0$ view of the symmetric solution demonstrates that this wave solution is sinusoidal rather than 'sinucose' or varicose, as observed by Waleffe (1997). This manifests itself as a sinusoidal modulation of both the fast and slow speed streaks along a single streamwise wavelength as opposed to a 'bulging' of one streak along with a corresponding narrowing of the other. In fact, Waleffe (1997) states that the fundamental sinusoidal mode is expected to be more unstable than both its subharmonic 'sinucose' mode (where one streak is modulated sinusoidally and the other bulges) and the fundamental varicose mode (where both streaks bulge) and then precedes to restrict the search for solutions only to solutions with such a downstream symmetry. The calculation here serves to demonstrate that this assumption about the form of the fastest growing mode is correct. Waleffe (1997) argues that the sinusoidal modes can be related to the formation of staggered rows of vortices whilst the sinucose or varicose modes can be related to the formation of horseshoe vortex structures.

Because of the imposed symmetry, for the marginal wave field for the asymmetric, unstratified $-Ra = 0$ solution, the streamwise velocities are zero on the midplane $y = 0$ and so we show instead the quaterplane $y = -0.5$. The streaks have two regions of high shear, one near each of the walls and one in the centre of the channel. The marginal wave is centred around the region of high shear in the centre of the channel only, away from the apparently stabilising effect of the near wall region. In contrast to the symmetric solution, the vertical velocity on a single vertical slice is of one sign only, and the resulting streaky SSP candidate solution is clearly no longer a sinusoidal modulation of a streamwise streak, but instead the waves are a 'bulging' varicose mode.

The wave fields of both symmetric and asymmetric solutions and both the upper and lower branches for $-Ra = 10$ and 100 are virtually indistinguishable from the unstratified wave fields, and for this reason we do not plot them here. The marginal modes are once more concentrated about regions of high shear. The perturbation density field Θ is large enough to create statically unstable regions in the density field, but despite this the wave fields do not concentrate about the

statically unstable regions. This is because the bulk Rayleigh number is so small, and so the local Rayleigh numbers in these statically unstable regions are also extremely small, and so we should not expect a dynamic instability. Of course, this problem could be avoided by reducing the roll amplitude $V = \max[\hat{V}(y)]$, which is directly proportional to the amplitude of Θ. The conclusion of this section is that the marginal wave fields are not much affected by the stratification, having very similar spatial structures as the unstratified results.

5.6 Feedback onto the rolls

Now that we have the wave fields, we can investigate how well the waves feed back nonlinearly onto the rolls. Including the wave nonlinear interaction terms in the roll equations gives

$$\left(\frac{\partial}{\partial t} - \frac{1}{Re}\nabla^2\right)\nabla^2\mathcal{V} = -Ri_B\frac{\partial^2\Theta}{\partial z^2} + \frac{\partial^3}{\partial z^2\partial y}\langle\hat{w}\hat{w} - \hat{v}\hat{v}\rangle_x + \left(\frac{\partial^2}{\partial y^2} - \frac{\partial^2}{\partial z^2}\right)\frac{\partial}{\partial z}\langle\hat{v}\hat{w}\rangle_x, \tag{5.61}$$

$$\left(\frac{\partial}{\partial t} - \frac{1}{RePr}\nabla^2\right)\Theta = \mathcal{V} - \frac{\partial}{\partial y}\langle\hat{v}\hat{\rho}\rangle_x - \frac{\partial}{\partial z}\langle\hat{w}\hat{\rho}\rangle_x. \tag{5.62}$$

Waleffe (1997) makes the observation that (5.61) can be viewed as an evolution equation for the streamwise mean streamwise vorticity $\langle\omega_x\rangle_x$, since $\nabla^2\mathcal{V} = -\partial\langle\omega_x\rangle_x/\partial z$.

The symmetries of the wave fields $(\hat{u}, \hat{v}, \hat{w}, \hat{\rho})$ mean that the forced response of (5.61 – 5.62) due to the waves takes the form of a cosine series for $\mathcal{V}$ with leading order term $\cos(kz)$, indicating at least that the correct structural form of roll is forced. To verify in detail whether the correct rolls are being reinforced, we consider the projection of (5.61 – 5.62) onto just the first mode, $\cos(kz)$, following Waleffe (1997).

Figure 5.12 shows both $\nabla^2\mathcal{V}$ for the original rolls, and the sum of the wave terms in the right-hand side of the roll feedback equation (5.61) projected onto $\cos(kz)$ for both the symmetric and asymmetric unstratified $-Ra = 0$ solutions. The sign of the wave forcing is such that $\mathcal{V}$ is reinforced for the symmetric solution, so that the wave forcing has the same sign as $\mathcal{V}$ over large parts of the domain.

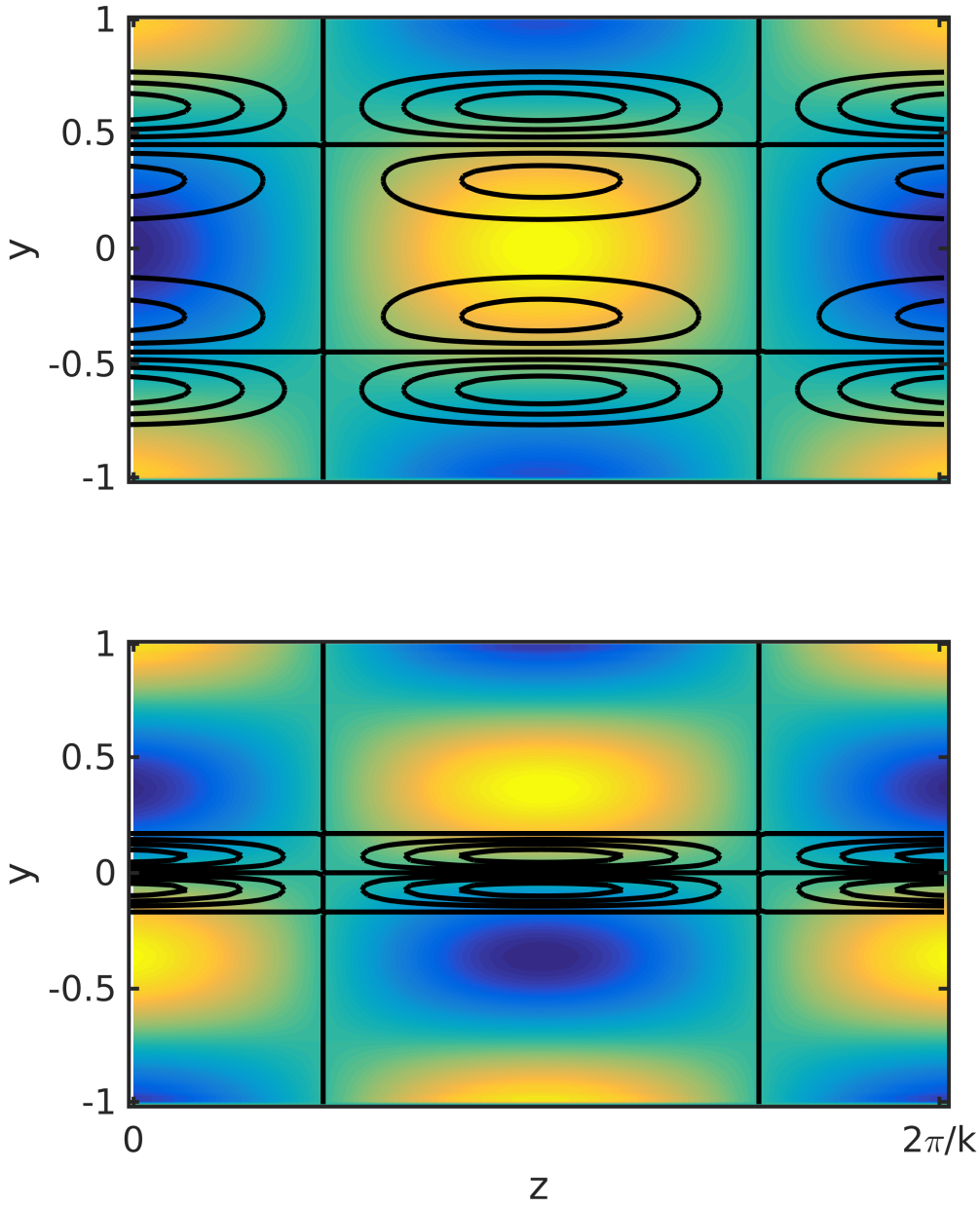

Figure 5.12: Colour: $\nabla^2 \mathcal{V}$ for the original roll solutions. Black: projection of the sum of the wave terms on the right-hand side of (5.61) for the symmetric (top) and asymmetric (bottom) solutions.

The spatial structure of the wave forcing suggests that in fact two separate sets of vortices, one above and one below the centreline, should be created. Waleffe (1997)

states that at such a low Reynolds number, $Re = 400$, the effect of the induced vortices on each other due to the high diffusion is likely to result in the two sets of vortices merging and forming one large structure that spans the whole height of the channel. When solving the roll equations in steady state given a fixed wave forcing, Waleffe (1997) finds that this is the case, and the produced rolls are very similar to the original roll solution.

In contrast, the asymmetric solution has wave forcing such that $\mathcal{V}$ is destroyed rather than reinforced. Waleffe (1997) indicates that this is to be expected, since the largest, critical streamwise wavenumber that can sustain turbulence at this Reynolds number is $\alpha_c \approx 1.14$, identified in the minimal box study of Hamilton *et al.* (1995), which is very close to the marginal streamwise wavenumber for the symmetric solution. However, the asymmetric solution has marginal streamwise wavenumber $\alpha_0 \approx 3.05$ and so we do not have sustained turbulence in such a small domain, and therefore cannot expect to find a self-sustaining process. The simplified model provided by Waleffe (1997) shows that there is a critical streamwise wavenumber beyond which the rolls are destroyed rather than reinforced, and that the structure of the forcing is not much changed as the wavenumber varies, only its sign.

There are two possible routes out of the problem of apparent roll destruction. One solution would be to reduce the amplitude of the original rolls, $V = \max[\hat{V}(y)]$, which produces smaller amplitude streaks, and reduces the marginal streamwise wavenumber, providing a larger domain in which to self-sustain. Another solution is to increase the Reynolds number. This would decrease the size of the domain in which a self-sustaining process is expected to arise, but is likely simultaneously to make the streaks more unstable and so could increase the marginal streamwise wavenumber further, requiring once more an adjustment of the roll amplitude $V = \max[\hat{V}(y)]$.

There is clearly a trade-off between changing the two parameters. Perhaps the most obvious solution for our purposes here is to use the Reynolds number of the minimal seeds and estimate from them a spanwise wavenumber to use in the SSP process. This is not particularly straightforward because in the narrow geometry N the rolls are not modal in structure. They instead consist of relatively wide rolls adjacent to relatively narrow rolls and so the extraction of a single spanwise

wavenumber is not obvious. In the wide geometry W the rolls are localised in the spanwise direction, consisting of a single wide roll flanked by two narrower rolls, and so once more it is difficult to identify a single spanwise wavenumber.

We have invested effort into trying these possible solutions, varying the roll amplitude and Reynolds number both independently and simultaneously, but we have been unable to find a set of parameters that reinforces the rolls. Such a set must exist, but it is clearly quite sensitive to the flow geometry and the other parameters. Keeping $k = 5/3$ fixed, we find that for both $Re = 400$ and 1000, as we decrease the roll amplitude $V = \max[\hat{V}(y)]$, the streaks stabilise completely before the marginal streamwise wavenumber α_0 decreases below its critical value for sustained turbulence α_c, and all the solutions have wave forcing structure extremely similar to the one presented here, and destroy the rolls. For example, when $Re = 1000$ and $V = 0.02$ there is an oscillatory branch of waves for small α and a non-oscillatory branch of waves for large α. The maximum growth rate over all streamwise wavenumbers is a non-oscillatory solution with $\alpha \equiv \alpha_{\max} > \alpha_c$. As V is decreased, the value of this maximum growth rate decreases but the streamwise wavenumber at which it occurs is little affected and continues to obey $\alpha_{\max} > \alpha_c$. As V is decreased further, the maximum growth rate becomes negative and all waves decay. The wavenumber corresponding to the maximum growth rate which is just neutral still has $\alpha_{\max} = \alpha_0 > \alpha_c$. This occurs for $4.0\times10^{-3} < V < 4.5\times10^{-3}$.

Since Waleffe (1997) suggests that the spatial structure of the wave forcing is correct and that only its sign is wrong at the current parameter values, we will continue to investigate it as we introduce stratification. The main result of this section is that the addition of stratification does not appear to affect the roll re-injection part of the self-sustaining process. For all the upper and lower branch solutions with $-Ra = 10$ and 100, the form of both $\nabla^2\mathcal{V}$ and the wave forcing are virtually indistinguishable from the unstratified versions, which is why we do not plot them here.

5.7 Discussion

We have closed the loop for the stratified self-sustaining process. The only effect of stratification on the self-sustaining process described by Waleffe (1997) is to

remove steady diffusing roll solutions through a bifurcation that results in oscillatory rolls for large enough stratification strengths, which makes sense on physical grounds. The solutions have a complicated dependence on Prandtl number, but the critical parameter that governs this transition from steady to oscillatory solutions is the Rayleigh number $Ra = Re^2(-Ri_B)Pr$, which is consistent with our assertion in Chapter 3 that SSP is significantly affected by the density field when $Ri_B = O(Re^{-2})$. For parameter values at which we have a steady roll solution, none of the other constituent parts of SSP are affected by the stable stratification.

We also extended the work of Waleffe (1997) by calculating asymmetric roll solutions as well as symmetric roll solutions. The primary reasons for doing so was that the minimal seeds in Chapter 3 appear to have asymmetric roll structures near the edge state, and also that asymmetric solutions allow a larger range of Rayleigh numbers Ra for a given streamwise wavenumber k that admit a steady roll solution. Unfortunately, we were unable to find the very sensitive parameter values that allowed for roll reinforcement by the waves rather than destruction.

The marginal streamwise wavenumber is affected by the Reynolds number, roll amplitude and spanwise wavenumber, and in order to have neutral wave solutions that reinforce the rolls it is necessary for the marginal streamwise wavenumber to be comparable to that for the smallest computational domain that admits turbulent motion. A simple trial-and-error approach to finding a set of parameter values was not successful in identifying a suitable marginal streamwise wavenumber. Given the apparent extreme sensitivity of the marginal wave solution on parameter values, we could instead perform a minimal box study for asymmetrically confined PCF to identify the smallest computational domain at which turbulence may just be maintained. It was precisely the minimal box study of Hamilton *et al.* (1995) that inspired the seemingly arbitrary parameter values used by Waleffe (1997).

For the stratified case, it is clear that a thorough investigation of the oscillatory solutions is needed. Again, this is not a particularly straightforward task due to the large number of parameters involved and the apparent sensitivity of the marginal wave solutions, and so a blind search is unlikely to be fruitful. A sensible approach would be to re-do the minimal box study of Hamilton *et al.* (1995) for stratified PCF to find the 'natural' choice of parameters. Such a study would be interesting in its own right since we expect minimal flows to in some sense contain

the essential processes that sustain turbulent motion. This would be particularly useful at large bulk Richardson numbers since it would show whether or not an oscillatory SSP/VWI ansatz is relevant at all bulk Richardson numbers, or only for a small range of bulk Richardson numbers beyond the initial SSP/VWI breakdown.

Another consideration for the oscillating solutions is how to calculate the wave fields. Since the frequency of oscillation scales with $\sqrt{Ri_B}$, the period of oscillation is very long for small bulk Richardson numbers just beyond the bifurcation. It is then unclear whether a Floquet-type analysis should be performed to find the waves, or if it would be better to look at a range of static base flows taken from different points in the oscillation, or to perform a WKB analysis in time. A preliminary examination of wave fields just beyond the bifurcation point for the symmetric solutions shows that the waves take the spatial form of the unstratified waves for long periods of time and very rapidly reflect about the midplane every time the base flow swaps sign, suggesting that a static base flow assumption may be a valid starting point.

CHAPTER 6

HORIZONTALLY SHEARED MINIMAL SEEDS

In this chapter we compute minimal seeds for turbulence in horizontally sheared stratified PCF. We begin by recalling the DAL method for horizontally sheared stratified PCF and discuss the differences between the DAL equations for the vertically and horizontally sheared cases. We also discuss briefly some phenomena in horizontally sheared stratified flows and how they differ from the vertically sheared case. We then move on to the computation of minimal seeds for horizontally sheared stratified PCF at the same parameter values as the vertically sheared minimal seeds found in Chapter 3, and discuss how the stratification affects the unstratified minimal seeds in this case. We find that for sufficiently large bulk Richardson numbers Ri_B the minimal seed trajectories depart significantly from their vertically sheared counterparts, which can be seen when we describe once more their evolution in terms of the components of the SSP process, decomposing into rolls, streaks and waves. Before concluding this chapter we discuss the difficulties of finding minimal seeds at larger bulk Richardson number and show the evolution of a 'turbulent seed' at bulk Richardson number $Ri_B = 0.1$ that displays spontaneous layering in the density field. The dynamics of the turbulent seed are quasi-one-dimensional for much of its evolution, and we show preliminary findings of a reduced model based on this observation.

6.1 Horizontal vs vertical shear

The equations of motion for horizontally sheared stratified PCF are

$$\frac{\partial \mathbf{u}}{\partial t} + (\mathbf{u}+\mathbf{U})\cdot\nabla(\mathbf{u}+\mathbf{U}) = -\nabla p - Ri_B\rho\hat{\mathbf{z}} + \frac{1}{Re}\nabla^2\mathbf{u}, \tag{6.1}$$

$$\frac{\partial \rho}{\partial t} + (\mathbf{u}+\mathbf{U})\cdot\nabla(\bar{\rho}+\rho) = \frac{1}{RePr}\nabla^2\rho, \tag{6.2}$$

$$\nabla\cdot\mathbf{u} = 0, \tag{6.3}$$

where the background fields are $\mathbf{U} = y\hat{\mathbf{x}}$ and $\bar{\rho} = -z$. We will consider the case in which the background density field $\bar{\rho}$ is considered to prescribe the density at the two walls located at $y = \pm 1$, and so we apply the Dirichlet boundary conditions on both the perturbation velocity and perturbation density fields,

$$\mathbf{u}(x,\pm 1,z,t) = 0, \quad \rho(x,\pm 1,z,t) = 0. \tag{6.4}$$

These boundary conditions can be thought of as applying a constant temperature boundary condition on the two walls, whose value increases linearly with z, and so the perturbation field is fixed to take zero values at these two walls. We could also imagine a case for which a background shear and background density field is prescribed over some large region, and we are considering the nonlinear growth on a local scale, under the assumption that the walls do not greatly affect the dynamics, which certainly appears to be the case for the vertically sheared minimal seeds presented in Chapter 3. The flow geometry is shown in Figure 2.2.

In the streamwise x and spanwise z directions we apply periodic boundary conditions on the perturbation velocity and density fields. It does not matter that the background density field $\bar{\rho} = -z$ is not periodic in the spanwise direction since we are restricting attention only to periodic perturbations on a given constant gradient background density field. The equations of motion do not depend directly on $\bar{\rho}$ but only on its gradient, $\nabla\bar{\rho} = -\hat{\mathbf{z}}$, which is periodic in the spanwise direction. This set of boundary conditions allows us to use the same version of the direct numerical time-stepper Diablo that we have used throughout, simply by changing the direction in which gravity acts. As in Chapter 3, we will consider $Re = 1000$ and $Pr = 1$ and vary Ri_B.

In order to maximise a given functional $\mathcal{J}$ we need to consider the following extended, constrained Lagrangian,

$$\begin{aligned}\mathcal{L}(\mathbf{u},\mathbf{u}_0,\rho,p,\mathbf{v},&\mathbf{v}_0,\eta,q,T,E_0,c) = \mathcal{J}[\mathbf{u}(\mathbf{x},t),\rho(\mathbf{x},t)]\\ &-\left[\eta,\,\frac{\partial\rho}{\partial t}+(\mathbf{u}+\mathbf{U})\cdot\nabla(\bar{\rho}+\rho)-\frac{1}{RePr}\nabla^2\rho\right]\\ &-\left[\mathbf{v},\,\frac{\partial\mathbf{u}}{\partial t}+\mathcal{N}\mathbf{u}+\nabla p+Ri_B\rho\hat{\mathbf{z}}-\frac{1}{Re}\nabla^2\mathbf{u}\right]\\ &-[q,\nabla\cdot\mathbf{u}]-\langle\mathbf{v}_0,\mathbf{u}(\mathbf{x},0)-\mathbf{u}_0\rangle-\langle\eta_0,\rho(\mathbf{x},0)-\rho_0\rangle\\ &-(\|\mathbf{u}_0\|^2+Ri_B\|\rho_0\|^2-2E_0)c,\end{aligned}\tag{6.5}$$

where $\mathcal{N}$ is the nonlinear advection operator as in (2.34).

Taking variations with respect to all the variables yields the following set of equations that must be satisfied by a nonlinear optimal perturbation $(\mathbf{u}_0(\mathbf{x}),\rho_0(\mathbf{x}))$,

$$\frac{\partial\mathbf{u}}{\partial t}+\mathcal{N}\mathbf{u}+\nabla p+Ri_B\rho\hat{\mathbf{z}}-\frac{1}{Re}\nabla^2\mathbf{u}=0,\tag{6.6}$$

$$\frac{\partial\rho}{\partial t}+(\mathbf{u}+\mathbf{U})\cdot\nabla(\bar{\rho}+\rho)-\frac{1}{RePr}\nabla^2\rho=0,\tag{6.7}$$

$$\nabla\cdot\mathbf{u}=0,\tag{6.8}$$

$$\mathbf{v}(\mathbf{x},T)=\frac{\delta\mathcal{J}}{\delta\mathbf{u}(\mathbf{x},T)},\tag{6.9}$$

$$\eta(\mathbf{x},T)=\frac{\delta\mathcal{J}}{\delta\rho(\mathbf{x},T)},\tag{6.10}$$

$$\frac{\partial\mathbf{v}}{\partial t}+\mathcal{N}^\dagger\mathbf{v}+\nabla q-\eta\nabla(\bar{\rho}+\rho)+\frac{1}{Re}\nabla^2\mathbf{v}=-\frac{\delta\mathcal{J}}{\delta\mathbf{u}(\mathbf{x},t)},\tag{6.11}$$

$$\frac{\partial\eta}{\partial t}+\mathbf{u}\cdot\nabla\eta-Ri_B\hat{\mathbf{z}}\cdot\mathbf{v}+\frac{1}{RePr}\nabla^2\eta=-\frac{\delta\mathcal{J}}{\delta\rho(\mathbf{x},t)},\tag{6.12}$$

$$\nabla\cdot\mathbf{v}=0,\tag{6.13}$$

$$\mathbf{v}(\mathbf{x},0)=2c\mathbf{u}_0(\mathbf{x}),\tag{6.14}$$

$$\eta(\mathbf{x},0)=2cRi_B\rho_0(\mathbf{x}),\tag{6.15}$$

provided that the adjoint fields satisfy the same boundary conditions as the direct

fields. The adjoint of the nonlinear advection operator, $\mathcal{N}^\dagger$, takes the same form as in (2.41).

The only changes to the adjoint equations in moving from vertically to horizontally sheared stratified PCF are the term $\eta\nabla\bar{\rho}$ in (6.11) acting on the spanwise component of $\mathbf{v}$ instead of the wall-normal component, and the term $Ri_B\hat{\mathbf{z}}\cdot\mathbf{v}$ in (6.12) depending on the spanwise component of $\mathbf{v}$ instead of the wall-normal component. Due to only a few minor changes in the forms of the equations, we use a slightly modified version of the Diablo-based DAL solver used in Chapter 3 to find the minimal seeds in horizontally sheared stratified PCF in this chapter.

In vertically sheared stratified PCF, Deusebio *et al.* (2015) showed that although the bulk Richardson number beyond which the flow does not have an attracting turbulent state increases as the Reynolds number increases, this critical bulk Richardson number remains below 0.2 for Reynolds numbers up to 10^5. This was explained by the observation that in a turbulent state, the mean velocity and density profiles are approximately uniform in the bulk of the fluid and transition to their boundary values occurs in thin boundary layers located close to the two walls. This produces very large local gradient Richardson numbers in the vicinity of the walls. Since in turbulent PCF the energy injection is through the walls and the near-wall region, the large local gradient Richardson number shuts down the energy pathway into the bulk of the fluid. The problem of high bulk Richardson number in the near-wall region is eliminated by considering no flux rather than fixed density boundary conditions at the two walls, but then the asymptotic state of the system has a completely well-mixed density field across the whole of the channel and so the density field ceases to play a role in the dynamics, leaving us with the more familiar unstratified PCF. The problem of sustaining turbulent dynamics in vertically sheared PCF is essentially one of boundary conditions, and perhaps a more natural flow to consider for vertically sheared stratified flow would be one of an unbounded shear.

In contrast, horizontally sheared stratifications often have an attracting turbulent state for bulk Richardson numbers much larger than vertically sheared counterparts. Physically, to induce turbulence in vertically sheared stratified flow, the shear must induce overturning in the direction of gravity, which has an associated energetic cost due to the inhibition of vertical motions by the stratification. In

horizontally sheared stratified flow, the shear is able to rearrange the density field on a horizontal plane without an associated energetic cost arising from the density field. Such two-dimensional motions can become quite energetic and themselves induce small vertical variations. These vertical variations can in turn be rearranged on a horizontal plane without an associated energetic cost, and statically unstable gradients in the density field can spontaneously arise. If the stratification is strong enough, these statically unstable gradients can overturn themselves, leading to sustained turbulent dynamics.

In addition to this physically motivated reasoning, there are additional considerations in the dynamics of horizontally sheared stratified flow. For example, there is the recently discovered zigzag instability of a co-rotating vertical vortex pair in a stratified fluid (see Billant & Chomaz, 2000; Otheguy *et al.*, 2007; Deloncle *et al.*, 2008), whose physical mechanism in its nonlinear evolution is precisely that of horizontal rearrangement of the density field to create statically unstable density gradients which overturn. However this instability requires the formation of such a vortex pair and so although the minimal seed trajectories may make use of this mechanism, it does not provide a linear instability for the base flow.

Another observed mechanism in horizontally sheared stratified flows is that of the spontaneous formation of layers in the density field. For example, Oglethorpe *et al.* (2013) observes that in stratified Taylor–Couette flow, the flow of a stratified fluid between two vertically aligned, concentric, counter-rotating cylinders, an initially linearly stratified fluid spontaneously develops layers in the density field. The resulting flow consists of well-mixed layers of near uniform density separated by sharp interfaces in which there is a very rapid change of density with height. The formation of these layers, in particular their characteristic height $0.2U/N$ where U is the forcing velocity scale and N is the buoyancy frequency, is a robust process. The local sharpening of density gradients to form layers is to be expected if the density flux in the system decreases with increasing stratification strength, as demonstrated by Phillips (1972). If the flow of interest is such that the density flux decreases with increasing stratification strength, then the formation of well-mixed layers is likely to assist in sustaining turbulence, but it is not yet clear by precisely what mechanism the density interfaces in the experiments of Oglethorpe *et al.* (2013) remain sharp and robust.

Preliminary results of the laddering down procedure with the DAL method suggest that for $Ri_B \geq 0.1$ the minimal seed trajectories induce spontaneous layer formation. However, these initial conditions require target times of $T \gtrsim 1000$ to transition to turbulence. In addition, large bulk Richardson numbers provide an additional constraint on the allowable time-step in the numerical integration code. For these reasons, we have been unable to converge to minimal seeds for bulk Richardson numbers $Ri_B \geq 0.1$, although we have attempted to do so for $Ri_B = 0.1$, 0.2, 0.25 and 0.3. This is primarily due to a lack of sufficient computational resources resulting in the laddering down procedure being infeasible over any reasonable time-scale.

In the next section we discuss the minimal seeds that we were able to converge adequately, namely the same parameter values in the same two geometries as the vertically sheared minimal seeds presented in Chapter 3.

6.2 Horizontally sheared minimal seeds

Using the laddering down procedure we have identified the minimal seeds for turbulence in horizontally sheared stratified PCF for $Re = 1000$ and $Pr = 1$ in the narrow geometry N with dimensions $13.66 \times 2 \times 3.31$ for bulk Richardson numbers $Ri_B = 10^{-4}$, 10^{-3}, 3×10^{-3} and 10^{-2} and in the wide geometry W with dimensions $13.66 \times 2 \times 6.62$ for bulk Richardson numbers $Ri_B = 3 \times 10^{-3}$ and 10^{-2}. Table 6.1 shows the calculated range for the critical initial energy density E_c for each set of parameters.

An immediate observation is that for these bulk Richardson numbers, E_c is higher for horizontally sheared than for vertically sheared minimal seeds, with the difference between the values of E_c increasing with bulk Richardson number. The reason for this appears to be dependent on the initial stage of evolution during which the precise value of E_c has most impact on the flow trajectory. For both vertically and horizontally sheared minimal seeds, the initial stage of evolution follows that of the unstratified minimal seeds for which a localised patch of flow structures aligned against the mean shear are tilted over by the mean shear and extract energy from the base flow via the Orr mechanism. For all of the vertically sheared minimal seeds, the density field of the initial condition is arranged in

Ri_B	E_c (N)	E_c (W)
0	$2.225 \times 10^{-6} < E_c < 2.250 \times 10^{-6}$	$8.925 \times 10^{-7} < E_c < 8.950 \times 10^{-7}$
10^{-4}	$2.275 \times 10^{-6} < E_c < 2.300 \times 10^{-6}$	N/A
10^{-3}	$2.800 \times 10^{-6} < E_c < 2.825 \times 10^{-6}$	N/A
3×10^{-3}	$4.250 \times 10^{-6} < E_c < 4.275 \times 10^{-6}$	$1.875 \times 10^{-6} < E_c < 1.900 \times 10^{-6}$
10^{-2}	$6.750 \times 10^{-6} < E_c < 6.775 \times 10^{-6}$	$2.950 \times 10^{-6} < E_c < 2.975 \times 10^{-6}$

Table 6.1: Values of the critical energy density E_c, the energy of the minimal seed, for various bulk Richardson numbers Ri_B in the two geometries N and W. The upper bound corresponds to the flow evolutions shown in subsequent figures. The lower bound corresponds to an E_0 at which a turbulent state cannot be attained.

such a way that the shear-based tilting of flow structures is enhanced in the wall-normal direction by a transfer of energy from available potential energy in the density field to kinetic energy due to gravity. The density field essentially provides an initial 'kick' to the flow in a direction that is useful for the Orr mechanism. In contrast, for the horizontally sheared minimal seeds, the direction of gravity is perpendicular to the plane in which the Orr mechanism occurs and so there can be no such enhancement by the density field in the initial stages. This manifests itself through the requirement for slightly larger initial energy densities for the minimal seeds.

We now discuss the trajectories of the minimal seeds case-by-case.

6.2.1 Geometry N

Figure 6.1 shows the evolution in time of the total perturbation energy density $E(t)$ for each of the minimal seed trajectories in the narrow geometry N. For comparison, we also plot the result for the unstratified minimal seed. Once more we see that for most bulk Richardson numbers the energy increases rapidly in the initial evolution, plateaus for a substantial period, and eventually increases rapidly once more during the final transition to turbulence. The notable exception to this is the evolution for bulk Richardson number $Ri_B = 10^{-2}$ for which the total energy increases well beyond the initial evolution for the other parameter

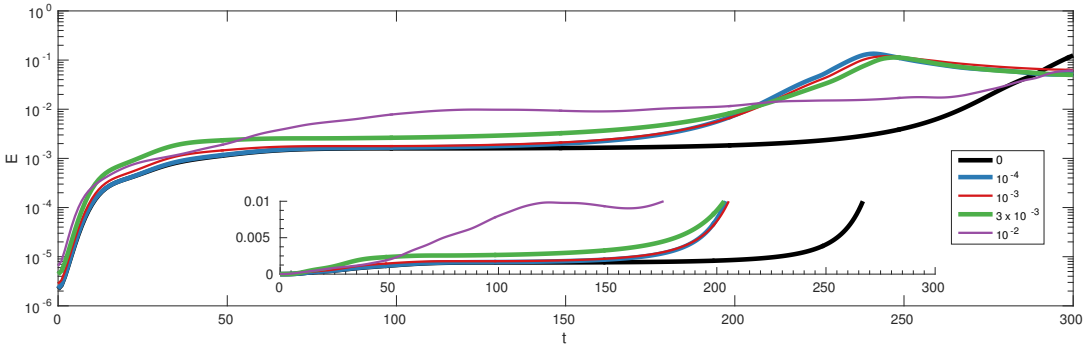

Figure 6.1: Time variation of energy density $E(t)$ as defined in (3.12) for the minimal seed trajectories in geometry N for $Ri_B = 0$, black, 10^{-4}, red, 10^{-3}, blue, 3×10^{-3}, green and 10^{-2}, purple.

values. The energy levels off at around $t = 120$, but instead of reaching a plateau it oscillates with a large period, before eventually transitioning to turbulence.

Figures 6.2, 6.3 and 6.4 show isosurfaces of perturbation streamwise velocity $u = \pm 0.6 \max(u)$ for each minimal seed trajectory at times $t = 0$ and 35, $t = 70$ and 150 and $t = 210$ and 280 respectively. We see once more that the two cases with smallest bulk Richardson number, $Ri_B = 10^{-4}$ and 10^{-3} are little affected by the stratification, and the flow evolution is extremely similar to the vertically sheared case discussed in Chapter 3.

The minimal seed trajectory for bulk Richardson number $Ri_B = 3 \times 10^{-3}$ differs slightly from the vertically sheared result, although the initial condition and its initial evolution are unchanged. The initial condition consists once more of a localised patch of flow structures aligned against the mean shear which unwrap via the Orr mechanism into an array of streamwise aligned structures with a distinct oblique component. However, the trajectory does not then use oblique wave mechanism to produce transient streamwise independent streaks. Instead, there is a rapid symmetry breaking in the spanwise direction that interrupts this process, and the flow quickly relaxes onto a long-lived coherent state that is evident in the fourth column of Figure 6.3.

The left-hand side of the domains in the fourth column of Figure 6.3 show a flow structure that is very similar to the coherent state visited by the vertically sheared minimal seed, shown in the fourth column of Figure 3.3. The flow structure in the right-hand side of the domains for the vertically sheared minimal seed

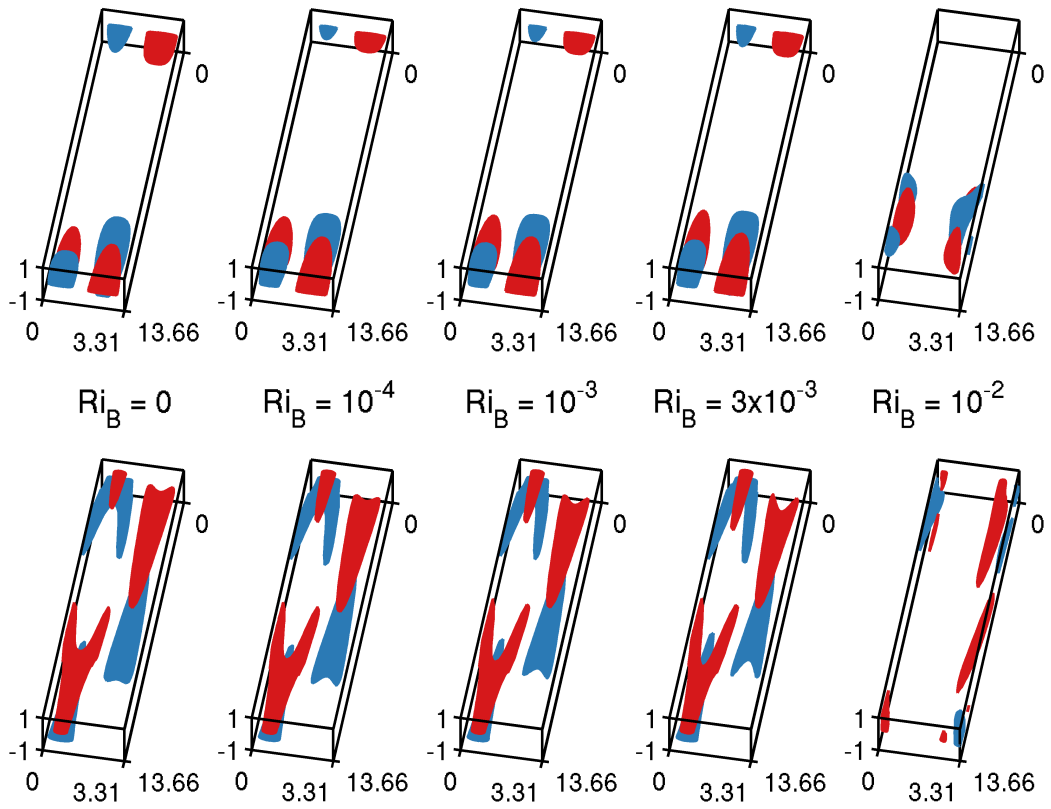

Figure 6.2: Isosurfaces of streamwise perturbation velocity $u = \pm 0.6 \max(u)$ at $t = 0$ (top row) and $t = 25$ (bottom row) for the minimal seed trajectories in geometry N for $Ri_B = 0$, 10^{-4}, 10^{-3}, 3×10^{-3}, and 10^{-2}, from left to right.

appears to be a streamwise shifted version of the left-hand side. In contrast, the right-hand side of the domains for the horizontally sheared minimal seed shown in the fourth column of Figure 6.3 contains a distinctly different flow structure than the left-hand side, although there is still an obvious oblique component to it, and the structure is not dissimilar to other oblique structures visited by this family of minimal seeds. The final transition to the turbulent state is very similar to the vertically sheared minimal seed and to the minimal seeds with smaller bulk Richardson numbers. We conclude that *in this geometry*, the main effect of changing from vertically sheared to horizontally sheared flow on the minimal seed trajectory for $Ri_B = 3 \times 10^{-3}$ is to introduce a spanwise quantisation on the admissible coherent structures.

In contrast, the minimal seed trajectory for the largest bulk Richardson number

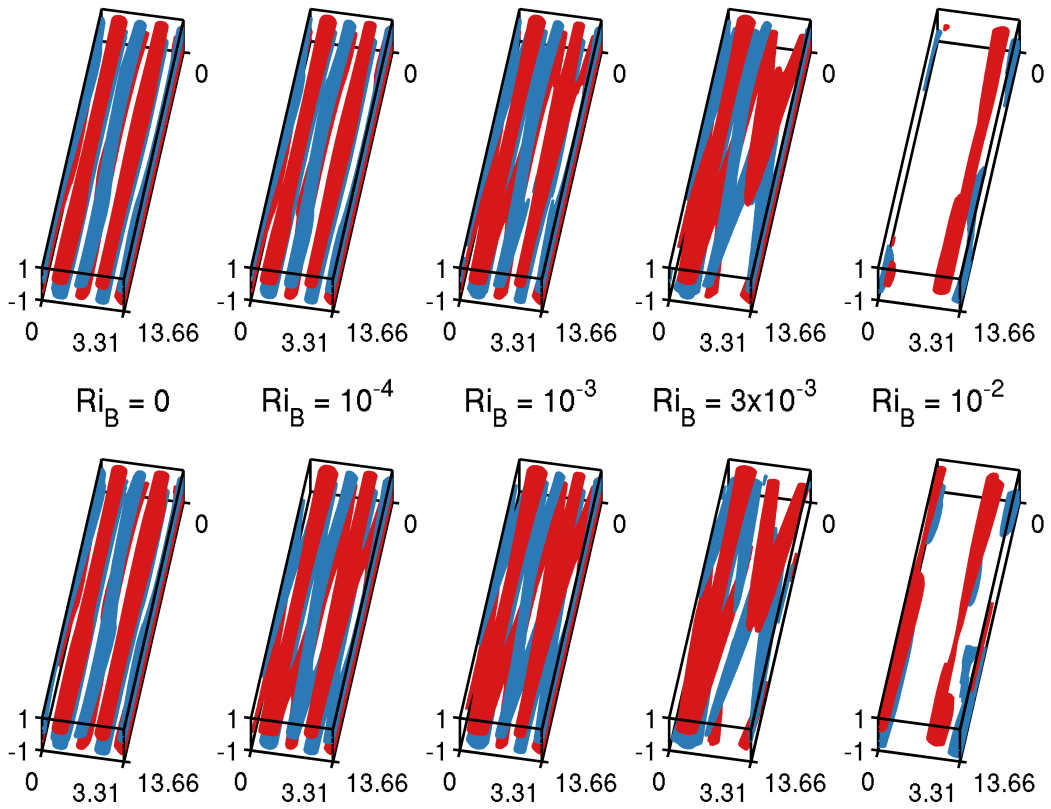

Figure 6.3: Isosurfaces of streamwise perturbation velocity $u = \pm 0.6 \max(u)$ at $t = 70$ (top row) and $t = 150$ (bottom row) for the minimal seed trajectories in geometry N for $Ri_B = 0$, 10^{-4}, 10^{-3}, 3×10^{-3}, and 10^{-2}, from left to right.

considered here, $Ri_B = 10^{-2}$ is very different to its vertically sheared counterpart. The initial condition and its whole trajectory show signs of spanwise localisation, which until now has not been seen in this narrow geometry. The initial condition consists of a spanwise localised patch of flow structures aligned against the mean shear which unwrap via the Orr mechanism onto an elongated set of streamwise aligned oblique structures. From this point the trajectory is chaotic, but more structured than the vertically sheared minimal seed. The set of streamwise aligned oblique structures are advected by a streamwise travelling wave whilst the oblique wave mechanism transfers their energy into a small number of streamwise aligned, nearly streamwise independent streaks. Defects on these streaks continue to be advected in the streamwise direction. Additional streaks appear and existing streaks are lost, strengthen and weaken, apparently chaotically but reasonably slowly, over

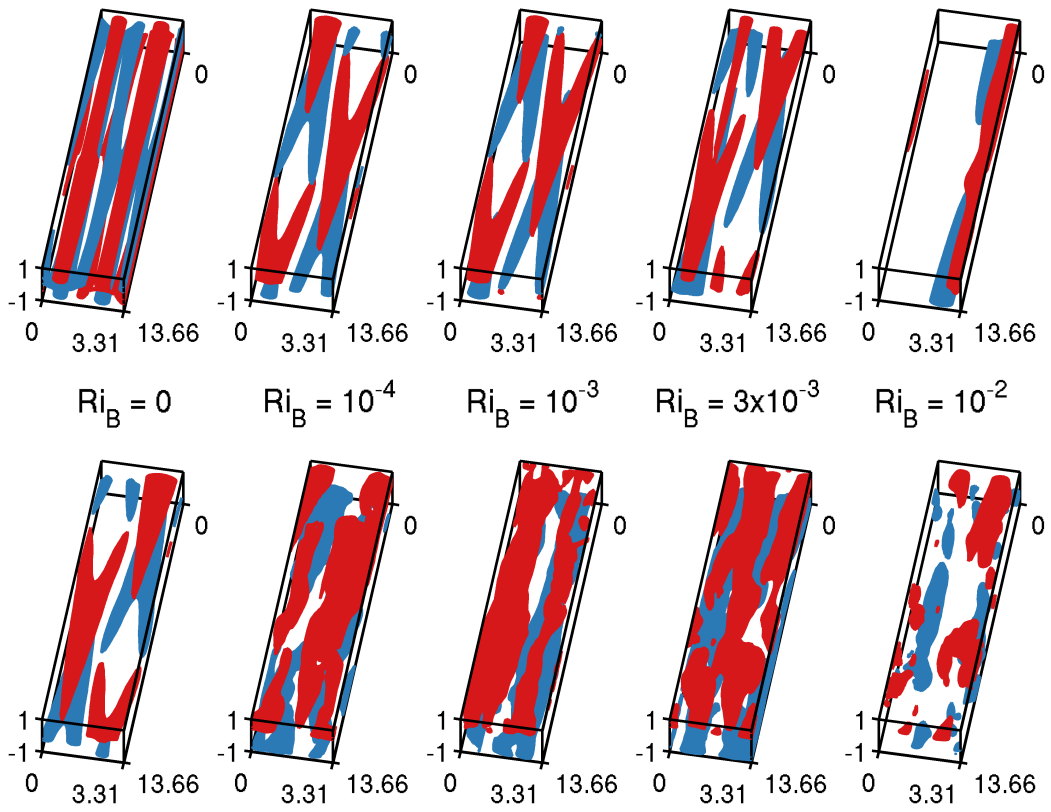

Figure 6.4: Isosurfaces of streamwise perturbation velocity $u = \pm 0.6 \max(u)$ at $t = 210$ (top row) and $t = 280$ (bottom row) for the minimal seed trajectories in geometry N for $Ri_B = 0$, 10^{-4}, 10^{-3}, 3×10^{-3}, and 10^{-2}, from left to right.

time scales comparable to those expected from the oscillations due to the buoyancy frequency $N = \sqrt{Ri_B}$.

It appears that horizontally sheared stratified PCF, for sufficiently large bulk Richardson numbers Ri_B has coherent states that are linked with the self-sustaining process of Waleffe (1997) and the vortex-wave interaction states of Hall & Sherwin (2010), unlike vertically sheared stratified PCF where this process is completely disrupted. There is a clear preference for nearly streamwise independent streaks, although these streaks must now oscillate in time. This observation should be compared to the calculations of Chapter 5 in which oscillating roll solutions were found for vertically sheared stratified SSP. It is conceivable that equivalent calculations for horizontally sheared stratified SSP would also reveal oscillating solutions at large enough bulk Richardson number.

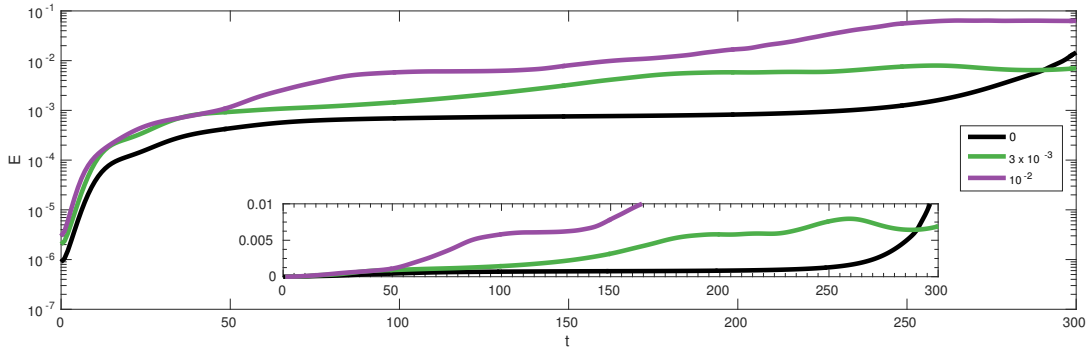

Figure 6.5: Time variation of energy density $E(t)$ as defined in (3.12) for the minimal seed trajectories in geometry W for $Ri_B = 0$, black, 3×10^{-3}, green, and 10^{-2}, purple.

6.2.2 Geometry W

Figure 6.5 shows the evolution in time of the total perturbation energy density $E(t)$ for each of the minimal seed trajectories in the wide geometry W. For comparison, we also plot the result for the unstratified minimal seed. For these two minimal seeds we were required to extend the target time in the DAL method to $T = 400$. We see that for both $Ri_B = 3 \times 10^{-3}$ and 10^{-2} the total energy increases well beyond the initial evolution for the unstratified case. In both cases the energy levels off slightly, but instead of reaching a plateau it oscillates with a large period, before eventually transitioning to turbulence.

Figures 6.6, 6.7 and 6.8 show isosurfaces of perturbation streamwise velocity $u = \pm 0.6 \max(u)$ for each minimal seed trajectory at times $t = 0$ and 35, $t = 70$ and 150 and $t = 210$ and 280 respectively. For both bulk Richardson numbers $Ri_B = 3 \times 10^{-3}$ and 10^{-2} the initial condition and initial evolution of the minimal seeds are very similar to the vertically sheared minimal seeds in Chapter 3, as shown by the similarity of the plots in Figures 6.6 and 3.6. After the initial period of tilting by the Orr mechanism, both stratified trajectories use the oblique wave mechanism to form streamwise aligned nearly streamwise independent streaks. These streaks are then maintained for a long period, changing slowly but chaotically in time.

The minimal seed trajectory for bulk Richardson number $Ri_B = 3 \times 10^{-3}$ contains a single slow speed streak flanked by a pair of high speed streaks. The

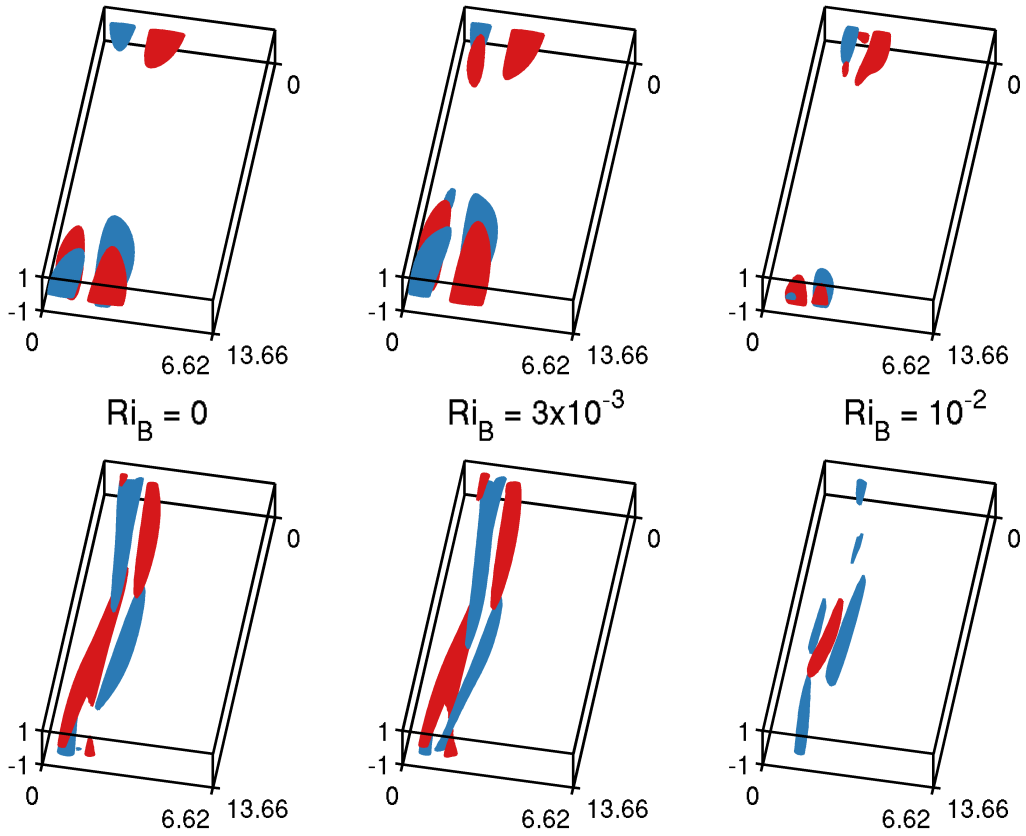

Figure 6.6: Isosurfaces of streamwise perturbation velocity $u = \pm 0.6 \max(u)$ at $t = 0$ (top row) and $t = 25$ (bottom row) for the minimal seed trajectories in geometry W for $Ri_B = 0$, 3×10^{-3}, and 10^{-2}, from left to right.

two outer high speed streaks remain nearly streamwise independent throughout, and only briefly weaken to the state seen in the top row of Figure 6.8 before re-emerging to the form seen in the bottom rows of Figures 6.7 and 6.8. Meanwhile, the inner slow speed streak does not remain nearly streamwise independent but instead oscillates during much of its evolution as a spanwise wave travels in the streamwise direction. For this case, turbulence is observed at $t \approx 325$ and so the flow is still very structured in the bottom of Figure 6.8.

In the minimal seed trajectory for bulk Richardson number $Ri_B = 10^{-2}$ the role of the low and high speed streaks are reversed. Much of the evolution has a single high speed streak flanked by a pair of low speed streaks. The streamwise

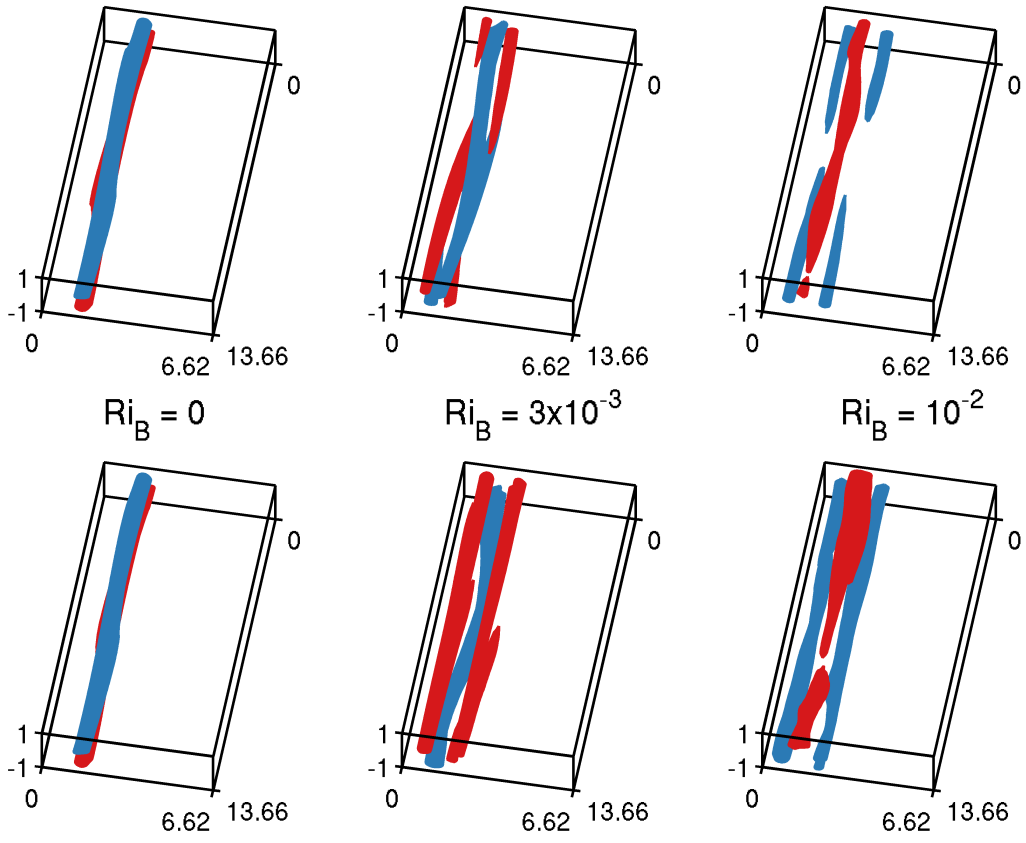

Figure 6.7: Isosurfaces of streamwise perturbation velocity $u = \pm 0.6 \max(u)$ at $t = 70$ (top row) and $t = 150$ (bottom row) for the minimal seed trajectories in geometry W for $Ri_B = 0$, 3×10^{-3}, and 10^{-2}, from left to right.

modulation of these streaks is much more complicated than for the smaller bulk Richardson number, and there is not such an obvious travelling wave on the inner streak, but the essential dynamics appear to be very similar to that for $Ri_B = 3 \times 10^{-3}$.

The two main conclusions from this pair of minimal seed trajectories are firstly that the larger spanwise dimension provided by the wide geometry W is necessary to observe the 'correct' dynamics for the intermediate bulk Richardson number $Ri_B = 3 \times 10^{-3}$. The result for geometry N clearly showed an asymmetry associated with quantisation in the spanwise direction, and the flow structures were mostly oblique, unlike for geometry W. This is to be contrasted with the vertically sheared

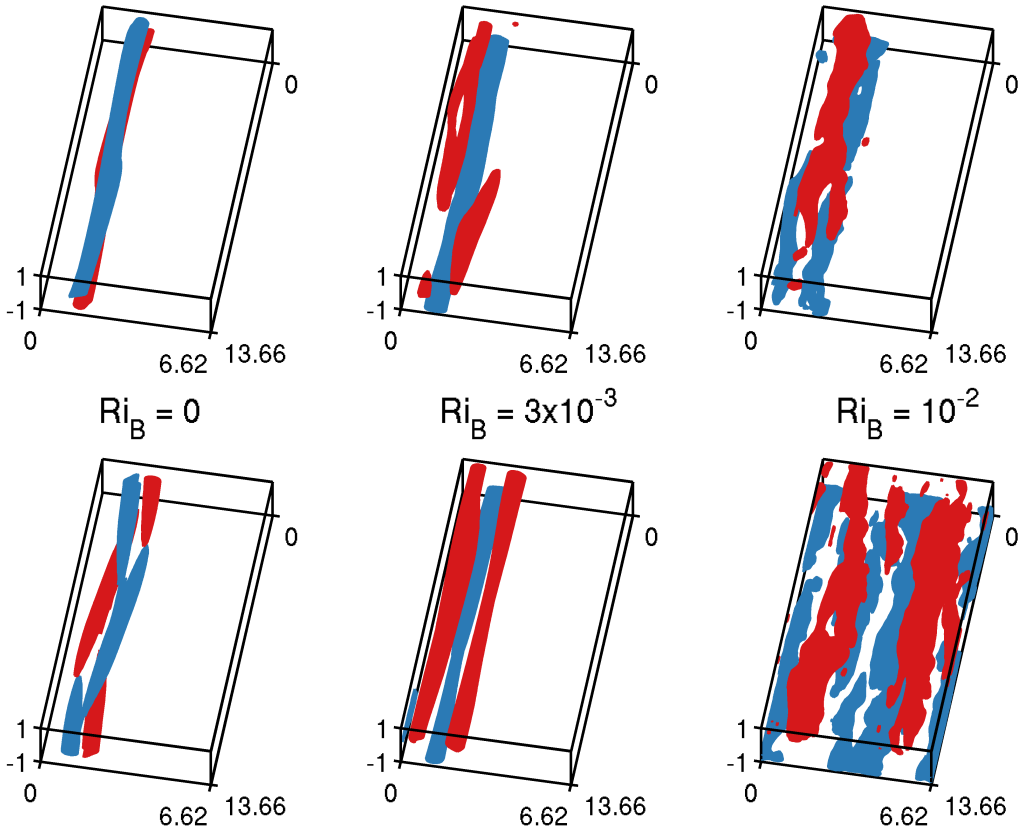

Figure 6.8: Isosurfaces of streamwise perturbation velocity $u = \pm 0.6 \max(u)$ at $t = 210$ (top row) and $t = 280$ (bottom row) for the minimal seed trajectories in geometry W for $Ri_B = 0$, 3×10^{-3}, and 10^{-2}, from left to right.

minimal seeds for which the dynamics in geometry W were clearly just a localised version of those in geometry N.

For vertically sheared stratified PCF there is no inherent natural spanwise lengthscale because all the bulk parameters depend only on quantities that vary in the wall-normal direction. However, in horizontally sheared stratified PCF there is a natural spanwise lengthscale given by $\Delta U/N = 1/\sqrt{Ri_B}$. The asymptotic layer height found in the experiments of Oglethorpe *et al.* (2013) scaled with some small fraction of this value, typically 1/5. Using this approximate scale, we find lengthscales of approximately 3.7 for $Ri_B = 3 \times 10^{-3}$ and 2.0 for $Ri_B = 10^{-2}$. This could explain why geometry N was too narrow for the lower bulk Richardson

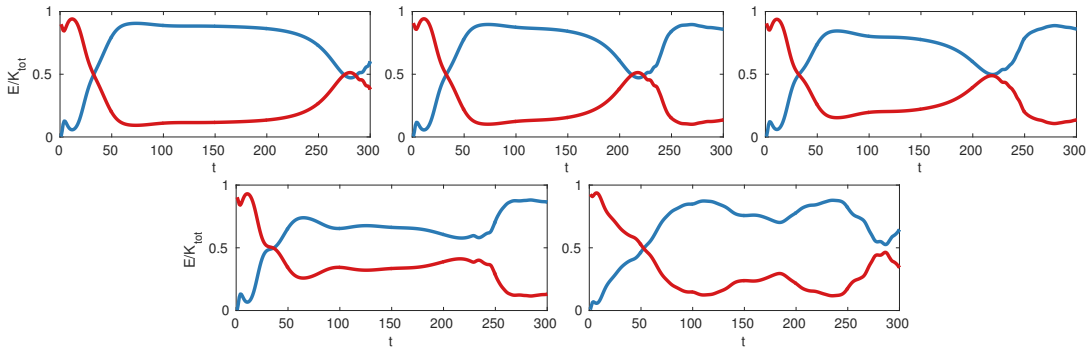

Figure 6.9: Time dependence of normalised streak kinetic energy density K_s/K as defined in (3.15) (plotted with a blue line) and normalised wave kinetic energy density K_w/K as defined in (3.17) (plotted with a red line) for the minimal seed trajectories in geometry N for $Ri_B = 0$ (upper left), 10^{-4} (upper middle), 10^{-3} (upper right), 3×10^{-3} (lower left), 10^{-2} (lower right).

number, but wide enough for the larger bulk Richardson number.

The second conclusion is that horizontally sheared stratified PCF readily admits SSP/VWI type solutions, provided that we allow for a temporal oscillation. We saw in Chapter 5 that temporally oscillating solutions might exist in vertically stratified shear flow, but we were unable to observe them in the minimal seed trajectories. We speculate that carrying over the reasoning of Waleffe (1997) into stratified shear flows is likely to be much more successful in the horizontally sheared case than for the vertically sheared case.

6.3 Rolls, streaks and waves

As for the vertically sheared minimal seeds shown in Chapter 3, we also plot the time evolution of the streak and wave energy components for the horizontally sheared minimal seeds. Figures 6.9 and 6.10 show the evolution of the streak K_s and wave K_w energies defined in (3.15) and (3.17), normalised by the total kinetic energy, for all the minimal seed trajectories in geometry N and W respectively.

For geometry N, the evolution of the energy components for $Ri_B = 0$, 10^{-4}, 10^{-3} and 3×10^{-3} in Figure 6.9 are almost indistinguishable from the equivalent plots for the vertically sheared minimal seeds shown in Figure 3.9. This is expected for the two smallest bulk Richardson numbers $Ri_B = 10^{-4}$ and 10^{-3} since, as noted

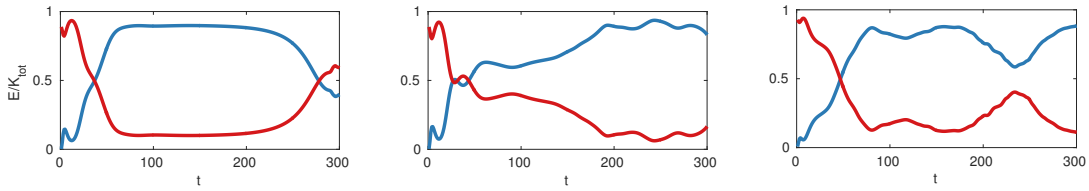

Figure 6.10: Time dependence of normalised streak kinetic energy density K_s/K as defined in (3.15) (plotted with a blue line) and normalised wave kinetic energy density K_w/K as defined in (3.17) (plotted with a red line) for the minimal seed trajectories in geometry W for $Ri_B = 0$ (left), 3×10^{-3} (middle) and 10^{-2} (right)

in Section 6.2, the vertically sheared and horizontally sheared flow trajectories are extremely similar. It is perhaps surprising that the evolutions for $Ri_B = 3 \times 10^{-3}$ are so similar, given that only half the flow domains display similar dynamics. However, this serves to strengthen our assertion that the issue with the horizontally sheared minimal seed in geometry N is primarily one of spanwise quantisation.

The difference between the vertically sheared and horizontally sheared cases in geometry N is clear for the largest bulk Richardson number $Ri_B = 10^{-2}$. During the vertically sheared evolution shown in Figure 3.9, much of the evolution consists of a chaotically oscillating near equipartition of streak and wave energy. For the horizontally sheared case shown in Figure 6.9 we clearly see the signature of the long-lived streaks in the flow shown in Section 6.2, as well as a slow oscillation coupled with a much faster oscillation. Both oscillations are related to the buoyancy frequency $N = \sqrt{Ri_B}$; the time interval between the two maxima of the streak energy is $t_{\text{slow}} \approx 126$, and we have $2t_{\text{buoy}} \equiv 4\pi/N \approx 125.7$. The faster oscillation is given approximately by $t_{\text{fast}} \lesssim t_{\text{buoy}}$.

For geometry W, the evolution of the energy components for both bulk Richardson numbers $Ri_B = 3 \times 10^{-3}$ and 10^{-2} shown in Figure 6.10 differ greatly from the vertically sheared results shown in Figure 3.10. For the larger bulk Richardson number $Ri_B = 10^{-2}$ the evolution is very similar to that for geometry N and so we should interpret it in the same way. This is not surprising since the trajectory in geometry N already displayed signs of spanwise localisation. The only difference is an apparent suppression of the faster time scale.

The evolution for the smaller bulk Richardson number $Ri_B = 3 \times 10^{-2}$ consists of a prolonged period of streak growth up to $t \lesssim 200$, after which an oscillation sets

in before the final transition to turbulence, which we recall occurs for $t \approx 325$. The oscillation is reasonably fast, and the trajectory does not shadow the edge manifold long enough for the identification of any additional longer time scale oscillation. We do not know why the oscillating streamwise streak state takes longer to develop for this bulk Richardson number than for $Ri_B = 10^{-2}$, but believe that once it appears the essential mechanisms involved are essentially the same.

We have demonstrated that for horizontally sheared stratified PCF, coherent states readily organise in a similar manner to SSP/VWI states, provided that we allow for temporal oscillation, and note that equivalent SSP calculations for horizontally sheared solutions to those in Chapter 5 are required if we wish to understand the underlying physical mechanisms. Preliminary investigations along these lines proved difficult due to the importance of the streamwise mean spanwise velocity $\mathcal{W}$ in the horizontally sheared case, which factored out straightforwardly in the vertically sheared case. It is possible to factor out $\mathcal{W}$ and solve only for $\mathcal{V}$ and Θ, but the functional form ansatz for these remaining functions is not obvious.

The equations for $(\mathcal{V}, \mathcal{W}, \Theta)$ in the horizontally sheared case are

$$\frac{\partial \mathcal{V}}{\partial t} + \frac{\partial P}{\partial y} - \frac{1}{Re}\nabla_2^2 \mathcal{V} = 0, \tag{6.16}$$

$$\frac{\partial \mathcal{W}}{\partial t} + \frac{\partial P}{\partial z} - \frac{1}{Re}\nabla_2^2 \mathcal{W} + Ri_B \Theta = 0, \tag{6.17}$$

$$\frac{\partial \mathcal{V}}{\partial y} + \frac{\partial \mathcal{W}}{\partial z} = 0, \tag{6.18}$$

$$\frac{\partial \Theta}{\partial t} - \mathcal{W} - \frac{1}{RePr}\nabla_2^2 \Theta = 0, \tag{6.19}$$

with boundary conditions $[\mathcal{V}, \mathcal{W}, \Theta](\pm 1) = 0$. We may choose the functional forms $(\mathcal{V}, \mathcal{W}, \Theta) = (\hat{V}(y)\cos kz, \hat{W}(y)\sin kz, \hat{\Theta}(y)\sin kz)\exp(-\lambda^2 t/Re)$ to reduce the equations (6.16 – 6.19) to the pair

$$(D^2 - k^2)(D^2 - k^2 + \lambda^2)\hat{V} = -ReRi_B k D\hat{\Theta}, \tag{6.20}$$

$$(D^2 - k^2 + Pr\lambda^2)\hat{\Theta} = \frac{RePr}{k} D\hat{V}, \tag{6.21}$$

with boundary conditions $[\hat{V}, D\hat{V}, \hat{\Theta}](\pm 1) = 0$, where $D \equiv \mathrm{d}/\mathrm{d}y$. We can further combine (6.20 – 6.21) into a single equation for $\hat{V}$,

$$(D^2 - k^2)(D^2 - k^2 + \lambda^2)(D^2 - k^2 + Pr\lambda^2)\hat{V} = RaD^2\hat{V}, \tag{6.22}$$

where $Ra = Re^2(-Ri_B)Pr$ is the Rayleigh number. We can contrast this equation for $\hat{V}$ with the equivalent equation (5.25) obtained for the vertically sheared case. The only difference between the two equations is that $-k^2$ in the right-hand side of (5.25) has been replaced here by D^2 in (6.22). In particular, this implies that for the horizontally sheared case, solutions with $k = 0$ are not inherently connected with unstratified solutions (which have $Ra = 0$), unlike for the vertically sheared case; a continuation of solutions using AUTO07p is in principle still possible, but there is a greater risk of missing important features of the solutions due to this added degree of freedom in its initialisation.

Unfortunately, we have been unable thus far to find an appropriate ansatz for $(\hat{V}, \hat{\Theta})$ that solves (6.20 – 6.21) and the boundary conditions, and is consistent with the unstratified limit. Since (6.20 – 6.21) imply that $D\hat{V}$ and $\hat{\Theta}$ must have the same functional form, it seems natural to choose a functional form for $D\hat{V}$ and $\hat{\Theta}$ that automatically satisfies the boundary conditions, and then to enforce boundary conditions on $\hat{V}$ to obtain the dispersion relation for $\lambda(k)$; at this preliminary stage it is not clear where this method breaks down.

6.4 Spontaneous layer formation

Before concluding this chapter, we discuss briefly the results of searching for minimal seeds at higher bulk Richardson numbers. We invested heavily in the search for minimal seeds at $Ri_B = 0.1$, 0.2, 0.25 and 0.3 in both geometry N and geometry W. A turbulent state exists for each of these parameter values, and hence a minimal seed, but the laddering down process proved too costly numerically. As mentioned in the introduction to this chapter, there is an additional time-step constraint associated with the buoyancy frequency $N = \sqrt{Ri_B}$ which dominates at these parameter values.

In addition, the dynamics of the minimal seed trajectories cause the trajectories to require target times up to $T = 1200$ in order to identify transition to turbulence. To demonstrate this change in dynamics, we discuss here the initial condition identified by the DAL procedure in geometry N for bulk Richardson number $Ri_B = 0.1$ at initial energy density $E_0 = 9.2 \times 10^{-6}$ and target time $T = 1200$. This initial condition is *not* the minimal seed for turbulence, but we believe that it is fairly

nearby to the minimal seed in state space. We will call it a 'turbulent seed'. We did not find turbulence at $E_0 = 9.15 \times 10^{-6}$ after four iterations of the DAL loop, each loop taking approximately 36 hours, at which point we decided to abandon our search for additional horizontally sheared minimal seeds.

The top panel in Figure 6.11 shows the evolution of the total energy density $E(t)$ along with the kinetic energy density $K(t)$ and potential energy density $P(t)$ components defined in (3.12) for the turbulent seed. We see that after an initial phase in which the kinetic energy dominates, the potential energy accounts for most of the total energy from $t \approx 35$ until $t \approx 1100$. During this period of potential energy dominance, the kinetic energy essentially hibernates. The kinetic energy oscillates about very small values from $t \approx 100$ until $t \approx 400$ after which it gradually increases until it is comparable with the potential energy at $t \approx 1100$. The time period of the oscillations is approximately 30 and the buoyancy period is $2\pi/N = 2\pi/\sqrt{Ri_B} \approx 20$. This suggests the presence of internal gravity waves with wavevector at an angle $\theta \approx 48.5°$ to the vertical spanwise direction. After $t \approx 1100$ the flow is chaotic and the two energy components both contribute to the dynamics. The final asymptotic turbulent state is reached at $t \approx 1700$.

The bottom panel in Figure 6.11 shows the time evolution of the roll, streak and wave components of the kinetic energy defined in (3.14), (3.15) and (3.17), normalised by the total kinetic energy. We see that during the oscillatory phase $100 \lesssim t \lesssim 400$ the oscillations are caused by a competition between the rolls and the streaks, which are out of phase with each other. A near equilibrium is sustained for $600 \lesssim t \lesssim 1100$. For $t \gtrsim 1100$, when the kinetic energy is comparable to the potential energy, the evolution becomes chaotic. Meanwhile, the wave energy is negligible for $100 \lesssim t \lesssim 1700$ and is in fact less than machine precision for $400 \lesssim t \lesssim 1600$, indicating that the velocity dynamics are essentially two-dimensional. The wave energy becomes comparable to the roll energy once the final asymptotic turbulent state is reached for $t \gtrsim 1700$. This should be contrasted sharply with unstratified SSP for which the attained balance has very small values of the roll energy and larger values of the wave energy.

To demonstrate the two-dimensionality of the velocity dynamics, we plot in Figure 6.12 isosurfaces of perturbation streamwise velocity $u = \pm 0.6 \max(u)$ at times $t = 0$, 20, 80, 200, 900, 1200, 1400 and 1700. The initial condition is a

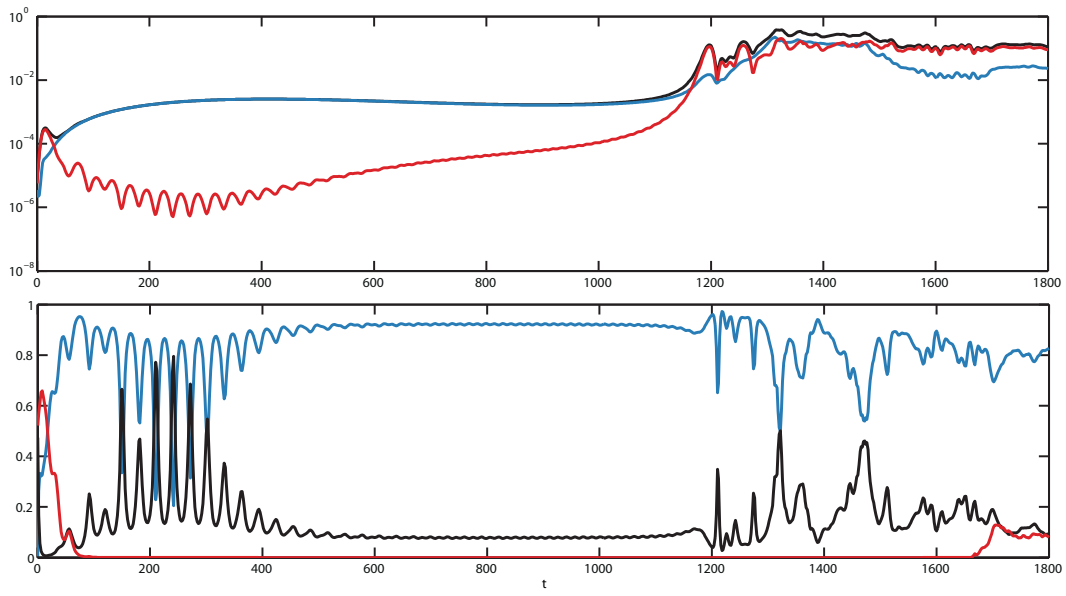

Figure 6.11: Top: Time variation of total energy density $E(t)$ (black), kinetic energy density (red) and potential energy density (blue) as defined in (3.12) for the turbulent seed with $Ri_B = 0.1$ for $E_0 = 9.2 \times 10^{-6}$ in geometry N. Bottom: Time variation of streak kinetic energy K_s/K (blue), wave kinetic energy K_w/K (red) and roll kinetic energy K_r/K (black) as defined in (3.14), (3.15) and (3.17).

spanwise localised patch of flow structures aligned against the mean shear, and its initial evolution once more consists of unwrapping via the Orr mechanism onto a set of streamwise elongated flow structures. At $t = 80$ a pair of streamwise independent streamwise streaks has formed, and by $t = 200$ these streaks fill the whole spanwise extent the domain. Once the streaks are fully formed, they form a spanwise travelling wave for $400 \lesssim t \lesssim 1000$ which has the structure shown at $t = 900$ in Figure 6.12. At $t = 1200$ the streaks are no longer centred about the mid-plane of the channel, but have migrated slightly to each wall. Around $t = 1400$ each wall has streaks of only one sign, and the position of these streaks fluctuates chaotically. We see that the flow has broken down to fully three-dimensional turbulence by $t = 1700$.

Given that for $35 \lesssim t \lesssim 1100$ the flow is dominated by the density field, we now consider its evolution in greater detail. We define the streak potential energy

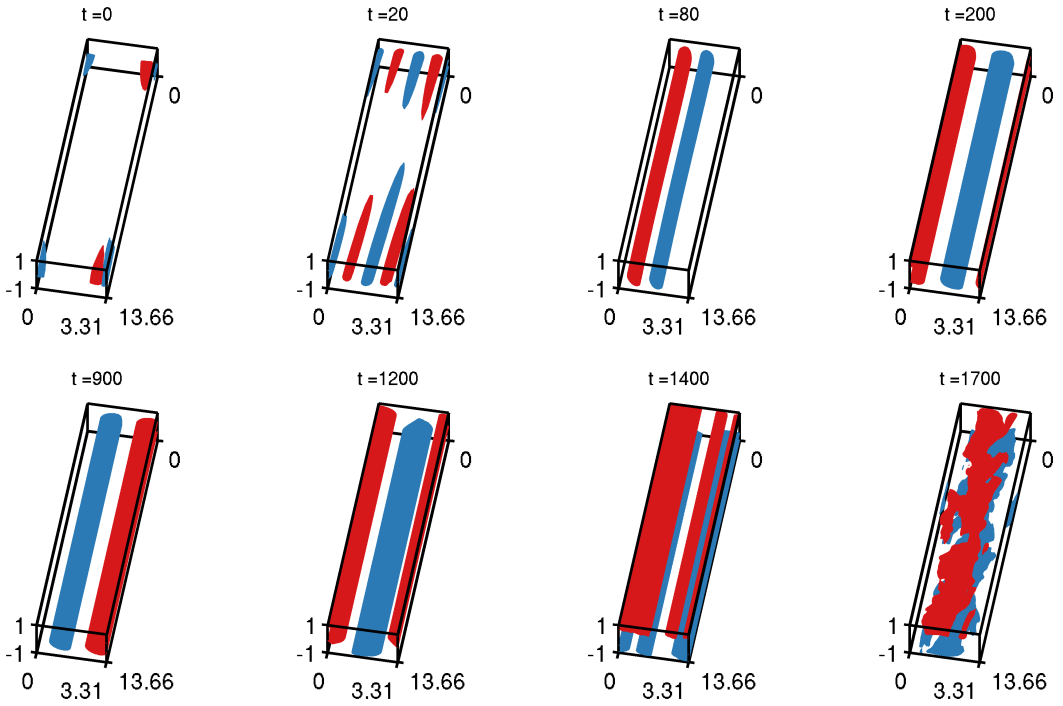

Figure 6.12: Isosurfaces of streamwise perturbation velocity $u = \pm 0.6 \max(u)$ at $t = 0$, 20, 80, 200, 900, 1200, 1400 and 1700 from left to right, top to bottom, for the turbulent seed trajectory in geometry N for $Ri_B = 0.1$.

density P_s and wave potential energy density P_w to be

$$P_s(t) = \frac{1}{2} Ri_B \langle \Theta^2 \rangle_{yz}, \quad P_w(t) = P(t) - P_s(t) = \frac{1}{2} Ri_B \langle \hat{\rho}^2 \rangle_{xyz}, \tag{6.23}$$

where Θ is the streak density and $\hat{\rho}$ is the wave density defined in Chapter 3 and $P(t)$ is the total potential energy density. Subscripts indicate integration in the associated directions, normalised by the corresponding length of the domain. The first plot in Figure 6.13 shows the time evolution of each of these quantities, normalised by $P(t)$. The wave potential energy density is negligible, smaller than machine precision, for $50 \lesssim t \lesssim 1600$, indicating that the density field also has two-dimensional dynamics for much of its evolution, with the onset of three-dimensionality only in the final asymptotic turbulent state.

Figure 6.13 also shows the time evolution of the 'streak-streak' P_{ss} and 'streak-wave' P_{sw} potential energy densities, defined as the the potential energy density of the spanwise average of Θ, and of the remaining density field respectively, so

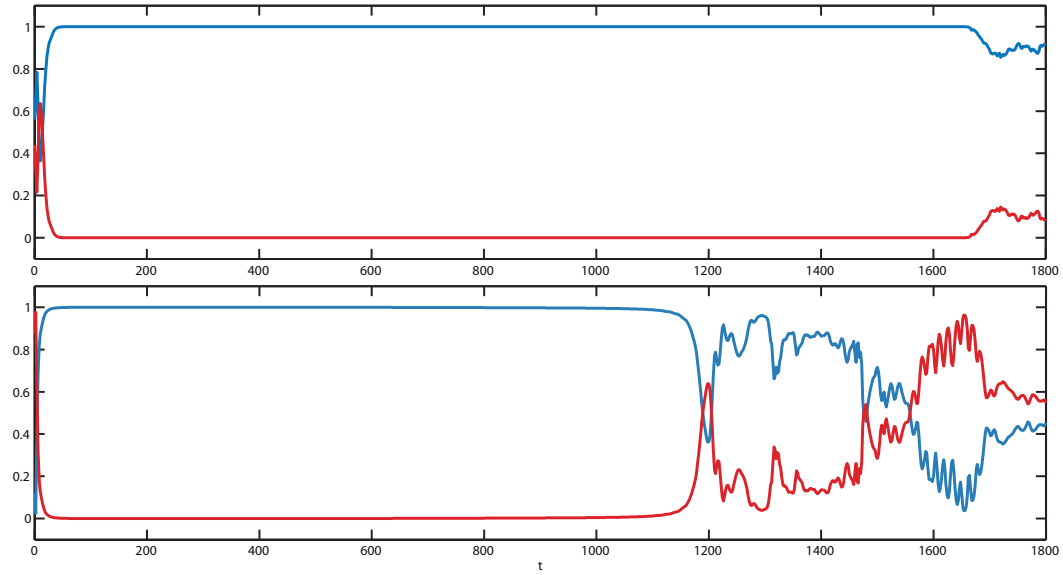

Figure 6.13: Top: Time variation of the streak potential energy P_s/P (blue) as defined in (6.23) and wave potential energy P_w/P (red) where $P_w = P - P_s$. Bottom: Time variation of the spanwise mean streak potential energy P_{ss}/P_s (blue) and the spanwise varying streak potential energy P_{sw}/P_s (red) as defined in (6.24).

that

$$P_{ss}(t) = \frac{1}{2} Ri_B \langle [\langle \Theta \rangle_z]^2 \rangle_y, \quad P_{sw}(t) = P_s(t) - P_{ss}(t). \tag{6.24}$$

Each quantity, normalised by the total streak potential energy density P_s, is plotted in Figure 6.13. For $50 \lesssim t \lesssim 1100$ the streak-wave energy density P_{sw} is very small, though not negligible. P_{sw}/P_s is several orders of magnitude larger than P_w/P, and is never below machine precision, and P_{sw} gradually increases from $t \approx 600$. As we show shortly, the density field is nearly one-dimensional for $50 \lesssim t \lesssim 1100$, but the effect of the streak-wave component P_{sw} is visible throughout. For $t \gtrsim 1100$ the density field becomes fully two-dimensional, and this corresponds to the onset of chaotic two-dimensional evolution of the velocity field. For $1600 \lesssim t \lesssim 1700$ there appears to be a violent event in the density field for which the streak-wave component P_{sw} dominates, and this appears to be the triggering event for transition to the final fully three-dimensional asymptotic turbulent state.

Since the density field is two-dimensional for much of its evolution, we plot in Figure 6.14 the two-dimensional streak density field $\Theta(y, z)$ at times $t = 0$,

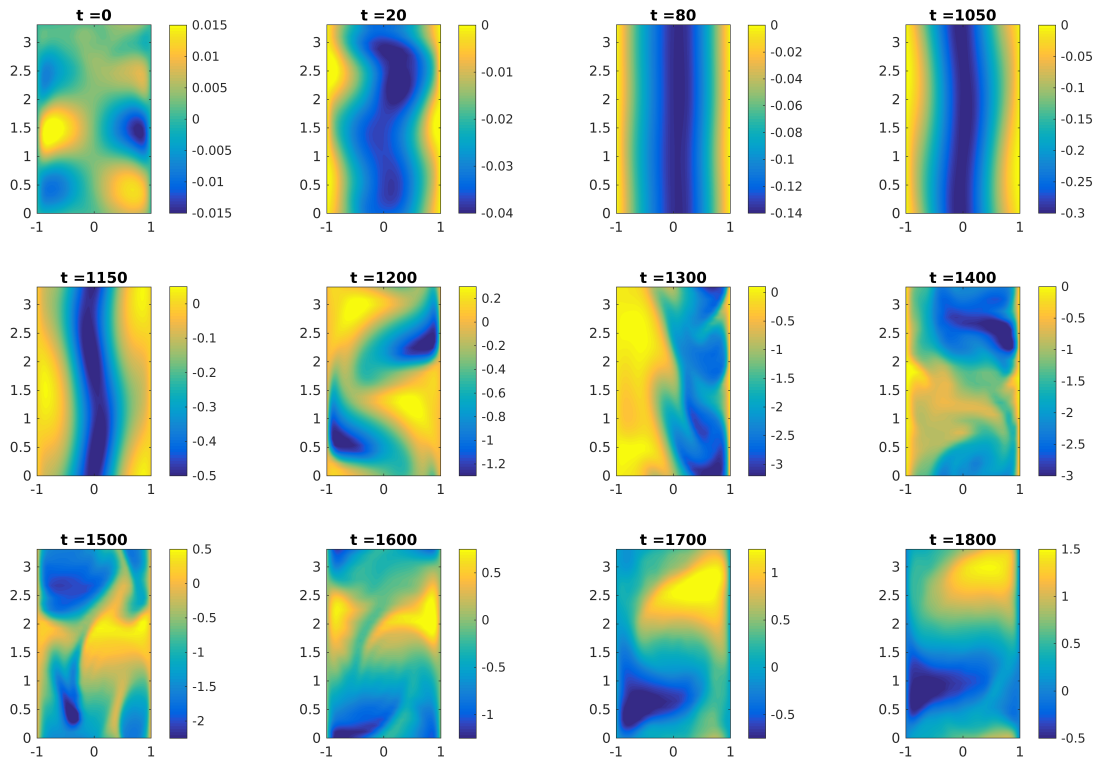

Figure 6.14: Evolution of the streak density $\Theta(y, z)$ with the gravitational direction z vertical and y horizontal at times $t = 0$, 20, 80, 1050, 1150, 1200, 1300, 1400, 1500, 1600, 1700 and 1800 from left to right, top to bottom for the turbulent seed in geometry N at $Ri_B = 0.1$.

20, 80, 1050, 1150, 1200, 1300, 1400, 1500, 1600, 1700 and 1800. The axes are oriented so that gravity acts in the vertical direction on the page. We see that the initial Orr-mechanism phase organises the density field onto a nearly spanwise independent structure by $t = 80$. This consists of a negative density perturbation along the centre of the channel which increases outwards to meet the homogeneous boundary conditions at $y = \pm 1$. This structure has a slight spanwise modulation.

The spanwise modulation moves as a travelling wave in the negative z direction, and its amplitude gradually increases over time, so that the modulation is clear at $t = 1050$. For $1050 \lesssim t \lesssim 1150$ the modulation becomes quite large in amplitude, and positive density perturbations accumulate near each wall. This is likely due to the density boundary condition at each wall allowing a normal flux of density. As the amplitude of the travelling wave increases further, there is a sudden ejection

of the positive perturbation density from the near wall region into the centre of the channel, as seen at $t = 1200$. This ejection disconnects the central region of negative density perturbation and temporarily creates a layered stratification. This state is visited only transiently, and at $t = 1300$ the flow is organised in two vertical streams of fluid, one with positive and one with negative perturbation density.

The flow once more forms a layered stratification by $t = 1400$ via a wall-normal directed ejection of positive perturbation density from one stream and of negative perturbation density from the other stream. This new layered stratification evolves chaotically through to $t \approx 1600$. During $1600 \lesssim t \lesssim 1700$ a three-dimensional instability appears and the flow settles onto its final asymptotic turbulent state, which can be seen at $t = 1700$ and 1800. The streamwise mean density field Θ fluctuates much less rapidly after having settled onto a three-dimensional layered stratification.

The simple nature of the flow throughout much of its evolution, namely the sustained period of one-dimensionality with weak spanwise modulation, suggests that good analytical progress could be made to describe much of its dynamics. Preliminary investigations into the structure of the z-independent SSP equations for horizontally sheared stratified PCF indicate that solutions of the form Θ, $\mathcal{W} \propto \cos \pi y/2$ are admitted. This functional form is a very good match to the spanwise mean of Θ throughout its quasi-one-dimensional evolution.

Eliminating the dependence on z from (6.16 – 6.19) we arrive at

$$\frac{\partial \mathcal{V}}{\partial t} + \frac{\partial P}{\partial y} - \frac{1}{Re}\frac{\partial^2 \mathcal{V}}{\partial y^2} = 0, \tag{6.25}$$

$$\frac{\partial \mathcal{W}}{\partial t} - \frac{1}{Re}\frac{\partial^2 \mathcal{W}}{\partial y^2} + Ri_B \Theta = 0, \tag{6.26}$$

$$\frac{\partial \mathcal{V}}{\partial y} = 0, \tag{6.27}$$

$$\frac{\partial \Theta}{\partial t} - \mathcal{W} - \frac{1}{RePr}\frac{\partial^2 \Theta}{\partial y^2} = 0. \tag{6.28}$$

Then the boundary conditions $\mathcal{V}(y = \pm 1) = 0$ combine with (6.27) to give $\mathcal{V} \equiv 0$, and so $P \equiv 0$ from (6.25). Searching for viscously decaying solutions with $\partial/\partial t =$

$-\lambda^2/Re$ gives

$$(D^2+\lambda^2)(D^2+Pr\lambda^2)\mathcal{W} = Ra\mathcal{W}, \tag{6.29}$$

where $D \equiv \mathrm{d}/\mathrm{d}y$ and $Ra = Re^2(-Ri_B)Pr$ is the Rayleigh number. The boundary conditions for $\mathcal{W}$ are $\mathcal{W}(\pm 1) = 0$ and $[D^2+\lambda^2]\mathcal{W}(\pm 1) = 0$. Equation (6.29) has two families of solutions, a family which is symmetric in y,

$$\mathcal{W} \propto \cos\left(\frac{(2n-1)\pi y}{2}\right),$$

$$\lambda^2 = \frac{1}{2Pr}\left[\frac{(2n-1)^2\pi^2}{4}(1+Pr) \pm \sqrt{\frac{(2n-1)^4\pi^4}{16}(Pr-1)^2 + 4PrRa}\right], \tag{6.30}$$

and a family that is asymmetric in y,

$$\mathcal{W} \propto \sin(n\pi y), \quad \lambda^2 = \frac{1}{2Pr}\left[n^2\pi^2(1+Pr) \pm \sqrt{n^4\pi^4(Pr-1)^2 + 4PrRa}\right], \tag{6.31}$$

where n is an integer. When $Pr = 1$ the solutions for λ^2 simplify to

$$\lambda^2 = \begin{cases} (2n-1)^2\pi^2/4 \pm i\sqrt{-Ra} & \text{if symmetric in } y \\ n^2\pi^2 \pm i\sqrt{-Ra} & \text{if asymmetric in } y \end{cases}. \tag{6.32}$$

For both the symmetric and asymmetric solutions there is predicted to be an oscillation with frequency $\sqrt{-Ra}/Re = \sqrt{Ri_B} = N$. For the parameters of the turbulent seed discussed in this section, this gives a period of oscillation $2\pi/N \approx 20$, and is exactly the period of oscillation observed in the energetics of the velocity field in Figure 6.11 during the early time evolution when the flow is closest to being one-dimensional. This calculation helps justify the claim that the dynamics are quasi-one-dimensional for much of the evolution towards the turbulent state.

6.5 Discussion

We have computed a number of minimal seeds for turbulence in horizontally sheared stratified PCF. In the narrow geometry N we saw that the minimal seeds and their subsequent trajectories are little affected by the change in the gravitational direction for the two smallest bulk Richardson numbers $Ri_B = 10^{-4}$ and 10^{-3}. For $Ri_B = 3\times 10^{-3}$ the visual structures of the minimal seed trajectory are affected by the spanwise quantisation, but the evolution of the streak and wave

velocity components shows that the flow still adheres to the same basic dynamics as the vertically sheared case in Chapter 3. The largest bulk Richardson number $Ri_B = 10^{-2}$ has spanwise localisation even in the narrow geometry N, which might be explained by the presence of a small spanwise length scale $0.2\Delta U/N$ as in Oglethorpe *et al.* (2013). Its subsequent evolution is very different from that in the vertically sheared case, displaying a preference once more for the streamwise streaks and rolls of SSP provided that a temporal oscillation occurs.

In the wide geometry W the dynamics are again fully localised in the spanwise direction, and we see the presence of oscillating streaks and rolls at both bulk Richardson numbers. This suggests that a successful re-examination of the stratified SSP calculations in Chapter 5 for the horizontally sheared case could produce immediately applicable results. In particular, we would like to identify any preferred spanwise, or vertical, wavenumber in the SSP formulation that could help explain the observed length scales in horizontally sheared stratified flow. Unfortunately, a preliminary investigation was unable to solve the horizontally sheared stratified SSP roll equations due to their unusual structure and the associated difficulty in finding an appropriate ansatz.

Finally, we discussed a turbulent seed in the narrow geometry N for bulk Richardson number $Ri_B = 0.1$. We believe that finding *minimal* seeds for $Ri_B \geq 0.1$ is infeasible at present due to the extremely large time horizons required to identify them properly. The turbulent seed discussed here displays surprisingly simple dynamics for much of its evolution, being quasi-one-dimensional, varying significantly only in the wall-normal direction. The velocity field is not important for much of the evolution, but the SSP velocity components showed much larger amplitude rolls than for unstratified SSP. The density field breaks down into layers first in two-dimensions, and only later in three-dimensions, and this spontaneous layering is likely due to the boundary conditions on the density field at the two walls. We believe that a careful analysis of this process is likely to provide a good analytical description of the layering process and the transition to turbulence. A preliminary analysis showed that one-dimensional roll solutions predict an oscillation period that exactly matches that found in the early quasi-one-dimensional energetics of the velocity field.

The overriding theme of this chapter has been the observation that the transi-

tion process in horizontally sheared stratified PCF is in some sense 'simpler' than that for vertically sheared stratified PCF. The flows exhibit reduced dimensionality throughout the transition process, and we speculate that further analytic modelling based upon these observations is likely to be successful and could help predict quantities like the preferred vertical length scales in horizontally sheared stratified flows. The experiments of Oglethorpe *et al.* (2013) demonstrated that spontaneous layering is generic in high Reynolds number, high bulk Richardson number stratified shear flows, but there have not been numerical observations to date. In addition to the spontaneous formation of layers, it is also unknown how such layers remain robust. The argument of Phillips (1972) demonstrates that layers will remain robust if the density flux is a decreasing function of local Richardson number, but we do not know which dynamical structures could be responsible for creating such a functional dependence. Given that a fuller understanding of the dynamics of layered stratified shear flows is needed, we devote the next chapter to an investigation of the linear stability properties and subsequent nonlinear dynamics of layered stratified PCF.

CHAPTER 7

TAYLOR INSTABILITY OF LAYERED SHEAR FLOW

In this chapter we consider the stability properties and nonlinear evolution of two-dimensional PCF for a statically stable Boussinesq three layer fluid of total depth $2H$ between two horizontal plates driven at constant velocity $\pm\Delta U$. Initially the three layers have equal depth $2H/3$ and densities $\rho_0+\Delta\rho$, ρ_0 and $\rho_0-\Delta\rho$, such that $\rho_0 \gg \Delta\rho$. At finite Reynolds and Prandtl number, we demonstrate that this flow is susceptible to distinct primary linear instabilities of the types first considered by Taylor (1931) and Holmboe (1962), provided the bulk Richardson number $Ri_B = g\Delta\rho H/(\rho_0\Delta U^2)$ is sufficiently large. For a given bulk Richardson number Ri_B, the 'Taylor' instability is always predicted to have the largest linear growth rate and to be an inherently two-dimensional instability. For flows with Prandtl number $Pr = 1$, we find that the most unstable Taylor instability, maximised across all choices of wavenumber and Ri_B, has a (linear) growth rate which is a nonmonotonic function of Reynolds number, with a global maximum at $Re = 700$ over 50% larger than the growth rate as $Re \to \infty$.

In a fully nonlinear evolution of the flows with $Re = 700$ and $Pr = 1$ the two interfaces between the three density layers diffuse more rapidly than than the underlying instability can grow from small amplitude. Instead, we investigate numerically the subsequent nonlinear evolution of small amplitude perturbations of the

flow both at $Re = 600$ and $Pr = 300$, which corresponds to the Reynolds number with maximum growth rate at $Pr = 300$, and at the asymptotically large Reynolds number $Re = 5000$ and moderate Prandtl number $Pr = 70$ in two-dimensional domains with streamwise extent equal to two wavelengths of the Taylor instability with the largest growth rate. At both sets of parameter values, the primary Taylor instability undergoes a period of identifiable exponential 'linear' growth. However, we demonstrate that unlike the so-called 'Kelvin–Helmholtz' instability that it superficially resembles the Taylor instability's finite amplitude state of an elliptical vortex in the middle layer appears not to saturate into a quasi-equilibrium state. Instead it is rapidly destroyed by the background shear. The decay process reveals Reynolds number dependent secondary processes associated with the induced baroclinic vorticity on the two strongly perturbed density interfaces. For the lower $Re = 600$ simulation, this decay allows the development to finite amplitude the co-existing primary Holmboe wave instability which has a substantially smaller linear growth rate, consistently with the theoretical predictions of Caulfield (1994), and the experimental observations of Caulfield *et al.* (1995). Conversely, for the higher $Re = 5000$ simulation, the Taylor instability decay induces a non-trivial modification of the mean velocity and density distributions, which then nonlinearly develop into a slow oscillation of finite amplitude Holmboe-type waves, consistently with the previous numerical calculations of Balmforth *et al.* (2012). In both cases, the Holmboe waves appear to be robust in that they saturate nonlinearly. For the higher $Re = 5000$ simulation, the nonlinear Holmboe waves undergo a coarsening process over long time scales.

7.1 Linear stratified shear instabilities

The problem of linear hydrodynamic stability is one of the canonical problems of fluid dynamics, and in particular there has been an enormous amount of research devoted to understanding the interplay between (statically stable) density variations and velocity shear since the seminal work of Helmholtz (1868) and Kelvin (1871) that considered discontinuous distributions of velocity and density. The classical linear stability analysis of a shear layer of finite depth with an inflection point in velocity by Rayleigh (1880) and Fjortoft (1950) has proved very useful

for predicting the wavelength of the most unstable mode of linear theory. Dating at least to the pioneering work of Rosenhead (1931), the finite amplitude form of this so-called 'Kelvin–Helmholtz' instability (KHI) as an array of elliptical vortices 'rolled up' from the initial uniform strip of spanwise vorticity has been very widely observed in numerical simulation (see e.g. Moser & Rogers (1991)), laboratory experiment (Thorpe, 1968) and the environment (see the recent data of Haren *et al.* (2014)). Although the finite amplitude 'billow' is prone to a rich array of secondary instabilities in both unstratified and stratified flows (Caulfield & Peltier, 2000; Arratia *et al.*, 2013; Mashayek & Peltier, 2012*a*,*b*), the observational, numerical and experimental evidence is overwhelming that the finite amplitude billow state is in some sense 'robust', in that a very broad range of initial conditions on an initially uniform shear layer are attracted to and 'saturate' as an array of elliptical billows for a non-trivial period of time.

As demonstrated by Holmboe (1962) and Hazel (1972), a stable density stratification which varies over a length scale comparable to the depth of the shear layer reduces the linear growth rate of the primary KHI, although the effect of stable stratification on the 'zoo' of secondary instabilities and the subsequent dynamics during the transition to turbulence is significantly more subtle (Mashayek & Peltier, 2012*a*,*b*; Mashayek *et al.*, 2013). However, if the density distribution is 'sharp', in that the density distribution varies over a substantially shorter length scale δ than the scale H over which the velocity varies, a qualitatively different linear instability is possible, known as 'Holmboe waves', or the 'Holmboe instability', and first predicted by Holmboe (1962). We will refer to this instability subsequently as the 'Holmboe wave instability' or HWI.

For sharp density distributions, the KHI is still predicted to occur for a range of wavenumbers when the density interface is 'weak', in the sense that the bulk Richardson number Ri_B is sufficiently small, where Ri_B is defined as

$$Ri_B = \frac{g\Delta\rho H}{\rho_0 \Delta U^2}, \tag{7.1}$$

g is the acceleration due to gravity, $\Delta\rho$ is the total density jump across the density interface of depth δ, ρ_0 is a reference density (with $\rho_0 \gg \Delta\rho$ so that the Boussinesq approximation applies, for simplicity), and the velocity difference ΔU occurs over a shear layer with characteristic depth $H \gg \delta$. However, as Ri_B increases, eventually

a bifurcation occurs and the flow becomes unstable (for a range of wavenumbers) to the qualitatively different HWI. Typically there continues to be a range of wavenumbers which are unstable to the HWI for all Ri_B, with the range narrowing and moving to higher mean wavenumber as Ri_B increases.

Also, unlike the KHI, which has a real phase velocity equal to the mean velocity of the shear layer (and hence a critical layer at the mid point of the shear layer) the HWI has a nonzero phase speed, and so has a critical layer between an edge of the shear layer and the relatively sharp density interface. If the flow is symmetric about the mid point of the shear layer, there are two such instabilities with equal growth rates and equal and opposite phase speeds localised above and below the density interface. If the flow is asymmetric, one of the instabilities will dominate, as discussed by Lawrence *et al.* (1991). The finite amplitude manifestation of this instability was observed qualitatively experimentally by Thorpe (1968), and numerically in detail by Smyth *et al.* (1988), and takes the form of propagating vortices localised at the linear instability's critical layer, which induce a cusping of the strong density interface. Unlike the KHI which rolls up and overturns a relatively weak density interface, the HWI merely scours the interface, and so appears to induce less mixing (Smyth & Winters, 2003; Meyer & Linden, 2014). Nevertheless, the HWI may also be thought of as 'robust', in that it has been widely observed experimentally (see for example Zhu & Lawrence (2001); Meyer & Linden (2014)) and numerically (see for example Smyth *et al.* (1988); Carpenter *et al.* (2010)) to survive for a substantial time.

As has been recently reviewed by Carpenter *et al.* (2011) (see also Sutherland (2010)), the physical mechanism underlying these instabilities can be interpreted as arising due to Doppler-shifted interaction between marginally stable waves localized either at the edge of the shear layer, or at the density interface, an interpretation which has been presented by many authors in various contexts (see for example Bretherton (1966), Cairns (1979)). It appears to have originally been proposed by Taylor in his 1915 Adams prize essay entitled 'Turbulent motions in fluids' and reported subsequently in Taylor (1931) along with his derivation of the 'Taylor–Goldstein equation', which describes the linear stability properties of an inviscid stratified shear flow. The equation was independently derived by Goldstein (1931) and Haurwitz (1931) (see Craik (1988) for a fuller discussion).

At the edge of a shear layer, where the spanwise vorticity is varying rapidly, a vorticity wave sometimes referred to as a 'Rayleigh wave' or 'Rossby edge wave' is localised. The KHI may be interpreted as arising from the two vorticity waves at either edge of the shear layer being appropriately Doppler-shifted by the prevailing flow such that they have the same phase speed, thus 'interacting' in the sense described by Carpenter *et al.* (2011). Analogously, the HWI may be interpreted as being an instability which only occurs in the presence of density stratification, as it arises through an interaction between an internal gravity wave on the sharp density interface and one of the vorticity waves at the edge of the shear layer.

However, as noted by Taylor (1931), it is not necessary for stratified shear instabilities to rely on interactions with vorticity waves, or equivalently on the presence of a finite depth shear layer. Taylor considered various scenarios with more than two density interfaces in the presence of uniform shear, and so the unstratified flow is not expected to be linearly unstable. In the simplest case, the density distribution is arranged in three layers, with an intermediate layer of finite depth d between two outer layers. In this case there are two density interfaces on which internal gravity waves can propagate. Due to Doppler-shifting by the background shear, it is then possible for internal waves on the two density interfaces to interact, leading to the prediction of another, inherently stratified instability, with critical layer within the intermediate layer.

When the intermediate layer is actually embedded within a finite depth shear layer, Caulfield (1994) demonstrated that both the Taylor instability and the HWI are predicted to be unstable in different wavenumber bands for a fixed value of Ri_B, with these bands being a function of the ratio d/H of the depth of the intermediate layer to the depth of the shear layer. Caulfield *et al.* (1995) considered such a three layer flow experimentally, and appeared to observe, at least qualitatively, both Taylor instabilities and HWI simultaneously for appropriate values of the ratio d/H. Perhaps to distinguish from other instabilities associated with G. I. Taylor, Carpenter *et al.* (2010) referred to this instability as the 'Taylor–Caulfield' instability, (see also Guha & Lawrence (2014); Heifetz & Mak (2015); Churilov (2016)). Therefore, we will refer to this instability as the TCI. In the experiments of Caulfield *et al.* (1995) it proved challenging to observe the finite amplitude manifestation of the TCI, as it is localised in the intermediate layer, which was

typically intensely dyed. Furthermore, the experimental design was such that the depth of the intermediate layer slowly decreased with time, making it difficult to determine quantitatively the base flow on which the observed structures had been unstable.

Such a multi-layer density distribution was also simulated numerically by Lee & Caulfield (2001) with a steady, two-dimensional base flow, and they made two key observations. Firstly, the finite amplitude manifestation of the primary TCI, although it is inherently a stratified instability and relies completely on the presence of sheared neighbouring density interfaces, bears a superficial resemblance to a KHI in that it takes the form of a connected array of elliptical vortices. Secondly, even in two dimensions at relatively low Reynolds number, they observed that the TCI was prone to strong secondary instabilities due to the intense baroclinic vorticity generation associated with the primary TCI elliptical vortices strongly perturbing the bounding density interfaces.

Such susceptibility to strong secondary instabilities was also observed by Balmforth *et al.* (2012), who considered a reduced, long wave asymptotic 'stratified defect' model to consider the two-dimensional finite amplitude behaviour of such layered stratified shear flows. Instabilities which could be identified as being of TCI type and HWI type grew to finite amplitude using this reduced model, although it is important to remember that the governing equations in this system are not the full Boussinesq Navier–Stokes equations. Nevertheless, Balmforth *et al.* (2012) also noted the interesting and somewhat surprising phenomenon of 'parasitic' secondary HWI, which in certain circumstances appear to destroy the primary TCI relatively rapidly.

These numerical calculations lead to the possibility of an alternative interpretation of the experiments discussed in Caulfield *et al.* (1995). They argued that the observation of TCI and HWI was consistent with the theoretical predictions of Caulfield (1994); i.e. that effectively in some parameter ranges the TCI and the HWI could both grow and saturate as primary instabilities in *parallel*, each localised around a different critical layer. This is somewhat at odds with the conventional argument that it is to be expected experimentally and numerically that the most unstable mode of linear theory will grow to dominate the nonlinear finite amplitude evolution of an unstable flow. However, numerical simulations are typi-

cally constructed with periodic streamwise boundary conditions, thus enforcing a quantisation of accessible streamwise wavenumbers. As demonstrated by Scinocca & Ford (2000), multiple wavenumbers of KHI with slightly different wavenumbers can grow to finite amplitude in sufficiently long computational domains, and so it is at least conceivable that qualitatively different primary instabilities with different growth mechanisms and critical layers can co-exist at finite amplitude when the boundary conditions allow.

The numerical calculations of Lee & Caulfield (2001), however, suggest a note of caution, in that the primary TCI was prone to very strong secondary instabilities, at least some of which could modify the base flow in such a way as to induce the development of secondary HWI in *serial*, consistently with the observations of Balmforth *et al.* (2012).

Taylor (1931) explained the delay in publishing his theoretical predictions at least in part because he was unable to 'undertake experiments designed to verify, or otherwise, the results', thus suggesting that he found it difficult to observe the finite amplitude manifestation of the TCI. There has been renewed interest in the TCI recently because of the formalisation and extension of the wave interaction theory to include transient growth phenomena in the linear regime (Guha & Lawrence, 2014). Furthermore, evidence is mounting that over a wide range of stratified turbulent mixing processes, (see e.g. Brethouwer *et al.* (2007); Oglethorpe *et al.* (2013); Mashayek *et al.* (2013)) layering of the density field is generic. As originally predicted by Phillips (1972) and discussed in Chapter 6, turbulence in a stratified fluid typically leads to the development of relatively deep, relatively well-mixed layers separated by thin interfaces of substantially enhanced density gradient. Such layered density profiles are precisely those which are predicted to be susceptible to the TCI if a larger scale shear is imposed, which is conceivable in the geophysical context.

Therefore, it seems natural to attempt to address three outstanding questions concerning the properties of layered stratified shear flow, and answering these questions is the aim of this chapter. First we wish to determine whether the finite amplitude manifestation of a primary TCI is robust, in the sense that it saturates at a finite amplitude for a sufficiently long time such that its finite amplitude form might possibly be observed in the laboratory or in nature. Secondly, we wish to

investigate whether it is possible to observe two qualitatively different primary instabilities, an observation which would give further weight to the interpretation of the experiments of Caulfield *et al.* (1995) in light of the primary instability argument presented by Caulfield (1994). Finally, we wish to determine if the serial development of secondary HWI does not depend on the reduced stratified defect model developed in Balmforth *et al.* (2012), such that the break down of a TCI as a solution to the full Navier–Stokes equations actually can lead in an inherently secondary fashion to propagating cusped waves characteristic of the HWI.

To address these three questions, we consider the linear stability properties and nonlinear evolution of two-dimensional PCF with an initial three layer density distribution. In PCF, there is no identifiable 'shear layer' with constant velocity outside, nor an inflection point in the velocity profile, and it is well-known (Romanov, 1973) that if the fluid is unstratified, there is no linear instability of this flow for all Reynolds numbers. However, as originally demonstrated by Huppert (1973), statically stable density distributions can actually linearly destabilise this flow. Therefore, this velocity profile is particularly well-suited to investigating the properties of the TCI without the complicating presence of inherently unstratified instabilities such as the KHI. For simplicity, we consider a three layer density distribution where initially the three layers have equal depth $2h/3$ and densities $\rho_0+\Delta\rho$, ρ_0 and $\rho_0-\Delta\rho$, such that $\rho_0 \gg \Delta\rho$, and so the Boussinesq approximation applies.

In Section 7.2, we define the specific characteristics of this flow, particularly clarifying the properties of the interfaces between the three layers, and the appropriate definition of the various nondimensional parameters. In Section 7.3, we perform two linear stability analyses: firstly for the analytically tractable case of an inviscid, non-diffusive, three layer fluid with a discontinuous stratification which is the natural structure to identify the key wave interactions; and secondly for a viscous fluid with a diffusive, smooth density profile. For the discontinuous stratification we identify only primary TCI, while for the finite Reynolds number flows we find both primary TCI and HWI. Interestingly, we find that the existence of different branches of primary TCI has a nonmonotonic dependence on Reynolds number of the global largest linear growth rate, (maximised across all wavenumbers and bulk Richardson numbers).

By application of a theorem originally due to Yih (1955), we can verify that this base flow is nevertheless subject to two-dimensional rather than three-dimensional primary instabilities. Therefore, we restrict our attention here to two-dimensional simulations. Although real flows are of course three-dimensional, the nonlinear evolution of flows susceptible to primary TCI is very poorly understood, not least because the TCI appears to require 'sharp' density interfaces with substantial computational demands associated with, for example, high values of Prandtl and Reynolds number, even in two-dimensional flows.

We devote Section 7.4 to a discussion of two-dimensional nonlinear numerical simulations of this base flow at two sets of parameter values, one corresponding to the global maximum of growth rate for the primary TCI at $Pr = 300$, which occurs at $Re = 600$ and one at appreciably higher Reynolds number, $Re = 5000$ and $Pr = 70$, which serves as an approximation to the $Re \to \infty$ limit. These two simulations have been specifically selected to address our second and third aims. For $Re = 600$ and $Pr = 300$, there is predicted both a primary TCI and a primary HWI with the same wavenumber (but different growth rates and phase speeds) which can in principle co-exist in parallel in the same periodic domain. Conversely, for $Re = 5000$ and $Pr = 70$, only a primary TCI is predicted to occur in the chosen periodic domain, but there is the possibility of substantial modification of the density and velocity distributions, leading potentially to the serial development of secondary HWI as observed by Balmforth *et al.* (2012).

The results at both parameter sets demonstrate conclusively that the primary TCI is not at all robust, and it is not appropriate to consider that this instability 'saturates' (and remains) at finite amplitude for any significant period. As the primary TCI is destroyed by the background shear, strongly Reynolds number dependent secondary processes arise associated with the strong baroclinic generation of vorticity due to the deflection of the density interfaces by the development of the primary TCI. At $Re = 600$, there is clear evidence of the eventual emergence of the primary HWI, whereas at $Re = 5000$, analogously with the stratified defect results of Balmforth *et al.* (2012), the decay of the TCI modifies the horizontally-averaged base flow in a way which is conducive to the secondary development of 'parasitic' HWI. Our simulations thus suggest that in layered flows HWI are highly likely to occur, either as primary or secondary instabilities, and that the TCI is

a very 'fragile' instability, prone to vigorous secondary instabilities, even in two dimensions. We discuss this issue further and draw our conclusions in Section 7.5.

7.2 Flow geometry

We consider a two-dimensional three-layer Boussinesq fluid in a PCF geometry, so that we have background dimensional velocity and density profiles given by

$$\mathbf{U}^*(y^*) = \Delta U y^* \hat{\mathbf{x}}; \quad \bar{\rho}^*(y) = \rho_0 - \Delta\rho \left[\tanh\frac{R}{H}(y^* - H/3) + \tanh\frac{R}{H}(y^* + H/3)\right], \tag{7.2}$$

where $y^* \in [-H, H]$ is the vertical coordinate, and asterisks denote dimensional quantities. The density profile is a smooth transition between the statically stable three layer stratification $\rho_0 - \Delta\rho$, ρ_0 and $\rho_0 + \Delta\rho$, with the sharpness of transition measured by the parameter R. We expect that this base flow will be susceptible to a primary TCI.

We consider two-dimensional perturbations around the base flow, so that the total velocity and density fields are

$$\mathbf{u}^*_{tot} = \mathbf{U}^*(y^*) + \mathbf{u}^*(x^*, y^*, t^*), \ \rho^*_{tot} = \bar{\rho^*}(y^*) + \rho^*(x^*, y^*, t^*), \tag{7.3}$$

with the boundary conditions $\mathbf{u}^* = 0$ and $\rho^* = 0$ at $y^* = \pm H$. Using H, ΔU and $\Delta\rho$ to nondimensionalise, we obtain the following equations of motion for the Boussinesq fluid

$$\frac{\partial \mathbf{u}}{\partial t} + (\mathbf{u} + \mathbf{U}) \cdot \nabla(\mathbf{u} + \mathbf{U}) = -\nabla p - Ri_B \rho \hat{\mathbf{y}} + \frac{1}{Re}\nabla^2 \mathbf{u}, \tag{7.4}$$

$$\frac{\partial \rho}{\partial t} + (\mathbf{u} + \mathbf{U}) \cdot \nabla(\rho + \bar{\rho}) = \frac{1}{RePr}\nabla^2 \rho, \tag{7.5}$$

$$\nabla \cdot \mathbf{u} = 0, \tag{7.6}$$

with boundary conditions

$$\mathbf{u}(y = \pm 1) = 0, \quad \rho(y = \pm 1) = 0, \tag{7.7}$$

where the Reynolds number Re, Prandtl number Pr and bulk Richardson number Ri_B are given by

$$Re = \frac{\Delta U H}{\nu}, \quad Pr = \frac{\nu}{\kappa}, \quad Ri_B = \frac{g\Delta\rho H}{\rho_0 \Delta U^2}. \tag{7.8}$$

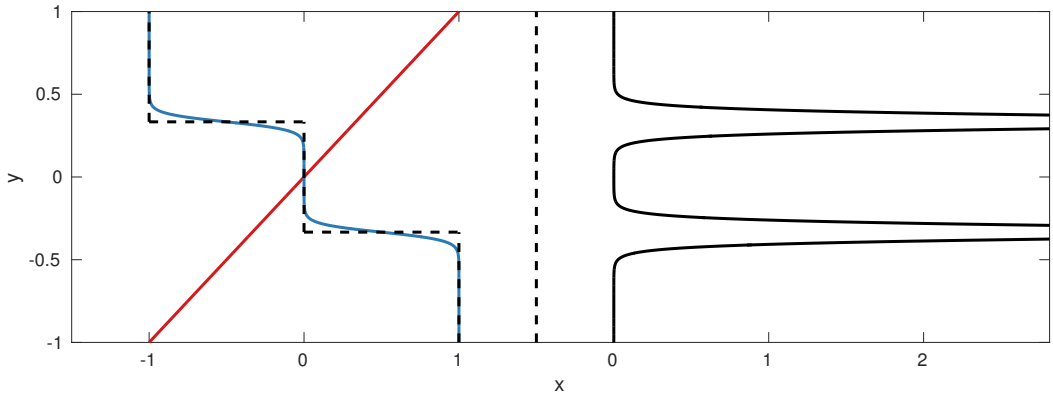

Figure 7.1: a) Vertical variation of base flow velocity $U(y)$ (red), base flow density distribution $\bar{\rho}(z) - \rho_0/\Delta\rho$ with $R = 20$ (blue) and $R \to \infty$ (dashed line) as defined in (7.9). b) Vertical variation of gradient Richardson number $Ri(y)$ as defined in (7.10) for the base flow density distribution with $R = 20$ shown in a).

In Figure 7.1 we plot the nondimensional streamwise base velocity distribution $U(y)$ and the initial base density distribution $\bar{\rho}(y) - \rho_0/\Delta\rho$ for $R = 20$ and $R \to \infty$, where

$$\mathbf{U}(y) = U(y)\hat{\mathbf{x}} = y\hat{\mathbf{x}}, \quad \bar{\rho}(y) - \frac{\rho_0}{\Delta\rho} = -\frac{1}{2}\left[\tanh R(y - 1/3) + \tanh R(y + 1/3)\right]. \tag{7.9}$$

The gradient Richardson number $Ri(y)$ is defined as

$$Ri(y) \equiv -Ri_B \frac{\frac{\partial \rho_{tot}}{\partial y}}{\left(\frac{\partial u_{tot}}{\partial y}\right)^2}, \tag{7.10}$$

and so, for the base flow defined by (7.9),

$$Ri(y) = \frac{Ri_B R}{2}\left[\mathrm{sech}^2 R(y - 1/3) + \mathrm{sech}^2 R(y + 1/3)\right] \tag{7.11}$$

which is very close to zero for a large range of y for all bulk Richardson numbers Ri_B. Specifically, there are broad regions of the flow for which $Ri(y) < 1/4$, and so by the Miles–Howard theorem (Miles, 1961; Howard, 1961) there is at least the possibility of linear instability for all values of Ri_B.

7.3 Linear stability analysis

7.3.1 Stability of step-like profiles in the $Re \to \infty$, $R \to \infty$ limit

Before investigating the full linear problem at finite Re, we perform a linear stability analysis on the simpler background density field that consists of step-like layers in the density profile, shown in Figure 7.1a with a dashed line, making the further assumptions that both $Re \to \infty$ and $RePr \to \infty$. As reviewed in Carpenter *et al.* (2011), such profiles allow substantial analytical progress to be made as the eigenvalue problem to determine the growth rate of normal modes reduces to the solution of a polynomial equation. This simplified problem retains many of the key features of the full, finite Re problem.

We consider normal mode perturbations to the base flow of the form

$$(\mathbf{u}, \rho) = [\hat{\mathbf{u}}(y), \hat{\rho}(y)] \exp(i\alpha[x - ct]),\ \alpha = \frac{k}{d},\ \alpha c_i = \sigma,\ \mathbf{u} = \nabla \times \psi, \tag{7.12}$$

where ψ is the streamfunction, α is the nondimensional wavenumber, assumed to be real and non-negative without loss of generality, and $c = c_r + ic_i$ is the (in general) complex phase speed, such that σ is the growth rate of the linear normal mode. Considering such infinitesimal perturbations to the base flow defined in (7.9), the linearised form of (7.6) (with $Re \to \infty$ and $RePr \to \infty$) can be reduced to the appropriate form of the (inviscid) Taylor–Goldstein equation for the streamfunction eigenfunction $\hat{\psi}(y)$,

$$\frac{\mathrm{d}^2\hat{\psi}}{\mathrm{d}y^2} - k^2\hat{\psi} + \frac{N^2\hat{\psi}}{(y-c)^2} = 0,\ N^2 = -Ri_B\frac{\mathrm{d}\bar{\rho}}{\mathrm{d}y}. \tag{7.13}$$

In the limiting case of interest with $R \to \infty$, giving discontinuous steps in the density field, the buoyancy frequency reduces to two δ-functions localised at each density interface and $N^2 = 0$ everywhere away from these interfaces. Therefore, $\hat{\psi}$ takes the form of exponential functions in each of the three layers, subject to kinematic and dynamic matching conditions at the two interfaces:

$$\left[\frac{\hat{\psi}}{y-c}\right]_-^+ = 0,\ \left[(y-c)\frac{\mathrm{d}\hat{\psi}}{\mathrm{d}y} - \hat{\psi} - \frac{Ri_B\bar{\rho}\hat{\psi}}{y-c}\right]_-^+ = 0. \tag{7.14}$$

Applying these conditions leads straightforwardly to the dispersion relation for the phase speed

$$c^2 = \frac{1}{9} + \frac{Ri_B}{2\alpha_D} \pm \sqrt{\frac{2Ri_B}{9\alpha_D} + \frac{Ri_B^2 \sinh^2 2\alpha/3}{4\alpha_D^2 \sinh^2 4\alpha/3}},\ \alpha_D = \frac{\alpha}{2}(\coth 4\alpha/3 + \coth 2\alpha/3). \tag{7.15}$$

The term under the square root is positive for all positive wavenumbers and so c^2 is real and any unstable modes must have zero (real) phase speed. The flow is unstable when $c^2 < 0$, which occurs in the wavenumber interval defined implicitly by

$$\frac{\alpha \sinh 2\alpha}{18 \sinh \alpha \cosh \alpha/3 \sinh 2\alpha/3} < Ri_B < \frac{\alpha \sinh 2\alpha}{18 \cosh \alpha \sinh \alpha/3 \sinh 2\alpha/3}. \tag{7.16}$$

We plot the associated contours of growth rate in Figure 7.2a. Using the wave interaction approach, which is effectively a large wavenumber limit as originally argued by Taylor (1931), we also plot with a dashed line the predicted wave interaction condition for this flow, which is $Ri_B = 2\alpha/9$. This condition corresponds to a Doppler-shifted interaction between the internal gravity waves on the two interfaces and so clearly shows that this is a TCI. The flow is only unstable for $Ri_B > 1/6$, which is consistent with the linear stability of unstratified inviscid plane Couette flow as demonstrated by Case (1960). In this idealised flow, there is a long-wave zero wavenumber instability predicted for $1/6 < Ri_B < 1/2$. The global maximum growth rate across all α and Ri_B is $\sigma = 0.085$, and occurs for $Ri_B = 0.46$ and $\alpha = 1.75$.

7.3.2 Stability of smooth density profiles at finite *Re* and *Pe*

As discussed in the introduction to this chapter, we wish to investigate the nonlinear evolution of the TCI numerically, and so it is necessary to consider initially the linear stability of a flow with smooth density profiles at finite Reynolds number Re and Peclet number $Pe = RePr$. We therefore consider the linear stability of the base flow defined in (7.9) at finite Reynolds number with $Pr = 1$ and $R = 30$. Linearising the full (finite Re) governing equations (7.6) about the base flow (7.9), and assuming normal mode perturbations of the form (7.12) we obtain a stratified

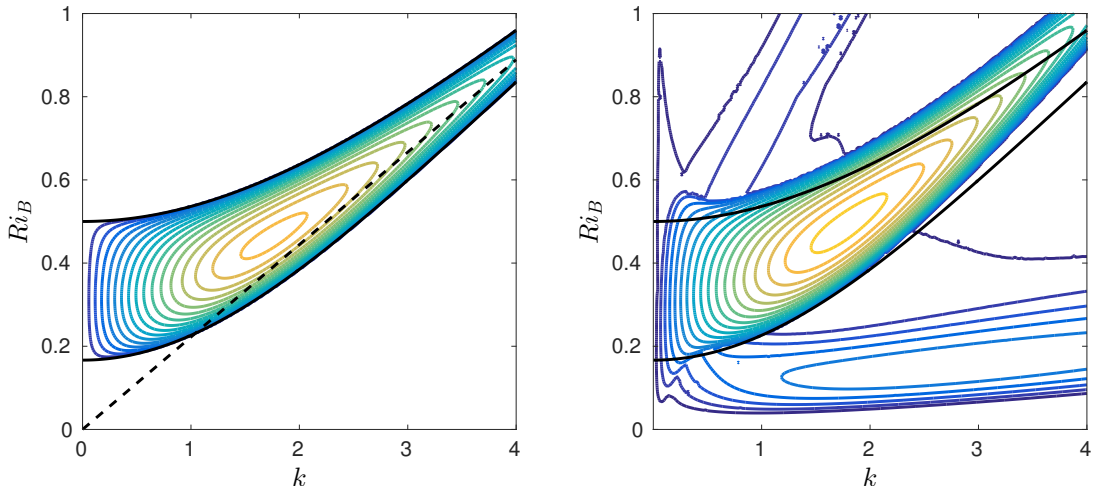

Figure 7.2: a) Contours of growth rate σ for the inviscid, non-diffusive step-like density profile with dispersion relation given by (7.15). The dashed line shows the large α wave interaction relationship $Ri_B = 2\alpha/9$. b) Contours of the largest modal growth rate for the viscous fluid with diffusive, smooth density profiles as defined in (7.12) for $Pr = 1$ and $Re = 10\ 000$. In both panels, the darkest blue contour has $\sigma = 0$, there is a constant contour interval of 0.005. Black lines show the theoretical stability boundary defined by (7.16).

version of an Orr–Sommerfeld equation coupling the vertical velocity eigenfunction $\hat{v}$ and the density eigenfunction $\hat{\rho}$,

$$-i\alpha c\left(\frac{\mathrm{d}^2}{\mathrm{d}y^2} - \alpha^2\right)\hat{v} = -i\alpha y\left(\frac{\mathrm{d}^2}{\mathrm{d}y^2} - \alpha^2\right)\hat{v} + Ri_B\alpha^2\hat{\rho} + \frac{1}{Re}\left(\frac{\mathrm{d}^2}{\mathrm{d}y^2} - \alpha^2\right)^2\hat{v}, \tag{7.17}$$

$$-i\alpha c\hat{\rho} = -i\alpha y\hat{\rho} - \hat{v}\frac{\mathrm{d}}{\mathrm{d}y}\bar{\rho} + \frac{1}{RePr}\left(\frac{\mathrm{d}^2}{\mathrm{d}y^2} - \alpha^2\right)\hat{\rho}. \tag{7.18}$$

Substituting the base flow profile for $\bar{\rho}$ from (7.9), these equations define an eigenvalue problem for the complex phase speed c, which can be solved numerically.

In Figure 7.2b, we plot contours for the growth rate αc_i as α and Ri_B is varied for a flow with $Re = 10\ 000$ and $Pr = 1$. We expect the growth rates at this Reynolds number to resemble the inviscid step-like limit to some extent, and so we also plot the stability boundary from Figure 7.2a. It is apparent that

the structure of the stability boundary has changed qualitatively. In particular, analogously to the results considered by Caulfield (1994), there are now multiple instability branches. The central branch, which still has the highest growth rates for a given value of Ri_B, is the viscous analogue of the TCI discussed in the previous section. The branch of instabilities with typically high wavenumber for a given value of Ri_B appears to be of HWI type, as it is associated with instabilities with nonzero phase speed, localised in the vicinity of the density interfaces. The low wavenumber branches (for a given Ri_B) share some properties with the so-called 'R modes' discussed by Caulfield (1994). However, since their growth rates are so small and, as we show below, the growth rates strongly decrease with Re, we will not discuss these instabilities in detail here.

There are several ways in which the finite values of the Reynolds number Re and the Peclet number $Pe = RePr$ appear to have affected the properties of the TCI themselves. There is no longer instability predicted to occur for $\alpha \to 0$, reflecting the singular perturbation associated with the introduction of the no-slip boundary condition at the channel walls and the associated fact that long wavelength modes are inevitably affected by the boundaries. For small nonzero wavenumbers there appears to be a close connection between the two stability boundaries, although at large wavenumbers, due to the finite thickness of the density interfaces for the flow with $Re = 10\ 000$, there is a non-trivial difference.

Although they undoubtedly have higher growth rates than the low wavenumber instabilities in the 'R' branch, the most unstable HWI at a given Ri_B always has a smaller growth rate than the equivalent most unstable TCI, although it is likely that this observation depends on the depth of the intermediate layer. For this particular Reynolds number, this strong separation in growth rate and associated wavenumbers for the TCI and the HWI make it straightforward to consider the nonlinear dynamics of a flow only subject to a primary TCI, as the streamwise extent, Re and Ri_B can be chosen to admit a strong TCI with no associated primary HWI.

We have solved the linear stability eigenvalue problem for a wide range of Reynolds numbers at this Prandtl number $Pr = 1$. In Figure 7.3 we plot the maximum growth rate over all Ri_B and α at each Reynolds number, $\sigma_m(Re) = \max_{Ri_B,\alpha}[\sigma(Re, Ri_B, \alpha)]$ against Reynolds number. We find that the flow is lin-

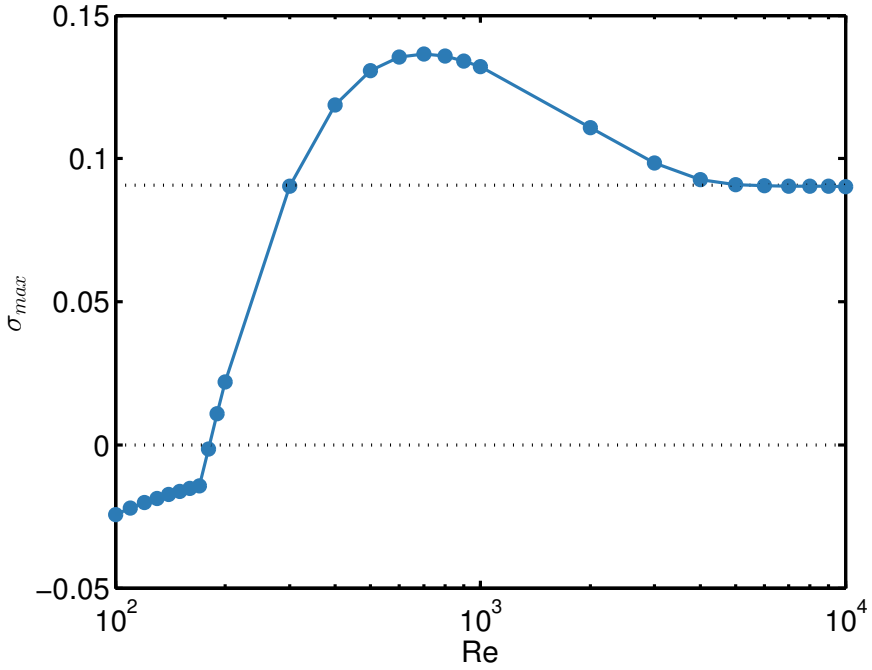

Figure 7.3: Variation of maximum growth rate $\sigma_m(Re)$ with Re. Dotted lines mark the zero growth rate and the maximum growth rate $\sigma_\infty = 0.0907$ for the inviscid limit with smooth density profiles.

early unstable to two-dimensional normal modes for $Re \geq 181$, (i.e. $\sigma_m > 0$ for $Re \geq 181$) and that $\sigma_m \to \sigma_\infty = 0.0907$ as $Re \to \infty$. The $Re = 10\,000$ flow has a very similar maximum growth rate of $\sigma_m = 0.0902$. However, between these two extremes, $\sigma_m(Re)$ varies nonmonotonically with Re, with a global (across Re at $Pr = 1$) maximum of $\sigma_m(700) = 0.137$.

Figure 7.4 shows the structure of the vertical velocity of two wavelengths of the instability with maximum growth rate at both $Re = 700$ and $Re = 10\,000$. In each case the eigenfunction is concentrated about the density interfaces. Unsurprisingly, the eigenfunction is more diffuse for the flow with $Re = 700$, apparently allowing a stronger interaction between the two density interfaces. In addition, for a given amplitude it has stronger gradients, yielding an associated vorticity field with larger maxima and minima.

There is an additional consideration in the linear problem at intermediate Re which modifies the spectral properties of the eigenvalue problem at wavenumbers

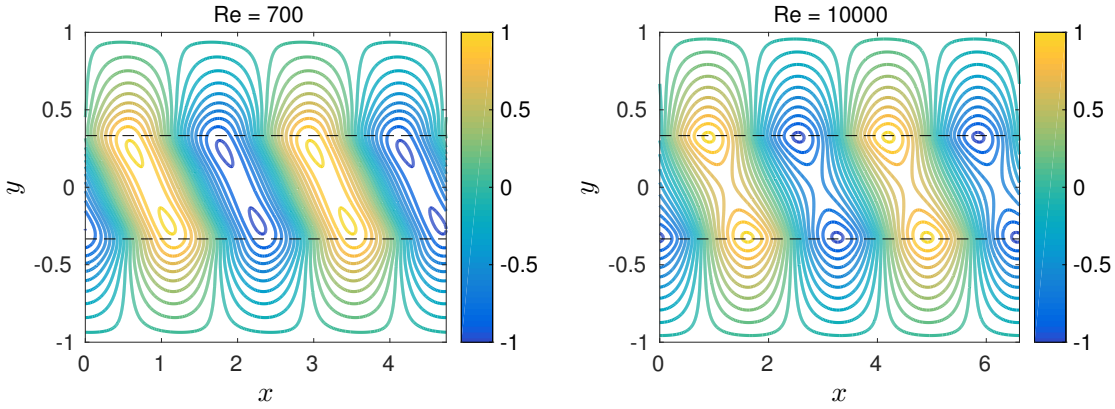

Figure 7.4: Structure of the vertical velocity for the instability with maximum growth rate $\sigma_m(Re)$ at $Pr = 1$ and : a) $Re = 700$; and b) $Re = 10\ 000$. Dashed lines show the location of the density interfaces.

and bulk Richardson numbers close to those associated with the instability with the maximum growth rate $\sigma_m(Re)$. In Figure 7.5, we plot contours of growth rate as a function of α and Ri_B for various Re with $Pr = 1$. It is clear that the 'R' instability branch shrinks in size as Re decreases, and indeed completely disappears for sufficiently small Re. As already noted, the growth rates of the globally most unstable TCI vary nonmonotonically with Reynolds number, reaching a maximum at $Re = 700$. The position, size and shape of the region of the $\alpha - Ri_B$ plane subject to TCI varies with decreasing Reynolds number. The principal effect of this is that the minimum wavenumber below which the system is stable increases, consistent with the increasingly stabilising effect of the walls on the largest wavelengths as the Reynolds number is decreased. Nevertheless, in broad terms the unstable TCI branch does not change its location substantially in the $\alpha - Ri_B$ plane as Re varies.

On the other hand, as the Reynolds number is varied the location of the unstable HWI branch does vary significantly in the $\alpha - Ri_B$ plane. The unstable HWI branch clearly moves towards the region of the unstable TCI branch as the Reynolds number is reduced from 10 000, and the two branches begin to overlap. Indeed, at $Re = 700$, which has the global maximum growth rate at $Pr = 1$, the unstable HWI branch straddles the unstable TCI branch. As the Reynolds number is reduced further, the unstable HWI branch emerges at smaller α/larger Ri_B relative to the unstable TCI branch, and the two branches of instability separate

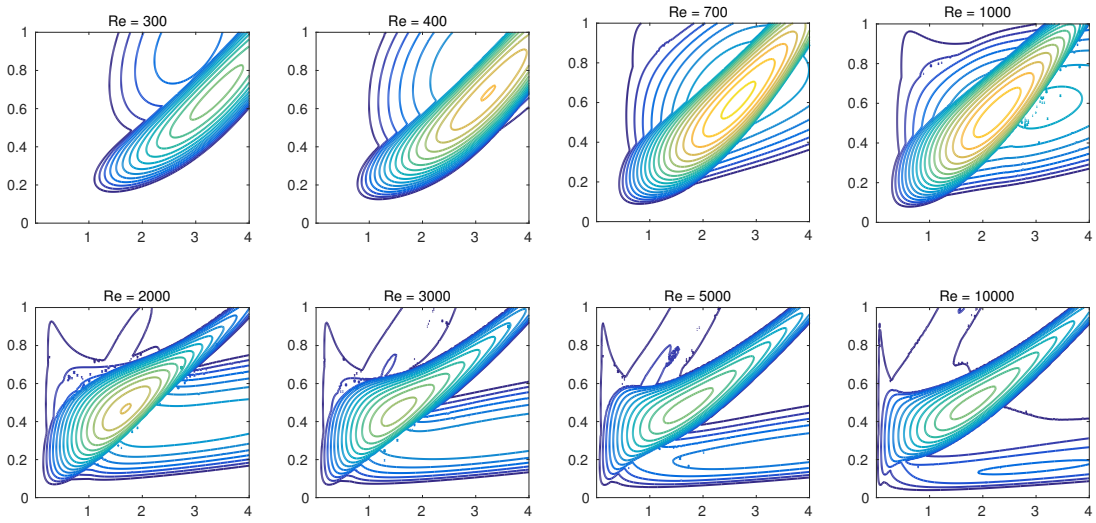

Figure 7.5: Contours of growth rate of the most unstable instability at $Pr = 1$ and $Re =$: a) 300; b) 400; c) 700; d) 1000; e) 2000; f) 3000; g) 5000; h) 10 000. The central, high growth rate (shown with red contours) branches have zero phase speed and represent TCI. The secondary branches of instabilities have nonzero phase speeds. Contours begin at $\sigma = 0$ and have 0.008 increments.

once more.

At $Re = 700$, the most unstable mode over all Ri_B and α is a TCI occurring at $Ri_B = 0.61$ and $\alpha = 2.65$, with growth rate $\sigma_m(700) = 0.137$. At these values of Ri_B and α there is a pair (due to symmetry about the midplane) of primary unstable HWI, which would be expected to manifest at finite amplitude as waves riding along the upper and lower density interfaces in the direction of the background flow. The phase speeds of these modes are $c = \pm 0.674$ and so their critical layers are situated well away from the density interfaces. It is therefore possible for both primary TCI and HWI to grow to finite amplitude in the same periodic flow domain in parallel.

7.3.3 Dimension of the primary instabilities

Since we observe nonmonotonic variation of growth rate of the various instabilities with both Re and Ri_B, it is important to investigate whether three-dimensional modes, with a wavenumber vector oriented at an angle to the mean flow, are actually more unstable than the two-dimensional modes considered above. Squire's

theorem (Squire, 1933) establishes that the primary linear instability of an unstratified viscous fluid is expected to be two-dimensional at a given Reynolds number Re_0 if

$$\frac{\mathrm{d}}{\mathrm{d}s}\left[Re\sigma_{max}(Re)\right]\Big|_{Re_0} > 0, \tag{7.19}$$

where σ_{max} is the maximum growth rate over α at fixed Reynolds number and $\mathrm{d}/\mathrm{d}s$ is the derivative in the direction of increasing Reynolds number along the curve of maximum growth rates. An analogous result due to Yih (1955) establishes that the primary linear instability of an inviscid stratified flow is expected to be two-dimensional at a given bulk Richardson number Ri_0 if

$$\frac{\mathrm{d}}{\mathrm{d}s}\left[\frac{\sigma_{max}(Ri_B)}{Ri_B^{1/2}}\right]\Big|_{Ri_0} < 0, \tag{7.20}$$

where now $\sigma_{max}(Ri_0)$ is the maximum growth rate over α at fixed bulk Richardson number, and $\mathrm{d}/\mathrm{d}s$ is the derivative in the direction of increasing bulk Richardson number along the curve of maximum growth rates. For the modes considered here, both of the above conditions are satisfied, and so the primary instabilities are expected to be two-dimensional.

7.4 Nonlinear evolution of the primary instabilities

When initialising a fully nonlinear, two-dimensional simulation of the evolution of the primary TCI and HWI instabilities at Prandtl number $Pr = 1$, interface sharpness $R = 30$ and Reynolds numbers in the range $500 \leq Re \leq 10\,000$, the two density interfaces diffuse into a state that does not admit a TCI or HWI quicker than the primary TCI and HWI can reach large enough amplitude to affect the subsequent dynamics of the flow significantly, due to the combination of the relatively weak growth rates and the rapid diffusion of such sharp interfaces, even at high Reynolds number. For this reason, we conducted another linear stability analysis with $Pr = 300$. In order for the linear stability code to converge adequately over a reasonable time horizon, we simultaneously reduced the interface sharpness to $R = 20$, and this combination of R and Pr leads to adequate convergence. The variations of the maximum growth rate over all wavenumbers and bulk

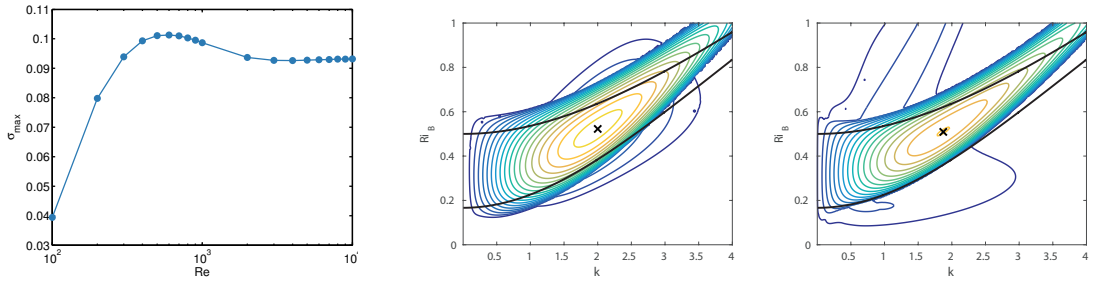

Figure 7.6: a) Maximum growth rate $\sigma_m(Re)$ at $Pr = 300$ and $R = 20$. b) Contours of the largest modal growth rate σ for $Re = 600$, $Pr = 300$ and $R = 20$. c) Contours of the largest modal growth rate σ for $Re = 5000$, $Pr = 70$ and $R = 20$. In both panels b) and c), the darkest blue contour has $\sigma = 0$, there is a constant contour interval of 0.005.

Richardson numbers, $\sigma_m(Re)$, for the case with $Pr = 300$ and $R = 20$ is shown in Figure 7.6a. We see the same qualitative behaviour as for $Pr = 1$, in particular the nonmonotonic behaviour with Re, but the maximum has shifted to occur for approximately $Re = 600$, and the stability threshold for which $\sigma_m = 0$ has moved to $Re < 100$.

Figure 7.6b shows the largest linear growth rate in the $\alpha - Ri_B$ plane for $Re = 600$ with $Pr = 300$ and $R = 20$ and we see again a region of primary TCI straddled by a region of primary HWI. The linear stability properties at $Pr = 300$ and $R = 20$ are qualitatively the same as for those at $Pr = 1$ and $R = 30$ across all Reynolds numbers. We chose to perform a fully nonlinear two-dimensional simulation of the flow at the parameter values corresponding to $\sigma_m(600) = 0.101$ at $Pr = 300$ and $R = 20$. We also want to investigate the dynamics at asymptotically high Reynolds number, but are unable to do this at $Pr = 300$. Instead, we consider $Re = 5000$ and $Pr = 70$. The largest linear growth rate in the $\alpha - Ri_B$ plane for these parameters is shown in Figure 7.6c, and the point with maximum growth rate for the TCI does not have an unstable HWI. We again see a clear qualitative similarity between the linear stability properties at these parameters as for those with $Pr = 1$ in the previous section.

We have performed two-dimensional, nonlinear numerical integrations of the equations of motion at two sets of parameter values, as identified above. In each

case the computational domain is a two-dimensional rectangular channel with no-slip boundary conditions along the (horizontal) channel walls, and periodic boundary conditions at the vertical boundaries of the channel, whose length we denote L_x. The parameter values we consider in detail here are those marked with crosses in Figure 7.6, although in each case we consider a periodic domain of streamwise length allowing two wavelengths of the primary linear instability with largest growth rate over all Reynolds numbers and bulk Richardson numbers. Specifically, for $Re = 600$ and $Pr = 300$ we have $Ri_B = 0.52$ and $L_x = 6.31$, corresponding to a TCI with growth rate $\sigma_m(600) = 0.101$. As already noted, there is also a primary HWI with the same wavelength at this Re, Pr and Ri_B, with growth rate $\sigma = 0.020$. For $Re = 5000$ and $Pr = 70$ we have $Ri_B = 0.51$ and $L_x = 6.72$, which corresponds to two wavelengths of the most unstable primary TCI, with growth rate $\sigma_m(5000) = 0.093$, and a situation where no primary unstable HWI is compatible with the periodic boundary conditions.

For each of these cases, we study the two-dimensional, nonlinear evolution of both primary and secondary instabilities. It appears that considering a nondimensional time interval $0 \leq t \leq 500$ is sufficient. Although it is well-known that primary KHI are susceptible to a wide 'zoo' of secondary instabilities, both inherently two-dimensional and three-dimensional (see for example the relatively recent studies of Mashayek & Peltier (2012*a*,*b*)) the nonlinear dynamics of layered stratified shear flows with primary TCI has been much less considered, and so it is a natural first step to investigate the two-dimensional nonlinear evolution of such flows.

For such simulations, it is natural to consider the time evolution of the perturbation energy. We consider the perturbation energy density integrated over the whole domain, normalised with respect to both the domain area and the kinetic energy of the initial laminar plane Couette flow, so that the perturbation kinetic energy density $K(t)$, the perturbation potential energy density $P(t)$, and the perturbation total energy density $E(t)$ are defined as

$$K(t) = \frac{1}{2L_x\overline{K}} \int_0^{L_x} \int_{-1}^{1} \frac{1}{2}\mathbf{u}\cdot\mathbf{u} \, \mathrm{d}y \, \mathrm{d}x, \tag{7.21}$$

$$P(t) = \frac{1}{2L_x\overline{K}} \int_0^{L_x} \int_{-1}^{1} \frac{Ri_B}{2}\rho^2 \, \mathrm{d}y \, \mathrm{d}x, \; E(t) = K(t) + P(t), \tag{7.22}$$

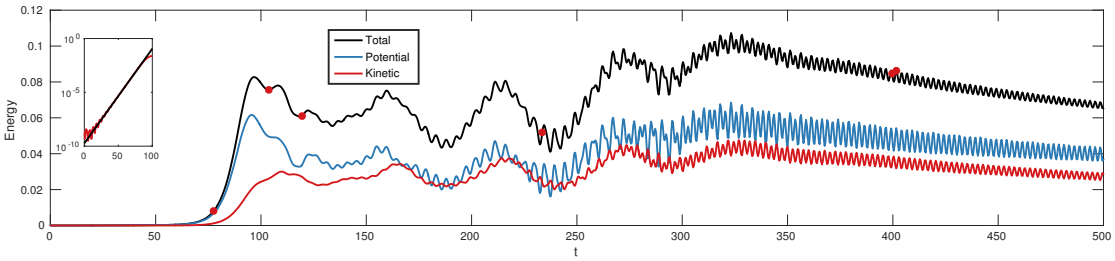

Figure 7.7: Total energy density (black), kinetic energy density (blue) and potential energy density (red) as a function of time for the simulation with $Re = 600$ and $Pr = 300$. Red circles mark the times shown in Figure 7.8. Inset: Time evolution of the total energy (red line) compared to the predicted energy growth of the primary TCI (black line).

$$\overline{K} \;=\; \frac{1}{2L_x}\int_0^{L_x}\int_{-1}^{1}\frac{1}{2}\mathbf{U}\cdot\mathbf{U}\;\mathrm{d}y\,\mathrm{d}x = \frac{1}{6}. \tag{7.23}$$

The equations of motion were integrated using Diablo. We use a 2048×2033 grid for both simulations, which is more than sufficient to capture the dynamics down to the Batchelor scale. We initialise both simulations with a small amplitude of the unstable TCI modal form and a smaller amplitude solenoidal noise field to allow for secondary instabilities. The noise accounts for 1% by amplitude of the initial condition perturbation. This initialisation gives $K(0) = P(0) = 6 \times 10^{-6}$.

7.4.1 $Re = 600$, $Pr = 300$, $Ri_B = 0.52$ and $L_x = 6.31$

Figure 7.7 shows the evolution of the perturbation energy densities of the flow for $Re = 600$, $Pr = 300$, $Ri_B = 0.52$ and $L_x = 6.31$. As is apparent in the inset, the initial energy growth is clearly associated with the linear growth rate of the most unstable TCI. The perturbation energy associated with the TCI reaches a peak amplitude at $t \approx 97$, and subsequently decays whilst slowly oscillating, suggesting strongly that it is not appropriate to describe the TCI as having a 'saturated' finite amplitude manifestation. This behaviour is qualitatively different from the behaviour of flows susceptible to primary KHI, which are known experimentally, numerically and observationally to saturate at finite amplitude as periodic arrays of the classical Kelvin–Helmholtz elliptical 'billows'.

In this flow, soon after the decay of perturbation energy from its peak value, rapid oscillations appear, as E once again increases, reaching a local maximum at $t \approx 160$. This local maximum is followed by a sequence of rapid oscillations of period $t_{\text{fast}} = 4.8 \pm 0.1$, and the period of oscillation for the primary HWI is $t_{\text{HWI}} \approx 4.7$. During this time the flow is modulated by a slow oscillation of period $t_{\text{slow}} \approx 56$ until the energy reaches its global maximum around $t \approx 320$, when it then decays at a substantially slower rate. Although the correspondence is not so clear as with the primary TCI, the oscillatory growth of the perturbation energy may be associated with the growth and eventual appearance of the primary HWI predicted at these parameter values. This suggests that it is indeed possible for qualitatively different primary instabilities to develop in parallel in a stratified shear flow. However, it is important to appreciate that there are undoubtedly profoundly nonlinear dynamics occurring within this flow as well, as for $t \gtrsim 270$ the rapid oscillation transitions to another oscillation with a higher frequency, giving a period $t_{\text{new}} = 2.8 \pm 0.1$. The system ultimately settles into this higher frequency, higher amplitude oscillation for $t \gtrsim 320$.

Figure 7.8 shows snapshots of the flow at different points during the evolution of the system, enabling us to interpret the observed dynamics of the energy in terms of flow structures. At each time, we plot the total density distribution $\rho_{tot}(x, y, t)$, (capturing the underlying three-layer structure) and the perturbation vorticity distribution, $\omega(x, y, t)$ defined as

$$\omega(x, z, t) = \frac{\partial u}{\partial y} - \frac{\partial w}{\partial x} - 1, \tag{7.24}$$

i.e. the vorticity in the $y-$direction after subtraction of the constant (unit in this nondimensionalisation) associated with the laminar background velocity $\mathbf{U} = y\hat{\mathbf{x}}$. We also plot the streamwise averages of the density distribution $\overline{\rho}(y, t)$ and the streamwise velocity $\overline{u}(y, t)$, where

$$\overline{\rho}(y, t) = \frac{1}{L_x} \int_0^{L_x} \rho_{tot} \, \mathrm{d}x; \; \overline{u}(y, t) = \frac{1}{L_x} \int_0^{L_x} u_{tot} \, \mathrm{d}x. \tag{7.25}$$

In addition, we plot a notional gradient Richardson number $Ri_n(y, t)$ from these horizontally averaged fields defined as

$$Ri_n(y, t) = -Ri_B \frac{\frac{\partial \overline{\rho}}{\partial y}}{\left(\frac{\partial \overline{u}}{\partial y}\right)^2}, \tag{7.26}$$

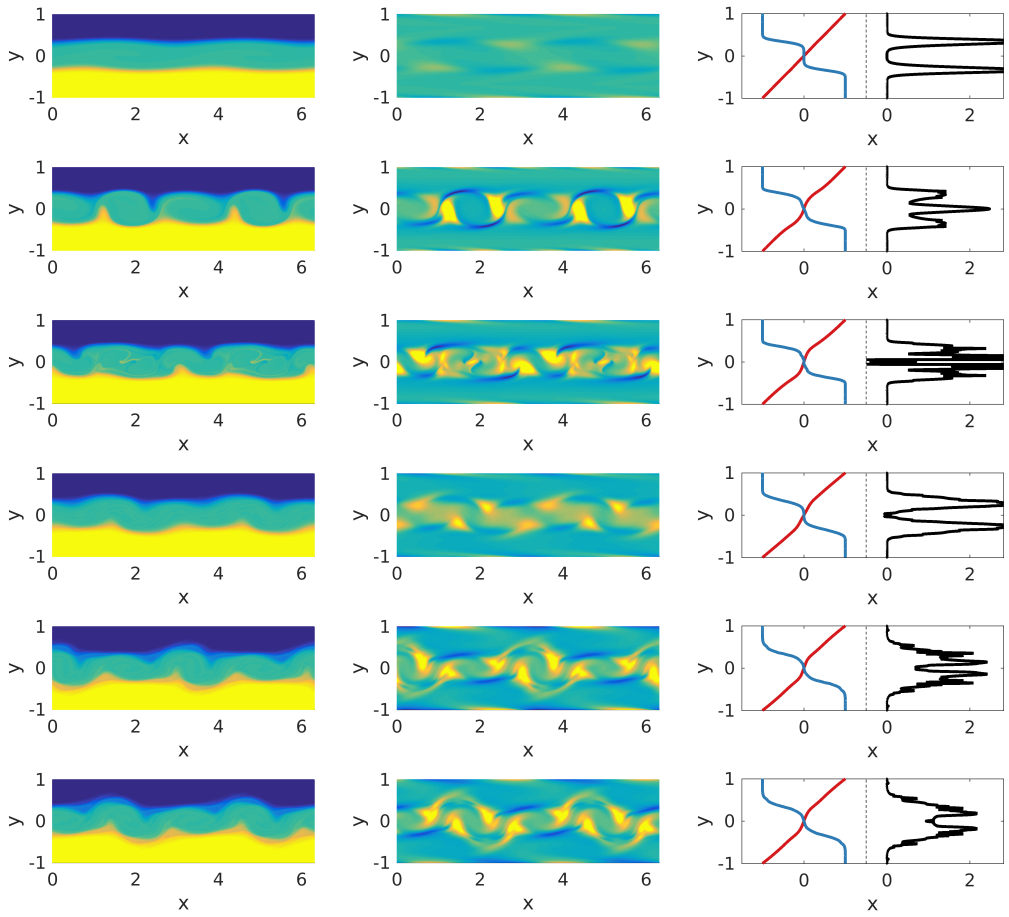

Figure 7.8: Snapshots of the $Re = 600$ and $Pr = 300$ flow evolution at the red circles shown in Figure 7.7. Left hand column shows total density field, middle column shows perturbation vorticity field and right hand column shows the mean horizontal velocity (red), mean density (blue) and notional gradient Richardson number (black) at $t = 77.6$, 103.6, 119.6, 233.6, 399.6, and 401.6.

which proves to be a useful measure for the extent to which nonlinear processes modify the linear stability properties of the flow. In particular, snapshots of $Ri_n(y,t)$ allow us to identify whether the fundamental three-layer structure of the flow subject to a larger scale, close to linear shear, persists or is substantially modified by nonlinear processes.

At early times, as is apparent in the first panel of Figure 7.8, the two density interfaces form inward-facing (i.e. towards the midpoint of the flow) cusps and

are drawn towards each other at these points. This is typical of the nonlinear manifestation of the TCI observed experimentally by Caulfield *et al.* (1995) and the previous two-dimensional numerical simulations of Lee & Caulfield (2001). These cusps are naturally induced by the (positive) vorticity redistributing into elliptical vortices, spanning the entire depth of the middle layer, a characteristic finite amplitude manifestation of the TCI. However, the induced cusps also lead to baroclinic vorticity generation, which is strongly negative at the interfaces' cusps. Unlike the KHI at finite amplitude, it is clear from the second and third panels of Figure 7.8 that the TCI consists of a coupled vortical structure, with a central (positive) vortical core flanked by two negative vortical wings. We also see that in the second panel of Figure 7.8, four vortical cores have formed from the wavelength two primary TCI, and in the third panel of Figure 7.8 two of these cores have grown to have larger streamwise extent than the other two cores. The formation of an extra pair of vortical cores is due to the attempted pinching together of the cusps on opposite density interfaces becoming misaligned due to the background shear, and so inducing two extra cusps on each interface.

The vortical cores appear to be tilted into the base shear, and thus have the potential to extract energy from the base flow transiently through the Orr mechanism (Orr, 1907*a*,*b*). However, this tilting also induces modifications of the density field, leading to annihilation of the different-signed vorticity distributions, and hence the primary TCI instability is almost entirely sheared out by the background flow, as is apparent in the fourth panel of Figure 7.8. The shearing out process has also lessened the extent of the asymmetry between the alternating large and small streamwise extent of the vortical cores. Indeed, the spatial periodicity of the primary TCI is typically rapidly destroyed by the secondary instabilities, and the two-mode primary TCI is only briefly apparent within the flow.

It is apparent in the fourth panel of Figure 7.8 showing the horizontally-averaged density and velocity profiles and the associated notional gradient Richardson number $Ri_n(y,t)$ that the growth (and decay) of the primary TCI does not modify the base flow qualitatively, in that there remains a clear bimodal peak in the Richardson number, associated with a smooth variation of velocity across the entire flow, with two relatively 'sharp' interfaces persisting to separate three close to constant density layers.

During shearing out of the remnants of the nonlinear evolution of the TCI, wavelength two Holmboe modes appear above the upper density interface and below the lower density interface. We believe that these modes are the eventual appearance of the primary HWI present in the original flow profile, which have a smaller growth rate $\sigma_{\mathrm{HWI}}(600) = 0.020$ than the primary TCI which has growth rate $\sigma_m(600) = 0.101$. Before the vortices are sheared out fully, the primary HWI has grown sufficiently to produce large amplitude nonlinear Holmboe waves which travel along the density interfaces. These nonlinear Holmboe waves prevent the vortices from developing any subsequent streamwise asymmetry, and they remain roughly equally spaced throughout the remaining evolution. The nonlinear Holmboe waves reach a peak total energy at $t \approx 320$, before slowly decaying. The characteristic feature of a (one-sided) nonlinear Holmboe wave is a patch of vorticity (in this case with positive sign) above the density interface that pulls wisps of fluid from the layer on the other side of the interface into the layer where the vorticity patch is. In this system, the nonlinear Holmboe waves that propagate consist of two wavelengths, and there are two patches of vorticity at each interface as can be seen in the bottom two panels of Figure 7.8. These patches grow in intensity and size over time, until they begin to interact with the positive signed wall-bounded perturbation vorticity that is located on each of the channel boundaries. This interaction appears to mediate the continued growth of the nonlinear Holmboe waves and initiates the slow decay for $t \gtrsim 320$, and is specific to PCF.

It is clear that a primary HWI of the initial base flow has grown in 'parallel' to the primary TCI, even though is growth rate is appreciably smaller. Therefore, consistently with the hypothesis of Caulfield *et al.* (1995), it is possible for multiple primary instabilities to grow to finite amplitude in layered stratified shear flows, with different growth rates and phase speeds (and hence localised critical layers). Furthermore, here the HWI is more robust than the TCI, calling into question the conventional assumption that the most unstable mode of linear theory will continue to dominate at finite amplitude as $t \to \infty$.

7.4.2 $Re = 5000$, $Pr = 70$, $Ri_B = 0.51$ and $L_x = 6.72$

Turning our attention to the higher Reynolds number flow, Figure 7.9 shows the evolution of the energy of the flow for $Re = 5000$, $Pr = 70$, $Ri_B = 0.51$ and

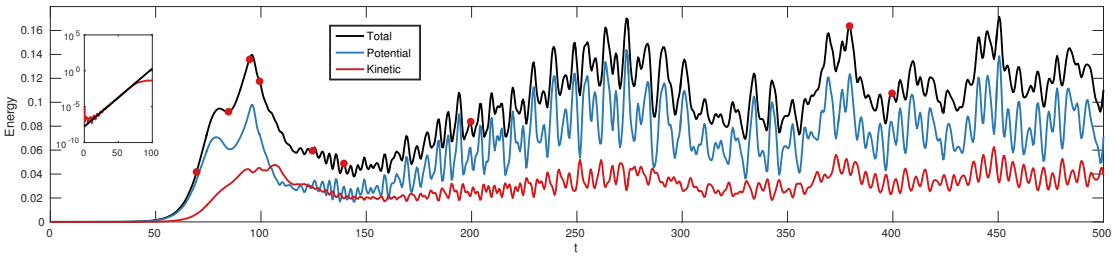

Figure 7.9: Total energy density (black), kinetic energy density (blue) and potential energy density (red) as a function of time for the simulation with $Re = 5000$ and $Pr = 70$. Red circles mark the times shown in Figure 7.10. Inset: Time evolution of the total energy (red line) compared to the predicted energy growth of the primary TCI (black line).

$L_x = 6.72$. There is a clear first peak in energy at $t \approx 80$ that results from the growth of the most unstable normal mode, and it is followed by another peak in energy at $t \approx 95$. After this second maximum the energy subsequently decays rapidly. There is then an onset of 'fast' oscillations, and the energy recovers until a maximum at $t \approx 275$, setting into a slower oscillation for $t \gtrsim 150$. After $t \approx 275$ the flow transitions into a yet slower oscillation coupled with an appreciably longer time-scale nonlinear modulation. This behaviour continues for $t \gtrsim 300$ and is reminiscent of the energetics of the nonlinear Holmboe wave state found by Balmforth *et al.* (2012). Figure 7.10 shows snapshots of the flow at different points during the evolution of the system, which we now discuss in detail.

As in the lower Reynolds number flow discussed above, the evolution of the unstable linear TCI results in cusps and streaks of vorticity forming on the density interfaces, pulling them towards each other as can be seen in the first panel of Figure 7.10. These vorticity streaks then begin to roll up to form two coherent vortical cores. Similarly to the low Reynolds number flow, the vortical cores begin to lose energy as they are sheared out. However, as the vortices are sheared out, there is once more a misalignment of the cusps on the density interfaces, resulting in the creation of two more vortical cores located between the primary pair of vortical cores as is evident in the second panel of Figure 7.10. The two newly created vortical cores begin to grow in size and appear to squeeze the two original vortical cores. This causes complex spatio-temporal vorticity dynamics within the

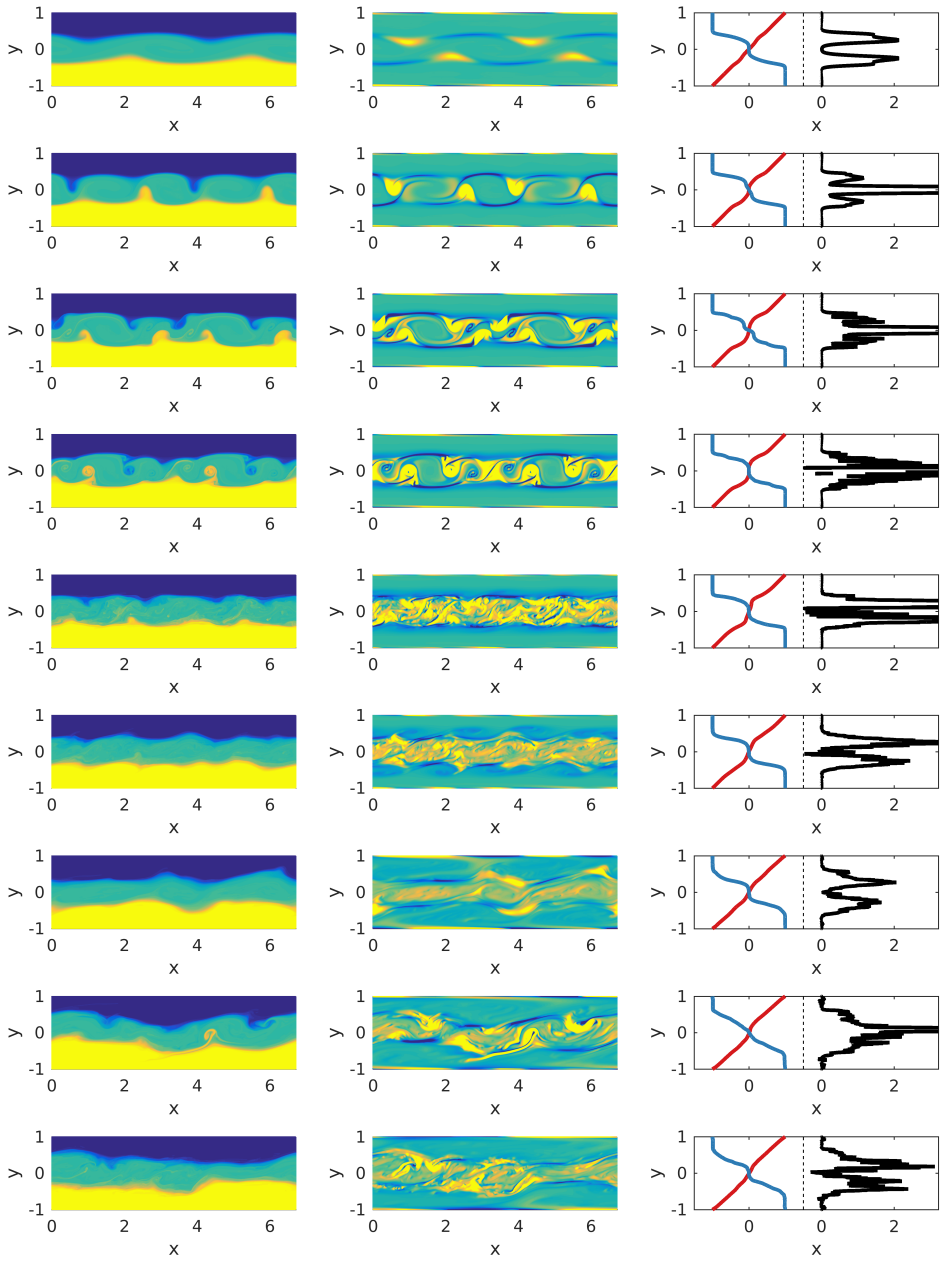

Figure 7.10: Snapshots of the $Re = 5000$ and $Pr = 70$ flow evolution at the red circles shown in Figure 7.9. Left hand column shows total density field, middle column shows perturbation vorticity field and right hand column shows the mean horizontal velocity (red), mean density (blue) and notional gradient Richardson number (black) at $t = 70$, 95, 100, 125, 140, 200, 380 and 400.

two original vortical cores, as is evident in the third and fourth panels of Figure 7.10. The squeezing of the two original vortical cores causes a cascade of secondary braid-like instabilities that results in small-scale disorder in the intermediate layer, and a destruction of the cusps on the two density interfaces due to vigorous mixing in the intermediate layer. The disordered vorticity field is evident in the fifth panel of Figure 7.10.

The mean velocity profile during this disordered state exhibits increased shear over the laminar profile at each of the two density interfaces. This increased shear spontaneously creates eight regions of negative vorticity, four above the upper density interface and four below the lower density interface, as seen in the sixth panel of Figure 7.10. These vortices also cause wisps of fluid from the intermediate density layer into both the upper and lower density layers, and are clearly associatively with the parasitic appearance of a nonlinear Holmboe wave. The HWI is categorically not a primary instability for this flow at this wavelength, and so the appearance of a parasitic nonlinear Holmboe wave has occurred in 'serial' to the nonlinear development and subsequent decay of the primary TCI. The vigorous mixing associated with the braid instability driven decay of the evolution of the primary TCI has rearranged the mean fields in just such a way to cause the flow to become susceptible to the appearance of HWI. Soon after the appearance of wavelength four nonlinear Holmboe waves there is a coarsening to wavelength two nonlinear Holmboe waves, as is apparent from the two vortices above the upper density interface and two vortices below the lower density interface in the seventh panel in Figure 7.10.

The wavelength two nonlinear Holmboe wave state gradually increases in energy throughout $150 \lesssim t \lesssim 275$. As for the lower Reynolds number case discussed above, the peak in energy at $t \approx 275$ appears to correspond with the wavelength two state interacting with the flow boundaries, and this mediates the end of continued energy growth. As the flow begins to decay, there is yet another coarsening event, and the flow settles onto a large amplitude single wavelength nonlinear Holmboe wave for $t \gtrsim 350$. This final state, which is visible in the bottom two panels of Figure 7.10, is reminiscent of the large amplitude nonlinear Holmboe wave found by Balmforth *et al.* (2012), and its appearance is associated with parasitic development on the remnants of the evolution of the primary TCI.

Although such two-dimensional simulations at high Reynolds number should be treated with caution, two key conclusions consistent with the results of Balmforth *et al.* (2012) can be drawn. First, the TCI is clearly 'fragile' and prone to strong secondary two-dimensional instabilities at high Reynolds number. Second, those secondary instabilities can modify the base flow in a way that then leads to the 'parasitic' development of HWI in 'serial' at later times in layered stratified shear flows. This is apparently due to the local intensification of shear at each of the relatively sharp density interfaces, as is apparent in the fifth panel of Figure 7.10.

7.5 Discussion

Layered stratified shear flow typically admits a number of linear instabilities, namely a stratified version of the well-known Kelvin–Helmholtz instability (KHI) (Helmholtz, 1868; Kelvin, 1871) and also the inherently stratified Holmboe wave instability (HWI) (Holmboe, 1962) and the so-called Taylor–Caulfield instability (TCI) (Taylor, 1931). We considered the linear modal stability of three layer stratified plane Couette flow that does not have an inflection point in the velocity field to exclude by construction the KHI and to focus only on inherently stratified instabilities. The analysis of Caulfield (1994), the experiments of Caulfield *et al.* (1995), the numerical simulation of Lee & Caulfield (2001) and the asymptotic stratified defect theory of Balmforth *et al.* (2012) suggest that this flow is unstable to primary TCI as well as HWI, depending on the various parameters in the problem.

The linear stability analysis presented here shows that this is indeed the case, and that the TCI is the most unstable linear mode for both an idealised inviscid, non-diffusive stepped three layer density profile and also over a range of Reynolds numbers for a viscous, diffusive hyperbolic tangent smoothed three layer density profile. The viscous, diffusive, smooth density profile is also subject to HWI with smaller growth rates than the primary TCI and the streamwise wavenumbers and bulk Richardson numbers for which the TCI and HWI occur varies with the Reynolds number. In particular, there are parameters for which both the TCI and HWI are unstable, and for which only the TCI is unstable. For Prandtl number $Pr = 1$ and $Pr = 300$ the largest growth rate over all streamwise wavenumbers

and bulk Richardson numbers is a nonmonotonic function of the Reynolds number; nevertheless, theorems due to Squire (1933) and Yih (1955) demonstrate that the primary instability is expected to be two-dimensional.

The numerical calculations of Lee & Caulfield (2001) and Balmforth *et al.* (2012) indicated that the nonlinear evolution of the TCI is dominated by the secondary appearance of finite amplitude Holmboe waves, and indicates that this could occur either in parallel due to the existence of a primary HWI or in serial due to a nonlinear modification of the initial flow fields that is conducive of the appearance of Holmboe waves. In order to investigate this more fully, we performed fully nonlinear two-dimensional evolutions of the Boussinesq Navier–Stokes equations in the plane Couette flow geometry for two cases, one with two wavelengths of both primary TCI and HWI, and another with two wavelengths of only primary TCI. We found that for small Prandtl numbers, such as $Pr = 1$, the density interfaces diffuse more rapidly than the TCI can grow to significant amplitude, and so simulated a flow for the first case with $Re = 600$ and $Pr = 300$ (for which there is both a primary TCI and HWI), and for the second case with $Re = 5000$ and $Pr = 70$ (for which there is only a primary TCI).

For the smaller Reynolds number case for which there is both a primary TCI and HWI, the faster growing TCI grows to large amplitude before decaying and does not saturate. During the decay of the nonlinear evolution of the primary TCI, we see clear evidence of the nonlinear manifestation of the primary HWI, having apparently grown in *parallel* to the primary HWI. The subsequent dynamics of the flow are inherently linked to the nonlinear Holmboe waves that appear from the primary HWI, and the nonlinear evolution of the primary TCI only sets the scale of the equally sized four elliptical vortical cores, a scale which is not predicted to be linearly unstable, that reside in the intermediate density layer, around which the nonlinear Holmboe waves propagate.

For the larger Reynolds number case for which there is only a primary TCI, the primary TCI once more grows to large amplitude before rapidly decaying. This nonlinear evolution once again forms four vortical cores, two large ones from the primary TCI and two secondary vortical cores. The two secondary vortical cores rapidly increase in size so that the two primary vortical cores are squeezed. This squeezing causes a cascade of braid instabilities, and causes the entire intermediate

density layer to become discorded. The mean properties of this newly created disordered state, which is the remains of the nonlinear evolution of the primary TCI, appears susceptible to the appearance of HWI. Wavelength four nonlinear Holmboe waves appear rapidly in the flow, which undergo a coarsening to a single wavelength nonlinear Holmboe wave due to the presence of the flow boundaries. This single wavelength nonlinear Holmboe wave persists for the remainder of the flow evolution we simulate, and is strongly reminiscent of the coarsening HWI found by Balmforth *et al.* (2012). It appears that nonlinear Holmboe waves grow parasitically, in *serial* to the TCI on the nonlinearly modified flow fields, even when there is no primary HWI. For both cases the TCI proves to be very fragile at finite amplitude, whereas HWI appear to be very robust in such two-dimensional flows.

We have demonstrated that in layered sheared flow, which is susceptible to both primary TCI and HWI, the nonlinear evolution of the TCI does not 'saturate' at finite amplitude, but instead the dynamics are dominated by the secondary appearance of either the primary HWI, if it exists, or of parasitic secondary nonlinear Holmboe wave dynamics even in the absence of a primary HWI. The nonlinear evolution of the TCI inevitably occurs alongside nonlinear Holmboe waves, consistent with the observations of Balmforth *et al.* (2012). This is to be contrasted with the traditional view of the nonlinear evolution of primary linear instabilities like the KHI, for which the nonlinear evolution saturates at finite amplitude, and is relatively robust in the sense that the primary billows survive for some time.

The investigation of the nonlinear evolution of primary TCI has been relatively neglected in comparison to that of primary KHI and HWI, and so although it is well-known that such instabilities are subject to a 'zoo' of secondary instabilities particularly in three dimensions (Mashayek & Peltier, 2012*a*,*b*; Mashayek *et al.*, 2013), an initial restriction to two-dimensional dynamics is warranted in this layered flow. Even for two-dimensional dynamics, we have identified a rich array of secondary processes associated with the appearance of nonlinear Holmboe waves as both the Reynolds number and Prandtl number are varied. We believe that a three-dimensional investigation of the nonlinear evolution of primary TCI is called for in order to understand better the dynamics of layered stratified shear flows, in particular to investigate whether the fragility of the TCI and the robustness of the HWI persist in flows which are free to evolve in three dimensions.

CHAPTER 8

CONCLUSIONS

8.1 Review

The dynamical systems view of transition and turbulence in fluid flows is essential for a complete understanding of critical thresholds for transition, the sequence of events during transition, and the underlying physical processes that play a key role both during transition from a laminar state and in the turbulent state. At the heart of this approach is a focus on the use of *structures*, not statistics, to describe the key dynamical processes. Such structures shape the state space of solutions; the edge state and its stable manifold, the edge manifold, control the nonlinear stability problem while the turbulent state itself is built from a 'scaffold' of exact solutions. This approach has become popular recently in the study of many canonical shear flows due to significant improvements in computing power allowing for efficient computation of algorithms to identify such structures recently generalised from either those used in linear or low-dimensional systems.

This thesis has focussed primarily on the extension of such ideas in transition to turbulence to stratified shear flows, and the investigation of the effects that stratification has on minimal seeds, self-sustaining edge states, and reduced models. Stratified shear flows are ubiquitous in the natural environment and in

industrial processes and so it is important to identify which, if any, conclusions from the study of unstratified canonical shear flows carry over into the stratified case. This thesis investigates such questions under the addition of a stable density stratification to plane Couette flow (PCF), finding minimal seeds in vertically and horizontally sheared stratified PCF, tracking Koopman modes during the transition to turbulence using dynamic mode decomposition (DMD), investigating the stratification of the self-sustaining process (SSP) and also investigating the nonlinear evolution of the multiple linear instabilities present in layered stratified shear flows. In addition, we report in the appendix a generalisation of the singular perturbation method (Balmforth *et al.*, 1994) for investigating the dynamics near homoclinic bifurcations, a common bifurcation route to low-dimensional chaos, to stochastic systems.

In Chapter 2 we discussed the mathematics behind and the history of the study of transient growth in fluid flows, from early investigations of the linear problem to the recently reported nonlinear direct-adjoint looping (DAL) method for finding minimal seeds for turbulence. The nonlinear DAL method was described in detail along with its implementation in this thesis which used the direct numerical simulation code Diablo (Taylor, 2008) as the required time-stepper. The implementation of the nonlinear DAL method necessitates a number of choices with regards to the methods of updating the initial condition and to the optimisation functional and so we dedicated the end of Chapter 2 to demonstrating that we can reproduce known stratified and unstratified results. Of particular note was the independence of the identified minimal seed on the choice of either perturbation energy or time averaged dissipation as the optimisation functional.

In Chapter 3 we presented a number of minimal seeds and their subsequent evolution towards the turbulent state in vertically sheared stratified PCF in a 'narrow' and a 'wide' geometry. The parameters considered covered only a relatively small range of bulk Richardson numbers because of the rapid switching off of the attracting turbulent state in these flows due to the critical control of energy injection through the boundary conditions. Nevertheless, we were able to identify a significant change from streamwise aligned streaks to three-dimensional oblique structures in the edge states visited by these trajectories as this occurred at yet smaller bulk Richardson numbers. Although the wide geometry allowed

for additional localisation of the minimal seeds and their subsequent trajectories, the essential characteristics were essentially unaffected by the geometry. This domain independence was highlighted by the scaling law which was identified. This showed that the SSP/VWI balance can be fully disrupted when $Ri_B = O(Re^{-2})$, and that this scaling is independent of the geometry when considering lower branch SSP/VWI solutions.

In Chapter 4 we highlighted the importance of reduced representations of fluid flows for the understanding of key physical processes, and produced reduced representations of minimal seed trajectories past the edge state. We summarised the DMD algorithm and its relation to Koopman modes and hypothesised that the assumptions leading to the DMD algorithm are particularly relevant for visits to saddle-like edge states, despite the fact that current Koopman mode analysis is valid only on an attractor. We proceeded to apply the DMD algorithm to the minimal seed trajectories found in Chapter 3 and found that the dynamics reduce to only two or three Koopman modes, provided that the edge state is not chaotic. Of particular note was the observation of the existence of neutral modes whose structure resembles the edge state since this points towards a diagnostic for the existence of nearby exact solutions on a state space trajectory. The ability of DMD to reproduce the minimal seed trajectories on the stable and unstable manifold of the edge state surpassed our initial expectations and suggests the possibility of constructing a theory of quasi-Koopman modes for flows not on an attractor.

In Chapter 5 we revisited the disruption of the SSP/VWI states identified in Chapter 3. We summarised the reasoning that leads to the SSP view of such structures, decomposing into symmetric rolls, streaks and waves and solving for each sequentially. We proceeded to solve for each stage of the process for vertically sheared stratified PCF and found that the roll solutions were the only part of the process significantly affected by the stratification. We found a bifurcation to oscillatory roll solutions strongly associated with the presence of standing internal gravity waves. The key parameter governing this bifurcation was the Rayleigh number $Ra = Re^2(-Ri_B)Pr$, validating the scaling law found in Chapter 3. We also extended previous unstratified work by examining asymmetric roll solutions but were unable to find the finely tuned set of parameters that allowed for proper feedback into the SSP process.

In Chapter 6 we calculated minimal seeds in horizontally sheared stratified PCF. At the same bulk Richardson numbers presented in Chapter 3, we found that spanwise localisation is essential to characterise properly the horizontally sheared case. Such localisation appears to be inherent in these transitions, to the extent that at the highest bulk Richardson number used in Chapter 3, the horizontally sheared case has spanwise localisation even in the narrow geometry. We rationalise this observation by noting that horizontally sheared stratified PCF has a length scale that is intrinsic to the density field, and that this length scale is absent in the vertically sheared case. Provided that spanwise localisation occurs, we find that the edge states visited by the minimal seed trajectories retain the streamwise aligned character of SSP/VWI states, but that oscillations comparable to the buoyancy frequency are necessary to self-sustain the identified structures. This is at least consistent with the calculations of Chapter 5, albeit with a different gravitational direction. We were unable to solve the horizontally sheared SSP equations, but we hypothesise that a successful reworking of Chapter 5 for the horizontally sheared case is likely to prove successful. The horizontally sheared case allows for sustained turbulence at much larger bulk Richardson numbers than for vertically sheared stratified PCF, and the turbulent state identified for these large bulk Richardson numbers naturally has layers in the density field. However, the nonlinear DAL method for finding minimal seeds at these larger bulk Richardson numbers appears at the moment to be impractical due to the extremely large time horizons needed for transition. We demonstrated such a transition for a (non minimal) seed and showed that for much of its evolution the dynamics are quasi-one-dimensional. We showed that the one-dimensional restriction of the horizontally sheared SSP equations has solutions that are consistent with the turbulent seed trajectory. A full model based on a reduced set of equations is likely to be successful.

In Chapter 7 we investigated the linear stability and subsequent nonlinear evolution of layered stratified PCF, which is susceptible to both Taylor and Holmboe instabilities, but not the Kelvin–Helmholtz instability. This not only highlighted the rich dynamical behaviour that may arise in the layered flows found in Chapter 6, but also served to demonstrate conclusively that even when a base flow has a linear instability, the subsequent nonlinear evolution of the flow is not necessarily inherently tied to this linear instability as it does not necessarily ‘saturate’ at

finite amplitude. Curiously, we found a nonmonotonic dependence on maximum growth rate with Reynolds number, along with a complicated interplay between Taylor and Holmboe instabilities as the parameter space was mapped. We conducted two-dimensional simulations of two parameter sets which allowed for both primary Taylor and Holmboe instabilities to be present and also just a primary Taylor instability. In both cases, the Taylor instability failed to saturate at finite amplitude, and the subsequent dynamics were dominated by nonlinear Holmboe waves, either in parallel due to the co-existence of a primary Holmboe instability, or in serial due to the parasitic emergence of nonlinear Holmboe waves on top of a rearranged flow profile.

8.2 Future work

The chapters presented in this thesis, and the topics herein, have reinforced the need to address outstanding questions in the field of nonlinear stability and stratified flows and also raised a wide range of unforeseen questions and directions for future work. There are clear future directions in all of the major topics listed in this thesis' title; adjoint-based optimisation, Koopman modes, and reduced models.

Adjoint-based optimisation

The nonlinear DAL method for finding minimal seeds is beginning to emerge from its infancy. Much of the early work in this field was dedicated to demonstrating that the formalism achieves its intended purpose of finding minimal seeds. Recently however, as demonstrated by the various topics contained in this thesis, there has been a shift in focus towards using nonlinear DAL and its minimal seeds as a *tool* to probe additional aspects of nonlinear stability properties and the transition to turbulence. Nevertheless, the minimal seeds themselves, and the algorithmic implementation of the nonlinear DAL method remain of great interest.

The minimal seeds presented in this thesis have focussed on changing only one parameter, the bulk Richardson number, while keeping the Reynolds and Prandtl numbers fixed. This had the computationally efficient advantage of pinpointing precisely what role the stratification plays in an otherwise fixed set-up, but leaves open questions about the variation of the critical energy E_c as a function of all

three parameters. In unstratified PCF, Duguet *et al.* (2013) discuss and identify scaling laws of the form $E_c(Re) = O(Re^{-\gamma})$, with $\gamma \approx 2.7$ for spanwise localised solutions. The functional form of $E_c(Re, Ri_B, Pr)$ is the key stability question in stratified PCF and the investigation of a number of different Reynolds and Prandtl numbers are needed in order to solve this problem fully.

Two choices that must be made in the search for minimal seeds are the objective functional and the update method. There is substantial evidence that the minimal seed found is independent of the choice of objective functional provided that it takes heightened values in the turbulent state. However, there is the possibility of improving the nonlinear DAL algorithm if an 'optimal' choice of objective functional is found. Does there exist an objective functional that minimises the number of iterations needed in the algorithm to find the minimal seed? A systematic investigation of the effect of objective functional on the convergence properties of the nonlinear DAL algorithm would help address this question.

Rabin (2013) investigated the convergence of the nonlinear DAL method under a number of different gradient-based update methods and found very little difference between them. However, all these methods had the idea in common of imposing the initial energy of the perturbation E_0. We used the simplest such method in this thesis and combined it with a 'laddering down' process in order to find E_c. Near to E_c the laddering down process suffers from the problem of wasting computing time while searching around initial conditions at fixed E_0 when in fact better initial conditions are all found at smaller E_0. The idea of fixing E_0 is in some sense a relic of the initial investigations of nonlinear transient growth, which consider a fixed energy budget, and are not necessarily identifying seeds for turbulence but instead dynamically interesting phenomena. However, by definition the minimal seed is the unique initial condition that maximises the energy gain over *all* E_0 provided that the target time T is large enough. This is because as $T \to \infty$, all initial conditions either return to the laminar state or transition to the turbulent attractor. In this limit, the initial conditions that return to the laminar state all have an energy gain of zero, and the initial conditions in the basin of attraction of the turbulent attractor all have nonzero energy gains, and the largest of these is the minimal seed (or an approximation to it infinitesimally above the edge manifold).

Whilst the minimal seed problem need not be constrained to constant E_0, an attempt to converge once more to the minimal seed of Rabin *et al.* (2012) starting from a random noise initial field did not converge when ignoring this constraint. It appears therefore that although the mathematical reasoning for the lack of necessity of E_0 may be valid, the nonlinear DAL method may need to take an initial guess that is at least close-by to the minimal seed. Whether this initial guess should be provided by the laddering down process or whether a natural choice of initial guess exists is up for debate. Another consideration for this proposal is that in the limit $T \to \infty$, the energy gain becomes a non-smooth function, taking different values just below, just above, and on the edge manifold. We would need to consider whether or not this has an effect on the nonlinear DAL algorithm; it is possible that the smoothing effect of finite target time T remedies this issue.

In any case, as was discussed in Chapter 6, significant improvements in the nonlinear DAL algorithm are needed before the investigation of horizontally sheared stratified PCF at large bulk Richardson numbers is made possible due to the restrictive time-step and long time horizons needed. Given the current interest in layered stratified shear flows, this task should be a priority.

Koopman modes

The Koopman operator provides the natural framework for deductive modal decompositions. However, most of the work investigating the Koopman operator and the DMD algorithm has focussed on the dynamics on an attractor. We demonstrated in Chapter 4 that DMD provides an excellent approximation to transient dynamics, provided that such dynamics are sufficiently simple. In particular, dynamics near a steady edge state are seen to be low-dimensional. These observations clearly raise a number of questions.

At a fundamental level, we would like to know whether there is a provable link between DMD modes and Koopman modes for dynamics not on an attractor. This would require extensive study of the Koopman operator for transient problems, and a development of the Koopman mode analysis to quasi-Koopman modes. Over finite time horizons, the Koopman operator certainly has a spectra and associated eigenfunctions, but their explicit calculation is yet to be determined.

With regards to the study of reduced dynamics nearby to an edge state, an

important question is whether or not the low-dimensionality of such trajectories is generic. It seems natural that simple steady edge states should reduce to two or three modes. However, it is not clear whether the same should be true for periodic or chaotic edge states. The DMD algorithm failed to reproduce the chaotic edge states examined in Chapter 4, but this is likely due to failings in the DMD algorithm and its implementation here rather than a fundamental problem with the Koopman mode approach.

Fully turbulent dynamics have been reported to reduce to only a handful of Koopman modes, and this gives hope that an improved DMD algorithm might successfully reduce even chaotic edge trajectories. A caveat to this supposition is that Koopman modes on an attractor are provably mutually orthogonal, and this might be the key ingredient that allows for successful low-dimensional decomposition of fully turbulent flows. Since chaotic edge states are attractors for the reduced space of the edge manifold, it might be the case that enough Koopman modes are mutually orthogonal to give a good representation. In order to address this issue properly however, we would need to examine carefully the action of the Koopman operator on transient chaotic systems. A prime test-bed could be the relatively simple three-disk scattering system of Cvitanović & Eckhardt (1989), for which it is likely that the Koopman operator itself may be computed explicitly.

Finally, we would like to know what relationship exists between neutral Koopman modes and nearby exact solutions on transient trajectories. Again, for simple steady edge states this seems intuitively appealing, but it might be possible to examine more complex edge state structures. Once more, the three-disk scattering system would be a good starting point because all the unstable periodic orbits that form the transient chaotic set are known explicitly, and a direct comparison with its Koopman modes should be possible.

Reduced models

Reduced models derived from equations of motion, under assumptions based on insight from observations, form a cornerstone of the mathematical investigation of fluid flows. The simplified dynamics of solutions based on the SSP/VWI formalism are appealing due to their simplicity and their inherent capturing of key physical processes. Chapters 3 and 6 demonstrated the significant effect that a stable

stratification has on the SSP/VWI process. Whilst we went some way towards examining in detail the initial effects of a stratification on the SSP/VWI process in Chapter 5, there are clear extensions that should be made.

The identification of a bifurcation to oscillatory solutions in vertically sheared stratified PCF in Chapter 5 raises the question of what happens next. Is it possible that oscillatory solutions can be sustained for all bulk Richardson numbers, or does another part of the balance break down as the bulk Richardson number is increased further? To answer this question under the SSP framework would require a careful Floquet analysis of the oscillatory solutions. As the bulk Richardson number becomes asymptotically large, the period of oscillation of the rolls shrinks to zero. In this rather singular limit, does the rest of the solution retain the oscillatory signal of the rolls for all bulk Richardson numbers, or is there a saturation effect at sufficiently large bulk Richardson number which washes out the rapid oscillations in the rolls? A minimal box study at large bulk Richardson numbers could be performed to identify the key physical processes that are needed in order to sustain turbulence and to help address these questions.

An obvious extension of the calculations in Chapter 5 is to the case of horizontally sheared stratified PCF. At small bulk Richardson numbers the dynamics observed in Chapter 6 retain the streamwise aligned nature of the SSP/VWI formalism and begin oscillating. Given the calculations for the vertically sheared case, the presence of such an oscillation is promising for the success in describing the horizontally sheared case. We saw that the horizontally sheared flows contain a natural spanwise length-scale, and the identification of a preferred length-scale via a streamwise aligned ansatz could be obtained.

By far the most promising observation of Chapter 6 in terms of searching for reduced models was that at higher bulk Richardson numbers the horizontally sheared case exhibits quasi-one-dimensional behaviour that leads to spontaneous layer formation. The full solution of a reduced equation set based on this observation may well contribute greatly to the understanding of layer formation in stratified shear flows.

Finally, on the subject of layered stratifications, we may consider an extreme form of reduced models: parametrisation. The accurate parametrisation of mixing in the ocean and atmosphere is a key component in global climate models and their

predictive ability. Given that layered stratifications are ubiquitous in the natural environment, a full understanding of their dynamics is required. Kelvin–Helmholtz events have been studied extensively, as have nonlinear Holmboe waves. However, the Taylor instability has received comparatively little attention. The results of Chapter 7 served to highlight the interesting and possibly unexpected dynamics associated with such instabilities, but only considered the two-dimensional flow. Fully three-dimensional simulations are needed in order to identify fully the secondary processes that occur in such flows.

Finally, the simulations in Chapter 7 highlighted the importance of the Prandtl number on the observed dynamics. For most of this thesis we have concentrated on unit Prandtl number for simplicity. However, in order to make closer the link between the calculations presented herein and observations in experiments and nature, a thorough study of the effect of Prandtl number is needed. In addition to Prandtl number considerations, the effects of boundary conditions, particularly on the density field should be investigated. In order to more closely align these calculations with experiments, for example, it would be necessary to impose Neumann rather than Dirichlet boundary conditions on the density field. This brings its own difficulties with regards to the nature of the final asymptotic state, and it is unclear exactly how crucial this change would be.

8.3 Concluding remarks

When I began this thesis I had previously studied transient growth phenomena, but was fairly unaware of the dynamical systems viewpoint of fluid flows, and how transient growth relates to it; few studies had gone beyond the identification of minimal seeds to use them as a tool for probing other properties of state space. What I hope this thesis has helped to demonstrate is that although minimal seeds are interesting in their own right, their identification in addition opens up a wide range of questions in the dynamical systems view of fluid flows, and provides a good starting point from which to answer them. Given the high dimensionality of fluid flows, the application of dynamical systems ideas to fluid dynamics is a relatively new though rapidly expanding field. I am glad to have had the opportunity to help expand this field via the research presented in this thesis.

Bibliography

Amsallem, D. & Farhat, C. 2012 Stabilization of projection-based reduced-order models. *Int. J. Num. Meth. Eng.* **91**, 358–377.

Arecchi, F. T., Lapucci, A. & Meucci, R. 1993 Poincare versus Boltzmann in Sil'nikov phenomena. *Physica D* **62**, 186–191.

Armbruster, D., Stone, E. & Kirk, V. 2003 Noisy heteroclinic networks. *Chaos* **13**, 71.

Arneodo, A, Coullet, P. H. & Spiegel, E. A. 1985 The dynamics of triple convection. *Geophys. Astrophys. Fluid Dyn.* **31**, 1–48.

Arratia, C., Caulfield, C. P. & Chomaz, J.-M. 2013 Transient perturbation growth in time-dependent mixing layers. *J. Fluid Mech.* **717**, 90–133.

Bagheri, S. 2013 Koopman-mode decomposition of the cylinder wake. *J. Fluid Mech.* **726**, 596–623.

Balmforth, N. J. 1995 Solitary waves and homoclinic orbits. *Ann. Rev. Fluid Mech.* **27**, 335–374.

Balmforth, N. J., Ierley, G. R. & Spiegel, E. A. 1994 Chaotic pulse trains. *SIAM J. Appl. Math.* **54**, 1291–1334.

Balmforth, N. J., Roy, A. & Caulfield, C. P. 2012 Dynamics of vorticity defects in stratified shear flow. *J. Fluid Mech.* **694**, 292–331.

Balmforth, N. J. & Spiegel, E. A. 2004 Pattern dynamics in a checkerboard map. *Chaos* **14**, 784–792.

Billant, P. & Chomaz, J.-M. 2000 Theoretical analysis of the zigzag instability of a vertical columnar vortex pair in a strongly stratified fluid. *J. Fluid Mech.* **419**, 29–63.

Bottin, S. & Chate, H. 1998 Statistical analysis of the transition to turbulence in plane Couette flow. *Eur. Phys. J. B* **6**, 143–155.

Bretherton, F. P. 1966 Critical layer instability in baroclinic flows. *Quart. J. Roy. Met. Soc.* **92**, 325–334.

Brethouwer, G., Billant, P., Lindborg, E. & Chomaz, J.-M. 2007 Scaling analysis and simulation of strongly stratified turbulent flows. *J. Fluid Mech.* **585**, 343–368.

Broer, H. & Takens, F. 1993 Mixed spectra and rotational symmetry. *Arch. Ration. Mech. Anal.* **124**, 13–42.

Butler, K. M. & Farrell, B. F. 1992 Three-dimensional optimal perturbations in viscous shear flow. *Phys. Fluids A* **4**, 1637–1650.

Cairns, R. A. 1979 The role of negative energy waves in some instabilities of parallel flows. *J. Fluid Mech.* **92**, 1–14.

Carpenter, J. R., Tedford, E. W., Heifetz, E. & Lawrence, G. A. 2011 Instability in stratified shear flow: Review of a physical interpretation based on interacting waves. *Appl. Mech. Rev.* **64**, 060801.

Carpenter, J. R., Tedford, E. W., Rahmani, M. & Lawrence, G. A. 2010 Holmboe wave fields in simulation and experiment. *J. Fluid. Mech.* **648**, 205–223.

Case, K. M. 1960 Stability of inviscid plane Couette flow. *Phys. Fluids* **3**, 143.

Caulfield, C. P. 1994 Multiple linear instability of layered stratified shear flow. *J. Fluid Mech.* **258**, 255–285.

Caulfield, C. P. & Peltier, W. R. 2000 The anatomy of the mixing transition in homogeneous and stratified free shear layers. *J. Fluid Mech.* **412**, 1–47.

Caulfield, C. P., Peltier, W. R., Yoshida, S. & Ohtani, M. 1995 An experimental investigation of the instability of a shear flow with multilayered density stratification. *Phys. Fluids* **7**, 3028.

Chandler, G. J. & Kerswell, R. R. 2013 Invariant recurrent solutions embedded in a turbulent two-dimensional Kolmogorov flow. *J. Fluid Mech.* **722**, 554–595.

Chantry, M. & Schneider, T. M. 2014 Studying edge geometry in transiently turbulent shear flows. *J. Fluid Mech.* **747**, 506–517.

Chantry, M., Tuckerman, L. S. & Barkley, D. 2016 Turbulent-laminar patterns in shear flows without walls. *J. Fluid Mech.* **791**, R8.

Chen, K., Tu, J. H. & Rowley, C. W. 2012 Variants of dynamic mode decomposition: boundary condition, Koopman, and Fourier analyses. *J. Nonlin. Sci.* **22**, 887–915.

Cherubini, S. & De Palma, P. 2013 Nonlinear optimal perturbations in a Couette flow: bursting and transition. *J. Fluid Mech.* **716**, 251–279.

Cherubini, S., De Palma, P., Robinet, J.-Ch. & Bottaro, A. 2010 Rapid path to transition via nonlinear localized optimal perturbations in a boundary-layer flow. *Phys. Rev. E* **82**, 066302.

Churilov, S. M. 2016 Stability of shear flows with multilayered density stratification and monotonic velocity profiles having no inflection points. *Geophys. Astrophys. Fluid Dyn.* **110**, 78–108.

Constantinou, N. C. & Ioannou, P. J. 2011 Optimal excitation of two dimensional Holmboe instabilities. *Phys. Fluids* **23**, 074102.

Craik, A. D. 1988 *Wave interactions and fluid flows*. Cam. Univ. Press.

Crutchfield, J. P., Farmer, J. D. & Huberman, B. A. 1982 Fluctuations and simple chaotic dynamics. *Phys. Rep.* **92**, 45–82.

Cvitanović, P. 1987 Invariant measurement of strange sets in terms of cycles. *Phys. Rev. Lett.* **61**, 2729–2732.

Cvitanović, P. & Eckhardt, B. 1989 Periodic-orbit quantization of chaotic systems. *Phys. Rev. Lett.* **63**, 823–826.

Deloncle, A., Billant, P. & Chomaz, J.-M. 2008 Nonlinear evolution of the zigzag instability in stratified fluids: a shortcut on the route to dissipation. *J. Fluid Mech.* **599**, 229–239.

Deusebio, E., Caulfield, C. P. & Taylor, J. R. 2015 The intermittency boundary in stratified plane Couette flow. *J. Fluid Mech.* **781**, 298–329.

Drazin, P. & Reid, W. 1981 *Hydrodynamic stability theory*. Cam. Univ. Press.

Duguet, Y., Monokrousos, A., Brandt, L. & Henningson, S. 2013 Minimal transition thresholds in plane Couette flow. *Phys. Fluids* **25**, 084103.

Duguet, Y., Willis, A. P. & Kerswell, R. R. 2008 Transition in pipe flow: the saddle structure on the boundary of turbulence. *J. Fluid Mech.* **613**, 255–274.

Eaves, T. S. 2015 Noisy homoclinic pulse dynamics. In *Proceedings, 2015 GFD Summer Program* (ed. J. Wettlaufer). WHOI.

Eaves, T. S. & Balmforth, N. J. 2016 Noisy homoclinic pulse dynamics. *Chaos* **26**, 043104.

Eaves, T. S. & Caulfield, C. P. 2015 Disruption of SSP/VWI states by a stable stratification. *J. Fluid Mech.* **784**, 548–564.

Eckhardt, B., Faisst, H., Schmiegel, A. & Schneider, T. M 2008 Dynamical systems and the transition to turbulence in linearly stable shear flows. *Philos. Trans. A. Math. Phys. Eng. Sci.* **366**, 1297–1315.

Farrell, B. F. 1988*a* Optimal excitation of baroclinic waves. *J. Atmos. Sci.* **46**, 1193–1206.

Farrell, B. F. 1988*b* Optimal excitation of perturbations in viscous shear flow. *Phys. Fluids* **31**, 2093.

Farrell, B. F. & Ioannou, P. J. 1993 Transient development of perturbations in stratified shear flow. *J. Atmos. Sci.* **50**, 2201–2214.

Farrell, B. F. & Ioannou, P. J. 1996*a* Generalized stability theory. Part I: Autonomous operators. *J. Atmos. Sci.* **53**, 2025–2040.

Farrell, B. F. & Ioannou, P. J. 1996*b* Generalized stability theory. Part II: Nonautonomous operators. *J. Atmos. Sci.* **53**, 2041–2053.

Fjortoft, R. 1950 Application of integral theorems in deriving criteria of stability for laminar flows and for the baroclinic circular vortex. *Geophys. Publ.* **17**, 1–52.

Foures, D. P. G., Caulfield, C. P. & Schmid, P. J. 2012 Variational framework for flow optimization using seminorm constraints. *Phys. Rev. E* **86**, 026306.

Foures, D P G, Caulfield, C P & Schmid, P J 2013 Localization of flow structures using ∞-norm optimization. *J. Fluid Mech.* **729**, 672–701.

Foures, D. P. G., Caulfield, C. P. & Schmid, P. J. 2014 Optimal mixing in two-dimensional plane Poiseuille flow at finite Peclet number. *J. Fluid Mech.* **748**, 241–277.

Fowler, A. C. & Sparrow, C. T. 1991 Bifocal homoclinic orbits in four dimensions. *Nonlinearity* **4**, 1159.

Glendinning, P. 1984 Bifurcations near homoclinic orbits with symmetry. *Phys. Lett. A* **103**, 163–166.

Glendinning, P. & Sparrow, C. 1984 Local and global behavior near homoclinic orbits. *J. Stat. Phys.* **35** (5-6), 645–696.

Glendinning, P. & Tresser, C. 1985 Heteroclinic loops leading to hyperchaos. *J. Phys. Lett.* **46**, 347–352.

Goldstein, S. 1931 On the stability of superposed streams of fluids of different densities. *Proc. R. Soc. Lond.* **132**, 524–548.

Guha, A. & Lawrence, G. A. 2014 A wave interaction approach to studying non-modal homogeneous and stratified shear instabilities. *J. Fluid Mech.* **755**, 336–364.

Hall, P. & Sherwin, S. 2010 Streamwise vortices in shear flows: harbingers of transition and the skeleton of coherent structures. *J. Fluid Mech.* **661**, 178–205.

Hall, P. & Smith, F. T. 1991 On strongly nonlinear vortex/wave interactions in boundary-layer transition. *J. Fluid Mech.* **227**, 641–666.

Hamilton, J., Kim, J. & Waleffe, F. 1995 Regeneration mechanisms of near-wall turbulence structures. *J. Fluid Mech.* **287**, 317.

Haren, H., Gostiaux, L., Morozov, E. & Tarakanov, R. 2014 Extremely long Kelvin–Helmholtz billow trains in the Romanche Fracture Zone. *Geophys. Res. Lett.* **41**, 8445–8451.

Haurwitz, B. 1931 *Zur Theorie der Wellenbewegungen in Luft und Wasser [On the theory of wave motion in air and water]*. Geophys. Inst. Univ. Leipzig.

Hazel, P. 1972 Numerical studies of the stability of inviscid stratified shear flows. *J. Fluid Mech.* **51**, 39–61.

Heifetz, E. & Mak, J. 2015 Stratified shear flow instabilities in the non-Boussinesq regime. *Phys. Fluids* **27**, 086601.

Helmholtz, H. 1868 On discontinuous movements of fluids. *Phil. Mag.* **36**, 337–346.

Hirsch, J. E., Nauenberg, M. & Scalapino, D. J. 1982 Intermittency in the presence of noise: a renormalization group formulation. *Phys. Lett. A* **87**, 391–393.

Holmboe, J. 1962 On the behavior of symmetric waves in stratified shear layers. *Geophys. Publ.* **24**, 67–113.

Holmes, P., Lumley, J. L. & Berkooz, G. 1998 *Turbulence, coherent structures, dynamical systems and symmetry*. Cam. Univ. Press.

Howard, L. N. 1961 Note on a paper of John W. Miles. *J. Fluid Mech.* **10**, 509–512.

Huppert, H. E. 1973 On Howard's technique for perturbing neutral solutions of the Taylor–Goldstein equation. *J. Fluid Mech.* **57**, 361–368.

Juel, A., Darbyshire, A. G. & Mullin, T. 1997 The effect of noise on pitchfork and Hopf bifurcations. *Proc. R. Soc. Lond. A* **453**, 2627–2647.

Kaminski, A. K., Caulfield, C. P. & Taylor, J. R. 2014 Transient growth in strongly stratified shear layers. *J. Fluid Mech.* **758**, R4.

Kawahara, G., Uhlmann, M. & van Veen, L. 2012 The significance of simple invariant solutions in turbulent flows. *Ann. Rev. Fluid Mech.* **44**, 203–225.

Kelvin 1871 Hydrokinteic solutions and observations. *Phil. Mag.* **42**, 362–377.

Kerswell, R. R., Pringle, C. C. T. & Willis, A. P. 2014 An optimisation approach for analysing nonlinear stability with transition to turbulence in fluids as an exemplar. *Rep. Prog. Phys.* **77**, 085901.

Koopman, B. O. 1931 Hamiltonian systems and transformation in Hilbert space. *Proc. Nat. Acad. Sci. USA* **17**, 315–318.

Kreilos, T. & Eckhardt, B. 2012 Periodic orbits in plane Couette flow. *Chaos* **22**, 047505.

Landahl, M. T. 1980 A note on an algebraic instability of inviscid parallel shear flows. *J. Fluid Mech.* **98**, 243–251.

Lawrence, G. A., Browland, F. K. & Redekopp, L. G. 1991 The stability of a sheared density interface. *Phys. Fluids A* **3**, 2360–2370.

Lee, V. & Caulfield, C. P. 2001 Nonlinear evolution of a layered stratified shear flow. *Dyn. Atmos. Ocean.* **34**, 103–124.

Luchini, P. & Bottaro, A. 2014 Adjoint equations in stability analysis. *Ann. Rev. Fluid Mech.* **46**, 493–517.

Mashayek, A., Caulfield, C. P. & Peltier, W. R. 2013 Time-dependent, non-monotonic mixing in stratified turbulent shear flows: implications for oceanographic estimates of buoyancy flux. *J. Fluid Mech.* **736**, 570–593.

Mashayek, A. & Peltier, W. R. 2012*a* The 'zoo' of secondary instabilities precursory to stratified shear flow transition. Part 1 Shear aligned convection, pairing, and braid instabilities. *J. Fluid Mech.* **708**, 5–44.

Mashayek, A. & Peltier, W. R. 2012*b* The 'zoo' of secondary instabilities precursory to stratified shear flow transition. Part 2 The influence of stratification. *J. Fluid Mech.* **708**, 45–70.

Meyer, C. R. & Linden, P. F. 2014 Stratified shear flow: experiments in an inclined duct. *J. Fluid. Mech.* **753**, 242–253.

Mezić, I. 2005 Spectral properties of dynamical systems, model reduction and decompositions. *Nonlin. Dyn.* **41**, 309–325.

Mezić, I. 2012 Analysis of fluid flows via spectral properties of the Koopman operator. *Ann. Rev. Fluid Mech.* **45**, 357–378.

Miles, J. W. 1961 On the stability of heterogeneous shear flows. *J. Fluid Mech.* **10**, 496–508.

Monokrousos, A., Bottaro, A., Brandt, L., Di Vita, A. & Henningson, D. S. 2011 Nonequilibrium thermodynamics and the optimal path to turbulence in shear flows. *Phys. Rev. Lett.* **106**, 134502.

Moore, A. M. & Farrell, B. F. 1992 Rapid perturbation growth on spatially and temporally varying oceanic flows determined using an adjoint method: application to the Gulf stream. *J. Phys. Ocean.* **23**, 1682–1702.

Morkovin 1969 The many faces of transition. New York: Plenum.

Moser, R. D. & Rogers, M. M. 1991 Mixing transition and the cascade to small scales in a plane mixing layer. *Phys. Fluids A* **3**, 1128–1134.

Nagata, M. 1990 Three-dimensional finite-amplitude solutions in plane Couette flow: bifurcation from infinity. *J. Fluid Mech.* **217**, 519–527.

Oglethorpe, R. L. F., Caulfield, C. P. & Woods, A. W. 2013 Spontaneous layering in stratified turbulent Taylor–Couette flow. *J. Fluid Mech.* **721**, R3.

Olvera, D. & Kerswell, R. R. 2014 Coherent structures in stratified plane Couette flows. *Bulletin of the APS* **59**, 255.

Orr, W. M'F. 1907*a* The stability or instability of the steady motions of a perfect liquid and of a viscous liquid. Part I: A perfect liquid. *Proc. R. Irish Acad. Sect. A* **27**, 9–68.

Orr, W. M'F. 1907*b* The stability or instability of the steady motions of a perfect liquid and of a viscous liquid. Part II: A viscous liquid. *Proc. R. Irish Acad. Sect. A* **27**, 69–138.

Orszag, S. A. 1971 Accurate solution of the Orr–Somerfeld stability equation. *J. Fluid Mech,* **50**, 689.

Otheguy, P., Billant, P. & Chomaz, J.-M. 2007 Theoretical analysis of the zigzag instability of a vertical co-rotating vortex pair in a strongly stratified fluid. *J. Fluid Mech.* **584**, 103.

Phillips, O. M. 1972 Turbulence in a strongly stratified fluid - is it unstable? *Deep-Sea Res.* **19**, 79–81.

Pringle, C. C. T. & Kerswell, R. R. 2010 Using nonlinear transient growth to construct the minimal seed for shear flow turbulence. *Phys. Rev. Lett.* **105**, 154502.

Pringle, C. C. T., Willis, A. P. & Kerswell, R. R. 2012 Minimal seeds for shear flow turbulence: using nonlinear transient growth to touch the edge of chaos. *J. Fluid Mech.* **702**, 415–443.

Rabin, S. M. E. 2013 A variational approach to determining nonlinear optimal perturbations and minimal seeds. PhD thesis, University of Cambridge.

Rabin, S. M. E., Caulfield, C. P. & Kerswell, R. R. 2012 Triggering turbulence efficiently in plane Couette flow. *J. Fluid Mech.* **712**, 244–272.

Rayleigh 1880 On the stability, or instability, of certain fluid motions. *Proc. Lond. Math. Soc.* **11**, 57.

Reimann, P. & Talkner, P. 1991 Invariant densities for noisy maps. *Phys. Rev. A* **44**, 6348.

Rempfer, D. 2003 Low-dimensional modelling and numerical simulation of transition in simple shear flows. *Ann. Rev. Fluid Mech.* **35**, 229–265.

Reynolds, O. 1883 An experimental investigation of the circumstances which determine whether the motion of water shall be direct or sinuous, and of the law of resistance in parallel channels. *Phil. Trans. R. Soc. Lond.* **174**, 935–982.

Romanov, V. A. 1973 Stability of plane-parallel Couette flow. *Func. Anal. Appl.* **7**, 137–146.

Rosenhead, L. 1931 The formation of vortices from a surface discontinuity. *Proc. Roy. Soc. A* **124**, 170–192.

Rowley, C. W., Mezić, I., Bagheri, S., Schlatter, P & Henningson, D. S. 2009 Spectral analysis of nonlinear flows. *J. Fluid Mech.* **641**, 115–127.

Rucklidge, A. M. 1993 Chaos in a low-order model of magnetoconvection. *Physica D* **62**, 323–337.

Satchell, J S & Sarkar, S 1986 Stochastic Shilnikov maps. *J. Phys. A* **20**, 1333–1343.

Schlichting, H. 1933 Zur Entstehung der Turbulenz bei der Plattenströmung [On the onset of turbulence in boundary layer flow]. *Z. Angew. Math. Mech.* **13**, 171–174.

Schmid, P. 2010 Dynamic mode decomposition of numerical and experimental data. *J. Fluid Mech.* **656**, 5–28.

Schmid, P. & Sesterhenn, J. 2008 Dynamic mode decomposition of numerical and experimental data. *Bulletin of the APS* **53**, 102.

Schmid, P. J. 2007 Nonmodal stability theory. *Ann. Rev. Fluid Mech.* **39**, 129–162.

Schmid, P. J. & Henningson, D. S. 2000 *Stability and transition in shear flows*. Springer App. Math. Sci.

Schneider, T. M., Marinc, D. & Eckhardt, B. 2010 Localized edge states nucleate turbulence in extended plane Couette cells. *J. Fluid Mech.* **646**, 441.

Schubauer, G. B. & Skramstad, H. K. 1947 Laminar boundary-layer oscillations and stability of laminar flow. *J. Aeronaut. Sci.* **14**, 69–78.

Scinocca, J. F. & Ford, R. 2000 The nonlinear forcing of large-scale internal gravity waves by a stratified shear instability. *J. Atmos. Sci.* **57**, 653–672.

Shil'nikov, A. L. 1993 On bifurcations of the Lorenz attractor in the Shimizu–Morioka model. *Physica D* **62**, 338–346.

Shilnikov, L. P. 1970 A contribution to the problem of the structure of an extended neighborhood of a rough equilibrium state of saddle-focus type. *Math. USSR-Sbornik* **10**, 91–102.

Shimizu, T. & Morioka, N. 1980 On the bifurcation of a symmetric limit cycle to an asymmetric one in a simple model. *Phys. Lett.* **76**, 201–204.

Simiu, E. & Frey, M. 1996 Noise-induced sensitivity to initial conditions. In *Fluctuations and order: the new synthesis* (ed. M. Millonas), chap. 6. Springer.

Smyth, W. D., Klaasen, G. P. & Peltier, W. R. 1988 Finite amplitude Holmboe waves. *Geophys. Astrophys. Fluid Dyn.* **43**, 181–222.

Smyth, W. D., Moum, J. N. & Nash, J. D. 2011 Narrowband oscillations in the upper equatorial ocean. Part II: Properties of shear instabilities. *J. Phys. Oceanogr.* **41**, 412–428.

Smyth, W. D. & Winters, K. B. 2003 Turbulence and mixing in Holmboe waves. *J. Phys. Oceanogr.* **22**, 967–711.

Sparrow, C. 2012 *The Lorenz equations: bifurcations, chaos, and strange attractors*. Springer Science & Business Media.

Squire, H. B. 1933 On the stability of three-dimensional disturbances of viscous flow between parallel walls. *Proc. Roy. Soc. A* **142**, 621–628.

Stone, E. & Armbruster, D. 1999 Noise and O(1) amplitude effects on heteroclinic cycles. *Chaos* **9**, 499–506.

Stone, E. & Holmes, P. 1990 Random perturbations of heteroclinic attractors. *SIAM J. Appl. Math.* **50**, 726–743.

Stone, E. & Holmes, P. 1991 Unstable fixed points, heteroclinic cycles and exponential tails in turbulence production. *Phys. Lett. A* **155**, 29–42.

Sutherland, B. R. 2010 *Internal gravity waves*. Cambridge University Press.

Taylor, G. I. 1931 Effect of variation in density on the stability of superposed streams of fluid. *Proc. R. Soc. Lond.* **132**, 449–523.

Taylor, J. R. 2008 Numerical simulations of the stratified oceanic bottom boundary layer. PhD thesis, Mech. Eng., UCSD.

Thorpe, S. A. 1968 A method of producing a shear flow in a stratified fluid. *J. Fluid Mech.* **32**, 693–704.

Tollmien, W. 1929 Über die Entstehung der Turbulenz [On the onset of turbulence]. *Nachr. Ges. Wiss, Göttingen, Math. Phys. Klasse* **1**, 21–44.

Tuckerman, L. S., Kreilos, T., Schrobsdorff, H., Schneider, T. M. & Gibson, J. F. 2014 Turbulent-laminar patterns in plane Poiseuille flow. *Phys. Fluids* **26**, 114103.

van Veen, L & Kawahara, G 2011 Homoclinic tangle on the edge of shear turbulence. *Phys. Rev. Lett.* **107**, 114501.

Vollmer, J., Schneider, T. M. & Eckhardt, B. 2009 Basin boundary, edge of chaos and edge state in a two-dimensional model. *New J. Phys.* **11**, 013040.

Waleffe, F. 1997 On a self-sustaining process in shear flows. *Phys. Fluids* **9**, 883–900.

Waleffe, F. 2001 Exact coherent structures in channel flow. *J. Fluid Mech.* **435**, 93–102.

Wedin, H. & Kerswell, R. R. 2004 Exact coherent structures in pipe flow: travelling wave solutions. *J. Fluid Mech.* **508**, 333–371.

Wilkie, J. 2004 Numerical methods for stochastic differential equations. *Phys. Rev. E* **70**, 017701.

Willis, A. P., Cvitanović, P. & Avila, M. 2013 Revealing the state space of turbulent pipe flow by symmetry reduction. *J. Fluid Mech.* **721**, 514–540.

Yih, C-S. 1955 Stability of two-dimensional parallel flows for three-dimensional disturbances. *Quart. Appl. Math.* **12**, 434–435.

Young, L. S. 2002 What are SRB measures, and which dynamical systems have them? *J. Stat. Phys.* **109**, 733–754.

Zhu, D. Z. & Lawrence, G. A. 2001 Holmboe's instability in exchange flows. *J. Fluid. Mech.* **429**, 391–409.

APPENDIX A

NOISY HOMOCLINIC PULSE DYNAMICS

The effect of stochastic perturbations on nearly homoclinic pulse trains are considered for three model systems: a Duffing oscillator, the Lorenz-like Shimizu–Morioka model, and a co-dimension-three normal form. Using the Duffing model as an example, it is demonstrated that the main effect of noise does not originate from the neighbourhood of the fixed point, as is commonly assumed, but due to the perturbation of the trajectory outside that region. Singular perturbation theory is used to quantify this noise effect and applied to construct maps of pulse spacing for the Shimizu–Morioka and normal form models. The dynamics of these stochastic maps is then explored to examine how noise influences the sequence of bifurcations that take place adjacent to homoclinic connections in Lorenz-like and Shilnikov-type flows.

Sequences of irregularly spaced pulses arise in a variety of nonlinear systems ranging from wavey fluid films and nerve axons to bursts in sheared convection and turbulent boundary layers. These solutions arise when the system is close to conditions under which there are homoclinic orbits connecting fixed points, and open analytical pathways to establishing key mathematical properties. Previously, these ideas have been exploited in deterministic systems to establish that strange attractors are possible in the form of trains of chaotically spaced pulses. Here, we

extend the theory to stochastically perturbed systems. Along the way, we show how the main effect of noise is felt on the excursions away from the fixed points, rather than over the neighbourhood of those equilibria.

A.1 Introduction

Sequences of irregularly spaced pulses arise in a variety of deterministic nonlinear systems when conditions are close to those required for the homoclinic connection of a fixed point. Owing to the extended intervals that the system spends near the fixed point, the locally linear flow over the surrounding neighbourhood sensitively controls the dynamics. In tandem with simplifying assumptions for the relatively fast, nearly homoclinic or heteroclinic transitions away from the fixed points, significant mathematical progress is then possible to understand the dynamics and, in particular, show that attractors are possible with the form of trains of chaotically spaced pulses (see Shilnikov, 1970; Sparrow, 2012).

The notion that the flow in the vicinity of the fixed points controls the dynamics leads naturally to the expectation that this region acts as the clock that dictates the timings of a pulse train and any perturbation to the system should first be felt there. Stone & Holmes (1990, 1991) thereby argued that stochastic perturbations of homoclinic (and heteroclinic) cycles take place near the fixed points and constructed a theory for how noise modified pulse timing (see also Satchell & Sarkar, 1986). In particular, they derived formulae for the mean pulse spacing of a stochastic Duffing equation and suggested how the pulse spacing distribution generically developed exponential tails. Further developments, including applications to other systems, can be found in Stone & Armbruster (1999) and Armbruster *et al.* (2003).

Our goals in this appendix are threefold. First, we show how the premise underlying Stone & Holmes's analysis is, in fact, unfounded: the neighbourhood of the fixed points is not the critical region that controls the dynamics under stochastic perturbation. Instead, noise acting over the fast, near-homoclinic transitions significantly perturbs the location at which trajectories arrive at the origin. In turn, this produces variances in the timing of the pulses that are at least an order of magnitude larger than those due to noise near the origin.

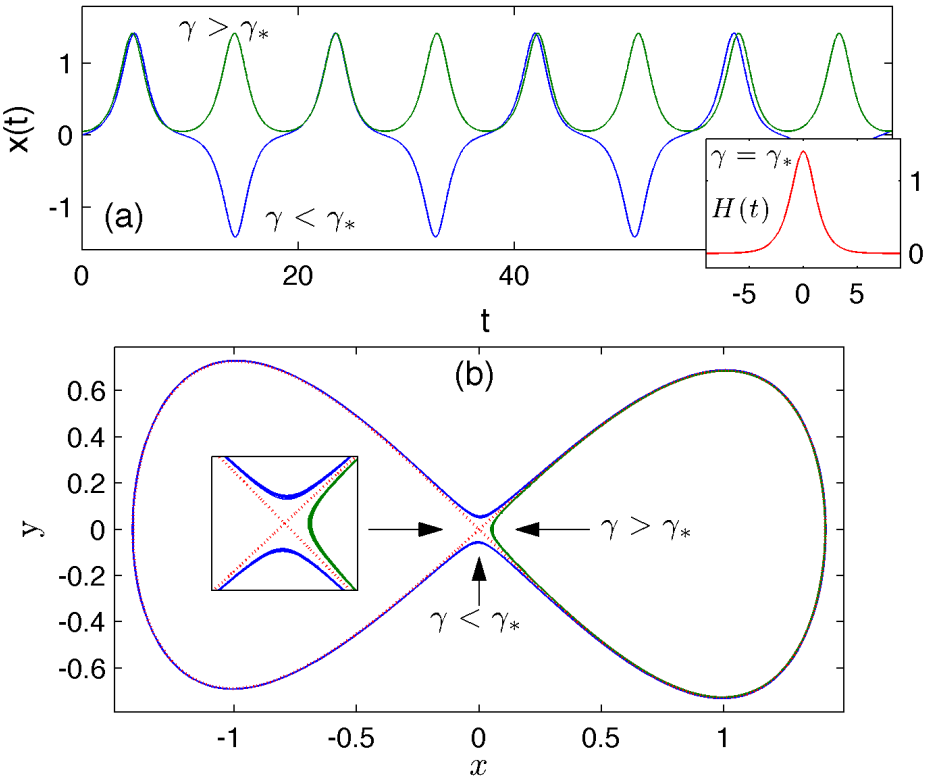

Figure A.1: The Duffing example in (A.1) with $\beta = 0.1$ and three values of γ: 0.079 ($< \gamma_*$), 0.081 ($> \gamma_*$) and 0.08001 ($\approx \gamma_*$). (a) shows time series of the three solutions and (b) a phase portrait on the $(x, \dot{x})$ plane.

To illustrate the point, we use the stochastic Duffing example of Stone & Holmes. The deterministic part of this example is

$$\dot{x} = y, \qquad \dot{y} = x - x^3 - \gamma y + \beta x^2 y, \tag{A.1}$$

solutions of which are displayed in Figure A.1 for particular choices of the parameters β and γ. The fixed point at the origin is connected to itself by a homoclinic orbit for a special value of one of these parameters; we take $\gamma \equiv \gamma_*(\beta)$ to denote this special value. For $\gamma \approx \gamma_*$ but $\gamma > \gamma_*$, the homoclinic connection is slightly broken and a train of periodically spaced pulses arise. Owing to the symmetry of the system $(x, y) \to (-x, -y)$, for each homoclinic pulse there is also an "antipulse", and when $\gamma \approx \gamma_*$ with $\gamma < \gamma_*$, there is an alternating sequence of pulses and antipulses.

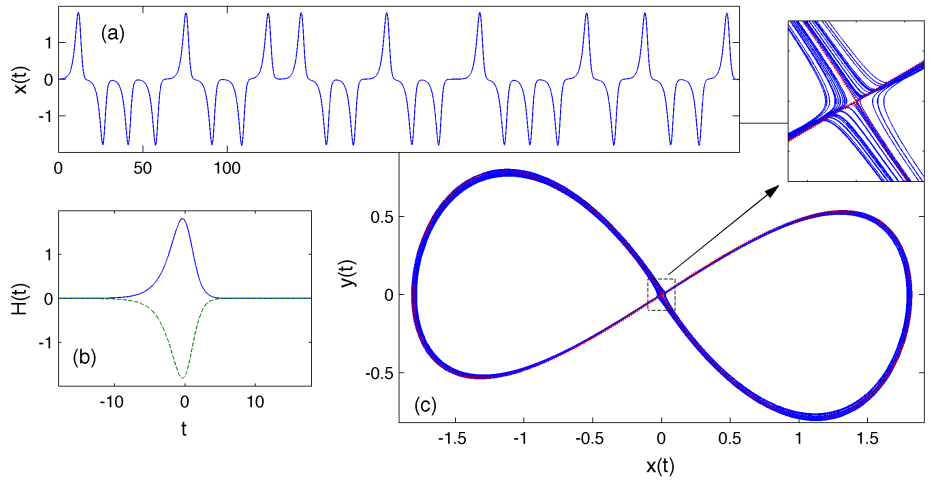

Figure A.2: The deterministic Shimizu–Morioka example in (A.2) with $\beta = 0.4$ and $\gamma = 1.19$. (a) shows time series of $x(t)$, (b) the homoclinic pulse and anti-pulse for $\gamma(\beta = 0.4) \approx 1.2054$, and (c) a portrait on the (x, y) plane. For the latter, a magnification of the neighbourhood of the origin is also overlaid and the homoclinic orbits are plotted (red lines).

Our second goal is to provide a formulation of the stochastically perturbed problem that accounts for the effect of noise away from the fixed points, and thereby enables us to predict the spacings of noisy pulse trains. For the task, we use singular perturbation theory (Balmforth *et al.*, 1994), which was developed originally to describe the weak interactions of coherent structures in spatially extended systems (see Balmforth, 1995). One attractive feature of this method is that it immediately furnishes the timing map of a pulse train in terms of a number of integrals involving both the homoclinic orbit and a related adjoint function. This avoids the introduction of arbitrary constants in the linear mapping away from the fixed points which follow from the usual assumptions in the more geometrical approach of Shilnikov (1970) and others. That is, the theory is a predictive one, free of fitting constants.

The third goal is to use the methodology to study how stochastic perturbation affects bifurcations expected near homoclinic connections. These bifurcations depend sensitively on the nature of the stable and unstable manifolds of the fixed points. The so-called Lorenz flow (see Sparrow, 2012) is typical when the dynamics near the fixed points is dominated by one-dimensional unstable and stable

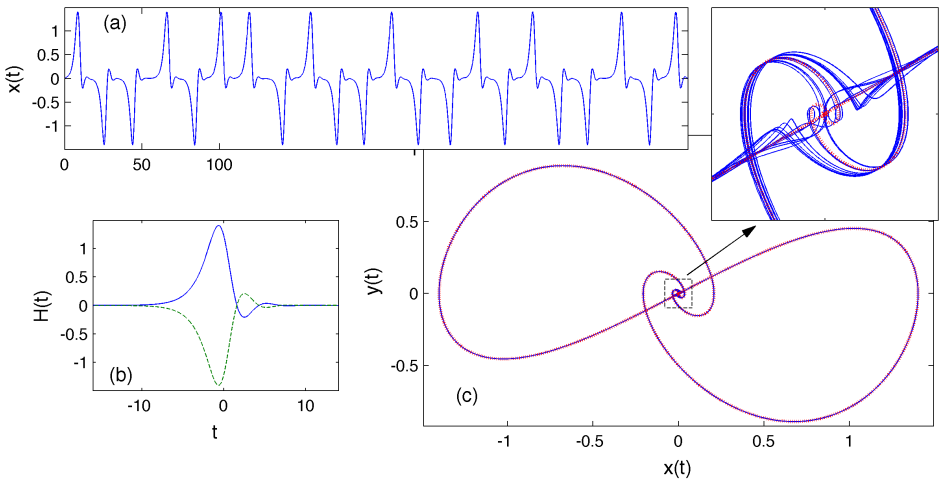

Figure A.3: The co-dimension-three normal form example in (A.3) with $\beta = 0.7$ and $\gamma = 1.108$. (a) shows time series of $x(t)$, (b) the homoclinic pulse and anti-pulse for $\gamma(\beta = 0.7) \approx 1.107887$, and (c) a portrait on the $(x, y = \dot{x})$ plane. For the latter, a magnification of the neighbourhood of the origin is also overlaid and the homoclinic orbits are plotted (red lines).

manifolds. The resulting second-order linear system is integral in connecting the overlapping tails of the monotonically growing and decaying pulses and helping to establish that systems like the Lorenz equations can possess a strange attractor. The union of unstable periodic orbits that comprise the attractor appear in a "homoclinic explosion"; further details of the bifurcation scenario are summarized in Sparrow (2012). An example of a Lorenz-like system is the Shimizu–Morioka model (Shimizu & Morioka, 1980; Shil'nikov, 1993; Rucklidge, 1993), given by

$$\dot{x} = y, \qquad \dot{y} = x(1 - z) - \gamma y, \qquad \dot{z} = \beta(x^2 - z), \tag{A.2}$$

as illustrated in Figure A.2 under nearly homoclinic conditions (for which, again, $\gamma = \gamma_*(\beta)$). For this example, there are again both pulses and antipulses and the solution now has chaotic spacings (for suitable saddle index).

When the flow near the fixed points is dominated by a one-dimensional unstable manifold and a two-dimensional stable manifold with complex eigenvalues, the homoclinic orbit trajectories grow monotonically, but decay in an oscillatory fashion. This leads to the Shilnikov bifurcation scenario in which a strange set of unstable periodic orbits can form through a complicated infinite sequence of

period doubling cascades. The co-dimension-three normal form considered by Arneodo *et al.* (1985) provides a setting for the Shilnikov scenario and is defined by the system,

$$\dddot{x} + \gamma\ddot{x} + \dot{x} - \beta x + x^3 = 0. \tag{A.3}$$

We illustrate this third model in Figure A.3.

By adding noise to the two models in (A.2) and (A.3), we study how the homoclinic explosion of the Lorenz flow and Shilnikov's bifurcation sequence are destroyed by noise. Our main tool is the spacing map furnished by the singular perturbation theory, which we verify provides a faithful first approximation of the dynamics of the stochastic differential systems. This extends earlier work on the effect of noise on single bifurcations and an isolated period doubling cascade (Hirsch *et al.*, 1982; Crutchfield *et al.*, 1982; Juel *et al.*, 1997) to more complicated bifurcation scenarios. A preliminary report of this work (Eaves, 2015) contains additional results including some generalizations of the analysis of Stone & Holmes.

A.2 Locating the noise effect; the stochastic Duffing equation

We add small noise terms to the system (A.1) to arrive at the stochastic ODEs,

$$\dot{x} = y + \varepsilon_x \xi_x(t), \tag{A.4}$$

$$\dot{y} = x - x^3 - \gamma y + \beta x^2 y + \varepsilon_y \xi_y(t), \tag{A.5}$$

where $(\varepsilon_x, \varepsilon_y) \ll 1$ parametrise the noise strengths and the precise form of the processes $\xi_x(t)$ and $\xi_y(t)$ will be prescribed presently.

In the vicinity of the origin, the deterministic system (A.1) can be linearised to show that this fixed point is a saddle with eigenvalues,

$$\lambda_\pm = \frac{1}{2}(-\gamma \pm \sqrt{\gamma^2 + 4}) \equiv \begin{cases} \lambda, \\ -\mu. \end{cases} \tag{A.6}$$

The coordinate axes can also be re-orientated so as to align them with the stable and unstable eigenvectors, which amounts to the linear transformation,

$$(x, y) \to (x_1, x_2), \quad x_1 = \frac{y - \lambda x}{\sqrt{1 + \lambda^2}} \quad x_2 = \frac{y + \mu x}{\sqrt{1 + \mu^2}}.$$

We may then define the local neighbourhood of the origin by $\mathcal{D}$, with $|x_1| \leq \delta$ and $|x_2| \leq \delta$ for some $\delta \ll 1$.

With reference to $\mathcal{D}$, we now prescribe the noise terms according to three specific scenarios:

I. Noisy origin: $\xi_x = \xi_y = 0$ outside of $\mathcal{D}$.

II. Deterministic origin: $\xi_x = \xi_y = 0$ inside $\mathcal{D}$.

III. Noise everywhere: $(\xi_x, \xi_y) \neq 0$.

Wherever the noise terms are not set to zero, we fix $\xi_x(t)$ and $\xi_y(t)$ to be independent realizations of the Gaussian white noise process $\xi(t)$ with

$$\mathbb{E}(\xi(t)) = 0, \quad \mathbb{E}(\xi(t)\xi(s)) = \delta(t-s). \tag{A.7}$$

For each scenario, we solve the stochastic ODEs numerically using a weak second-order scheme (see Wilkie, 2004) with a fixed time-step of $\Delta t = 0.01$. The timings of the pulses and antipulses can then be extracted by finding the largest maxima of $|x(t)|$ over the times $t_n = n\Delta t$, $n = 0, 1, \ldots$ (*i.e.* we avoid any interpolation within time-steps); their differences furnish the pulse spacings $\Delta_n = t_n - t_{n-1}$.

Spacing distributions for the three scenarios I–III are displayed in Figure A.4 for the same choices of β and γ as in Figure A.1. Evidently, the spacing distributions for scenarios II and III are practically indistinguishable, with mean spacings $\langle\Delta\rangle \approx 10.2$. By contrast, scenario I is different, with a mean spacing of $\langle\Delta\rangle \approx 13.2$. Given that the stochastic perturbations reduce $\langle\Delta\rangle$, the higher mean spacing for scenario I suggests that the effective noise level is lower than in the other two scenarios. Another statistic of interest is the relative frequency for polarity reversal (the frequency at which a pulse switches to an antipulse, or *vice versa*). For the three scenarios this statistic is measured to be approximately 0.72, 0.51 and 0.52, all ± 0.01, again confirming the equivalence of scenarios II and III, but not of I. In other words, adding noise everywhere is not equivalent to stochastically perturbing the dynamics in the vicinity of the origin.

Stone & Holmes assume that γ and β are relatively small and set $\varepsilon_x = \varepsilon_y = \varepsilon$ for the noise strengths. In this limit, $\lambda \approx \mu \approx 1$ and the homoclinic orbit is given by

$$H(t) = \sqrt{2}\,\mathrm{sech}(t), \tag{A.8}$$

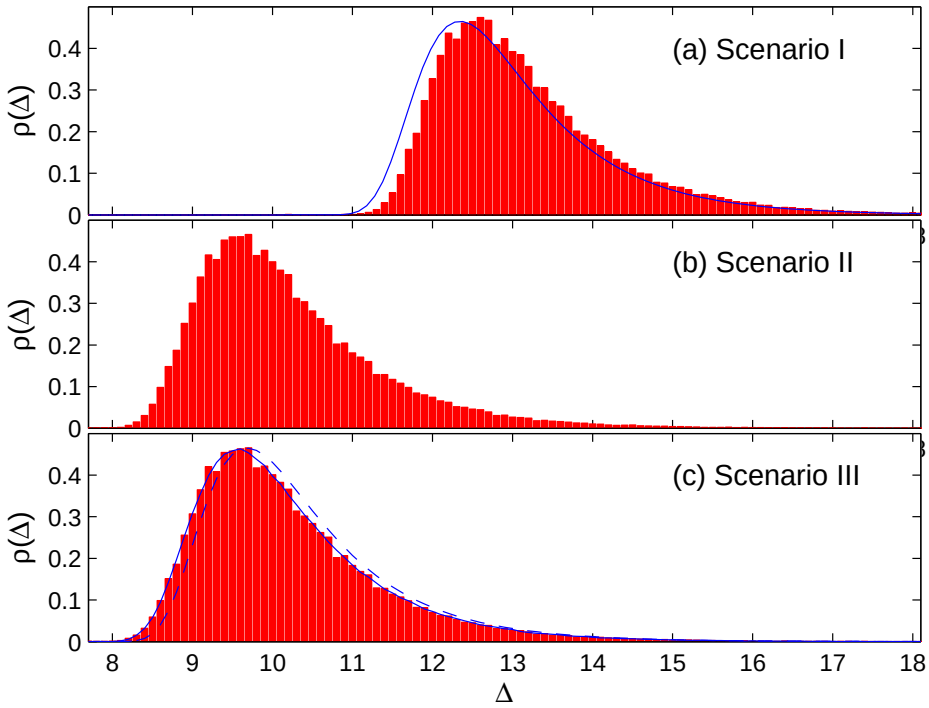

Figure A.4: Histograms of pulse spacings for the stochastic Duffing equation with $\varepsilon_x = \varepsilon_y = 0.0006$, $\beta = 0.1$ and $\gamma = 0.08$, for scenarios I–III. In (a), the blue line shows the Stone & Holmes distribution in (A.10). In (c), the solid blue line shows the distribution predicted by the asymptotic timing map in (A.29), and the dashed line shows the approximation (A.32).

which indicates that

$$T_R \approx 2 \log \left(\frac{4}{\delta} \right) \tag{A.9}$$

is the time-of-flight outside of $\mathcal{D}$ (*i.e.* the time taken to proceed from $x \approx y \approx \delta/\sqrt{2}$ to $x \approx -y \approx \delta/\sqrt{2}$). For homoclinic conditions, Stone & Holmes then derive a form for the distribution of pulse spacings within $\mathcal{D}$,

$$\begin{aligned} \rho(\Delta) = \; & \tfrac{2\lambda\sqrt{\Lambda}e^{-\Lambda}}{\sqrt{\pi}(1-e^{-2\lambda s})}, \qquad \Lambda = \tfrac{\lambda\delta^2}{\varepsilon^2(e^{2\lambda s}-1)}, \\ & s = \Delta - T_R + \tfrac{1}{2\lambda} \ln \left(1 + \tfrac{\lambda}{\mu} \right), \end{aligned} \tag{A.10}$$

which is compared with numerical data for scenario I in Figure A.4. For larger spacing, the factor $1 - e^{-2\lambda s} \to 1$ in the denominator of $\rho(\Delta)$. It then follows that $Z = e^{-\lambda\Delta}$ is a Gaussian random variable with variance

$$\sigma_{SH}^2 = \frac{\delta\varepsilon}{16}; \tag{A.11}$$

up to a scaling, the variable Z corresponds to the coordinate at which the incoming trajectory intersects the border of $\mathcal{D}$.

Stone & Holmes continue on to establish that the mean pulse spacing is

$$\langle \Delta \rangle \sim T_R + \frac{1}{\lambda} \ln\left(\frac{\delta}{\varepsilon}\right) \operatorname{erf}\left(\frac{\delta}{\varepsilon}\sqrt{\mu}\right). \tag{A.12}$$

For $\delta\sqrt{\mu} \gg \varepsilon$, as in our example, this reduces to

$$\langle \Delta \rangle \sim 2\log\left(\frac{4}{\delta}\right) + \frac{1}{\lambda}\log\left(\frac{\delta}{\varepsilon}\right) \sim \log\left(\frac{16}{\varepsilon\delta}\right), \tag{A.13}$$

which implies $\langle \Delta \rangle \sim 12.6$, and is close to the measured value of 13.2 for scenario I; computing the mean of (A.10) gives the somewhat better value of 13.0. Evidently, the theory of Stone & Holmes can be applied to scenario I. Notably, the mean spacing in (A.13) depends on δ, which has no significance in scenario III. The analysis with noise acting purely near the origin cannot therefore characterize the noise-everywhere case.

A.3 Spacing maps

A.3.1 Pulse-train asymptotics

To predict the timing between the pulses and antipulses of a noisy train, we add stochastic perturbations to the singular perturbation theory of Balmforth *et al.* (1994). To pave the way, we first write our three model systems in the compact vectorial form,

$$\frac{\mathrm{d}}{\mathrm{d}t}\boldsymbol{x} = A\boldsymbol{x} + \boldsymbol{f}(\boldsymbol{x}) + \varepsilon\boldsymbol{\xi}, \tag{A.14}$$

where $\boldsymbol{x}$ is the vector of dependent variables, A is a constant matrix, the nonlinear terms are represented by $\boldsymbol{f}(\boldsymbol{x})$, and $\varepsilon\boldsymbol{\xi}$ denotes the vector of noise terms.

The matrix A contains the parameter γ, which we adjust to be order $\epsilon \ll 1$ close to the homoclinic value γ_*: $\gamma = \gamma_* + \epsilon\gamma_1$. The small parameter ϵ therefore measures the breakage of the homoclinic connection in parameter space, and we assume that $\varepsilon = O(\epsilon)$ so that stochastic perturbations are introduced at the same order. The adjustment of γ requires us to expand A as $A_0 + \epsilon A_1$.

Let $\boldsymbol{H}(t) = (H^x, H^y)$ or (H^x, H^y, H^z) be the homoclinic pulse. Our model systems are reflection symmetric such that the antipulse is either $-\boldsymbol{H}(t)$ for the Duffing and normal-form cases, or $(-H^x, -H^y, H^z)$ for the Shimizu–Morioka model.

To distinguish the pulses and antipulses, we therefore introduce the operation $\vartheta \boldsymbol{H} = \theta \boldsymbol{H}$ or $(\theta H^x, \theta H^y, H^z)$, defined using the polarity $\theta = \pm 1$.

We now look for a solution of the form,

$$\boldsymbol{x} = \sum_{k=-\infty}^{\infty} \boldsymbol{H}_k + \epsilon \boldsymbol{R} + ..., \tag{A.15}$$

where $\boldsymbol{H}_k = \vartheta_k \boldsymbol{H}(t - t_k)$ denotes a homoclinic solution centred at time t_k, and $\epsilon \boldsymbol{R}$ denotes a remainder term which accounts for the fact that the overlap of neighbouring homoclinic orbits does not vanish and so the first sum in (A.15) is not an exact solution. However, we take the pulses to be well separated so that $\boldsymbol{H}_k \cdot \boldsymbol{H}_{k\pm 1} = O(\epsilon)$. In other words, we consider the distinguished limit in which the breakage of the homoclinic connection, the overlap of the pulses and the stochastic perturbation are all $O(\epsilon)$.

Substituting the ansatz (A.15) into (A.14) leads to a cancellation of the order-one terms in view of the equation satisfied by each $\boldsymbol{H}_k$. At the following order $O(\epsilon)$, in the vicinity of t_k, we obtain

$$\mathcal{L}_k \boldsymbol{R} = \frac{1}{\epsilon} \boldsymbol{J}(\boldsymbol{H}_k)(\boldsymbol{H}_{k+1} + \boldsymbol{H}_{k-1}) + A_1 \boldsymbol{H}_k + \frac{\varepsilon}{\epsilon} \boldsymbol{\xi}, \tag{A.16}$$

where

$$\mathcal{L}_k = \frac{\mathrm{d}}{\mathrm{d}t} - A_0 - \boldsymbol{J}(\boldsymbol{H}_k), \tag{A.17}$$

and $J_{ij}(\boldsymbol{x}) = \partial f_i / \partial x_j$ is the Jacobian matrix of the nonlinear function $\boldsymbol{f}(\boldsymbol{x})$. Note that the true operator acting on R involves the sum $\sum_k \boldsymbol{J}(\boldsymbol{H}_k)$, which includes all the pulses and antipulses. This sum is sharply peaked about each homoclinic trajectory, and so we may approximate the full operator by splitting up the sum and requiring R to satisfy a simpler equation for each k, incurring an error of higher order in ϵ.

The operator $\mathcal{L}_k$ has adjoint

$$\mathcal{L}_k^\dagger = -\frac{\mathrm{d}}{\mathrm{d}t} - A_0^\dagger - \boldsymbol{J}(\boldsymbol{H}_k)^\dagger, \tag{A.18}$$

with null vector $\boldsymbol{N}_k \neq 0$ satisfying $\mathcal{L}_k^\dagger \boldsymbol{N}_k = 0$. The null vector again possesses a reflection symmetry for the three models. For the Duffing and normal-form examples, we take the null vector to be $\boldsymbol{N}_k = \vartheta_k \boldsymbol{N} = \theta_k \boldsymbol{N}(t - t_k)$ in terms of the k^{th} polarity and the null vector $\boldsymbol{N} = (N^x(t), N^y(t), N^z(t))$ of the homoclinic pulse.

For the Shimizu–Morioka model, we set $\boldsymbol{N}_k = \vartheta_k \boldsymbol{N} = (\theta_k N^x(t-t_k), \theta_k N^y(t-t_k), N^z(t-t_k))$.

Now we may take the dot product of (A.16) with $\boldsymbol{N}_k$ and integrate to obtain

$$0 = \int_{-\infty}^{\infty} \boldsymbol{N}_k \cdot \left[\frac{1}{\epsilon} \boldsymbol{J}(\boldsymbol{H}_k)(\boldsymbol{H}_{k+1} + \boldsymbol{H}_{k-1}) + A_1 \boldsymbol{H}_k + \frac{\varepsilon}{\epsilon} \boldsymbol{\xi} \right] \mathrm{d}t. \tag{A.19}$$

With suitable changes of integration variable, and bearing in mind the dependences on polarity, the first two overlap terms on the right of (A.19) may be written more compactly in terms of pulse spacing, $\Delta_k = t_k - t_{k-1}$, and the integral function,

$$F_{k,l}(\Delta) = -\frac{1}{\epsilon} \int_{-\infty}^{\infty} \vartheta_k \boldsymbol{N}(t) \cdot \boldsymbol{J}(\vartheta_k \boldsymbol{H}(t)) \vartheta_l \boldsymbol{H}(t+\Delta) \, \mathrm{d}t. \tag{A.20}$$

In particular, we may write the spacing map,

$$F_{k,k+1}(-\Delta_{k+1}) = c + m\eta_k - F_{k,k-1}(\Delta_k), \tag{A.21}$$

where

$$c = \int_{-\infty}^{\infty} \boldsymbol{N}(t) \cdot A_1 \boldsymbol{H}(t) \, \mathrm{d}t, \tag{A.22}$$

and the noise term is written as the product of a Gaussian random variable η_k with zero mean and unit variance, and an amplitude m given by

$$m^2 = \int_{-\infty}^{\infty} \sum_{j=1}^{\ell} \left[\frac{\varepsilon_j}{\epsilon} N^j(t) \right]^2 \, \mathrm{d}t, \tag{A.23}$$

where $\ell = 2$ or 3 is the order of each model. Note that (A.21) determines both the spacing and polarity of the next pulse according to the size and sign of the combination, $c + m\eta_k - F_{k,k-1}(\Delta_k)$, respectively. Moreover, the introduction of a new variable, $Z_{k+1} = F_{k,k+1}(-\Delta_{k+1})$, turns (A.21) into a more obvious one-dimensional map with additive noise.

A.3.2 Revisiting Duffing

For the Duffing equation we may write $(H^x, H^y) = (H, \dot{H})$ and $(N^x, N^y) = (\dot{N}, N)$. The spacing function and detuning constant in (A.19) and (A.22) can then be written in the more transparent forms,

$$F_{k,l}(\Delta) = \frac{1}{\epsilon} \theta_k \theta_l \int_{-\infty}^{\infty} [3N(t) + \beta \dot{N}(t)] H^2(t) H(t+\Delta) \, \mathrm{d}t \tag{A.24}$$

and

$$c = -\gamma_1 \int_{-\infty}^{\infty} N(t)\dot{H}(t)\ \mathrm{d}t. \tag{A.25}$$

Provided the pulses are well spaced, we may further reduce $F_{k,l}(\Delta)$ using the tails of the homoclinic orbit:

$$\begin{aligned} H(t+\Delta_k) &\sim h_\infty e^{-\mu(t+\Delta_k)}, \\ H(t-\Delta_{k+1}) &\sim h_0 e^{\lambda(t-\Delta_{k+1})}. \end{aligned} \tag{A.26}$$

Hence,

$$F_{k,k+1}(-\Delta_{k+1}) \sim \frac{h_0}{\epsilon}\Theta_{k+1}e^{-\lambda\Delta_{k+1}}\int_{-\infty}^{\infty}(3N+\beta\dot{N})H^2e^{\lambda t}\ \mathrm{d}t \equiv \frac{A}{\epsilon}\Theta_{k+1}e^{-\lambda\Delta_{k+1}}, \tag{A.27}$$

and

$$F_{k,k-1}(\Delta_k) \sim \frac{h_\infty}{\epsilon}\Theta_k e^{-\mu\Delta_k}\int_{-\infty}^{\infty}(3N+\beta\dot{N})H^2e^{-\mu t}\ \mathrm{d}t \equiv \frac{B}{\epsilon}\Theta_k e^{-\mu\Delta_k}, \tag{A.28}$$

where the relative polarity is $\Theta_k = \theta_k\theta_{k-1}$. We are then left with the timing map

$$\Theta_{k+1}e^{-\lambda\Delta_{k+1}} = C + \Theta_k D e^{-\mu\Delta_k} + \sigma\eta_k, \tag{A.29}$$

where $C = \epsilon c/A$, $D = -B/A$ and $\sigma = \epsilon m/|A|$.

When γ and β are small, the limiting analytical form of the homoclinic pulse in (A.8) along with $N = \dot{H}$ imply $C \to \epsilon\gamma_1/12$, $D \to 1$ and $\sigma \to (\varepsilon_y^2/3 + 7\varepsilon_x^2/15)^{1/2}/8$. For the numerical example provided in Section A.2, these constants turn out to be $C = -1.3621\times10^{-6}$, $D \approx 1.3767$ and $\sigma \approx 7.8532\times10^{-5}$. The resulting spacing map is illustrated in Figure A.5, and is double-valued owing to polarity reversals (see Balmforth & Spiegel, 2004, for a full discussion). Sample iterations with added noise are also included in the figure, and scatter increasingly far from the deterministic map on raising the noise level. The spacing distribution determined by iterating the resulting map a million times also shows satisfying agreement with that measured from solving the stochastic ODE (see Figure A.4(c); the mean pulse spacing from the map is $\langle\Delta\rangle \approx 10.2$).

We can convert (A.29) into the more conventional looking one-dimensional map,

$$Z_{k+1} = C + \mathrm{sgn}(Z_k)D|Z_k|^{\mu/\lambda} + \sigma\eta_k. \tag{A.30}$$

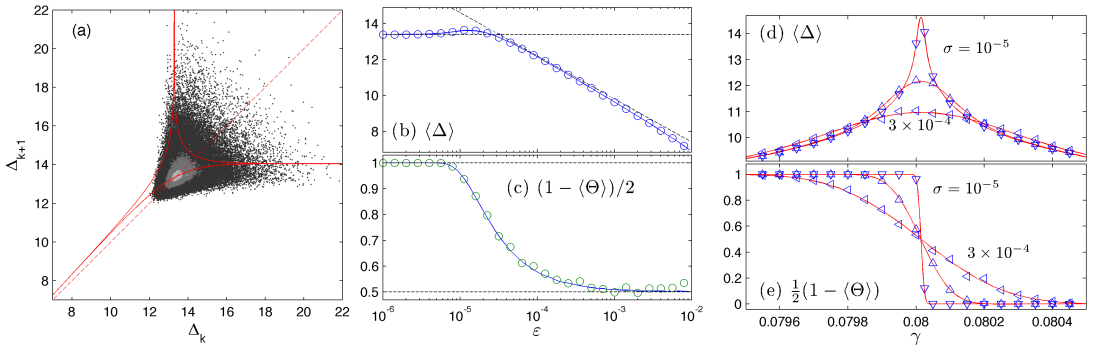

Figure A.5: (a) The deterministic spacing map of the Duffing equation for $\gamma = 0.08$ and $\beta = 0.1$ (red curves); the dashed line is the diagonal. The points show iterations of the noisy map with $\sigma = 10^{-5}$, 3×10^{-6} and 10^{-6} (with the grey shading increasing with σ). (b) and (c) show how the mean pulse spacing, $\langle\Delta\rangle$, and frequency of polarity reversal, $(1-\langle\Theta\rangle)/2$, vary with noise level ε for numerical computations of the stochastic ODEs (circles) and from iterations of the map (solid lines). The dashed lines show the asymptotes in (A.33) for (b), and the limits $\frac{1}{2}$ and 1 in (c). (d) and (e) plot mean spacings and reversal frequencies against γ for $\sigma = 10^{-5}$, 10^{-4} and 3×10^{-4}; solid lines show results from the map, and triangles from the stochastic ODEs.

where $Z_k = \Theta_k e^{-\lambda\Delta_k}$ is equivalent to a scaled coordinate on a Poincaré section at the border of the neighbourhood of the origin, as in Section A.2. The breakage of the homoclinic connection is measured by C. The second term on the right of (A.30) represents the effect of the previous close passage by the origin. The final noise term is additive, has an amplitude set by $\sigma = O(\epsilon)$, and corresponds to the uncertainty in the location where the trajectory re-enters the origin's vicinity due to stochastic perturbation of the nearly homoclinic pulse. In Stone & Holmes' analysis, noise near the origin generates uncertainty in the residence time there, equivalent to a stochastic perturbation of the second term on the right of (A.30). The corresponding amplitude, σ_{SH} in (A.11), is $O(\delta\epsilon)$, which is $O(\delta) \ll 1$ smaller than the noise term in (A.30). This rationalizes our observation that scenarios II and III are equivalent, but scenario I is different and effectively less noisy.

Given that $\mu > \lambda$, the map (A.30) has a stable deterministic fixed point $Z_k = Z_* = O(\epsilon)$. When the noise level is relatively low, one then expects an approximate

stationary distribution for Z_k given by Reimann & Talkner (1991)

$$\rho_Z(Z) = \frac{1}{\sqrt{2\pi\Sigma^2}} \exp\left[-\frac{(Z-Z_*)^2}{2\Sigma^2}\right], \tag{A.31}$$

where $\Sigma = \sigma/\sqrt{1-[f'(Z_*)]^2}$ and $|f'(Z)| = \mu|Z|^{\mu/\lambda-1}/\lambda$. The corresponding spacing distribution is

$$\rho_\Delta(\Delta) = \frac{\lambda e^{-\lambda\Delta}}{\sqrt{2\pi\Sigma^2}} \left\{\exp\left[-\frac{(e^{-\lambda\Delta}-Z_*)^2}{2\Sigma^2}\right] + \exp\left[-\frac{(e^{-\lambda\Delta}+Z_*)^2}{2\Sigma^2}\right]\right\}, \tag{A.32}$$

which is also drawn in Figure A.4(c). From $\rho_\Delta(\Delta)$, we may estimate the mean pulse spacing:

$$\langle\Delta\rangle = \int_0^\infty \Delta\rho_\Delta(\Delta)\,\mathrm{d}\Delta \sim \begin{cases} \lambda^{-1}\log\left(Z_*^{-1}\right), & \Sigma \ll |Z_*|, \\ \lambda^{-1}\log\left(\Sigma^{-1}\right) + \frac{1}{2}\lambda^{-1}(\gamma_e + \log 2), & |Z_*| \ll \Sigma, \end{cases} \tag{A.33}$$

where γ_e is Euler's gamma constant. The two limits here correspond to the deterministic spacing value at the fixed point and the noise-driven spacing under homoclinic conditions. The latter gives the leading-order estimate

$$\langle\Delta\rangle \sim \lambda^{-1}\log\left(\Sigma^{-1}\right) \to \tfrac{1}{2}\log\left(\frac{192}{\varepsilon_y^2 + 7\varepsilon_x^2/5}\right) \tag{A.34}$$

for small γ and β, providing a counterpart to Stone & Holmes' prediction in (A.13). Figure A.5(b) plots mean pulse spacing against noise level $\varepsilon = \varepsilon_y$ with $\varepsilon_x = 0$, for both numerical solutions of the stochastic ODEs and iterations of the spacing map; the agreement is again satisfying. Both sets of data converge to the limits in (A.33) for relatively low and high noise levels, at least until the weak-noise approximation underlying (A.32) fails for $\varepsilon > 10^{-3}$.

For the value of γ in Figures A.4 and A.5, a periodic train of pulses and antipulses emerges without noise ($\gamma < \gamma_*$). The relative frequency for polarity reversal, $\frac{1}{2}(1 - \langle\Theta\rangle)$, is therefore one. As the deterministic dynamics becomes washed out by noise, on the other hand, the polarity reverses on average every other excursion away from the origin, and so $\frac{1}{2}(1-\langle\Theta\rangle) \to \frac{1}{2}$. The passage between these two limits is illustrated in Figure A.5(c). The progression of the mean spacing and polarity reversal frequency as γ passes through its homoclinic value is shown in Figure A.5(d) and (e) for different levels of noise; the noise limits the mean spacings reached for $\gamma \to \gamma_*$ and smooths out the switch from $\frac{1}{2}(1-\langle\Theta\rangle) = 1$ to 0. All the while, there is agreement between the results from the map and stochastic ODEs.

A.4 Noisy Lorenz maps; the stochastic Shimizu–Morioka model

For the Shimizu–Morioka model, the eigenvalues at the origin are

$$-\beta, \quad -\tfrac{1}{2}(-\gamma - \sqrt{4+\gamma^2}) \quad \text{and} \quad \lambda = \tfrac{1}{2}(\sqrt{4+\gamma^2} - \gamma). \tag{A.35}$$

We consider the case $\frac{1}{2}(-\gamma - \sqrt{4+\gamma^2}) > \beta$, and so the homoclinic orbit therefore has the leading-order tails,

$$\begin{aligned} \boldsymbol{H} &\sim (h_0^x, h_0^y, 0)\, e^{\lambda t} \quad \text{as } t \to -\infty, \\ \boldsymbol{H} &\sim (0, 0, h_\infty^z)\, e^{-\beta t} \quad \text{as } t \to \infty, \end{aligned} \tag{A.36}$$

(omitting the other stable eigenvalue is equivalent to assuming that strong contraction in the corresponding direction renders trajectories essentially two-dimensional when passing near the origin; *cf.* Figure A.2). Thence,

$$F_{k,k-1}(\Delta_k) \sim \frac{h_\infty^z}{\epsilon} e^{-\beta\Delta_k} \int_{-\infty}^{\infty} H^x N^y e^{-\beta t}\, \mathrm{d}t \equiv \frac{B}{\epsilon} e^{-\beta\Delta_k}, \tag{A.37}$$

and

$$F_{k,k+1}(-\Delta_{k+1}) \sim \frac{h_0^x}{\epsilon} \Theta_{k+1} e^{-\lambda\Delta_{k+1}} \int_{-\infty}^{\infty} (H^z N^y - 2\beta H^x N^z) e^{\lambda t} \mathrm{d}t \equiv -\frac{A}{\epsilon} e^{-\lambda\Delta_{k+1}} \Theta_{k+1}, \tag{A.38}$$

which furnish the spacing map,

$$\Theta_{k+1} e^{-\lambda\Delta_{k+1}} = C + D e^{-\beta\Delta_k} + \sigma\eta_k, \tag{A.39}$$

where

$$C = \epsilon\gamma_1 A^{-1} \int_{-\infty}^{\infty} N^y H^y\, \mathrm{d}t. \tag{A.40}$$

Here, again, η_k is a Gaussian random variable with zero mean and unit variance, the noise strength is $\sigma = \epsilon m/|A|$ and $D = B/A$, but with the different definitions of A and B implicit in (A.37) and (A.38).

The (single-valued) spacing map in (A.39) is illustrated in Figure A.6 for the parameter settings of Figure A.2. Panel (a) compares the deterministic map with spacing data extracted from a numerical solution of the ODEs. For this example, the agreement between the two is less satisfactory than for the Duffing example,

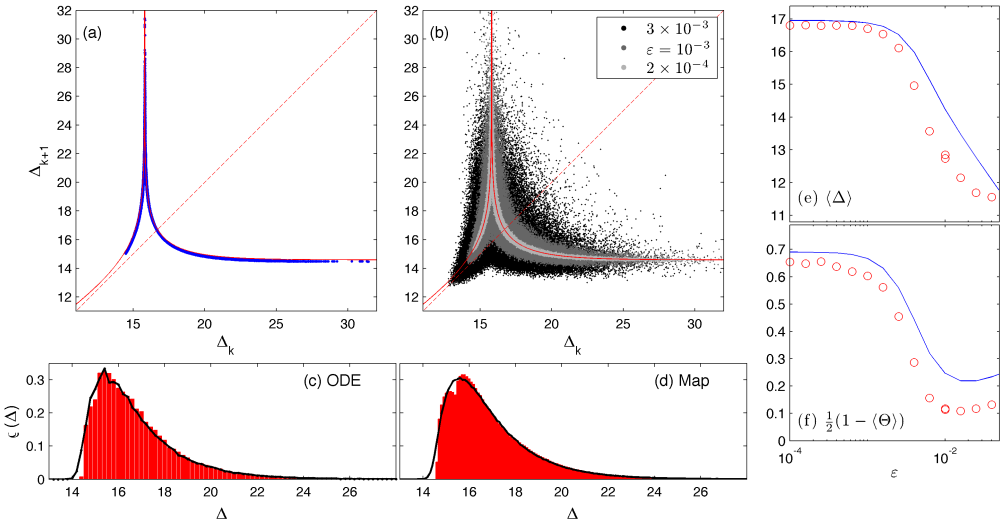

Figure A.6: Spacing map for the Shimizu–Morioka system with $\gamma = 1.19$ and $\beta = 0.4$. In (a) the spacing map (solid line) is compared with timing data extracted from a solution to the deterministic ODEs (points); the dashed line shows the diagonal. In (b), the spacing map is redrawn, and iterates of the noisy map are added with $\varepsilon = 2 \times 10^{-4}$, 10^{-3} and 3×10^{-3} (points, with grey shading increasing with ε). Underneath we show spacing distributions computed using (c) the stochastic ODEs and (d) the spacing map. The histograms indicate the deterministic case; the lines represent noisy cases with $\varepsilon = 10^{-3}$. (d) and (e) show the mean spacing and polarity reversal frequency against noise level; the solid lines show results from the map, the circles from the stochastic ODEs.

primarily because the proximity to homoclinicity is less well tuned (the pulses are less separated) and because we neglect the second stable eigenvalue in constructing the map.

Note that the iterates from the ODE only superficially form a one-dimensional map; fractal structure is hidden in the finer details of the spacing plot (see Balmforth *et al.*, 1994). This is familiar from the Lorenz system, where the return maps from Poincaré sections conceal fractal structure (see Sparrow, 2012). Indeed, by defining $Z_k = \Theta_k \exp(-\lambda \Delta_k)$, we may turn the spacing map into the more standard form

$$Z_{k+1} = C + \mathrm{sgn}(Z_k) B |Z_k|^{\beta/\lambda} + \sigma \eta_k, \tag{A.41}$$

which, without the noise term, is equivalent to the return map used to illustrate

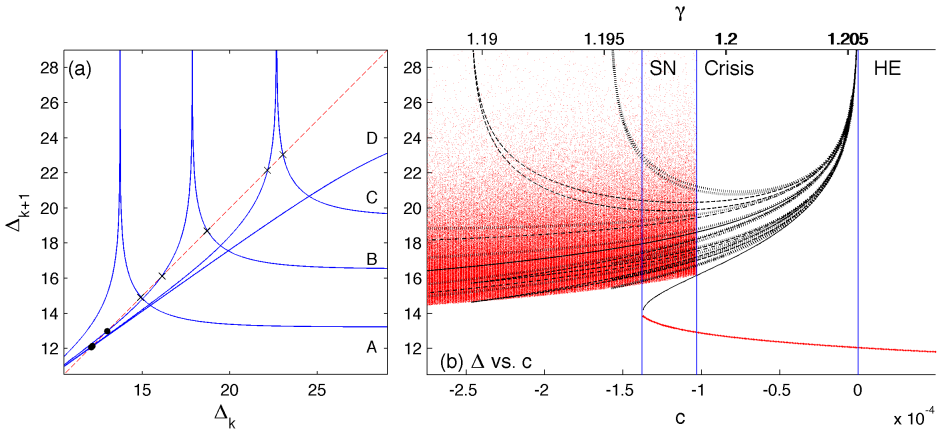

Figure A.7: (a) A sequence of spacing maps for $\gamma = 1.17$ (A), 1.1986 (B), 1.2044 (C) and 1.2054 (D), showing the change in structure due to the homoclinic explosion (HE), crisis of the strange attractor and the saddle node (SN); stable fixed points are plotted at dots, unstable ones as crosses. (b) a bifurcation diagram showing spacing against homoclinicity parameter C. Red dots indicate map iterations with transients removed, obtained by both raising and lowering C. The black lines show the unstable fixed points (solid), and period-2 (dot-dashed), period-3 (dashed) and period-4 (dotted) orbits.

the Lorenz bifurcation sequence.

To illustrate the effect of noise, we set $\varepsilon_x = \varepsilon_y = \varepsilon_z = \varepsilon$. As displayed in the second panel in Figure A.6, noise smears out the spacing iterations around the curve of the deterministic map and shortens the lowest spacings sampled by the train (panel (b)). Simultaneously, the noise smooths out any structure in the spacing distribution (panels (c) and (d)), which have exponential tails, both with and without noise (*cf.* Stone & Holmes, 1991). As shown in panels (d) and (e), noise lowers both the mean spacing and frequency of polarity reversal, although the comparison of the results from the map and stochastic ODEs is again less satisfactory.

The deterministic part of the spacing map (A.41) (setting $\sigma = 0$) captures the bifurcations to chaos that characterize nearly homoclinic Lorenz flow (provided the 'saddle index' $\beta/\lambda < 1$): at $C = 0$, an infinite number of unstable periodic orbits appear in a homoclinic explosion. This set does not immediately form a strange attractor, however, because the set is contained within the basin of attraction of

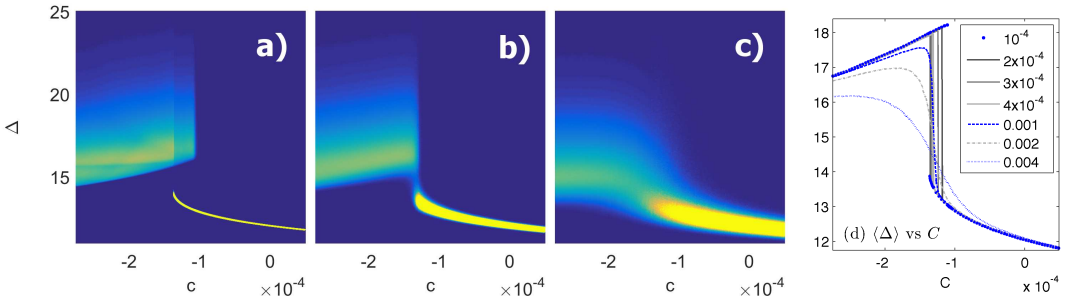

Figure A.8: Noisy bifurcation diagrams of spacing against C for (a) $\varepsilon = 10^{-4}$, (b) 10^{-3} and (c) 4×10^{-3}, with $\beta = 0.4$. In each case a fixed number of map iterations (with transients removed) are turned into a density on the $(C, \Delta)-$plane. The corresponding mean spacings are shown in (d), together with additional results for more values of ε (as indicated).

a coexisting stable fixed point. As C is decreased below zero, the set moves out of the basin of attraction at a boundary crisis, to turn into a strange attractor. At a sufficiently negative value of C, the stable fixed point disappears in a saddle node, leaving the strange set as the only attractor. These three bifurcations are all familiar from the Lorenz equations (see Sparrow, 2012), and their impact on the map structure is illustrated in the sequence shown in Figure A.7. Also shown is a bifurcation diagram plotting spacing iterations from the map against the homoclinicity parameter C, together with all the unstable fixed points and period-2, 3 and 4 orbits (some of which disappear at smaller C in secondary homoclinic bifurcations). Between the saddle-node and crisis, both the stable fixed point and strange attractor co-exist, and the system is hysteretic if C is raised or lowered through this interval.

The effect of adding noise to the map on the bifurcation diagram is shown in Figure A.8. The noise widens and smooths the spacing distributions around the stable fixed point and strange attractor. More importantly, however, it enables iterations to escape from the chaotic attractor for some of the parameter settings for which the two attractors co-exist deterministically, narrowing the window of C (and the number of iterations) for which hysteresis can be observed. For sufficiently strong noise, the hysteresis of the deterministic system becomes completely lost, with the broad peak in spacing density adjusting sharply in the vicinity of the

saddle node from the relic of the strange set to the noisy stable fixed point.

A.5 A stochastic Shilnikov system

The normal-form model has a saddle at the origin with a one-dimensional unstable direction and a two-dimensional stable manifold in which the dynamics is a focus. We may write $(H^x, H^y, H^z) = (H, \dot{H}, \ddot{H})$ and $(N^x, N^y, N^z) = (\ddot{N}, \dot{N}, N)$. For the homoclinic orbit,

$$H \sim \begin{cases} h_0 e^{\lambda t} & \text{as } t \to -\infty, \\ h_\infty e^{-\mu t} \cos(\omega t + \phi) & \text{as } t \to \infty, \end{cases} \tag{A.42}$$

where $-\mu \pm i\omega$ denotes the complex stable eigenvalue, for some h_0, h_∞ and ϕ. With these tails for $H(t)$, we find

$$F_{k,k+1}(-\Delta_{k+1}) \sim \frac{3}{\epsilon} h_0 \Theta_{k+1} e^{-\lambda\Delta_{k+1}} \int_{-\infty}^{\infty} NH^2 e^{\lambda t}\, \mathrm{d}t \equiv \frac{A}{\epsilon} e^{-\lambda\Delta_{k+1}} \Theta_{k+1}, \tag{A.43}$$

and

$$\begin{aligned} F_{k,k-1}(\Delta_k) &\sim \frac{3}{\epsilon} h_\infty \Theta_k e^{-\mu\Delta_k} \int_{-\infty}^{\infty} NH^2 e^{-\mu t} \cos[\omega(t+\Delta_k)+\phi]\, \mathrm{d}t \\ &\equiv \frac{B}{\epsilon} e^{-\mu\Delta_k} \Theta_k \cos(\omega\Delta_k + \Phi). \end{aligned} \tag{A.44}$$

The spacing map is then

$$\Theta_{k+1} e^{-\lambda\Delta_{k+1}} = C + \Theta_k D e^{-\mu\Delta_k} \cos(\omega\Delta_k + \Phi) + \sigma\eta_k, \tag{A.45}$$

where $D = -B/A$, A and B are now defined by (A.43)–(A.44), the noise term is written as for the other two models, and

$$C = \epsilon\gamma_1 A^{-1} \int_{-\infty}^{\infty} NH\, \mathrm{d}t, \tag{A.46}$$

The map (A.45) was written down previously without any derivation by Arecchi *et al.* (1993).

The deterministic spacing map is illustrated in Figure A.9 and compared with spacing iterations from corresponding numerical solutions of the ODE. The map is rendered double-valued by polarity replication or reversal, and fractal structure

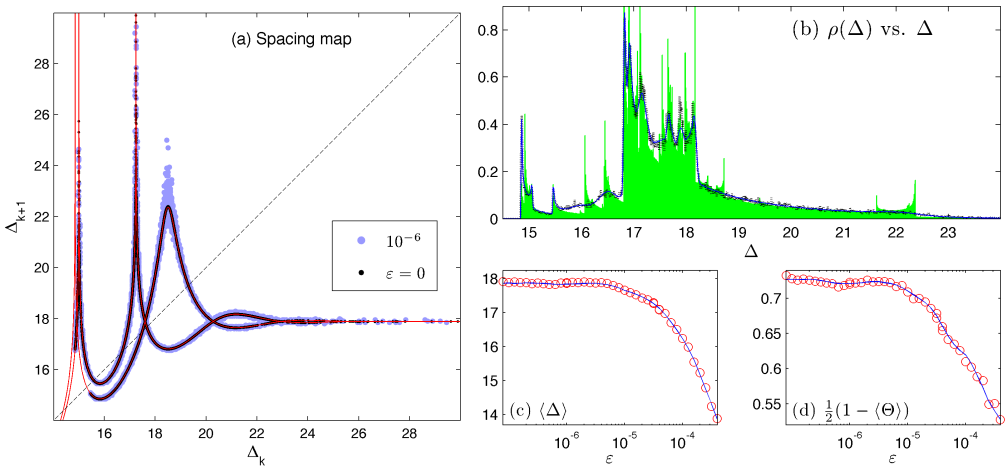

Figure A.9: (a) Spacing map (A.45) for $\gamma = 1.108$ and $\beta = 0.7$. The red lines show the double-valued deterministic map (A.45) and the dashed line is the diagonal. The dark and light (blue) points show 15000 pulse spacings extracted from numerical solutions of the ODE with noise levels of $\varepsilon = 0$ and 10^{-6}. (b) the distribution of pulse spacings from the ODE for $\varepsilon = 10^{-6}$ (dotted line), and from the map for $\varepsilon = 0$ (light green histogram) and 10^{-6} (solid line). Panels (c) and (d) plot the mean spacing and polarity reversal frequency against noise level.

is concealed in the finer details of the ODE data (see Balmforth *et al.*, 1994). The iterates of the map and ODE agree to within the thickness of the plotted curves and points (the mean spacing of both is $\langle\Delta\rangle \approx 17.8$; the polarity reversal frequency is $(1 - \langle\Theta\rangle)/2 = 0.74 \pm 0.01$ for the ODE, and 0.73 ± 0.01 for the map).

We illustrate the effect of noise by taking $\varepsilon_z = \varepsilon$ and $\varepsilon_x = \varepsilon_y = 0$. Figure A.9 includes a weakly noisy solution of the ODE for $\varepsilon = 10^{-6}$; the spacing iterations spread slightly about the deterministic map. Despite this mild effect, the spacing distribution is significantly smoothed by the addition of this low level noise. For $\varepsilon = 0$, the spacing distribution is a highly structured invariant measure that is awkward to compare between map and ODE. The agreement between the noisy distributions with $\varepsilon = 10^{-6}$ is, however, satisfying (see panel (b)), as is the comparison of mean spacing and polarity reversal frequency for varying noise level (panels (c–d)).

The influence of stronger levels of noise is illustrated using the map in Figure A.10. The most significant effect is chiefly at larger spacing for weaker noise levels (in terms of the spread of expected spacing about the deterministic map). The

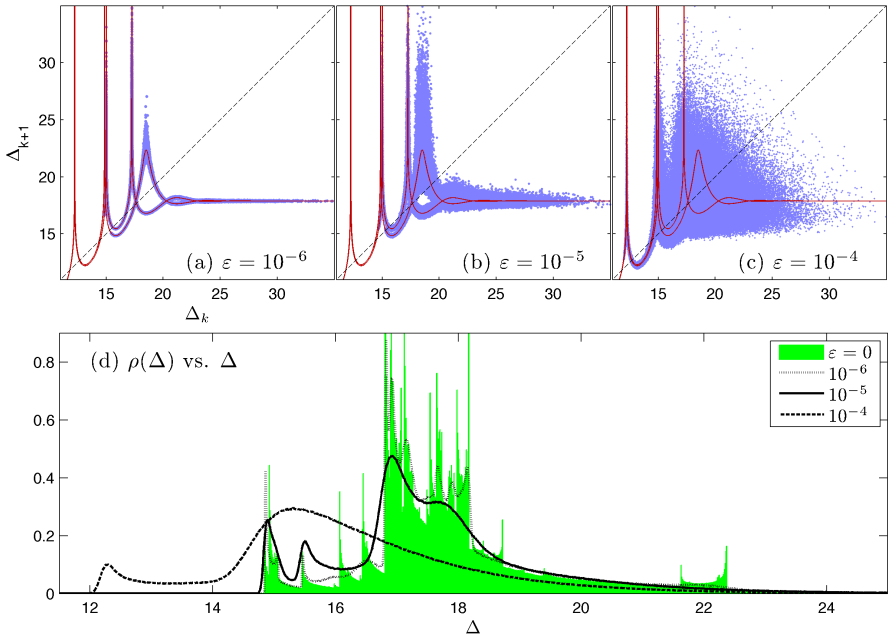

Figure A.10: Noisy Shilnikov maps for (a) $\varepsilon = 10^{-6}$, (b) $\varepsilon = 10^{-5}$ and (c) $\varepsilon = 10^{-4}$ ($\gamma = 1.108$, $\beta = 0.7$). The solid (red) lines show the double-valued deterministic map and the dashed line is the diagonal. Panel (d) shows spacing distributions for the same noise levels; the light (green) histogram shows the deterministic invariant measure.

effect amplifies and spreads to shorter spacings as the noise level is raised. The noise also prompts sudden expansions in the spacing distribution (noise-induced boundary crises, Simiu & Frey, 1996), when fluctuations repeatedly drive iterations beyond fixed points at smaller spacing, exposing additional loops in the curve of the map (corresponding to fewer turns around the origin in the Shilnikov flow). Such expansions eventually lead to a breakdown of the map once spacings are reduced sufficiently that the pulses are no longer widely spaced.

Bifurcation diagrams for the spacing map are shown in Figure A.11. Such diagrams are intricate owing to the fixed point that winds up to infinite period and the associated period-doubling cascades (Shilnikov, 1970; Glendinning & Sparrow, 1984). For the current map, the situation is made yet more convoluted by the pulse-antipulse symmetry, which introduces a second fixed point and set of cascades that appear as a mirror image in the bifurcation diagram (Glendinning, 1984). The first panel of Figure A.11 focusses on a part of the bifurcation diagram for

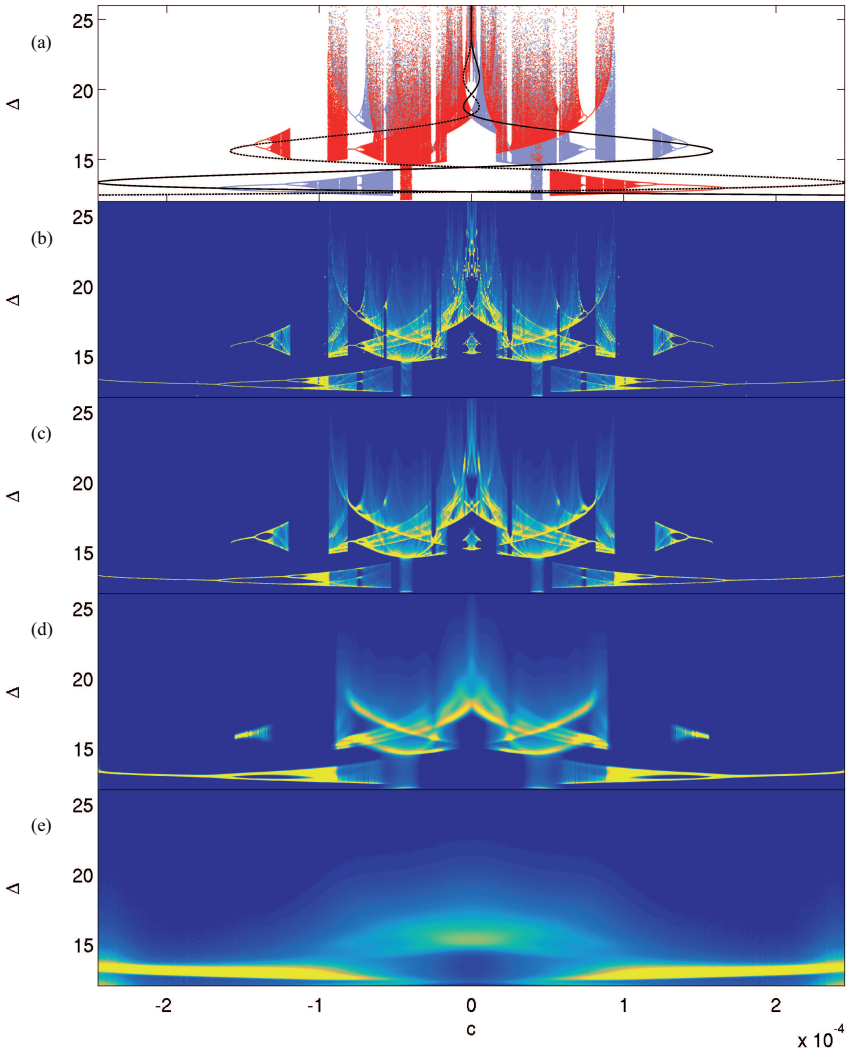

Figure A.11: Bifurcation diagrams for Shilnikov spacing maps. (a) plots fixed points and iterations of the deterministic map against C, with polarity replication (reversals) spacings shown as solid (dashed) lines and blue (red) points. Transients are removed for the iterations. (b)–(e) show iterations of the noisy map with $\varepsilon = 10^{-7}$, 10^{-6}, 10^{-5} and 10^{-4}, collected as densities on the $(C, \Delta)-$plane.

the deterministic map; the loci of the two winding fixed points are visible along with a number of period-doubling cascades, stable periodic-orbit windows and boundary crises. In this plot there are a number of distinct attractors, uncovered by repeating the scans in C with different initial conditions.

The subsequent panels of Figure A.11 show iterations of the noisy map drawn as densities on the $(C, \Delta)-$plane for different levels of noise. For $\varepsilon = 10^{-7}$, the density is a slightly smoothed version of the deterministic case (although the noise exposes another unsampled deterministic attractor around $C = 0$ and $\Delta = 15$). Increasing ε up to 10^{-6} further blurs the structure in the density, truncates the doubling cascades at higher periods, and fills in the narrower windows of stable periodic orbits. By $\varepsilon = 10^{-5}$, the densities become much smoother, many of the attractors merge, and larger spacings become infrequent. For the highest noise level ($\varepsilon = 10^{-4}$) the density is much less structured, with no isolated attractors and the remnants of period-doubling cascades disappearing.

A.6 Conclusions

For a large class of nearly homoclinic systems, we have characterized the most significant effect of noise. The main effect is not on the dynamics near to the fixed point, in contrast to the premise of Stone & Holmes (1990) and others. More significant are stochastic perturbations to the nearly homoclinic transitions away from the fixed point, which critically control where that orbit returns to the neighbourhood of the fixed point, and which in turn dictate the ensuing time of residence. To gauge the true effect of noise, we generalized a singular perturbation analysis of nearly homoclinic pulse trains (Balmforth *et al.*, 1994) to stochastic systems. This furnishes a map that dictates both the pulse spacing and, when the system has reflection symmetry, whether a polarity reversal occurs and a pulse switches to an antipulse or vice versa. The map is a convenient and powerful tool to explore stochastically perturbed homoclinic dynamics and, with a simple change of variable, can be recast into the more conventional form of a one-dimensional map with additive noise. Existing results for such maps can then be immediately carried over to our nearly homoclinic continuous dynamical systems.

Armed with the spacing maps, we explored the impact of noise on the deterministic bifurcation sequences expected near homoclinic connections. In particular, we studied how noise affects the homoclinic explosion of Lorenz flows and the Shilnikov bifurcation sequence. These are the two most commonly encountered scenarios for transition to chaos involving homoclinic orbits. Yet more complex

scenarios are possible, however, and one could envision extending our analysis to other situations. For example, much of what we have considered applies to trains of nearly heteroclinic solutions, or noisy front dynamics. Other examples include heteroclinic networks (Armbruster *et al.*, 2003), bifocal homoclinic solutions (Fowler & Sparrow, 1991) and inverse Shilnikov orbits (Glendinning & Tresser, 1985). Further afield still, one can envision applying the methodology to analysing the dynamics of coherent structure solutions to stochastically perturbed PDEs (see Balmforth, 1995).